# DIR

## Diagnostic and Interventional
# Radiology

# Instructions to Authors

Diagnostic and Interventional Radiology (Diagn Interv Radiol) is a medium for disseminating scientific information based on research, clinical experience, and observations pertaining to diagnostic and interventional radiology. The journal is the double-blind peer-reviewed, bimonthly, open-access publication organ of the Turkish Society of Radiology and its publication language is English. Diagnostic and Interventional Radiology is currently indexed by Science Citation Index Expanded, PubMed MEDLINE, Web of Science, PubMed Central, DOAJ, TUBITAK ULAKBIM TR Index, HINARI, EMBASE, CINAHL, Scopus, Gale and CNKI.

The journal is a medium for original articles, reviews, pictorial essays, technical notes related to all fields of diagnostic and interventional radiology.

The editorial and publication process of the Diagnostic and Interventional Radiology are shaped in accordance with the guidelines of the International Committee of Medical Journal Editors (ICMJE), World Association of Medical Editors (WAME), Council of Science Editors (CSE), Committee on Publication Ethics (COPE), European Association of Science Editors (EASE), and National Information Standards Organization (NISO). The journal is in conformity with the Principles of Transparency and Best Practice in Scholarly Publishing.

## Authorship

Each individual listed as an author should fulfill the authorship criteria recommended by the International Committee of Medical Journal Editors (ICMJE - www.icmje.org). To be listed as an author, an individual should have made substantial contributions to all four categories established by the ICMJE: (a) conception and design, or acquisition of data, or analysis and interpretation of data, (b) drafting the article or revising it critically for important intellectual content, (c) final approval of the version to be published, and (d) agreement to be accountable for all aspects of the work in ensuring that questions related to the accuracy or integrity of any part of the work are appropriately investigated and resolved. Individuals who contributed to the preparation of the manuscript but do not fulfill the authorship criteria should be acknowledged in an acknowledgements section, which should be included in the title page of the manuscript. If the editorial board suspects a case of "gift authorship", the submission will be rejected without further review.

## Ethical standards

For studies involving human or animal participants, the authors should indicate whether the procedures followed were in accordance with the ethical standards of the responsible committee on human and animal experimentation (institutional or regional) and with the Helsinki Declaration. Application or approval number/year of the study should also be provided. The editorial board will act in accordance with COPE guidelines if an ethical misconduct is suspected.

It is the authors' responsibility to carefully protect the patients' anonymity and to verify that any experimental investigation with human subjects reported in the submission was performed with informed consent and following all the guidelines for experimental investigation with human subjects required by the institution(s) with which all the authors are affiliated with. For photographs that may reveal the identity of the patients, signed releases of the patient or of his/her legal representative should be enclosed.

Prospective human studies require both an ethics committee approval and informed consent by participants. Retrospective studies require an ethics committee approval with waiver of informed consent. Authors may be required to document such approval.

All submissions are screened by a similarity detection software (iThenticate by CrossCheck). Manuscripts with an overall similarity index of greater than 20%, or duplication rate at or higher than 5% with a single source are returned back to authors without further evaluation along with the similarity report.

In the event of alleged or suspected research misconduct, e.g., plagiarism, citation manipulation, and data falsification/fabrication, the Editorial Board will follow and act in accordance with COPE guidelines.

## Withdrawal Policy

Articles may be withdrawn under certain circumstances.

The article will be withdrawn if it;

- violates professional ethical codes,
- is subject to a legal dispute,
- has multiple submissions,
- includes fake claims of authorship, plagiarism, misleading data, and false data that may pose a severe health risk.

The editorial board will follow the principles set by COPE (Committee on Publication Ethics) in case of an article withdrawal.

## Manuscript Preparation

The manuscripts should be prepared in accordance with ICMJE-Recommendations for the Conduct, Reporting, Editing, and Publication of Scholarly Work in Medical Journals (updated in May 2022 - https://www.icmje.org/recommendations/).

Original Investigations and Reviews should be presented in accordance with the following guidelines: randomized study – CONSORT, observational study – STROBE, study on diagnostic accuracy – STARD, systematic reviews and meta-analysis PRISMA, nonrandomized behavioral and public health intervention studies – TREND.

Diagnostic and Interventional Radiology will only evaluate manuscripts submitted via the journal's self-explanatory online manuscript submission and evaluation system available at mc04.manuscriptcentral.com/dir. Evaluation process of submitted manuscripts takes 4 weeks on average.

Manuscripts are evaluated and published on the understanding that they are original contributions, and do not contain data that have been published elsewhere or are under consideration by another journal. Authors are required to make a full statement at the time of submission about all prior reports and submissions that might be considered duplicate or redundant publication, and mention any previously published abstracts for meeting presentations that contain partial or similar material in the cover letter. They must reference any similar previous publications in the manuscript.

Authors must obtain written permission from the copyright owner to reproduce previously published figures, tables, or any other material in both print and electronic formats and present it during submission. The original source should be cited within the references and below the reprinted material.

**Cover letter:** A cover letter must be provided with all manuscripts. This letter may be used to emphasize the importance of the study. The authors should briefly state the existing knowledge relevant to the study and the contributions their study make to the existing knowledge. The correspondent author should also include a statement in the cover letter declaring that he/she accepts to undertake all the responsibility for authorship during the submission and review stages of the manuscript.

# Instructions to Authors

**Title page:** A separate title page should be submitted with all manuscripts and should include the title of the manuscript, name(s), affiliation(s), and major degree(s) of the author(s). The name, address, telephone (including the mobile phone number) and fax numbers and e-mail address of the corresponding author should be clearly listed. Grant information and other sources of support should also be included. Individuals who contributed to the preparation of the manuscript but do not fulfill the authorship criteria should also be acknowledged in the title page. Manuscripts should not be signed by more than 6 authors unless they are multicenter or multidisciplinary studies.

## Main document

**Abstract:** All submissions (except for Letters to the Editor) should be accompanied by an abstract limited to 400 words. A structured abstract is only required with original articles and it should include the following subheadings: PURPOSE, METHODS, RESULTS, CONCLUSION.

**Main points:** Each submission should be accompanied by 3 to 5 "main points", which should emphasize the most striking results of the study and highlight the message that is intended to be conveyed to the readers. As these main points would be targeting radiology residents, experts and residents of other fields of medicine, as well as radiology experts, they should be kept as plain and simple as possible. These points should be constructed in a way that provides the readers with a general overview of the article and enables them to have a general idea about the article.

The main points should be listed at the end of the main text, above the reference list.

**Example:** Liu S, Xu X, Cheng Q, et al. Simple quantitative measurement based on DWI to objectively judge DWI-FLAIR mismatch in a canine stroke model. Diagn Interv Radiol 2015;(4)21:348–354.

• The relative diffusion-weighted imaging signal intensity (rDWI) of ischemic lesions might be helpful to identify the status of fluid attenuated inversion recovery (FLAIR) imaging in acute ischemic stroke.

• The relative apparent diffusion coefficient (rADC) value appears not useful to identify the status of FLAIR imaging in the acute period.

• Based on our embolic canine model, rDWI increased gradually in the acute period, while the rADC kept stable, which might explain why rDWI is helpful to identify the status of FLAIR imaging, while rADC is not.

## Main text

### Original Articles

Original articles should provide new information based on original research. The main text should be structured with Introduction, Methods, Results, and Discussion subheadings. The number of cited references should not exceed 50 and the main text should be limited to 4500 words. Number of tables included in an original article should be limited to 4 and the number of figures should be limited to 7 (or a total of 15 figure parts).

### Introduction

State briefly the nature and purpose of the work, quoting the relevant literature.

### Methods

Include the details of clinical and technical procedures.

## Research ethics standards compliance

All manuscripts dealing with human subjects must contain a statement indicating that the study was approved by the Institutional Review Board or a comparable formal research ethics review committee. If none is present at your institution, there should be a statement that the research was performed according to the Declaration of Helsinki principles (www.wma.net/e/policy/b3.htm). There should also be a statement about whether informed consent was obtained from research subjects.

## Results

Present these clearly, concisely, and without comment. Statistical analysis results should also be provided in this section to support conclusions when available.

## Discussion

Explain your results and relate them to those of other authors; define their significance for clinical practice. Limitations, drawbacks, or shortcomings of the study should also be stated in the discussion section before the conclusion paragraph. In the last paragraph, a strong conclusion should be written.

## Review Articles

Review articles are scientific analyses of recent developments on a specific topic as reported in the literature. No new information is described, and no opinions or personal experiences are expressed. Reviews include only the highlights on a subject. Main text should be limited to 4000 words and the number of cited references should not exceed 75. Number of tables included in a review article should be limited to 4 and the number of figures should be limited to 15 (or a total of 30 figure parts).

## Pictorial Essay

This is a continuing medical education exercise with the teaching message in the figures and their legends. Text should include a brief abstract; there may be as many as 30 figure parts. No new information is included. The value of the paper turns on the quality of the illustrations. Authors can submit dynamic images (e.g. video files) or include supplemental image files for online presentation that further illustrate the educational purpose of the essay. Maximums: Pages of text – 4 (1,500 words); References – 20; Figures – 15 or total of 30 images; No table Main text should be limited to 1500 words and the number of cited references should not exceed 15.

## Technical Notes

Technical note is a brief description of a specific technique, procedure, modification of a technique, or new equipment of interest to radiologists. It should include a brief introduction followed by Technique section for case reports or Methods section for case series, and Discussion is limited to the specific message, including the uses of the technique, equipment, or software. Literature reviews and lengthy descriptions of cases are not appropriate.

Main text should be limited to 1500 words and the number of cited references should not exceed 8. Number of tables included in a technical note should be limited to 4 and the number of figures should be limited to 3 (or a total of 6 figure parts).

# Instructions to Authors

## Letter to the Editor and Reply

Letters to the Editor and Replies should offer objective and constructive criticism of published articles within last 6 months. Letters may also discuss matters of general interest to radiologists and may include images. Material being submitted or published elsewhere should not be duplicated in letters.

Main text should be limited to 500 words and the number of cited references should not exceed 6. No tables should be included and the number of figures should be limited to 2 (or a total of 4 figure parts).

## Recommendations for Manuscripts:

| Type of manuscript | Word limit | Abstract word limit | Reference limit | Author limit | Table limit | Figure limit |
|---|---|---|---|---|---|---|
| Original Article | 4500 | 400 (Structured) | 50 | 6* | 4 | 7 or total of 15 images |
| Review Article | 4000 | 200 | 75 | 5 | 4 | 15 or total of 24 images |
| Pictorial Essay | 1500 | 400 | 20 | 5 | 1 | 15 figures or total of 30 figure parts |
| Technical Note | 1500 | 200 | 8 | 5 | 2 | 3 figures or total of 6 figure parts |
| Letter | 500 | N/A | 6 | 4 | No tables | 2 figures or total of 4 figure parts |

*Manuscripts should not be signed by more than 6 authors unless they are multicenter or multidisciplinary studies.
**Considering the specific condition of the manuscript, minor flexibilites may be applied for the recommendations upon the decision of Editor-in-Chief or the Section Editors.

## References

Both in-text citations and the references must be prepared according to the AMA Manual of style.

While citing publications, preference should be given to the latest, most up-to-date publications. Authors are responsible for the accuracy of references If an ahead-of-print publication is cited, the DOI number should be provided. Journal titles should be abbreviated in accordance with the journal abbreviations in Index Medicus/MEDLINE/PubMed. When there are six or fewer authors, all authors should be listed. If there are seven or more authors, the first three authors should be listed followed by "et al." In the main text of the manuscript, references should be cited in superscript after punctuation. The reference styles for different types of publications are presented in the following examples.

**Journal Article:** Economopoulos KJ, Brockmeier SF. Rotator cuff tears in overhead athletes. Clin Sports Med. 2012;31(4):675-692.

**Book Section:** Fikremariam D, Serafini M. Multidisciplinary approach to pain management. In: Vadivelu N, Urman RD, Hines RL, eds. Essentials of Pain Management. New York, NY: Springer New York; 2011:17-28.

**Books with a Single Author:** Patterson JW. Weedon's Skin Pahology. 4th ed. Churchill Livingstone; 2016.

**Editor(s) as Author:** Etzel RA, Balk SJ, eds. Pediatric Environmental Health. American Academy of Pediatrics; 2011.

**Conference Proceedings:** Morales M, Zhou X. Health practices of immigrant women: indigenous knowledge in an urban environment. Paper presented at: 78th Association for Information Science and Technology Annual Meeting; November 6-10; 2015; St Louis, MO. Accessed March 15, 2016. https://www.asist.org/files/meetings/am15/proceedings/openpage15.html

**Thesis:** Maiti N. Association Between Behaviours, Health Charactetistics and Injuries Among Adolescents in the United States. Dissertation. Palo Alto University; 2010.

**Online Journal Articles:** Tamburini S, Shen N, Chih Wu H, Clemente KC. The microbiome in early life: implications for health outcometes. Nat Med. Published online July 7, 2016. doi:10.1038/nm4142

**Epub Ahead of Print Articles: Websites:** International Society for Infectious Diseases. ProMed-mail. Accessed February 10, 2016. http://www.promedmail.org

## Tables

Tables should be included in the main document and should be presented after the reference list. Tables should be numbered consecutively in the order they are referred to within the main text. A descriptive title should be provided for all tables and the titles should be placed above the tables. Abbreviations used in the tables should be defined below by footnotes (even if they are defined within the main text). Tables should be created using the "insert table" command of the word processing software and they should be arranged clearly to provide an easy reading. Data presented in the tables should not be a repetition of the data presented within the main text but should be supporting the main text.

## Figures and figure legends

Figures, graphics, and photographs should be submitted as separate files (in TIFF or JPEG format) through the submission system. The files should not be embedded in a Word document or the main document. When there are figure subunits, the subunits should not be merged to form a single image. Each subunit should be submitted separately through the submission system. Images should not be labelled (a, b, c, etc.) to indicate figure subunits. Thick and thin arrows, arrowheads, stars, asterisks, abbreviations and similar marks can be used on the images to support figure legends. Like the rest of the submission, the figures too should be blind. Any information within the images that may indicate the institution or the patient should be removed.

Figure legends should be listed at the end of the main document.

## General

All acronyms and abbreviations used in the manuscript should be defined at first use, both in the abstract and in the main text. The abbreviation should be provided in parenthesis following the definition.

Statistical analysis should be performed in accordance with guidelines on reporting statistics in medical journals (Altman DG, Gore SM, Gardner MJ, Pocock SJ. Statistical guidelines for contributors to medical journals. Br Med J 1983: 7; 1489–1493.). Information on the statistical analysis process of the study should be provided within the main text.

When a drug, product, hardware, or software mentioned within the main text product information, the name and producer of the product should be provided in parenthesis in the following format: "Discovery St PET/CT scanner (GE Healthcare)."

# Instructions to Authors

All references, tables, and figures should be referred to within the main text and they should be numbered consecutively in the order they are referred to within the main text.

## Initial evaluation and peer review process

Manuscripts submitted to Diagnostic and Interventional Radiology will first go through a technical evaluation process where the editorial office staff will ensure that the manuscript is prepared and submitted in accordance with the journal's guidelines. Submissions that do not conform the journal's guidelines will be returned to the submitting author with technical correction requests.

All submissions are screened by a similarity detection software (iThenticate by CrossCheck), and those with an overall similarity index of greater than 20%, or duplication rate at or higher than 5% with a single source are returned back to authors without further evaluation along with the similarity report.

Manuscripts meeting the requirements mentioned in journal's guideline will go under the review process. The initial review will be performed by Editor-in-Chief and the Section Editor, which include the evaluation of the manuscript for its originality, importance of the findings, scientific merit, interest to readers and compliance with the policy of the journal in force. Manuscripts with insufficient priority for publication are not sent out for further review and rejected promptly at this level to allow the authors to submit their work elsewhere without delay.

Manuscripts that pass through the initial review are sent to peer review, which is performed in a blinded manner by least two external and independent reviewers. During the review process, all original articles are evaluated by at least one senior consultant of statistics for proper handling and consistency of data, and use of correct statistical method. The Section Editor and / or Editor-in-Chief are the final authority in the decision-making process for all submissions.

## Revisions

When submitting a revised version of a paper, the author must submit a detailed "Response to reviewers" that states point by point how each issue raised by the reviewers has been covered and where it can be found (each reviewer's comment followed by the author's reply and line numbers where the changes have been made) as well as an annotated copy, and a clear copy of the main document.

Revised manuscripts must be submitted within 30 days from the date of the decision letter. If the revised version of the manuscript is not submitted within the allocated time, the revision option will be automatically cancelled by the submission system. If the submitting author(s) believe that additional time is required, they should request an extension before the initial 30-day period is over.

## Proofs and DOI Number

Accepted manuscripts are copy-edited for grammar, punctuation, and format by professional language editors. Following the copyediting process, the authors will be asked to review and approve the changes made during the process. Authors will be contacted for a second time after the layout process and will be asked to review and approve the PDF proof of their article for publication. Once the production process of a manuscript is completed it is published online on the journal's webpage as an ahead-of-print publication before it is included in its scheduled issue.

## Publication Fee Policy

Diagnostic and Interventional Radiology (DIR) applies an Article Processing Charge (APCs) for only accepted articles. No fees are requested from the authors during submission and evaluation process. All manuscripts must be submitted via Manuscript Manager.

An APC fee of and local taxes will be applied depending on the article type (see Table 1)

| | |
|---|---|
| Review | $ 1250 |
| Original Article | $ 1000 |
| Pictorial Essay | $ 750 |
| Technical Note | |

## Table 1. Article Types and Fees

The APCs will be accepted through the link that will be sent to the corresponding author of each article via the online article system. In the next step, the authors will be receiving a receipt of their payment.

*Please note that the Article Processing Charge (APC) will not affect neither the editorial and peer-review process nor the priority of the manuscripts by no means. All submissions will be evaluated by the Editorial Board and the external reviewers in terms of scientific quality and ethical standards.

## Refund Policy:

Returning the article to the author; Diagnostic and Interventional Radiology (DIR) will refund the submission fees with a coupon code if the article is returned to the author. Using this code, authors can use the submission fees of different articles without making a new payment.

## Article Retraction:

Infringements of publication/research ethics, such as multiple submissions, bogus claims of authorship, plagiarism, and fraudulent use of data could lead to article retraction.

A retraction statement titled "Retraction: [article title]" must be signed by the authors and/or the editor. The original article is marked as retracted but a PDF version remains available to readers, and the retraction statement is linked to the original published paper.

# Contents

*Full text of these articles can be accessed online at www.dirjournal.org or through PubMed (https://www.ncbi.nlm.nih.gov/pmc/journals/2754/).*

# Virtual non-enhanced dual-energy computed tomography reconstruction: a candidate to replace true non-enhanced computed tomography scans in the setting of suspected liver alveolar echinococcosis

Mecit Kantarcı [ID]
Sonay Aydın [ID]
Ayşegül Kahraman [ID]
Hayri Oğul [ID]
Barış İrgül [ID]
Akın Levent [ID]

**PURPOSE**

When a suspected hepatic alveolar echinococcosis (AE) lesion is detected on a contrast enhanced computed tomography (CT) scan, an additional triphasic or non-enhanced CT scan is required to determine the presence of calcification and enhancement. As a result, imaging costs and exposure to ionizing radiation will increase. We can create a non-enhanced series from routine contrast-enhanced images using dual-energy CT (DECT) and virtual non-enhanced (VNE) images. This study's objective is to assess virtual non-enhanced DECT reconstruction as a potential diagnostic tool for hepatic AE.

**METHODS**

Triphasic CT scans and a routine dual energy venous phase were acquired using a third-generation DECT system. A commercially available software package was used to generate VNE images. Individual evaluations were conducted by two radiologists.

**RESULTS**

The study population consisted of 100 patients (30 AE, 70 other solid liver masses). All AE cases were diagnosed [no false positives/negatives, 95% confidence interval (CI) sensitivity: 91.3%–100%; 95% CI specificity: 95.3%–100%]. Interrater agreement was k: 0.79. In total, 33 (33.00%) of the patients had AE, which was detected using both true non-enhanced (TNE) and VNE images. The mean dose-length product of a standard triphasic CT was significantly higher than biphasic dual-energy VNE images.

**CONCLUSION**

In terms of diagnostic confidence, VNE images are comparable with actual non-enhanced imaging when evaluating hepatic AE. Further, VNE images could replace TNE images with a substantial radiation dose reduction. Advances in knowledge: hepatic cystic echinococcosis and AE are serious and severe diseases with high fatality rates and a poor prognosis if managed incorrectly, especially AE. Moreover, VNE images produce equal diagnostic confidence to TNE images for assessing liver AE, with a significant reduction in radiation dose.

**KEYWORDS**

DECT, virtual non-enhanced, alveolar echinococcosis, DLP, radiation

From the Department of Radiology (M.K., H.O.), Atatürk University, Faculty of Medicine, Erzurum, Turkey; Department of Radiology (S.A., B.İ. ✉ barisirgul@gmail.com, A.L.), Erzincan Binali Yıldırım University, Faculty of Medicine, Erzincan, Turkey; Department of Radiology (A.K.), İnönü University, Faculty of Medicine, Malatya, Turkey.

Echinococcosis is a largely global zoonotic illness caused by Echinococcus-genus family cestodes. Both *Echinococcus granulosus* and *Echinococcus multilocularis* (*E. granulosus*) are medically and publicly significant because they cause cystic echinococcosis (CE) and alveolar echinococcosis (AE), respectively. Both hepatic CE and AE are severe disorders with significant mortality rates and a poor prognosis if improperly treated, especially AE. The prev-

alence of AE is highest in the northern hemisphere, specifically in Central Europe, Turkey, Russia, Japan, Alaska, North America, and China. Approximately 18,000 new cases of AE are reported annually across the globe.[1-3]

Untreated hepatic AE is invariably fatal, and the therapeutic response is difficult to evaluate once detected. Importantly, radiologists must guarantee rapid referral to experts and imaging follow-up; however, due to the variability of AE imaging findings, initial misinterpretation is prevalent, particularly in non-endemic regions. Imaging methods such as ultrasonography, computed tomography (CT), and magnetic resonance imaging work well together to aid in the diagnosis, morphology, and treatment choices of AE lesions.[4,5] Typical hepatic AE calcifications are best seen on non-enhanced CT images. Moreover, demonstrating the absence of enhancement in AE lesions is a critical diagnostic feature for differentiating AE from hepatic tumors.

When a suspected hepatic AE lesion is detected on a contrast-enhanced CT scan, an additional triphasic or non-enhanced CT scan is required to determine the presence of calcification and enhancement. As a result, imaging costs and exposure to ionizing radiation will increase. It is possible to create a non-enhanced series from routine contrast-enhanced images using dual energy CT (DECT) and virtual non-enhanced (VNE) images with a significantly reduced radiation dose.[6] Previously, DECT was evaluated for the diagnosis of hepatic AE. Previous studies primarily emphasized DECT's ability to define the micro-perfusion status of the periparasitic granulomatous reaction and the consistency of DECT findings with positron emission tomography-CT results.[7,8] Consequently, the objective of this study is to investigate the diagnostic potential of VNE DECT reconstruction for hepatic AE.

## Methods

### Study population

A database search was conducted using electronic archives for patients who were imaged for liver mass characterization between December 2016 and December 2021 for this retrospective cohort study. Approval from the Ethics Committee was acquired (Erzincan Binali Yıldırım University Clinical Research Ethics Committee, EBYU-KAEK-2022- 01.003-28). Patients were included if they had the following: I) liver mass; and II) a multiphasic/triphasic CT exam. Exclusion criteria included the following: I) mono- or biphasic CT examinations; and II) multiphase CT examinations without the use of dual energy. The study included only those patients with an AE diagnosis. To avoid selection bias and to create a more diverse study group, patients with non-AE liver masses (twice the number of patients with an AE diagnosis) were also randomly selected and included in the study group. One author formed the study group independently of the authors who evaluated the images.

Imaging protocol: triphasic CT scans with ADMIRE strength 2 (advanced modeled iterative reconstruction) and routine dual energy venous phase were obtained via a third-generation dual-source dual-energy 2x192 slice-CT system (Siemens Somatom Force, Siemens Healthcare, Erlangen, Germany).

True non-enhanced (TNE) images scan parameters were as follows: the reference tube voltage was 120 kVp, the effective tube current was adapted to the patient's body mass, the quality reference mAs was 147 QrefmAs, the dose modulation was CARE dose 4D, the CARE kV was turned on, the slice thickness was 3 mm, and the reconstruction kernel was Br40. For contrast-enhanced phases, the following scan parameters were used: reference tube voltage: 100 kVp, effective tube current: patient body mass adjusted, quality reference mAs: 190 QrefmAs, dose modulation: CARE dose 4D, CARE kV: on, slice thickness: 3 mm, reconstruction kernel: Bf40 (venous), and Br40 (venous) (arterial).

Iohexol was injected at a flow rate of 4 mL/s and adapted to the patients' body weight (1 mL/kg body weight), followed by a saline flush. TNE images were acquired first, followed by arterial and venous phase images 20 and 80 seconds after contrast agent injection, respectively.

### VNE image calculation

A commercially available software package (SyngoVia VB20A, Siemens Healthcare, Forchheim, Germany) was used to generate VNE datasets (Figures 1, 2). Reconstruction was performed axially with the same slice thickness of 3 mm as for TNE images to obtain identical images.
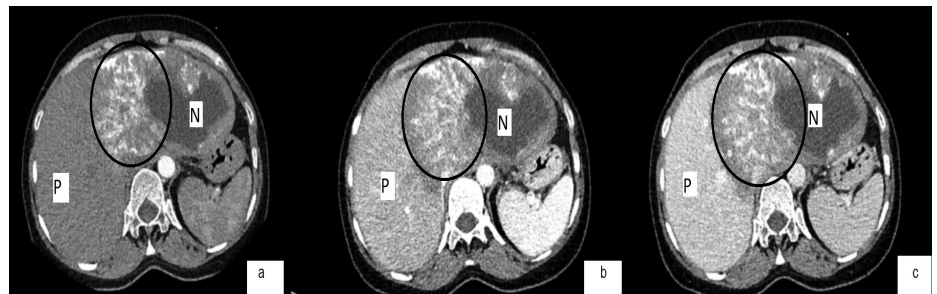


**Figure 1.** Arterial (**a**), portal venous (**b**), hepatic venous (**c**), axial computed tomography images of a hepatic alveolar echinococcosis with typical calcification pattern (circle), necrotic areas (**N**), and irregular contours with normal parenchyma (**P**).
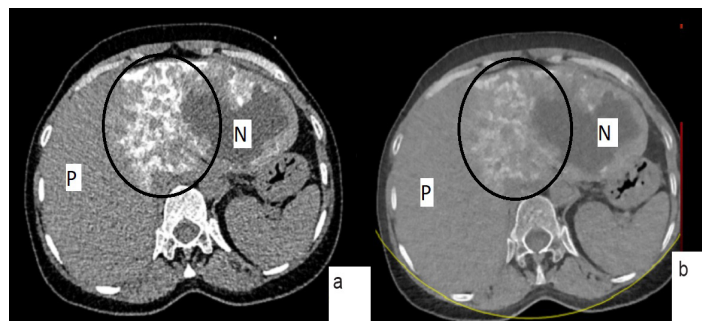


**Figure 2.** True non-enhanced (**a**) and virtual non-enhanced (**b**) images of a hepatic alveolar echinococcosis with typical calcification pattern (circle), necrotic areas (**N**), and irregular contours with normal parenchyma (**P**).

**Main points**

- Virtual non-enhanced (VNE) images can be used effectively in place of true non-enhanced images to diagnose hepatic alveolar echinococcosis (AE).

- Using VNE images reduces exposure to ionizing radiation.

- Despite a considerable drop in noise, sharpness, and image quality in VNE, both non-enhanced scans detect liver AE comparably.

## Assessment of image quality

Two radiologists with 8 and 25 years' experience in abdominal imaging evaluated the image quality independently. If two independent readers disagreed on the diagnosis of an adverse event, a consensus reading was conducted. To reduce recall bias, all cases were evaluated randomly and anonymously in two sessions separated by eight weeks. The following datasets were provided by the studying supervisor for these sessions: 1. venous, arterial, and VNE images; and 2. venous, arterial, and TNE images. The various datasets were distributed randomly and blindly to both readers during the initial session. During the second session, the non-enhanced phase of the dataset was evaluated for the first time. Both readers scored TNE and VNE images on a 5-point Likert scale for overall image quality, noise, artefacts, and sharpness (5 being the best outcome of the evaluated category and 1 being the worst).

## Diagnostic performance

The researchers were asked to make a diagnosis of AE or non-AE based on the presence and absence of calcification enhancement. With TNE or VNE images in conjunction with the arterial and venous phases and a 5-point Likert scale, diagnostic confidence in the presence or absence of AE was evaluated (1 not confident, 2 low confidence, 3 moderate confidence, 4 confident, and 5 high confidence).

## Radiation dose

To evaluate the reduction in X-ray exposure, the total dose-length product (DLP) of all three phases (TNE, arterial, and venous) and the total DLP of only the arterial and venous phases were determined for each patient.

## Statistical analysis

SPSS was used to conduct the statistical analysis (IBM SPSS Statistics 24). To evaluate the normally distributed data, the Kolmogorov–Smirnov test was utilized. Continuous variables with normal distribution [age, Hounsfield units (HU) values, and DLP values] were represented by their mean and standard deviation, numerical variables with non-normal distribution were given as the median (min–max) (image quality, noise, sharpness, diagnostic confidence, and artefact elimination scores), while the categorical variables (gender) were represented by their percentage (%). The Wilcoxon paired test was used to compare the overall image quality, noise, sharpness, artefact elimination, and diagnostic confidence. Sensitivity and specificity were calculated using cross tabulation and expressed in percent (%), including the 95% confidence interval (CI). The paired t-test was utilized to determine the DLP's significance. Cohen's kappa coefficient was used to determine the interrater agreement for the image quality, noise, sharpness, artefact elimination, and diagnostic confidence. Kappa values (k) of agreement were defined as poor between 0.01 and 0.20, fair between 0.21 and 0.40, moderate between 0.41 and 0.60, substantial between 0.61 and 0.80, and nearly perfect between 0.81 and 1.00.[9]

The level of significance was accepted as α: 0.05.

# Results

The study population consisted of 100 patients (30 AE, 70 other solid liver masses). The mean age of the population was 56.23 ± 11.72 years (min – max, 31–78 years). A total of 63 (63%) of the patients were male and 37 (37%) were female (Table 1).

## Image quality

A comparison of the TNE and VNE image quality revealed statistically significant variations ($P < 0.001$). In terms of the overall image quality, noise, and sharpness, TNE images outperformed VNE images, whereas VNE images exceeded TNE images in terms of artefact elimination. Interrater agreement was substantial for the aforementioned categories (k: 0.63–0.75) (Figure 3) (Tables 2, 3).

## Diagnostic performance

Both non-enhanced series had excellent diagnostic confidence, with TNE images indicating statistically significant superiority ($P = 0.030$). Significant interrater agreement was observed (k: 0.79, $P = 0.006$) (Tables 4, 5). In total, 33% of the enrolled individuals had adverse events that were recognized using both TNE and VNE images. All AE cases were detected (no false positives or negatives), resulting in a sensitivity and specificity of 100% (95% CI sensitivity: 91.3%–100%; 95% CI specificity: 95.3%–100%). Perfect agreement existed between the researchers regarding the detection of AE (k: 1, $P = 0.001$).

The ROIs positioned in the solid portions of the lesions had a substantially higher mean HU values for TNE than VNE images ($P = 0.03$), and the measurement error was 21.1 ± 10.30 (45.3 ± 11.8 vs. 61.7 ± 10.4 HU).

## Radiation dose

Biphasic dual-energy CT with VNE images had a mean DLP of 1613.8 ± 421.7 mGy cm,

**Table 1.** Characteristics of the study population

| Characteristic | Value |
|---|---|
| Number of patients | 100 |
| Distribution of the lesions | 30 alveolar echinococcosis, 70 other solid liver masses |
| Mean age | 56.23 ± 11.72 years |
| Number of males and females | M: 63 (63%), F: 37 (37%) |

M, male; F, female.

**Table 2.** Median quality parameters

| Image quality parameters | Median score | | P value |
|---|---|---|---|
| | TNE n = 100 | VNE n = 100 | |
| Overall image quality | 4 (1–5) | 3 (1–4) | 0.001 |
| Noise | 4 (1–5) | 2 (1–5) | 0.001 |
| Sharpness | 4 (1–5) | 2 (2–5) | 0.001 |
| Artefact elimination | 2 (2–5) | 4 (1–4) | 0.001 |

TNE, true non-enhanced; VNE, virtual non-enhanced.

**Table 3.** Interobserver reliability data for quality parameters

| Image quality parameters | Kappa value (k) | P value |
|---|---|---|
| Overall image quality | 0.63 | 0.004 |
| Noise | 0.69 | 0.010 |
| Sharpness | 0.75 | 0.020 |
| Artefact elimination | 0.71 | 0.008 |
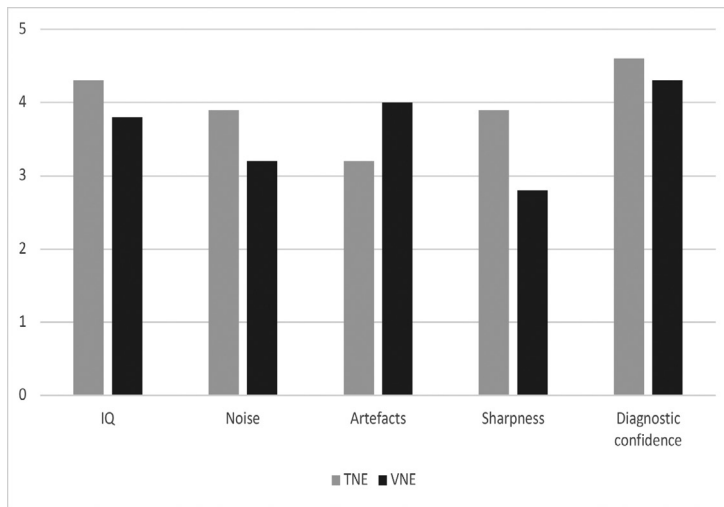
**Figure 3.** Subjective image analysis and diagnostic confidence as rated by the primary reader for TNE and VNE. The data are expressed as the mean (range). IQ, image quality; TNE, true non-enhanced; VNE, virtual non-enhanced.

**Table 4.** Diagnostic performance of both methods

| Diagnostic performance | Median score | | P value |
|---|---|---|---|
| | TNE<br>n = 100 | VNE<br>n = 100 | |
| Diagnostic confidence according to presence of calcification | 5 (3–5) | 4 (2–5) | 0.030 |

TNE, true non-enhanced; VNE, virtual non-enhanced.

**Table 5.** Interobserver reliability for diagnostic performance of the methods

| Diagnostic performance | Kappa value (k) | P value |
|---|---|---|
| Diagnostic confidence according to presence of calcification | 0.79 | 0.006 |

indicating a significant reduction in radiation exposure in comparison with standard triphasic CT, where the DLP was 1,985.3 ± 343 mGy cm (P < 0.001).

## Discussion

The objective of this investigation was to compare VNE DECT reconstruction with actual non-enhanced CT scans for the diagnosis of hepatic AE. The authors demonstrated that VNE images can be used effectively in place of TNE images to diagnose hepatic AE. Additionally, using VNE images reduces exposure to ionizing radiation.

Despite a considerable drop in noise, sharpness, and image quality in VNE, this study revealed that both non-enhancedscans detect liver AE comparably. The authors were able to demonstrate that compared with TNE images, VNE images significantly reduced artefacts.

As a result of these findings, the authors believe that the genuine non-enhanced phase can be substituted with VNE images, which enables a substantial reduction in radiation dose. If an elimination can be succeeded in artefacts of VNE images, this method may provide even more information than TNE images. Although VNE attenuation is believed to be comparable with that of TNE images, the literature has already showed discrepancies between 5 and 15 HU.[10-12] Toepker et al.[13] found a mean difference of -3.6 ± 8.3 HU between the non-enhanced and enhanced datasets. Consequently, comparable attenuation values are observed between TNE and VNE images.[13] Additional studies demonstrated that organ-specific attenuation values exist. Renal parenchyma, liver, and aorta all exhibited statistically significant variations; however, spleen and fat attenuation did not.[14] We believe that by achieving perfect interrater agreement between VNE and TNE images, we can overcome the limitations imposed by HU differences.

Sun et al.[15] examined dual-source DECT versus TNE images in 112 suspected gastrointestinal bleeding cases and stated that VNE had lower image quality and noise levels than TNE. These results contradict those of this study, which demonstrated a significant change in the image quality and an increase in noise levels in VNE images.[15] Nonetheless, the findings were consistent regarding the use of VNE images.

Overall, CT was commonly emphasized as the best imaging modality to diagnose hepatic AE, as it enables anatomic and morphologic characterization of lesions and provides the most accurate representation of the calcification pattern. Along with the calcification pattern, enhancement characteristics are critical, particularly when differentiating tumoral lesions. After administration of an intravenous contrast medium, no significant enhancement was observed within the hepatic AE lesion; however, the fibroinflammatory component surrounding the parasitic tissue may have been slightly enhanced in the delayed phase.[3,16] The primary issue with CT examinations in clinical practice, particularly triphasic CT examinations, is the exposure to high doses of radiation.[8,16]

Although the role of DECT in liver AE has been studied recently, previous research has focused on the perfusion characteristics of hepatic AE lesions, the use of perfusion differences to differentiate AE from hepatic malignancies, the role of perfusion imaging in monitoring treatment response, and the presence of periparasitic granulomatous tissue as increased prefusion.[16,17] There are no prior studies that the authors are aware of that examines the diagnostic success of VNE images in the diagnosis of liver AE.

Other abdominal pathologies have been studied to determine the diagnostic success of VNE imaging. When comparing the detection rates of diseases in VNE and TNE images in 15 patients with "acute abdominal pain", Im et al.[18] discovered that the detection rates and visual quality of the unmodified photographs were practically comparable. Flors et al.[19] observed equivalent results while evaluating the presence of endoleak in 48 patients following endovascular aortic repair (EVAR). By comparing a standard triphasic procedure with actual non-enhanced images and a monophasic and biphasic protocol to VNE images, they concluded that VNE images plus a delayed phase can be employed in place of the usual triphasic protocol for post-EVAR CT examinations.[19]

This study is not without limitations. First, the retrospective nature of the study may have introduced a selection bias. However, the study included randomly selected patients to ensure a representative sample. Sec-

ond, due to the transferable clinical setting, image quality was only subjectively assessed. Third, the authors simulated non-enhanced images using a single piece of software without comparing it with other pieces of software. As a result, more advanced software may exist. As in previous studies, VNE images had lower HU values than TNE images. When compared with enhanced images, it is possible that this situation will be misinterpreted as contrast enhancement. However, because this HU change occurs in normal liver parenchyma as well, comparing the HU values of normal parenchyma and the lesion together will resolve the previously mentioned potential confusion. To confirm these preliminary results, a larger cohort or external cross-validation is required.

In conclusion, the findings show that VNE images produce equal diagnostic confidence and perfect agreement with TNE images for assessing liver AE. This implies that VNE images could replace TNE images, resulting in a significant reduction in the radiation dose.

### Conflict of interest disclosure

The authors declared no conflicts of interest.

## References

1. Romig T, Deplazes P, Jenkins D, et al. Ecology and life cycle patterns of Echinococcus species. *Adv Parasitol*. 2017;95:213-314. [CrossRef]

2. Guo H, Liu W, Wang J, Xing Y. Extrahepatic alveolar echinococcus on multi-slice computed tomography and magnetic resonance imaging. *Sci Rep*. 2021;11(1):9409. [CrossRef]

3. Kantarci M, Bayraktutan U, Karabulut N, et al. Alveolar Echinococcosis: spectrum of findings at cross-sectional imaging. *Radiographics*. 2012;32(7):2053-2070. [CrossRef]

4. Sade R, Kantarci M, Ogul H, Gundogdu B, Aydınlı B. Differentiation between hepatic alveolar echinococcosis and primary hepatic malignancy with diffusion-weighted magnetic resonance imaging. *Diagn Interv Imaging*. 2018;99(3):169-177. [CrossRef]

5. Chouhan MD, Wiley E, Chiodini PL, Amin Z. Hepatic alveolar hydatid disease (Echinococcus multilocularis), a mimic of liver malignancy: a review for the radiologist in non-endemic areas. *Clin Radiol*. 2019;74(4):247-256. [CrossRef]

6. Walter SS, Schneeweiß S, Maurer M, et al. Virtual non-enhanced dual-energy CT reconstruction may replace true non-enhanced CT scans in the setting of suspected active hemorrhage. *Eur J Radiol*. 2018;109:218-222. [CrossRef]

7. Sade R, Kantarci M, Genc B, Ogul H, Gundogdu B, Yilmaz O. Computed tomography perfusion ımaging for the diagnosis of hepatic alveolar Echinococcosis. *Eurasian J Med*. 2018;50(1):1-5. [CrossRef]

8. Liu W, Delabrousse É, Blagosklonov O, et al. Innovation in hepatic alveolar echinococcosis imaging: best use of old tools, and necessary evaluation of new ones. *Parasite*. 2014;21:74. [CrossRef]

9. McHugh ML. Interrater reliability: the kappa statistic. *Biochem Med (Zagreb)*. 2012;22(3):276-282. [CrossRef]

10. Bonatti M, Lombardo F, Zamboni GA, Pernter P, Pozzi Mucelli R, Bonatti G. Dual-energy CT of the brain: comparison between DECT angiography-derived virtual unenhanced images and true unenhanced images in the detection of intracranial haemorrhage. *Eur Radiol*. 2017;27(7):2690-2697. [CrossRef]

11. Kaufmann S, Sauter A, Spira D, et al. Tin-filter enhanced dual-energy-CT: image quality and accuracy of CT numbers in virtual noncontrast imaging. *Acad Radiol*. 2013;20(5):596-603. [CrossRef]

12. Kaza RK, Raff EA, Davenport MS, Khalatbari S. Variability of CT attenuation measurements in virtual unenhanced ımages generated using multimaterial decomposition from fast kilovoltage-switching dual-energy CT. *Acad Radiol*. 2017;24(3):365-372.

13. Toepker M, Moritz T, Krauss B, et al. Virtual non-contrast in second-generation, dual-energy computed tomography: reliability of attenuation values. *Eur J Radiol*. 2012;81(3):e398-e405. [CrossRef]

14. Sahni VA, Shinagare AB, Silverman SG. Virtual unenhanced CT images acquired from dual-energy CT urography: accuracy of attenuation values and variation with contrast material phase. *Clin Radiol*. 2013;68(3):264-271. [CrossRef]

15. Sun H, Hou XY, Xue HD, et al. Dual-source dual-energy CT angiography with virtual non-enhanced images and iodine map for active gastrointestinal bleeding: image quality, radiation dose and diagnostic performance. *Eur J Radiol*. 2015;84(5):884-891. [CrossRef]

16. Bulakçı M, Kartal MG, Yılmaz S, et al. Multimodality imaging in diagnosis and management of alveolar echinococcosis: an update. *Diagn Interv Radiol*. 2016;22(3):247-256. [CrossRef]

17. Oğul H, Kantarcı M, Genç B, et al. Perfusion CT imaging of the liver: review of clinical applications. *Diagn Interv Radiol*. 2014;20(5):379-389. [CrossRef]

18. Im AL, Lee YH, Bang DH, Yoon KH, Park SH. Dual energy CT in patients with acute abdomen; is it possible for virtual non-enhanced images to replace true non-enhanced images? *Emerg Radiol*. 2013;20(6):475-483. [CrossRef]

19. Flors L, Leiva-Salinas C, Norton PT, Patrie JT, Hagspiel KD. Endoleak detection after endovascular repair of thoracic aortic aneurysm using dual-source dual-energy CT: suitable scanning protocols and potential radiation dose reduction. *AJR Am J Roentgenol*. 2013;200(2):451-460. [CrossRef]

# A model incorporating clinicopathologic and liver imaging reporting and data system-based magnetic resonance imaging features to identify hepatocellular carcinoma in LR-M observations

Xin-Xing Hu* 
Dong Bai* 
Zhen-Lei Wang 
Yi Zhang 
Jue Zhao 
Mei-Ling Li 
Jia Yang 
Lei Zhang 

**\*Contributed equally to this work as the first authors.**

**PURPOSE**

To evaluate the predictive value of a combination model of Liver Imaging Reporting and Data System (LI-RADS)-based magnetic resonance imaging (MRI) and clinicopathologic features to identify atypical hepatocellular carcinoma (HCC) in LI-RADS category M (LR-M) observations.

**METHODS**

A total of 105 patients with HCC based on surgery or biopsy who underwent preoperative MRI were retrospectively reviewed in the training group from hospital-1 between December 2016 and November 2020. The LI-RADS-based MRI features and clinicopathologic data were compared between LR-M HCC and non-HCC groups. Univariate and least absolute shrinkage and selection operator regression analyses were used to select the features. Binary logistic regression analysis was then conducted to estimate potential predictors of atypical HCC. A predictive nomogram was established based on the combination of MRI and clinicopathologic features and further validated using an independent external set of data from hospital-2.

**RESULTS**

Of 113 observations from 105 patients (mean age, 61 years; 77 men) in the training set, 47 (41.59%) were classified as LR-M HCC. Following multivariate analysis, aspartate aminotransferase >40 U/L [odds ratio (OR): 4.65], alpha-fetoprotein >20 ng/mL (OR: 13.04), surface retraction (OR: 0.16), enhancing capsule (OR: 5.24), blood products in mass (OR: 8.2), and iso/hypoenhancement on delayed phase (OR: 10.26) were found to be independently correlated with LR-M HCC. The corresponding area under the curve for a combined model-based nomogram was 0.95 in the training patients (n = 113) and 0.90 in the validation cohort (n = 53).

**CONCLUSION**

The combined model incorporating clinicopathologic and MRI features demonstrated a satisfactory prediction result for LR-M HCC.

**KEYWORDS**

Liver Imaging Reporting and Data System, hepatocellular carcinoma, LR-M, magnetic resonance imaging, model

From the Department of Radiology (X-X.H., Y.Z., J.Z., M-L.L., J.Y., L.Z. ✉ lei.zhang2@shgh.cn), Shanghai General Hospital, Shanghai Jiao Tong University School of Medicine, Shanghai, China; Department of Anesthesiology (D.B.), Shanghai Municipal Hospital of Traditional Chinese Medicine, Shanghai University of Traditional Chinese Medicine, Shanghai, China; Department of General Practice (Z-L.W.), Changhai Hospital, Naval Military Medical University, Shanghai, China.

The Liver Imaging Reporting and Data System (LI-RADS) is a comprehensive, dynamic system that is constantly updated with user feedback, evolving knowledge, and technological advancements for patients with or at risk of hepatocellular carcinoma (HCC).[1,2] In the most recent version, published in 2018 (v2018), the LI-RADS M category (LR-M) represents observations that are probably or definitely malignant but not specific to HCC. However, based on current LI-RADS data, approximately one-third of all LR-M lesions are categorized as HCC, approximately two-thirds are categorized as non-HCC malignancies, and approximately 5% are categorized as benign.[1,3] HCC with atypical features in the LR-M category should be diagnosed early to determine treatment options, as the biological behavior and prognoses differ between HCC and non-HCC malignancies.[1,4] However, more importantly, distinguishing HCC from non-HCC malignancies remains extremely challenging,[1,5] especially under the assumption that the presence of any LR-M features indicates LR-M. Due to the partial overlap between LR-M HCC and LR-M non-HCC malignancies with respect to the pathological components, clinical presentations, and imaging features, a biopsy is required for diagnosis.[5-7] Additionally, imaging is usually required for guidance.[5]

For the diagnosis of HCC, multimodality imaging in cross-sections, especially dynamic contrast-enhanced magnetic resonance imaging (MRI), is one of the most effective tools due to the diagnostic information obtained from different MRI sequences.[1,5,7,8] The LR-M diagnosis criteria are

### Main points

- This retrospective study of 113 hepatocellular carcinomas (HCCs) at dynamic-enhanced magnetic resonance imaging (MRI) evaluated the predictive value to identify Liver Imaging Reporting and Data System (LI-RADS) M (LR-M) HCC in a combination model incorporating LI-RADS-based MRI and clinicopathologic features.

- In the combined model, aspartate aminotransferase >40 U/L [odds ratio (OR): 4.65], alpha-fetoprotein >20 ng/mL (OR: 13.04), surface retraction (OR: 0.16), enhancing capsule (OR: 5.24), blood products in mass (OR: 8.2) and iso/hypoenhancement on delayed phase (OR: 10.26) were independent predictors of LR-M HCC.

- The nomogram-based model had satisfactory performance to discriminate LR-M HCC from LR-M non-HCC (area under the curve: 0.95 for the training set and 0.90 for the validation set).

composed of non-targetoid and targetoid masses. The latter represents intrahepatic cholangiocarcinoma (ICC), combined hepatocellular-cholangiocarcinoma, or HCC with atypical features. In addition, there are many other features, such as major and ancillary features, that favor HCC specifically or that are not included in LI-RADS.[1] Therefore, if support can be found for LR-M HCC in numerous features not restricted to LR-M criteria, it may not be necessary for some patients with a high risk of LR-M malignancies to undergo a biopsy. In this way, it may be possible to optimize the discrimination of HCC from non-HCC in LR-M lesions and to avoid significant complications by invasive tissue sampling. Following the identification of discriminative features, relative models were developed based on a variety of feature sets. Previous studies have focused on the discrimination of LR-M categories with different imaging features.[9-13] However, few studies have proposed a non-invasive and comprehensive contrast-enhanced MRI model for the status of LR-M HCC with serology tests that are reasonably priced and readily available.

Based on these gaps in the literature, this study aimed to evaluate the predictive value of a combined model of MRI and clinicopathological features for identifying atypical HCC in LR-M observations.

## Methods

### Training patients

The protocol for this retrospective study was approved by the Shanghai General Hospital Institutional Review Board [(2023) 171, 5/16/2023] of the two hospitals in the study, and the requirement for informed consent was waived. A total of 375 consecutive patients were first identified from the first center [Hospital-1, Shanghai General Hospital-North (city center)] between December 2016 and November 2020. The inclusion criteria based on the LI-RADS v2018 diagnostic algorithm were as follows: (a) adult patients (≥18 years old), (b) patients with cirrhosis and/or chronic hepatitis B viral infection, (c) patients who had undergone a preoperative contrast-enhanced MRI within 3 weeks before surgery or biopsy, and (d) patients with LR-M features based on MRIs.[1] A total of 160 patients without eligible clinical and imaging data were excluded for the following reasons: (a) they had prior hepatic malignancies (n = 25), (b) important clinical data relating to them, such as levels of alpha-fetoprotein (AFP), carbohydrate antigen-199, carcinoem-

bryonic antigen, and aspartate aminotransferase (AST) were not available (n = 78), (c) they had received oncological treatment before undergoing MRI (n = 50), or (d) their MRI were of insufficient quality (n = 7), including 5 patients without the optimal timing arterial phase. Additionally, after imaging analysis, 110 patients were excluded for the following reasons: (e) they had coexisting LR-4 (probable HCC) and/or LR-5 (definite HCC) lesions (n = 78) for the reason that there was no way to determine either LR-M lesions or the coexisting LR-4 and/or LR-5 lesions contributing to serum tumor marker levels, (f) they had tumors in the vein (n = 30), or (g) they had cirrhosis due to a vascular disorder or diffuse nodular regenerative hyperplasia based on LI-RADS v2018 (n = 2). Ultimately, 105 patients were included in the study, and each patient was categorized into the LR-M HCC group (n = 43) or the non-HCC group (n = 62) (Figure 1).

### Magnetic resonance image acquisition

All MRI abdominal images were obtained on a 3.0-Tesla clinical scanner [Philips Ingenia (Philips Healthcare) or General Electrical (GE) Discovery 750W (GE Healthcare)] using a body phased-array coil. The conventional abdominal MRI protocol consisted of the following sequences: T1-weighted (in-phase and out-of-phase), T2-weighted, and diffusion-weighted imaging (DWI) ($b$ = 0, 500, 1,000 s/mm$^2$). Corresponding maps of the apparent diffusion coefficient (ADC) were automatically calculated by the MRI system. For dynamic contrast-enhanced imaging, a three-dimensional gradient echo sequence with T1 high-resolution isotropic volume examination or liver acquisition with volume acceleration was performed before and after intravenous injection of gadopentetate dimeglumine. The contrast media (Magnevist; Bayer Healthcare, Germany, 0.1 mmol/kg) was injected at a rate of 1–2 mL/sec followed by a flush with a maximum dose of 20 mL saline. Hepatic arterial (early and late), portal, and equilibrium phase images were obtained at 15–25, 60–80, and 180 sec after contrast medium injection, respectively. The hepatobiliary agents were not used for abdominal MRI. Detailed MRI scanner parameters are shown in Supplementary Table 1.

### Imaging analysis

All MRIs were assessed using the same picture archiving and communication system (Pathspeed, GE Medical Systems Integrated Imaging Solutions, Prospect, IL). An analysis of the images was performed independent-

**Figure 1.** A flowchart illustrating the inclusion and exclusion criteria used in enrolling our Liver Imaging Reporting and Data System M observations of training **(a)** and validation **(b)** sets. LR-4, probable HCC; LR-5, definite HCC; LI-RADS v2018, LI-RADS version published in 2018; HCC, hepatocellular carcinoma; LI-RADS, Liver Imaging Reporting and Data System.

**Table 1.** The clinicopathologic characteristics of training and validation patients

| Characteristics | Training patients | | | Comparison with validation patients | | |
| --- | --- | --- | --- | --- | --- | --- |
| | HCC group | Non-HCC group | P value | Training set | Validation set | P value |
| No. of patients* | 43 (40.95) | 62 (59.05) | | 105 | 50 | |
| Sex* (no. of male/female) | 31 (72.09)/12 (27.91) | 46 (74.19)/16 (25.81) | 0.682 | 77 (73.33)/28 (26.67) | 36 (72)/14 (28) | 0.141 |
| Mean age (years)^ | 57 ± 14 | 63 ± 13 | **0.034** | 61 ± 14 | 59 ± 13 | 0.182 |
| Etiology of liver disease* | | | 1.000 | | | 0.262 |
| Hepatitis B virus | 41 (95.35) | 57 (91.94) | | 98 (93.33) | 47 (94) | |
| Hepatitis C virus | 1 (2.33) | 0 (0) | | 1 (0.95) | 0 (0) | |
| Alcoholic liver disease | 0 (0) | 1 (1.61) | | 1 (0.95) | 0 (0) | |
| None or other virus | 1 (2.33) | 4 (6.45) | | 5 (4.76) | 3 (6) | |
| Cirrhosis* | 25 (58.14) | 23 (37.10) | 0.146 | 48 (45.71) | 21 (42) | 0.431 |
| **Blood tests** | | | | | | |
| Total bilirubin level (umol/L)# | 18.0 (6.0–76.0) | 14.7 (6.3–119.5) | 0.206 | 16.0 (6.0–119.5) | 18.0 (32.1–151.0) | 0.986 |
| Albumin level (g/L)^ | 38.6 ± 5.2 | 38.6 ± 7.7 | 0.994 | 38.6 ± 6.8 | 36.6 ± 6.1 | 0.098 |
| AST level (U/L)* (≤40/>40) | 24 (51.06)/23 (48.94) | 55 (83.33)/11 (16.67) | **0.002** | 79 (69.91)/34 (30.09) | 36 (67.92)/17 (32.08) | >0.999 |
| ALT level (U/L)* (≤50/>50) | 30 (63.83)/17 (36.17) | 50 (75.76)/16 (24.24) | 0.169 | 80 (70.80)/33 (29.20) | 39 (73.58)/14 (26.42) | >0.999 |
| Alkaline phosphatase level (U/L)# | 87.0 (35.0–215.0) | 99.6 (27.0–354.0) | 0.625 | 90.0 (27.0–354.0) | 81.0 (29.0–300.0) | 0.613 |
| Blood platelet level (x10⁹/L)^ | 174.0 ± 84.6 | 182.5 ± 62.6 | 0.539 | 179.0 ± 72.4 | 181.4 ± 79.6 | 0.695 |
| **Serum tumor markers*** | | | | | | |
| AFP (ng/mL) (≤20/>20) | 20 (42.55)/27 (57.45) | 57 (86.36)/9 (13.64) | **<0.001** | 77 (68.14)/36 (31.86) | 32 (60.38)/21 (39.62) | 0.972 |
| CA19-9 (U/mL) (≤37/>37) | 37 (78.72)/10 (21.28) | 44 (66.67)/22 (33.33) | 0.161 | 81 (71.68)/32 (28.32) | 39 (73.58)/14 (26.42) | 0.494 |
| CEA (μg/mL) (≤5/>5) | 41 (87.23)/6 (12.77) | 45 (68.18)/21 (31.82) | 0.019 | 86 (76.11)/27 (23.89) | 43 (81.13)/10 (18.87) | 0.969 |
| Pathologic diagnosis* | | | 0.447 | | | 0.088 |

**Table 1.** Continued

| Characteristics | Training patients | | | Comparison with validation patients | | |
|---|---|---|---|---|---|---|
| | HCC group | Non-HCC group | P value | Training set | Validation set | P value |
| HCC | 47 (100) | 0 (0) | | 47 (41.59) | 20 (37.74) | |
| Non-HCC malignancies | ND | 56 (84.85) | | 56 (49.56) | 32 (60.38) | |
| ICC | ND | 34 (51.52) | | | 27 (50.94) | |
| cHCC-CCA | ND | 7 (16.67) | | | 2 (3.77) | |
| Metastasis | ND | 10 (15.15) | | | 2 (3.77) | |
| Other primary liver malignancies | ND | 5 (7.58) | | | 1 (1.89) | |
| Benign lesions* | ND | 10 (15.15) | | 10 (8.85) | 1 (1.89) | |
| No. of LR-M observations | 47 | 66 | 0.714 | 113 | 53 | |
| One/two | 39 (90.70)/4 (9.30) | 58 (93.55)/4 (6.45) | | 97 (92.38)/8 (7.62) | 47 (94)/3 (6) | |
| Maximum diameter of tumor (mm)# | 46.0 (12.0–148.0) | 56.5 (12.0–76.0) | 0.616 | 52.0 (12.0–176.0) | 38.0 (5.0–106.6) | 0.747 |
| Subgroup (mm)* (<20/≥20) | 7 (14.89)/40 (85.11) | 5 (7.58)/61 (92.42) | 0.350 | 12 (10.62)/101 (89.38) | 7 (13.21)/46 (86.79) | >0.999 |
| MRI morphology type* | | | 0.205 | | | 0.995 |
| Round or oval | 20 (42.55) | 30 (45.45) | | 50 (44.25) | 27 (50.94) | |
| Round or oval with focal protrusions | 6 (12.77) | 2 (3.03) | | 8 (6.19) | 4 (7.55) | |
| Lobulated | 4 (8.51) | 10 (15.15) | | 14 (12.39) | 5 (9.43) | |
| Irregular growth | 17 (36.17) | 24 (36.36) | | 41 (36.28) | 17 (32.08) | |

All *P* values less than 0.05 are bold. Except where indicated, data are the number of patients or observations. *Numbers in parentheses are percentages; ^data are means ± standard deviations; #date are median (min–max). ND, stands for not done; No.; number of training or validation patients; AST, aspartate aminotransferase; ALT, alanine aminotransferase; AFP, alfa-fetoprotein; CA19-9, carbohydrate antigen 19-9; CEA, carcinoembryonic antigen; HCC, hepatocellular carcinoma; ICC, intrahepatic cholangiocarcinoma; cHCC-CCA, combined HCC-cholangiocarcinoma; MRI, magnetic resonance imaging.

ly by two abdominal radiologists, X-X.H. and L.Z., who had 7 and 23 years of experience in hepatic imaging, respectively. They were both blinded to any outcome information of patients, and disagreements were resolved by discussion based on bookmarked images, which were used as a guide.

The MRI morphological features were evaluated according to the LI-RADS v2018, including major, ancillary, and LR-M signs. The threshold growth was not included because there was only one examination per patient in the analysis. Moreover, the MRI signal intensity was evaluated at T1-weighted, T2-weighted, DWI, and postcontrast phase for the whole observation. Furthermore, the enhancement pattern of each observation was evaluated at the postcontrast phase. To avoid the influence of variable internal nodules, compartments, or septations on signal intensity in mosaic architecture, the hyper/iso/hypo signal intensity was defined as >50% of the whole observation showing visually assessed hyper/iso/hypo signal in the dynamic enhancement MRI and DWI within an observation.

## Model building

First, for LR-M HCC, screening the risk factors consisting of clinicopathology and MRI was performed using univariate analysis. Second, the least absolute shrinkage and selection operator (LASSO) regression was used for further screening of the selected variables to discourage the use of overfit data in the model. Additionally, as a result of constraints, those variables with a prevalence (<5% or >95%) were also discarded, considering their limited application in identifying different LR-M observations to ease model overfitting. Finally, a binary logistic regression analysis was conducted with backward stepwise selection. Variables with *P* values <0.05 were recognized as potential risk factors for LR-M HCC, and corresponding models were simultaneously established (Figure 2).

## Validation patients

Another retrospective validation study consisting of 50 patients from the second center [Hospital-2, Shanghai General Hospital-South (Songjiang new city)] between December 2020 and March 2022 was available to verify the proposed predictive model. Patients were included and excluded using the same criteria as those in the training set, which were then used to validate (Figures 1, 2).

## Statistical analysis

The descriptive statistics of data were given as mean ± standard deviation for nor-malized variables and median (min–max) for non-normalized variables after a normality analysis of continuous variables using the Shapiro–Wilk test. For the categorical variables, descriptive statistics were reported as numbers and percentages (n, %). Continuous variables were compared using Student's t-test or the Mann–Whitney U test. Categorical variables were analyzed with the $\chi^2$ test or Fisher's exact test where applicable. Univariate analysis and LASSO regression analysis were performed to identify the risk factors to discriminate LR-M HCC and LR-M non-HCC. Binary logistic regression analysis was then conducted to build clinicopathologic, MRI, and combined models. Receiver operating characteristics (ROC) analysis was finally performed with corresponding areas under the curve (AUCs) computed. Inter-observer agreement analysis for MRI features was performed using Cohen's kappa statistics (slight, 0.00–0.20; fair, 0.21–0.40; moderate, 0.41–0.60; substantial, 0.61–0.80; perfect, 0.81–1.00). Values of *P* < 0.05 were considered statistically significant. All data analyses were performed using MedCalc software (MedCalc 20.022; MedCalc, Mariakerke, Belgium) and R software (version 3.4.1).

## Results

### Clinicopathologic characteristics

A total of 105 patients (mean age, 61 ± 14 years; 77 men) with 113 liver observations were classified as the training set, which comprised 47 (41.59%) LR-M HCC malignancies, 56 (49.56%) LR-M non-HCC malignancies, and 10 (8.85%) benign lesions. Seven patients were diagnosed by biopsy, and each patient had one observation. A total of 50 patients (mean age, 59 ± 13 years; 36 men) with

53 liver observations were classified as the validation set. The training set comprised an HCC group (mean age, 57 ± 14 years; 31 men, 12 women) and a non-HCC group (mean age, 63 ± 13 years; 46 men, 16 women) ($P = 0.03$ ). There was no significant difference between the sex distributions of the two groups ($P = 0.682$), but there was a statistically significant difference in the ages of the two groups ($P = 0.034$). In the training set, hepatitis B virus infection was observed in most patients, whether in the HCC group [41 (95.35%)] or in the non-HCC group [57 (91.94%9], where-

as other etiologies occurred rarely. The AST levels >40 U/L and serum AFP levels >20 ng/mL were both significantly higher ($P = 0.002$, $P < 0.001$, respectively) in the HCC group [23 (48.94%); 27 (57.45%)] than in the non-HCC group [11 (16.67%); 9 (13.64%)]. However, serum carcinoembryonic antigen levels ≤5 µg/mL were more likely to be lower in the HCC group [41 (87.23%)] than in the non-HCC group [45 (68.18%)] ($P = 0.019$). There were no significant differences in the remaining demographic variables between the two groups. Additionally, no variables were significantly different between the training and validation sets. An overview of the data is presented in Table 1.

### Univariate analysis of magnetic resonance imaging features

The MRI features of the LR-M HCC and non-HCC groups are summarized in Table 2. Fifteen MRI features remained after univariate analysis. For the LR-M targetoid appearance, 14 (29.79%) cases had peripheral washout in the HCC group compared with 6 (9.09%) in the non-HCC group ($P = 0.004$), whereas only 3 (6.38%) cases had delayed central enhancement in the HCC group compared with 16 (24.24%) cases in the non-HCC group ($P = 0.012$). For LR-M nontargetoid appearance, marked diffusion restriction [11 (23.40%) cases], surface retraction [6 (12.77%) cases] and peritumoral bile duct dilatation [5 (10.64%) cases] were less frequent in the HCC group than in the non-HCC group [28 (42.42%), 32 (48.48%), and 29 (43.94%) cases, respectively] ($P = 0.036$, $P < 0.001$, $P < 0.001$, respectively). In regard to major features, capsular enhancement was more frequent in the HCC group [25 (53.19%) cases] than in the non-HCC group [15 (22.73%) cases] ($P = 0.001$). Regarding the ancillary features favoring HCC, all variables were significantly different between the two groups. For the signal intensity and enhancement pattern, washout or isoenhancement on the portal venous or delayed phase (DP) was present among 21 cases in the HCC group (44.68%) and only 4 cases in the non-HCC group (6.06%) ($P < 0.001$). Hyperenhancement was not significantly more common in the portal venous phase or DP in the HCC group than in the non-HCC group. The hyperintensity on DWIs constituted the majority of observations in both groups, with $P = 0.016$.

### Feature selection

The results of the selection algorithm are detailed in Figure 2. A total of 19 variables related to clinicopathology and MRI met the
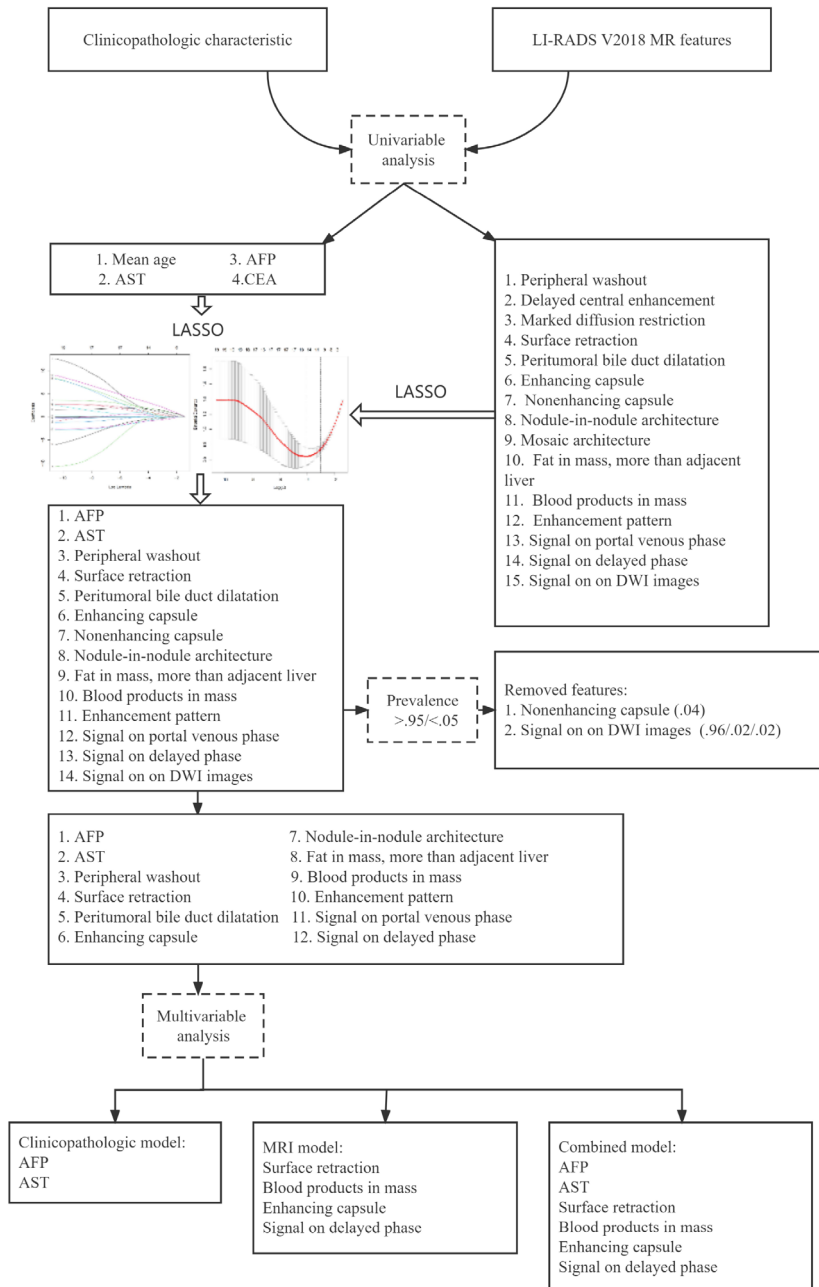


**Figure 2.** A workflow for creating clinicopathologic, MRI, and combined diagnostic models identifying Liver Imaging Reporting and Data System M hepatocellular carcinoma. LI-RADS v2018, LI-RADS version published in 2018; AFP, alpha-fetoprotein; AST, aspartate aminotransferase; CEA, carcinoembryonic antigen; LASSO, least absolute shrinkage and selection operator; DWI, diffusion-weighted imaging; MRI, magnetic resonance imaging; LI-RADS, Liver Imaging Reporting and Data System.

**Table 2.** MRI Features based on LI-RADS for identifying LR-M HCC and non-HCC: univariate analysis

| MRI features LR-M | HCC group (n = 47) | Non-HCC group (n = 66) | Kappa value | Prevalence | *P* value |
|---|---|---|---|---|---|
| **Targetoid appearance^** | | | | | |
| Rim APHE | 36 (76.60) | 51 (77.27) | 0.91 | | 0.933 |
| Peripheral washout | 14 (29.79) | 6 (9.09) | 0.89 | 0.18 | **0.004** |
| Delayed central enhancement | 3 (6.38) | 16 (24.24) | 0.90 | 0.17 | **0.012** |
| Targetoid restriction | 15 (31.91) | 22 (33.33) | 0.84 | | 0.874 |
| **Non-targetoid appearance^** | | | | | |
| Infiltrative appearance | 20 (42.55) | 24 (36.36) | 0.78 | | 0.506 |
| Marked diffusion restriction | 11 (23.40) | 28 (42.42) | 0.86 | 0.35 | **0.036** |
| Necrosis or severe ischemia | 16 (34.04) | 21 (31.82) | 0.80 | | 0.804 |
| Surface retraction | 6 (12.77) | 32 (48.48) | 0.95 | 0.34 | **<0.001** |
| Peritumoral bile duct dilatation | 5 (10.64) | 29 (43.94) | 0.87 | 0.30 | **<0.001** |
| **Major features^** | | | | | |
| Non-rim APHE | 5 (10.64) | 3 (4.55) | 0.81 | | 0.274 |
| Non-peripheral washout | 1 (2.13) | 0 (0) | 0.67 | | 0.416 |
| Enhancing capsule | 25 (53.19) | 15 (22.73) | 0.92 | 0.35 | **0.001** |
| **Ancillary features^ Favoring HCC** | | | | | |
| Non-enhancing capsule | 5 (10.64) | 0 (0) | 0.70 | 0.04 | 0.011 |
| Nodule-in-nodule architecture | 7 (14.89) | 1 (1.52) | 0.81 | 0.07 | **0.009** |
| Mosaic architecture | 16 (34.04) | 10 (15.15) | 0.88 | 0.23 | **0.019** |
| Fat in mass, more than adjacent liver | 15 (31.91) | 0 (0) | 0.96 | 0.13 | **<0.001** |
| Blood products in mass | 19 (40.43) | 6 (9.09) | 0.91 | 0.22 | **<0.001** |
| **Favoring malignancy** | | | | | |
| Corona enhancement | 7 (14.89) | 17 (25.76) | 0.81 | | 0.164 |
| Fat sparing in solid mass | 2 (4.26) | 4 (6.06) | 0.79 | | 1.000 |
| Iron sparing in solid mass | 1 (2.13) | 1 (1.52) | 0.72 | | 1.000 |
| Restricted diffusion | 46 (97.87) | 65 (98.48) | 0.95 | | 1.000 |
| Mild-moderate T2 hyperintensity | 42 (89.36) | 57 (86.36) | 0.96 | | 0.634 |
| **Other features** | | | | | |
| Enhancement pattern^ | | | 0.80 | | **<0.001** |
| Progressive or persistent/washout or iso enhancement on PVP or DP | 26 (55.32)/21 (44.68) | 62 (93.94)/4 (6.06) | | 0.78/0.22 | |
| Signal intensity on AP^ Hyper/(iso/hypo) | 40 (85.11)/7 (14.89) | 56 (84.85)/10 (15.15) | 0.97 | | 0.97 |
| Signal intensity on PVP^ Hyper/(iso/hypo) | 26 (55.32)/21 (44.68) | 56 (84.85)/10 (15.15) | 0.93 | 0.73/0.27 | **0.001** |
| Signal intensity on DP^ Hyper/(iso/hypo) | 21 (44.68)/26 (55.32) | 59 (89.39)/7 (10.61) | 0.91 | 0.71/0.29 | **<0.001** |
| Signal intensity on T1-weighted images* Hyper/iso/hypo | 3 (6.38)/2 (4.26)/42 (89.36) | 1 (1.52)/3 (4.55)/62 (93.94) | 0.96 | | 0.355 |
| Signal intensity on T2-weighted images* Hyper/iso/hypo | 44 (93.62)/2 (4.26)/1 (2.13) | 64 (96.97)/2 (3.03)/0 (0) | 0.96 | | 0.299 |
| Signal intensity on DWI images* Hyper/iso/hypo | 43 (91.49)/2 (4.26)/2 (4.26) | 66 (100)/0 (0)/0 (0) | 0.90 | 0.96/0.02/0.02 | **0.016** |

All *P* values less than 0.05 are bold. Data are numbers of observations, with percentages in parentheses. ^Chi-square test; *Mann–Whitney U test; LI-RADS, Liver Imaging Reporting and Data System; HCC, hepatocellular carcinoma; APHE, arterial phase hyperenhancement; PVP, portal venous phase; DP, delayed phase; AP, arterial phase; DWI, diffusion-weighted imaging; MRI, magnetic resonance imaging.

criteria for univariate analysis. By performing a LASSO regression analysis, 14 variables with non-zero coefficients were then entered into the training set (λ: 0.017655622). Finally, two variables (non-enhancing capsule and signal on DWIs) were removed from the model due to the prevalence being too high or low.

**Multivariate analysis**

Detailed results are presented in Table 3. The diagnostic model of LR-M HCC based on only clinicopathological characteristics showed that both AST [odds ratio (OR): 6.72; 95% confidence interval (CI): 2.44, 18.49; *P* < 0.001] and AFP (OR: 11.19; 95% CI: 4.05, 30.90; *P* < 0.001) were significant risk factors for

HCC. The second model based on only MRI features showed that surface retraction (OR: 0.11; 95% CI: 0.03, 0.40; *P* < 0.001), capsular enhancement (OR: 6.69; 95% CI: 2.13, 21; *P* = 0.001), blood products in mass (OR: 6.25; 95% CI: 1.7, 23; *P* = 0.006), and iso/hypoenhancement on DP (OR: 12.76; 95% CI: 3.67, 44.36; *P* < 0.001) were significant risk factors for HCC. The combined model consisting of clinicopathological and MRI factors showed that all of the abovementioned variables with different ORs and 95% CIs were associated with HCC (Figure 3). As a final step, a forest plot and nomogram were developed after identifying those factors.

**Diagnostic performance of different models from the training and validation sets**

An assessment of diagnostic test results using ROC curve analysis was further performed to identify LR-M HCC for different models (Figure 4). The AUCs with 95% CIs were 0.81 (0.72, 0.88), 0.89 (0.81, 0.94), and 0.95 (0.89, 0.98) for the clinicopathological model, MRI model, and combined model in the training set, respectively. The AUCs with 95% CIs were 0.74 (0.61, 0.85), 0.88 (0.76, 0.95), and 0.90 (0.76, 0.97) for the clinicopathological model, MRI model, and combined model in the validation set, respectively. The corresponding sensitivities, specificities, positive predictive values, negative predictive values, positive likelihood ratios, negative likelihood ratios, and cut-off values are detailed in Table 4.

**Prediction of the nomogram and construction of external validation**

A ROC curve was also drawn to assess the diagnostic accuracy of LR-M HCC in the validation set (Figure 4). The AUC value of the combined model [OR (95% CI), 0.90 (0.76,
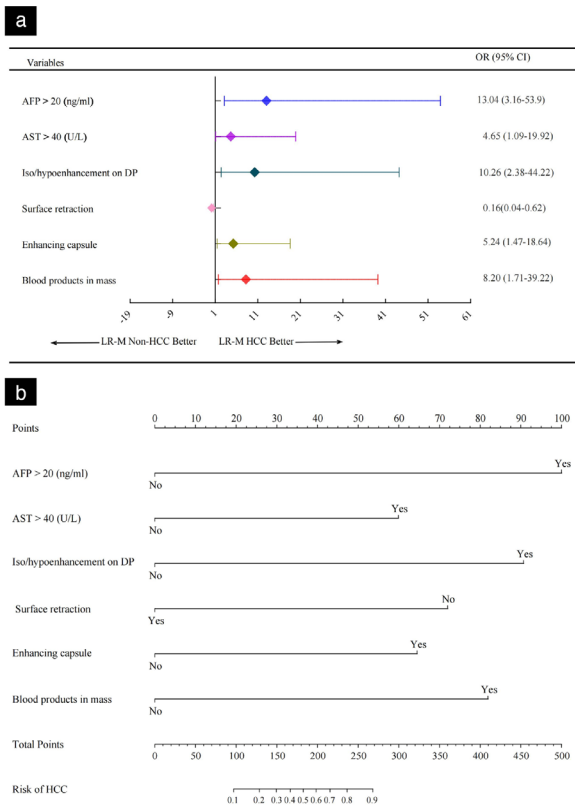
**Figure 3.** A forest plot **(a)** used to display the prognostic factors of the Liver Imaging Reporting and Data System (LI-RADS) M (LR-M) hepatocellular carcinoma (HCC) in the combined model. A nomogram **(b)** for predicting the LR-M HCC probabilities based on the combined model. The points were obtained by drawing a vertical line from the single variable axis to the point axis for each factor. The total points were then projected onto the bottom axis to obtain a personalized probability of LR-M HCC risk. AFP, alpha-fetoprotein; AST, aspartate aminotransferase; DP, delayed phase; HCC, hepatocellular carcinoma; OR, odds ratio; CI, confidence interval.

**Table 3.** Clinicopathologic and MRI features associated with LR-M HCC: binary logistic regression analysis

| Features | Clinicopathologic model | | MRI model | | Combined model | |
|---|---|---|---|---|---|---|
| | OR (95% CI) | *P* value | OR (95% CI) | *P* value | OR (95% CI) | *P* value |
| **Clinicopathologic** | | | | | | |
| AST (>40)* | 6.72 (2.44, 18.49) | 0.002 | | | 4.65 (1.09, 19.92) | 0.038 |
| AFP (> 20)* | 11.19 (4.05, 30.90) | <0.001 | | | 13.04 (3.16, 53.90) | <0.001 |
| **MRI** | | | | | | |
| Surface retraction (non)* | | | 0.11 (0.03, 0.40) | <0.001 | 0.16 (0.04, 0.62) | 0.008 |
| Enhancing capsule (no)^ | | | 6.69 (2.13, 21.00) | 0.001 | 5.24 (1.47, 18.64) | 0.012 |
| Blood products in mass (non)* | | | 6.25 (1.70, 23.00) | 0.006 | 8.20 (1.71, 39.22) | 0.008 |
| Signal intensity on DP (iso/hypo)* | | | 12.76 (3.67, 44.36) | <0.001 | 10.26 (2.38, 44.22) | 0.002 |

*/^Contents in parentheses are reference categories. Non/no stands for the negative of the variables. "No" refers to only no enhancing capsule, but not refers to non-enhancing capsule, which was removed from the analysis due to low prevalence. Hosmer and Lemeshow goodness of fit test was performed for the combined model with a *P* value of 0.370, illustrating no evidence of poor fit. LI-RADS M, Liver Imaging Reporting and Data System M; HCC, hepatocellular carcinoma; OR, odds ratio; CI, confidence intervals; AST, aspartate aminotransferase; AFP, alpha-fetoprotein; DP, delayed phase, MRI, magnetic resonance imaging.

0.97)] was greater than that of both the clinicopathological [0.74 (0.61, 0.85)] and MRI models [0.88 (0.76, 0.95)] in the validation set, similar to the results mentioned earlier in the training set. Overall, the combined model had the strongest predictive value in both the training and validation sets, with a concordance index (C-index) of 0.948 and 0.899, respectively. As shown by the calibration plots (Figure 4), both the training and validation sets showed good consistency between the predictions and the actual obser-
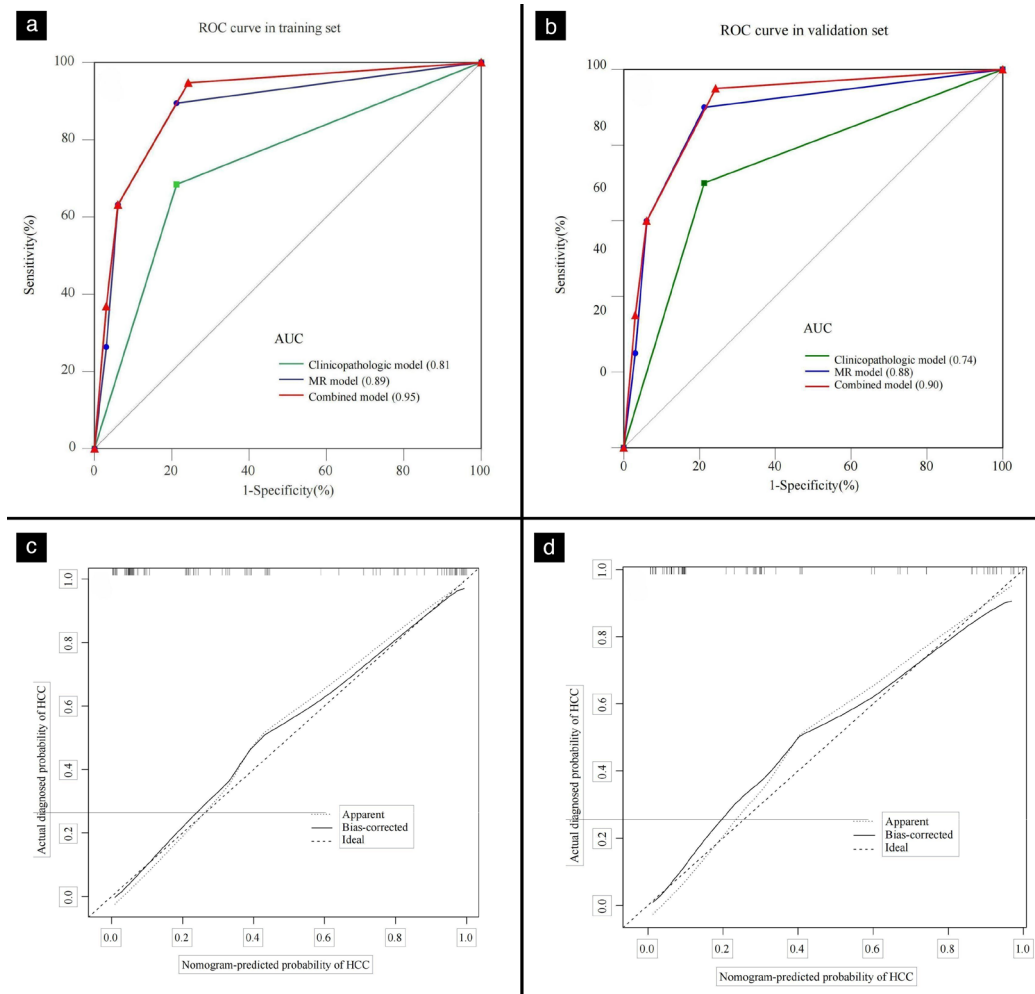


**Figure 4.** A receiver operating characteristic curve used to evaluate the diagnostic value for the Liver Imaging Reporting and Data System M hepatocellular carcinoma of clinicopathologic, MRI, and combined model in the training **(a)** and validation **(b)** sets. A calibration curve was used to evaluate the calibration performance of the combined model in the training **(c)** and validation **(d)** sets. ROC, receiver operating characteristic; AUC, area under the curve; HCC, hepatocellular carcinoma; MRI, magnetic resonance imaging.

**Table 4.** The diagnostic performance of the clinicopathologic, MRI, and combined model for identifying LR-M HCC and non-HCC

| Model | Training patients | | | Validation patients | | |
|---|---|---|---|---|---|---|
| | Clinicopathologic model | MRI model | Combined model | Clinicopathologic model | MRI model | Combined model |
| AUC (95% CI) P value | 0.81 (0.72, 0.88) <0.001 | 0.89 (0.81, 0.94) <0.001 | 0.95 (0.89, 0.98) <0.001 | 0.74 (0.61, 0.85) 0.003 | 0.88 (0.76, 0.95) <0.001 | 0.90 (0.76, 0.97) <0.001 |
| Sensitivity (95% CI) | 83.0 (69.2, 92.4) | 85.1 (71.7, 93.8) | 93.6 (82.5, 98.7) | 70.0 (45.7, 88.1) | 90.0 (68.3, 98.8) | 95.0 (75.1, 99.9) |
| Specificity (95% CI) | 71.2 (58.7, 81.7) | 84.9 (73.9, 92.5) | 87.9 (77.5, 94.6) | 78.8 (61.1, 91.0) | 78.8 (61.1, 91.0) | 75.8 (57.7, 88.9) |
| PPV (95% CI) | 67.2 (57.9, 75.4) | 80.0 (69.1, 87.8) | 84.6 (74.1, 91.4) | 66.7 (49.4, 80.4) | 72.0 (56.7, 83.5) | 70.4 (56.3, 81.4) |
| NPV (95% CI) | 85.5 (75.4, 91.8) | 88.9 (80.0, 94.1) | 95.1 (86.6, 98.3) | 81.2 (68.4, 89.6) | 79.5 (69.2, 87.0) | 96.2 (78.6, 99.4) |
| PLR (95% CI) | 2.88 (1.93, 4.30) | 5.62 (3.13, 10.1) | 7.72 (4.02, 14.9) | 3.3 (1.61, 6.76) | 4.2 (2.16, 8.32) | 3.92 (2.13, 7.22) |
| NLR (95% CI) | 0.24 (0.12, 0.46) | 0.18 (0.09, 0.35) | 0.07 (0.02, 0.22) | 0.38 (0.19, 0.76) | 0.43 (0.25, 0.73) | 0.07 (0.01, 0.45) |
| Cut-off value | 0.15 | 0.24 | 0.33 | 0.19 | 0.10 | 0.07 |

LI-RADS M, Liver Imaging Reporting and Data System M; HCC, hepatocellular carcinoma; AUC, area under the curve; CI, confidence intervals; PPV, positive predictive value; NPV, negative predictive value; PLR, positive likelihood ratio; NLR, negative likelihood ratio; MRI, magnetic resonance imaging.

vations. The clinical use of decision curve analysis for the LR-M HCC nomogram is presented in Figure 5. Ultimately, two examples of a nomogram application in practice are presented in Figure 6.

## Discussion

Recently, various prognostic models for LR-M lesions have been described,[11-15] but an ideal model combining clinicopathologic and MRI features for discriminating LR-M HCC from other observations has not been developed. In a previous study,[12] targetoid tumors and enhancing capsules were combined to identify LR-M HCC, which showed high specificity (93.8%) but low sensitivity (76.6%). In this study, the authors established a nomogram-based combined model including AST, AFP, and MRI (surface retraction, enhancing capsule, blood products in mass, and iso/hypoenhancement on DP) features to classify LR-M HCC. The model had a high sensitivity (training, 93.6%; validation, 95%) for identifying LR-M HCC with specificity (training, 87.9%; validation, 75.8%). The nomogram

for identifying LR-M HCC yielded satisfactory results in the training (C-index 0.948) and validation (C-index 0.899) datasets.

High AFP levels [OR: 13.04; 95% CI: (3.16, 53.9)] had the strongest association with LR-M HCC and had the highest weight in the nomogram-based model. AFP levels played an important role in distinguishing LR-M HCC from other observations in previous studies,[16-18] and AFP expression was also higher in cytokeratin 19-positive patients with HCC who were more coincident with imaging features for LR-M HCCs.[13,19] Thus, AFP levels may be used to identify LR-M HCCs, but with the consideration that AFP levels were also high in patients with combined HCC-cholangiocarcinoma (cHCC-CCA). In our current study, cHCC-CCA was comprised of only 10.61% of LR-M non-HCC in the training set and only 6.06% in the validation set. A relatively small amount of cHCC-CCA may have had an impact on the significance of AFP. Therefore, discrimination between LR-M HCCs and LR-M non-HCCs based on AFP levels remains to be further confirmed in

a larger study. The AST levels [OR: 4.65; 95% CI, (1.09, 19.92)] were of minimal importance for our model, even though it was regarded as a predictor for LR-M HCC. It is possible that the microenvironment of the chronic inflammatory response of the liver and subsequent liver damage contributed to HCC,[7,20,21] which resulted in clinically higher AST levels among patients with impaired hepatic function.

As the strongest contributor to the MRI model, iso/hypoenhancement on DP [OR: 10.26; 95% CI, (2.38, 44.22)] ranked second only to AFP levels for identifying LR-M HCC in the combined model. Previous studies showed that hyperintensity on DP was more common in ICC than in atypical HCC.[6,15] These findings were similar to the authors' findings that hyperintense lesions accounted for most LR-M non-HCC lesions (89.39%), of which more than half were ICC. The reason may be linked to the relatively abundant pathological fibrosis of ICC compared with LR-M HCC, which can mimic conventional HCC.[22,23] On the contrary, sparing fibrosis in LR-M HCC makes a relatively weak contribution to the prolonged retention of extracellular gadolinium contrast agent, which results in iso-intense or hypointense on DP in LR-M HCC.

In addition to iso/hypoenhancement on DP, both enhancing capsule [OR: 5.24; 95% CI: (1.47, 18.64)] and surface retraction [OR: 0.16; 95% CI, (0.04, 0.62)] were correlated with LR-M HCC. Enhancing capsule suggested more fibrous tissue peripherally, which represented expansile growth in atypical HCC.[14,22] In contrast, more than half (51.52%) of the non-HCC cases in the study were ICC cases, which contained a higher proportion of tumor cells peripherally, manifesting an uncommon capsule appearance.[24] Although a small fraction of HCCs may mimic pathological findings of ICCs based on similar biliary differentiation,[25,26] enhancing capsule still reliably predicted LR-M HCC. Conversely, surface retraction occurred less frequently [6/47 (12.77%)] in the LR-M patients with HCC. It is possible that surface retraction was frequently observed in mass-forming ICC with a relatively fibrotic component instead of HCC, as described in previous studies.[15,27]

Blood products in mass [OR: 8.2; 95% CI, (1.71, 39.22)] was associated with LR-M HCC. This feature accounted for 40.43% of LR-M HCC lesions, similar to a 50% proportion reported by Jiang et al.[13] Another study indicated that blood products in mass may be useful for differentiating LR-M HCC from non-HCC malignancies.[28] Usually, hemorrhage represents rapidly growing tumors
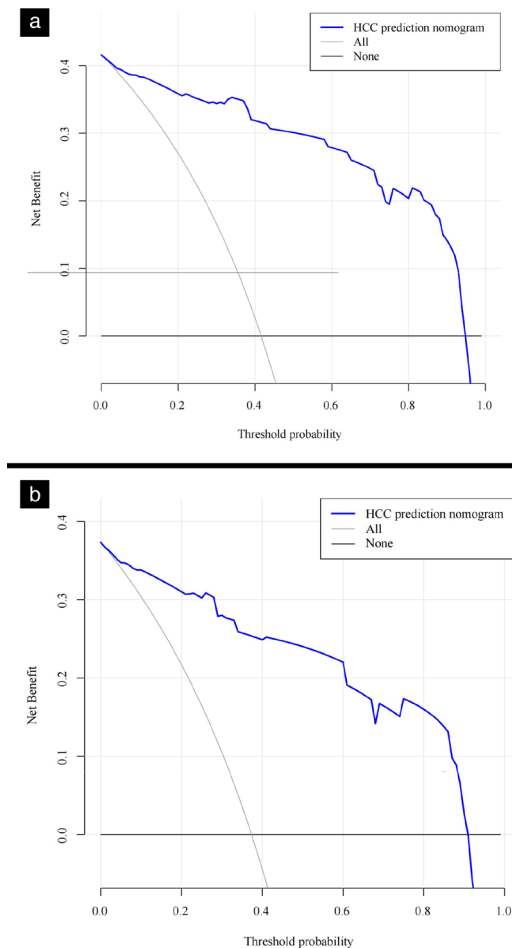
**Figure 5.** A decision curve analysis performed to characterize the potential decision thresholds in the training **(a)** and validation **(b)** sets. HCC, hepatocellular carcinoma.

with an increasing level of malignancy, and the tumor vasculature is correspondingly disrupted. Compared with conventional HCC, LR-M patients with HCC experienced a worse prognosis and were also characterized by abundant blood supply.[19,25,29] This may explain why LR-M HCC cases had a significantly higher incidence of blood products than non-HCC cases with a relatively insufficient blood supply.

The study's predictive model of LR-M HCC was developed using univariate, LASSO, and multivariate analysis, which effectively enabled the feature selection. For the training cohort, the prediction model that contained six selected factors yielded an AUC of 0.95. The calibration curve results showed satisfactory agreement between the predicted LR-M HCC rates and observed probability. The validation of the nomogram-based model is crucial in avoiding overfitting and determining the generalization.[30] Thus, external experimental data were validated in our combined model. The AUC reached 0.90 for the validation set when distinguishing LR-M HCC and demonstrated a good calibration power in which the bias-corrected curve was close to the ideal curve. Additionally, the combined model with the decision curve provided more benefits for making clinical decisions within a range of 0.01–0.94 and 0.02–0.90 threshold probability in the training and validation sets, respectively. By using the nomogram-based model, clinicians can accurately predict the HCC risk of individuals with LR-M observations.

Several limitations were identified in this study. First, it was done retrospectively. Second, a relatively small sample was used in the multivariate analysis; however, another study demonstrated that relaxing the rule of ten events for one variable in logistic regression was acceptable in certain contexts.[31] Third, the authors could not evaluate MRI features in the transitional and hepatobiliary phases without performing gadoxetic acid-enhanced MR imaging due to medical insurance considerations. Fourth, a large prevalence of hepatitis B virus infection might limit the utility in Western countries. Fifth, there was a limited number of combined-type HCC-CCA lesions, which made it particularly challenging to differentiate LR-M observations. Sixth, patients diagnosed by biopsy may not exclude the possibility of cHCC-CCA, even though only seven patients were involved. Finally, it was not possible to perform quantitative measurements for ADC value and contrast-enhanced MRI parameters due to the use of different MRI scanners.

In conclusion, the overall analysis of this combined nomogram-based model incorporating clinicopathologic and MRI items demonstrated a satisfactory prediction result for LR-M HCC, and data are easily available via routine blood tests and MRI examination. The model may have substantial clinical utility not only in terms of individualized risk estimation but also in terms of its clinical application for minimizing or eliminating the need for biopsy.
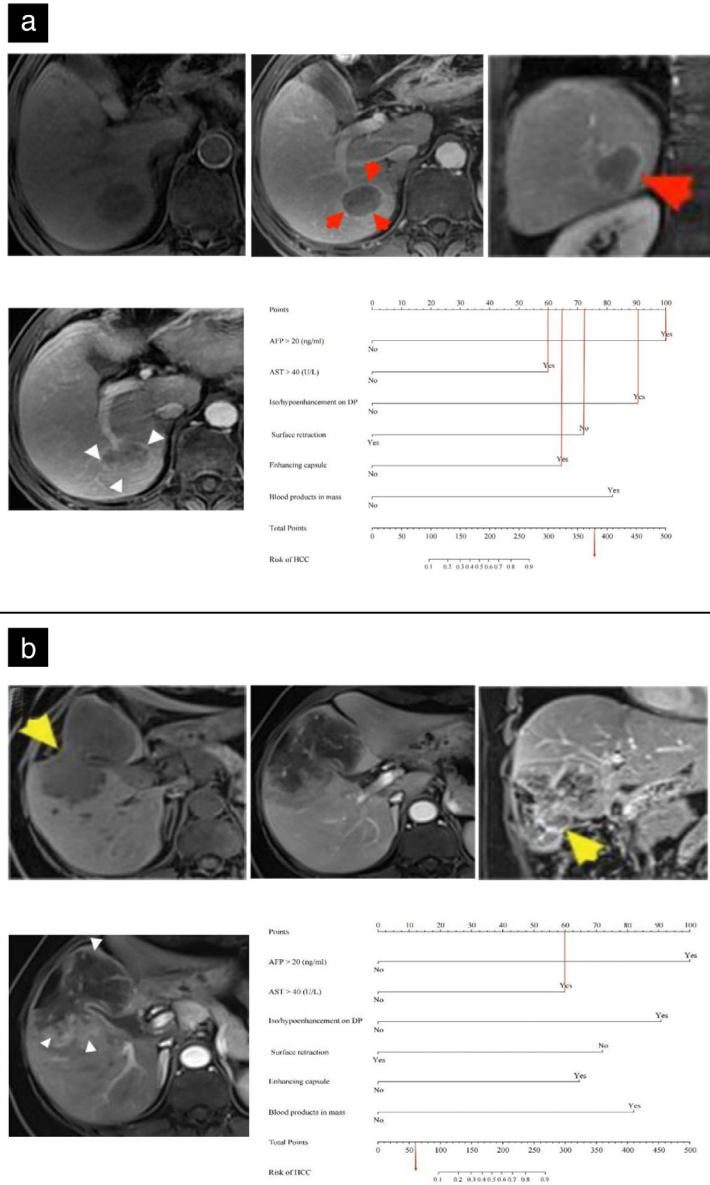


**Figure 6.** Illustration of the nomogram for clinical application. **(a)** Surgically confirmed hepatocellular carcinoma (HCC) with LI-RADS M (LR-M) features in a 60-year-old man who had an aspartate aminotransferase (AST) level of 120 U/L and an alpha-fetoprotein (AFP) level of 300 ng/mL. The tumor showed no blood products sign on precontrast T1-weighted imaging (top, left), slight hyperenhancement (white arrow) peripherally on arterial phase (bottom, left), enhancing capsule (red arrow) on both portal venous phase (top, middle) and coronal delayed phase (top, right), hypoenhancement on coronal delayed phase (top, right), and no surface retraction sign on all images. Total points of 388 represented an LR-M HCC risk >0.9 (bottom, right). **(b)** Surgically confirmed intrahepatic cholangiocarcinoma with LR-M features in a 55-year-old woman who had an AST level of 80 U/L and an AFP level of 12 ng/mL. The tumor showed no blood products sign on precontrast T1-weighted imaging (top, left), heterogeneous hyperenhancement peripherally (white arrow) on arterial phase (bottom, left), no enhancing capsule on both portal venous phase (top, middle) and coronal delayed phase (top, right), heterogeneous hyperenhancement on coronal delayed phase (top, right) and surface retraction (yellow arrow) on precontrast T1-weighted imaging (top, left) and coronal delayed phase (top, right). Total points of 60 represented an LR-M non-HCC risk of <0.1 (bottom, right).

## Conflict of interest disclosure

The authors declared no conflicts of interest.

## References

1. American College of Radiology. Liver Imaging reporting and data system version 2018. [CrossRef]

2. Cerny M, Bergeron C, Billiard JS, et al. LI-RADS for MR imaging diagnosis of hepatocellular carcinoma: performance of major and ancillary features. *Radiology*. 2018;288(1):118-128. [CrossRef]

3. Tang A, Singal AG, Mitchell DG, et al. Introduction to the Liver Imaging Reporting and Data System for Hepatocellular Carcinoma. *Clin Gastroenterol Hepatol*. 2019;17(7):1228-1238. [CrossRef]

4. Torimura T, Iwamoto H. Treatment and the prognosis of hepatocellular carcinoma in Asia. *Liver Int*. 2022;42(9):2042-2054. [CrossRef]

5. Marrero JA, Kulik LM, Sirlin CB, et al. Diagnosis, staging, and management of hepatocellular carcinoma: 2018 practice guidance by the American Association for the Study of Liver Diseases: Marrero et al. *Hepatology*. 2018;68(2):723-750. [CrossRef]

6. Rimola J, Forner A, Reig M, et al. Cholangiocarcinoma in cirrhosis: absence of contrast washout in delayed phases by magnetic resonance imaging avoids misdiagnosis of hepatocellular carcinoma. *Hepatology*. 2009;50(3):791-798. [CrossRef]

7. Llovet JM, Kelley RK, Villanueva A, et al. Hepatocellular carcinoma. *Nat Rev Dis Primers*. 2021;7(1):6. [CrossRef]

8. Davenport MS, Khalatbari S, Liu PSC, et al. Repeatability of diagnostic features and scoring systems for hepatocellular carcinoma by using MR imaging. *Radiology*. 2014;272(1):132-142. [CrossRef]

9. Kim DH, Choi SH, Park SH, et al. Liver imaging reporting and data system category M: a systematic review and meta-analysis. *Liver Int*. 2020;40(6):1477-1487. [CrossRef]

10. Shin J, Lee S, Hwang JA, et al. MRI-diagnosis of category LR-M observations in the Liver Imaging Reporting and Data System v2018: a systematic review and meta-analysis. *Eur Radiol*. 2022;32(5):3319-3326. [CrossRef]

11. Jang JK, Choi SH, Byun JH, et al. New strategy for Liver Imaging Reporting and Data System category M to improve diagnostic performance of MRI for hepatocellular carcinoma ≤ 3.0 cm. *Abdom Radiol (NY)*. 2022;47(7):2289-2298. [CrossRef]

12. Min JH, Kim JM, Kim YK, et al. A modified LI-RADS: targetoid tumors with enhancing capsule can be diagnosed as HCC instead of LR-M lesions. *Eur Radiol*. 2022;32(2):912-922. [CrossRef]

13. Jiang H, Song B, Qin Y, et al. Diagnosis of LI-RADS M lesions on gadoxetate-enhanced MRI: identifying cholangiocarcinoma-containing tumor with serum markers and imaging features. *Eur Radiol*. 2021;31(6):3638-3648. [CrossRef]

14. Min JH, Kim YK, Choi SY, et al. Differentiation between cholangiocarcinoma and hepatocellular carcinoma with target sign on diffusion-weighted imaging and hepatobiliary phase gadoxetic acid-enhanced MR imaging: classification tree analysis applying capsule and septum. *Eur J Radiol*. 2017;92:1-10. [CrossRef]

15. Sheng RF, Zeng MS, Rao SX, Ji Y, Chen LL. MRI of small intrahepatic mass-forming cholangiocarcinoma and atypical small hepatocellular carcinoma (≤3 cm) with cirrhosis and chronic viral hepatitis: a comparative study. *Clin Imaging*. 2014;38(3):265-272. [CrossRef]

16. Galle PR, Foerster F, Kudo M, et al. Biology and significance of alpha-fetoprotein in hepatocellular carcinoma. *Liver Int*. 2019;39(12):2214-2229. [CrossRef]

17. Huang JY, Li JW, Ling WW, et al. Can contrast enhanced ultrasound differentiate intrahepatic cholangiocarcinoma from hepatocellular carcinoma? *World J Gastroenterol*. 2020;26(27):3938-3951. [CrossRef]

18. Langenbach MC, Vogl TJ, von den Driesch I, et al. Analysis of Lipiodol uptake in angiography and computed tomography for the diagnosis of malignant versus benign hepatocellular nodules in cirrhotic liver. *Eur Radiol*. 2019;29(12):6539-6549. [CrossRef]

19. Hu XX, Wang WT, Yang L, et al. MR features based on LI-RADS identify cytokeratin 19 status of hepatocellular carcinomas. *Eur J Radiol*. 2019;113:7-14. [CrossRef]

20. Huang H, Tohme S, Al-Khafaji AB, et al. Damage-associated molecular pattern-activated neutrophil extracellular trap exacerbates sterile inflammatory liver injury. *Hepatology*. 2015;62(2):600-614. [CrossRef]

21. Llovet JM, Castet F, Heikenwalder M, et al. Immunotherapies for hepatocellular carcinoma. *Nat Rev Clin Oncol*. 2022;19(3):151-172. [CrossRef]

22. Chen Q, Wang M, Wang M, Jin S, Xiao SY, Tian S. Expansile invasive growth pattern is definite evidence for the diagnosis of small hepatocellular carcinomas: a comparative study of 37 cases. *Hum Pathol*. 2018;80:130-137. [CrossRef]

23. Chung YE, Kim MJ, Park YN, et al. Varying appearances of cholangiocarcinoma: radiologic-pathologic correlation. *Radiographics*. 2009; 29(3):683-700. [CrossRef]

24. Zhang H, Yang T, Wu M, Shen F. Intrahepatic cholangiocarcinoma: epidemiology, risk factors, diagnosis and surgical management. *Cancer Lett*. 2016;379(2):198-205. [CrossRef]

25. Wang W, Gu D, Wei J, et al. A radiomics-based biomarker for cytokeratin 19 status of hepatocellular carcinoma with gadoxetic acid-enhanced MRI. *Eur Radiol*. 2020;30(5):3004-3014. [CrossRef]

26. Murakami Y, Kubo S, Tamori A, et al. Comprehensive analysis of transcriptome and metabolome analysis in intrahepatic cholangiocarcinoma and hepatocellular carcinoma. *Sci Rep*. 2015;5(1):16294. [CrossRef]

27. Panick CEP, Ward RD, Coppa C, Liu PS. Hepatic capsular retraction: an updated MR imaging review. *Eur J Radiol*. 2019;113:15-23. [CrossRef]

28. Park HJ, Kim YK, Cha DI, et al. Targetoid hepatic observations on gadoxetic acid-enhanced MRI using LI-RADS version 2018: emphasis on hepatocellular carcinomas assigned to the LR-M category. *Clin Radiol*. 2020;75(6):478. [CrossRef]

29. Shinmura R, Matsui O, Kobayashi S, et al. Cirrhotic nodules: association between MR imaging signal intensity and intranodular blood supply. *Radiology*. 2005;237(2):512-519. [CrossRef]

30. Alba AC, Agoritsas T, Walsh M, et al. Discrimination and calibration of clinical prediction models: users' guides to the medical literature. *JAMA*. 2017;318(14):1377-1384. [CrossRef]

31. Vittinghoff E, McCulloch CE. Relaxing the rule of ten events per variable in logistic and cox regression. *Am J Epidemiol*. 2007;165(6):710-718. [CrossRef]

**Supplementary Table 1.** Scanner sequences and parameter of MRI system

| | Ingenia 3.0T | | | | 750W 1.5T | | | |
|---|---|---|---|---|---|---|---|---|
| Parameter | TSE T2WI | DWI | 3D-THRIVE | T1WI-mDIXON | FSE T2WI | DWI | 3D-LAVA | T1WI (in/out of phase) |
| TR (ms) | 2725 | 1353 | 3.7 | 3.7 | 8000 | 12857 | 5.04 | 5.4 |
| TE (ms) | 78 | 72 | 1.32 | 1.32 | 82 | 66 | 2.31 | 2.3/1.2 |
| NEX | 1 | 1 | 1 | 1 | 1 | 1 | 1 | 1 |
| Matrix | 165 × 320 | 128 × 80 | 200 × 352 | 180 × 320 | 207 × 384 | 112 × 128 | 250 × 512 | 144 × 256 |
| FOV (mm²) | 285 × 214~285 × 380 | 285 × 214~285 × 380 | 285 × 214~285 ×3 80 | 285 × 214~285 × 380 | 330 × 330~380 × 380 | 330 × 330~380 × 380 | 330 × 330~380 × 380 | 330 × 330~380 × 380 |
| Inversion angle | 140° | / | 9° | 70° | 150° | / | 10° | 70° |
| Slice thickness (mm) | 5 | 5 | 4 | 4 | 7 | 7 | 4-5 | 7 |
| Slice gap (mm) | 1 | 1 | -2 | -2 | 2.1 | 2.1 | 0 | 2.1 |

TSE, turbo spin echo; T2WI, T2-weighted imaging; DWI, diffusion-weighted imaging; 3D-THRIVE, three dimension T1 high resolution isotropic volume examination; T1WI-mDIXON, T1-weighted imaging-modified DIXON; FSE, fast spin echo; 3D-LAVA, three dimension liver acquisition with volume acceleration; TR, repetition time; TE, echo time; NEX, number of excitation; FOV, field of view; MRI, magnetic resonance imaging.

# Prostate zones and tumor morphological parameters on magnetic resonance imaging for predicting the tumor-stage diagnosis of prostate cancer

Shanshan Xu 
Xiaobing Liu 
Xiaoqin Zhang 
Huihui Ji 
Runyuan Wang 
Huilin Cui 
Jinfeng Ma 
Yongjian Nian 
Yi Wu 
Ximei Cao 

**PURPOSE**

To determine whether the morphological parameters of prostate zones and tumors on magnetic resonance imaging (MRI) can predict the tumor-stage (T-stage) of prostate cancer (PCa) and establish an optimal T-stage diagnosis protocol based on three-dimensional reconstruction and quantization after image segmentation.

**METHODS**

A dataset of the prostate MRI scans and clinical data of 175 patients who underwent biopsy and had pathologically proven PCa from January 2018 to November 2020 was retrospectively analyzed. The authors manually segmented and measured the volume, major axis, and cross-sectional area of the peripheral zone (PZ), transition zone, central zone (CZ), anterior fibromuscular stroma, and tumor. The differences were evaluated by the One-Way analysis of variance, Pearson's chi-squared test, or independent samples $t$-test. Spearman's correlation coefficient and receiver operating characteristic curve analyses were also performed. The cut-off values of the T-stage diagnosis were generated using Youden's J index.

**RESULTS**

The prostate volume (PV), PZ volume (PZV), CZ volume, tumor's major axis (TA), tumor volume (TV), and volume ratio of the TV and PV were significantly different among stages T1 to T4. The cut-off values of the PV, PZV, CZV, TA, TV, and the ratio of TV/PV for the discrimination of the T1 and T2 stages were 53.63 cm³, 11.60 cm³, 1.97 cm³, 2.30 mm, 0.90 cm³, and 0.03 [area under the curves (AUCs): 0.628, 0.658, 0.610, 0.689, 0.724, and 0.764], respectively. The cut-off values of the TA, TV, and the ratio of TV/PV for the discrimination of the T2 and T3 stages were 2.80 mm, 8.29 cm³, and 0.12 (AUCs: 0.769, 0.702, and 0.688), respectively. The cut-off values of the TA, TV, and the ratio of TV/PV for the discrimination of the T3 and T4 stages were 4.17 mm, 18.71 cm³, and 0.22 (AUCs: 0.674, 0.709, and 0.729), respectively.

**CONCLUSION**

The morphological parameters of the prostate zones and tumors on the MRIs are simple and valuable diagnostic factors for predicting the T-stage of patients with PCa, which can help make accurate diagnoses and lateral treatment decisions.

**KEYWORDS**

Magnetic resonance imaging, prostate neoplasms, prostate zones, tumor volume, neoplasm-stage

From the Department of Digital Medicine (S.X., X.L., X.Z., R.W., Y.N., Y.W. ✉wuy1979@tmmu.edu.cn), College of Biomedical Engineering and Medical Imaging, Army Medical University (Third Military Medical University), Chongqing, China; Department of Histology and Embryology (S.X., H.J., R.W., H.C., X.C. ✉caoximei@163. com), Shanxi Medical University, Taiyuan, China; Department of Urology (X.L.), Xinqiao Hospital of Army Medical University, Chongqing, China; Department of General Surgery (J.M.), Shanxi Province Cancer Hospital of Shanxi Medical University, Taiyuan, China, Yu-Yue Pathology Research Center, Jinfeng Laboratory (S.X., Y.W.) Chongqing 401329, People's Republic China.

Prostate cancer (PCa) is the second most frequent cancer with the fifth highest mortality rate worldwide.[1] The prostate is an anatomically heterogeneous organ, mainly including the peripheral zone (PZ), transition zone (TZ), central zone (CZ), and anterior fibromuscular stroma (AFMS).[2] On pathological biopsies, PCa is often a multifocal cancer with histologic heterogeneity of different tumor foci, with most tumors in the PZ. As the disease progresses, the tumor invades the adjacent zones and the surrounding fat, seminal vesicles (SV), bladder, and rectum, causing distant metastasis. Thus, PCa can rapidly progress from local inertia to fatal metastatic disease. Furthermore, as the aging population has increased, the incidence of

PCa has also considerably increased, posing an important diagnostic challenge.

Traditionally, patients with suspected PCa after a digital rectal examination (DRE) or prostate-specific antigen (PSA) test require a trans-rectal ultrasound (TRUS)-guided systematic biopsy, which is the current gold standard for diagnosing PCa.[3] However, magnetic resonance imaging (MRI) examinations have become the preferred option since they reduce the number of biopsies carried out and allow more patients to be enrolled in active surveillance programs. There are also many benefits of using MRI for diagnosis. First, unlike DRE and TRUS, MRI is non-invasive.[4] Second, MRI displays the anatomical regions of the prostate better than computed tomography exams. Third, MRI is the gold standard for delineating tumor volume (TV) in PCa, which directly contributes to the tumor-node-metastasis stage (TNM) diagnosis; the TNM stage is critical for selecting the treatment strategy, improving the prognosis, and avoiding or reducing side effects.[5] Fourth, the prostate volume (PV) calculated from a three-dimensional (3D) reconstruction model based on slide-by-slide, manually segmented MRIs is more accurate than the PV calculated from the commonly used ellipsoid formula based on ultrasound images.[6]

Accurately measuring the morphological parameters of the prostate zones and the tumor is necessary for diagnosing and treating PCa.[7-9] For example, the PV helps to determine the appropriate radiotherapy, and the TV has been associated with clinical manifestations of PCa. In addition, some studies have reported the relationship between some morphological parameters (PZ volume, TZ volume, and PV) and benign prostatic hyperplasia (BPH) and PCa. However, few anatomical or pathological studies on the four prostate zones (PZ, TZ, CZ, and AFMS) exist.[10-12] However, to the best of the authors' knowledge, there is little research on the morphological parameters and tumor-stage (T-stage) diagnosis of PCa in the literature that the authors have retrieved.

Herein, the authors investigated the diagnostic roles of the morphological parameters of the prostate zones and prostate tumor on the PCa T-stage to assist clinicians with T-stage diagnoses, prognostic judgments, and the surgical selection of patients with PCa.

## Methods

### Study population and data acquisition

#### Patients

This retrospective study was approved by the Medical Ethics Committee of Shanxi Cancer Hospital (2021051) and The Second Affiliated Hospital of Army Medical University, PLA (2022-YD 460-01). The informed consent requirement was waived since these MRI scans were acquired during routine clinical care.[8]

For this study, the authors obtained the detailed medical histories of 221 patients with PCa treated at the Shanxi Cancer Hospital (n = 42) and The Second Affiliated Hospital of Army Medical University (n = 179) from January 2018 to November 2020. The inclusion criteria were (1) patients who had had an MRI scan due to an increase of PSA and/or the suspicion of PCa by DRE and (2) had undergone multiparametric MRI (mp-MRI) with subsequent 12-core TRUS–guided biopsy and an MRI/TRUS fusion biopsy. The exclusion criteria were patients (1) with a history of (a) endocrine therapy (n = 13), (b) laparoscopic radical prostatectomy (n = 10), and/or (c) transurethral resection (n =

16), and / or (2) who had substandard image quality where the PZ, TZ, CZ, and AFMS were unidentifiable (n = 7). Finally, a total of 175 patients were enrolled in the study. Figure 1 shows the patient selection process.

### Magnetic resonance imaging protocol

MRI exams were performed using a Philips 3 Tesla scanner (Philips Intera, release 10.3; Philips Medical Systems Nederland B.V., Best, the Netherlands) and a General Electric 1.5 Tesla scanner (Signa Horizon EchoSpeed, version 5.8; General Electric Healthcare, Milwaukee, WI, USA). All patients received a routine scan and an enhanced scan. Foam pads were placed in the lower abdomen to reduce breathing and motion artifacts.

The T2-weighted turbo spin-echo sequence was used in the transverse plane with the following parameters in the Shanxi Cancer Hospital: repetition time (RT): 3,590 ms; time to echo (TE): 120 ms; matrix: 432 × 432 mm; slice thickness: 4 mm; pixel spacing: 0.46 mm × 0.46 mm; series number: 602; and pixel bandwidth: 74 Hz/pixel. In The Second Affiliated Hospital of Army Medical University, the parameters were: RT: 4,000 ms; TE: 103 ms; matrix: 512 × 512 mm; slice thickness: 4 mm; pixel spacing: 0.50 mm × 0.50 mm; series number: 7; and pixel bandwidth, 122 Hz/pixel.

The parameters of the diffusion-weighted imaging (DWI) in the Shanxi Cancer Hospital were as follows: RT: 2,750 ms; TE: 50 ms; matrix: 256 × 256 mm; slice thickness: 5 mm; pixel spacing: 1.46 mm × 1.46 mm; series number: 901; and pixel bandwidth: 3,641 Hz/pixel. In The Second Affiliated Hospital of Army Medical University, the parameters were: RT: 5,600 ms; TE: 65 ms; matrix: 256 ×

---

### Main points

- A positive correlation exists between the tumor-stage (T-stage) and quantitative morphological parameters of prostate cancer (PCa).

- The tumor's major axis, tumor volume, and volume ratio of the tumor and prostate can be used as important factors to diagnose the T-stage of PCa.

- The quantitative morphological parameters of the tumor are valuable in improving prognostic and lateral treatment decisions.

---
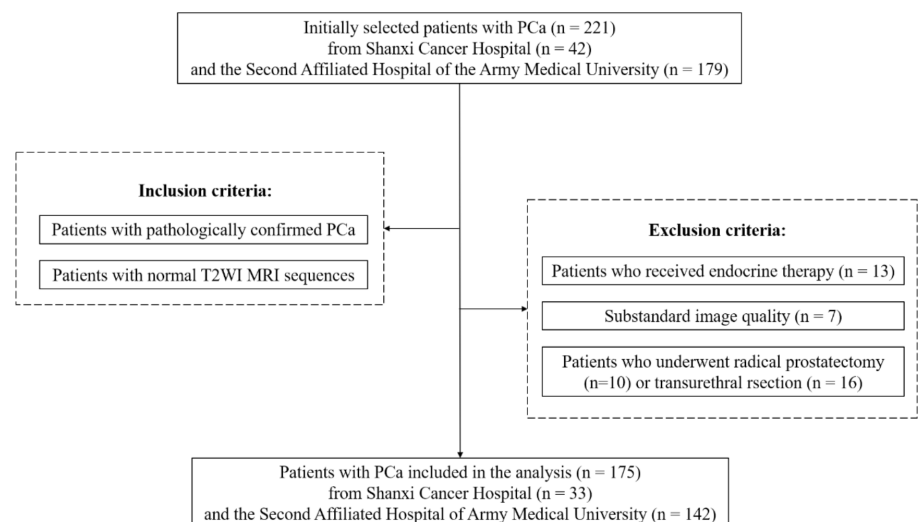


**Figure 1.** Flowchart of patient inclusion and exclusion. PCa, prostate cancer; T2WI, T2-weighted imaging; MRI, magnetic resonance imaging.

The flowchart contains:
- Initially selected patients with PCa (n = 221) from Shanxi Cancer Hospital (n = 42) and the Second Affiliated Hospital of the Army Medical University (n = 179)
- Inclusion criteria: Patients with pathologically confirmed PCa; Patients with normal T2WI MRI sequences
- Exclusion criteria: Patients who received endocrine therapy (n = 13); Substandard image quality (n = 7); Patients who underwent radical prostatectomy (n=10) or transurethral rsection (n = 16)
- Patients with PCa included in the analysis (n = 175) from Shanxi Cancer Hospital (n = 33) and the Second Affiliated Hospital of Army Medical University (n = 142)

256 mm; slice thickness: 4 mm; pixel spacing: 1.56 mm × 1.56 mm; series number: 7; and pixel bandwidth: 1.953 Hz/pixel.

## Clinical information

The authors collected clinical information on each patient from their medical records, including age, body mass index (BMI), free-PSA and total-PSA (f-PSA/t-PSA) levels, pathological T-stage, SV invasion or not, invasion of the surrounding structures, such as the bladder, rectum, or neurovascular bundles (NVB), and the tumor location.

## Image pre-processing and segmentation

The patients were divided into four groups based on their pathological T-stage (T1–T4). To obtain a PCa 3D reconstruction model for further analysis, the authors uploaded the MRI images in Digital Imaging and Communications in Medicine (DICOM) format from the workstation to Amira software (Vision 2019, Thermo Fisher Scientific Inc., Waltham, MA, USA). The window level and window width were adjusted to optimize the visualization of the prostate zones. The segmentation of each MRI image in this study was performed by a junior urological surgeon with 3 years of working experience, and the segmentation result was further reviewed and corrected, if necessary, by a senior radiologist with 14 years of working experience, with the modified results being used for the morphological parameter calculations. The segmentation process was based on the division theory of prostate anatomical zones proposed by McNeal[2], and the recording of the tumor location refers to the sequences of apparent diffusion coefficient and DWI (b = 1000 s/mm$^2$) (Figure 2).

## Three-dimensional prostate cancer reconstruction

After image segmentation, the 3D PCa models were reconstructed through the Generate Surface module of the Amira software. In this software, the models can move, scale, and rotate in all directions.

## Data measurement based on the two-dimensional plane and three-dimensional prostate cancer reconstruction

According to the guidelines of the European Society of Urogenital Radiology, all images in the two-dimensional (2D) plane were retrospectively analyzed by a senior radiologist (with 14 years of working experience) who was unaware of the pathological results and all the clinical information.[13] The staging of the mpMRI was performed using the extracapsular extension (ECE) score introduced by Mehralivand et al.[14] The ECE score criteria were as follows: (a) grade 0, no suspicion of pathological ECE; (b) grade 1, either a curved contact length ≥1.5 cm or an irregular capsule or bulge; (c) grade 2, both of the above in grade 1; and (d) grade 3, obvious envelope breakthrough. The tumor's major axis (TA) was the maximal value of the tumor's diameter in three-axis planes using a MicroDICOM viewer (Solvusoft Corporation, Las Vegas, NV, USA).

In the 3D PCa reconstruction model, the PV, PZ volume (PZV), TZ volume (TZV), CZ volume (CZV), AFMS volume (AFMSV), and TV were measured using the surface area volume module in the Amira software. These were then used to analyze the relationship between the volume and T-stage. After that, the PZV/PV, TZV/PV, CZV/PV, and AFMSV/PV ratios were obtained by individually dividing PZV, TZV, CZV, and AFMSV by PV.

## Statistical analysis

All statistical analyses were performed using the Statistical Package for the Social Sciences Statistics, version 25.0 (IBM Corp., Armonk, NY, USA). The number of PCa lesions was expressed as frequencies (percentages). Categorical data were analyzed using Pearson's chi-squared test and continuous data with the One-Way analysis of variance and independent samples t-test. Spearman's rank correlation coefficient was used to analyze the relationship between the multivariate parameters and the T-stage. All $P$ values were two-sided, and those $P < 0.050$ were considered statistically significant.[15]

The receiver operating characteristic (ROC) curves analysis was used to determine the cut-off values of the different T-stages and evaluate the predictive performance of the morphological parameters for the T-stage diagnosis. The performance characteristics, including the area under the curve (AUC) of the ROC curve, sensitivity, and specificity, were also analyzed. The optimal cut-off values were calculated according to the formula (Youden's J index = sensitivity + specificity - 1), which is meaningful when its AUC >0.6.[16,17]

## Results

### Baseline characteristics

In this study, the authors enrolled 175 patients with PCa treated at the Shanxi Cancer Hospital (n = 40) and The Second Affiliated Hospital of Army Medical University (n = 135). According to the eighth edition of the American Joint Committee on Cancer staging criteria, the patients were divided into T1 (n = 25), T2 (n = 80), T3 (n = 36), and T4 (n = 34) stages. Age and BMI did not differ among the T-stage groups ($P = 0.261$ and $P = 0.315$), but the f-PSA/t-PSA levels significantly decreased from T1 to T4 ($P < 0.001$), 51.43% of patients (126/175) had a Gleason score (GS) of 4 + 4 or greater ($P < 0.001$), and the ECE score increased in accordance with the pathological T-stage ($P < 0.001$) (Table 1).

### Tumor location

Table 2 presents the tumor locations based on the T-stage. In all patients, most tumors were in the PZ (45.7%), followed by the PZ and TZ (33.7%), then the TZ (7.6%). No tumors were in the CZ or AFMS. Approximately 24.0% of T1 and 10.0% of T2 tumors were difficult to identify on MRI. Furthermore, 58.3% (21/36) of T3 and 76.5% (26/34) of T4 tumors had invaded the SV. Approximately 50.0% (17/34) of T4 tumors had invaded the urethra, bladder, rectum, NVB, or other surrounding structures. Figure 3 illustrates the tumor changes in randomly selected, representative cases from each T-stage; these images show how the tumor area gradually increased from T1 to T4, indicating an overall increase in tumor aggressiveness.
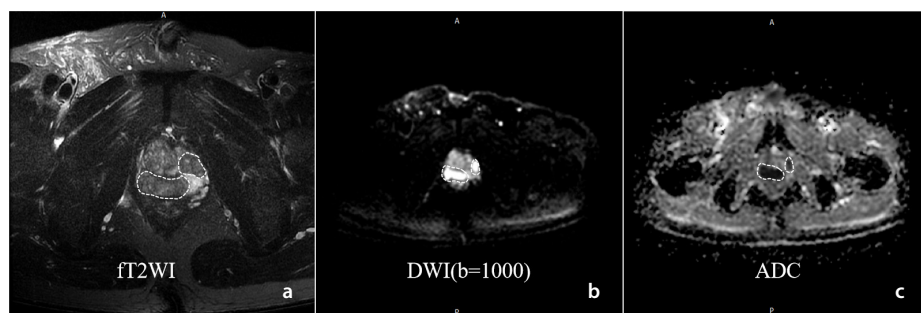


**Figure 2.** Tumor segmentation (dashed box) on different magnetic resonance imaging sequences, including T2WI **(a)**, DWI (b = 1000 s/mm$^2$) **(b)**, and ADC map **(c)** (Software: Syngo Quick Brower). fT2WI, fat-suppressed T2 weighted imaging; DWI, diffusion-weighted imaging; ADC, apparent diffusion coefficient.

**Table 1.** Demographic information of patients with prostate cancer at different tumor stages

| | T1 (n = 25) | T2 (n = 80) | T3 (n = 36) | T4 (n = 34) | P | Total |
|---|---|---|---|---|---|---|
| Age (y) | 73.88 ± 9.50 | 70.61 ± 10.53 | 71.47 ± 7.98 | 71.48 ± 9.16 | 0.261[a] | 71.67 ± 8.88 |
| BMI (kg/m$^2$) | 21.86 ± 3.26 | 24.63 ± 3.44 | 23.48 ± 3.09 | 23.28 ± 2.95 | 0.315[a] | 22.15 ± 3.53 |
| f-PSA/t-PSA (ng/mL) | 0.20 ± 0.07 | 0.18 ± 0.12 | 0.15 ± 0.10 | 0.11 ± 0.08 | 0.000[a] | 0.16 ± 0.13 |
| MRI-based ECE score | | | | | 0.000[b] | |
| 0 | 25/25(100.00%) | 74/80 (92.50%) | 0/36 (0.00%) | 0/34 (0.00%) | - | 99/175 (56.57%) |
| 1 | 0/25 (0.00%) | 6/80 (7.50%) | 7/36 (19.44%) | 0/34 (0.00%) | - | 13/175 (7.43%) |
| 2 | 0/25 (0.00%) | 0/80 (0.00%) | 29/36 (80.56%) | 6/34 (17.65%) | - | 35/175 (20.00%) |
| 3 | 0/25 (0.00%) | 0/80 (0.00%) | 0/36 (0.00%) | 28/34 (100.00%) | - | 28/175 (16.00%) |
| Biopsy GS | | | | | 0.000[b] | |
| GS = 3 + 3 | 13/25 (52.94%) | 9/80 (11.25%) | 1/36 (2.12%) | 0/34 (0.00%) | - | 23/175 (13.14%) |
| GS = 3 + 4 | 12/25 (47.06%) | 14/80 (17.50%) | 5/36 (14.89%) | 0/34 (0.00%) | - | 31/175 (17.71%) |
| GS = 4 + 3 | 0/25 (0.00%) | 17/80 (21.25%) | 8/36 (21.27%) | 6/34 (17.39%) | - | 31/175 (17.71%) |
| GS ≥ 4 + 4 | 0/25 (0.00%) | 40/80 (50.00%) | 22/36 (61.70%) | 28/34 (82.61%) | - | 90/175 (51.43%) |

Unless indicated otherwise, the data specifies the number of cases, with percentages in parentheses. [a], One-Way analysis of variance; [b], Pearson's chi-squared test. T, tumor; BMI, body mass index; PSA, prostate-specific antigen; f-PSA/t-PSA, free-PSA/total-PSA; MRI, magnetic resonance imaging; ECE, extracapsular extension; GS, Gleason score.

**Table 2.** Tumor distributions of patients with prostate cancer at different tumor stages

| Distribution of cancer foci (number of patients, ratio) | T-stage of PCa | | | | Total |
|---|---|---|---|---|---|
| | T1 (n = 25) | T2 (n = 80) | T3 (n = 36) | T4 (n = 34) | |
| **Tumors located only in the PZ** | 16 (64.0%) | 43 (53.8%) | 12 (33.3%) | 10 (26.5%) | 81 (46.3%) |
| **Tumors located only in the TZ** | 2 (8.0%) | 7 (8.7%) | 4 (11.1%) | 0 (0.0%) | 13 (7.4%) |
| **Tumors located in the PZ and TZ** | 1 (4.0%) | 22 (27.5%) | 20 (55.6%) | 24 (67.6%) | 67 (38.3%) |
| **Tumors invading the SV** | 0 (0.0%) | 0 (0.0%) | 21 (58.3%) | 26 (76.5%) | 47 (26.9%) |
| **Tumors invading adjacent structures** | 0 (0.0%) | 0 (0.0%) | 0 (0.0%) | 17 (50.0%) | 17 (9.7%) |
| **Tumors that are difficult to identify** | 6 (24.0%) | 8 (10.0%) | 0 (0.0%) | 0 (0.0%) | 14 (8.0%) |

The data specifies the number of cases, with percentages in parentheses. T, tumor; PCa, prostate cancer; PZ, peripheral zone; TZ, transition zone; SV, seminal vesicles.
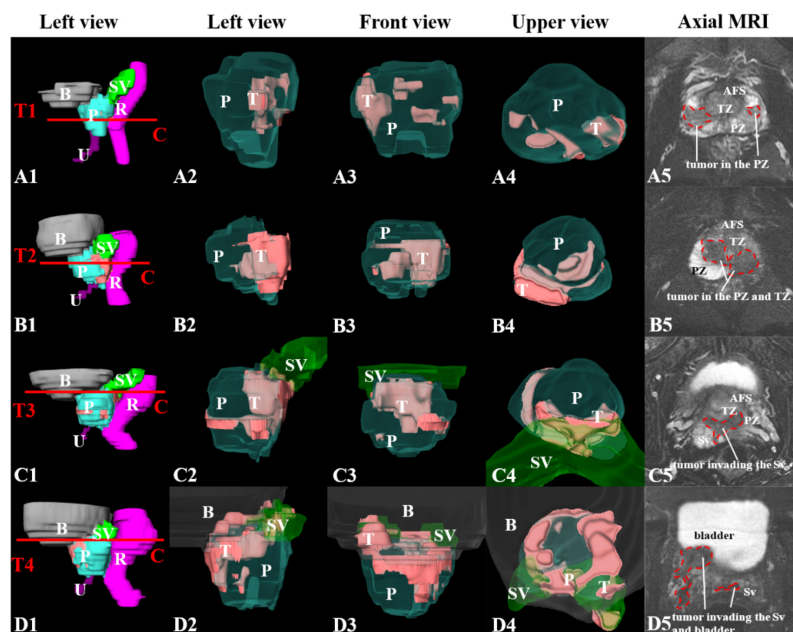


**Figure 3.** Three-dimensional reconstruction, spatial relationship, and location of prostate cancer lesions in different T-stages. **Column A1–D1**, three-dimensional reconstruction of the prostate and adjacent structures in the left view. **Column A2–D2, A3–D3, and A4–D4**, three-dimensional reconstruction of the tumor and prostate in the left, front, and upper views, in which the prostate, seminal vesicles, and bladder are semi-transparent. **Column A5–D5**, tumor segmentation in axial magnetic resonance images. **Row A1–A5**, T1 PCa; row **B1–B5**: T2 PCa; **row C1–C5**, T3 PCa; **row D1–D5**, T4 PCa. PCa, prostate cancer; PZ, peripheral zone; TZ, transition zone; CZ, central zone; AFMS, anterior fibromuscular stroma; B, bladder; SV, seminal vesicles; R, rectum; U, urethral canal; P, prostate; T-stages, tumor-stages.

### Measurement and comparison of different tumor-stage three-dimensional models of prostate cancer

The PV, PZV, CZV, TA, TV, and TV/PV significantly differed as the T-stage increased (Table 3). The mean PZV value initially decreased and then increased from T1 to T4 (P = 0.001), and T2 was the inflection point. The mean PV and CZV values continuously decreased from T1 to T4 ($r_s$: -0.213, P = 0.005 and $r_s$: -0.288, P = 0.006). The TZV, AFMSV, PZV/TZV, PZV/PV, TZV/PV, CZV/PV, and AFMSV/PV did not differ based on the T-stage. Figure 4 demonstrates the prostatic zone changes in a randomly selected, representative case from each T-stage. The mean TA, TV, and TV/PV values significantly and continuously increased from T1 to T4 (P < 0.050) (Table 3).

The PV, PZV, CZV, TA, TV, and TV/PV significantly differed in the T1 to T2 group (P = 0.001, P < 0.001, P = 0.021, P = 0.008, P = 0.003, and P < 0.001, respectively). Furthermore, the TA, TV, and TV/PV significantly differed in the T2 to T3 group (P < 0.001, P = 0.020, and P = 0.005, respectively). Finally, the TA, TV, and TV/PV significantly differed in the T3 to T4 group (P = 0.004, P = 0.010, and P = 0.008, respectively) (Table 4).

### Receiver operating characteristic curve analysis

A ROC curve analysis was used to predict the performance of the morphological

**Table 3.** Morphological parameter comparisons among the tumor stages of prostate cancer

| | T-stage of PCa | | | | | Total (n = 175) |
|---|---|---|---|---|---|---|
| | T1 (n = 25) | T2 (n = 80) | T3 (n = 36) | T4 (n = 34) | P | |
| PV (cm) | **47.83 ± 18.80** | **38.39 ± 21.64** | **36.35 ± 28.72** | **34.17 ± 15.87** | **0.040** | **37.41 ± 20.95** |
| PZV (cm) | **17.42 ± 9.77** | **11.47 ± 5.22** | **11.57 ± 10.02** | **12.95 ± 7.29** | **0.003** | **12.33 ± 7.56** |
| TZV (cm) | 25.76 ± 14.39 | 18.41 ± 13.36 | 22.97 ± 22.14 | 22.43 ± 18.67 | 0.204 | 21.18 ± 16.83 |
| CZV (cm) | **2.28 ± 1.60** | **1.76 ± 1.53** | **1.50 ± 1.49** | **0.94 ± 1.24** | **0.006** | **1.62 ± 1.54** |
| AFMSV (cm) | 2.38 ± 1.13 | 2.53 ± 1.74 | 2.16 ± 1.73 | 1.81 ± 1.20 | 0.153 | 2.29 ± 1.59 |
| PZV/TZV | 0.89 ± 0.47 | 1.22 ± 2.11 | 0.77 ± 0.60 | 0.64 ± 0.60 | 0.219 | 0.28 ± 0.14 |
| PZV/PV | 0.38 ± 0.12 | 0.36 ± 0.17 | 0.35 ± 0.18 | 0.36 ± 0.19 | 0.992 | 0.36 ± 0.17 |
| TZV/PV | 0.50 ± 0.14 | 0.49 ± 0.17 | 0.53 ± 0.19 | 0.52 ± 0.23 | 0.732 | 0.51 ± 0.18 |
| CZV/PV | 0.05 ± 0.04 | 0.05 ± 0.04 | 0.05 ± 0.05 | 0.04 ± 0.05 | 0.357 | 0.05 ± 0.05 |
| AFMSV/PV | 0.05 ± 0.03 | 0.07 ± 0.04 | 0.05 ± 0.04 | 0.07 ± 0.08 | 0.115 | 0.07 ± 0.05 |
| TA (mm) | **1.55 ± 0.84** | **2.23 ± 1.13** | **3.39 ± 1.25** | **4.45 ± 1.67** | **0.000** | **2.80 ± 1.59** |
| TV (cm) | **1.91 ± 2.68** | **7.10 ± 14.13** | **15.52 ± 18.5** | **29.93 ± 25.14** | **0.000** | **12.52 ± 19.45** |
| TV/PV | **0.04 ± 0.04** | **0.14 ± 0.16** | **0.25 ± 0.24** | **0.42 ± 0.20** | **0.000** | **0.20 ± 0.21** |

Bold are the results of good predictive performance. P, One-Way analysis of variance. T, tumor; PV, prostate volume; PZV, peripheral zone volume; TZV, transition zone volume; CZV, central zone volume; AFMSV, anterior fibromuscular stroma volume; PZV/TZV, the ratio of PZV and TZV; PZV/PV, the ratio of PZV and PV; TZV/PV, the ratio of TZV and PV; CZV/PV, the ratio of CZV and PV; AFMSV/PV, the ratio of AFMSZV and PV; TA, tumor's major axis; TV, tumor volume; TV/PV, the ratio of TV and PV.
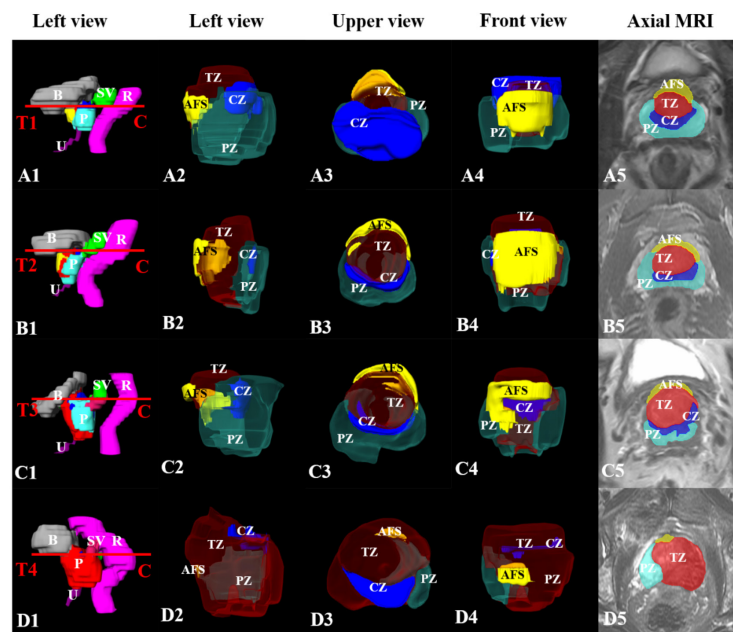


**Figure 4.** Anatomic morphology, three-dimensional shape, and spatial relationship of prostatic zones in different tumor stages. **Column A1–D1**, three-dimensional reconstruction of the prostate and adjacent structures in the left view. **Column A2–D2, A3–D3, and A4–D4**, three-dimensional reconstruction of the PZ, TZ, CZ, and AFMS in the left, upper, and front view, in which the PZ and TZ are semi-transparent. **Column A5–D5**, PZ, TZ, CZ, and AFMS segmentation in axial magnetic resonance imaging. **Row A1–A5**, T1 PCa; **row B1–B5**, T2 PCa; **row C1–C5**, T3 PCa; **row D1–D5**, T4 PCa. PCa, prostate cancer; PZ, peripheral zone; TZ, transition zone; CZ, central zone; AFMS, anterior fibromuscular stroma; B, bladder; SV, seminal vesicle; R, rectum; U, urethral canal; P, prostate.

parameters in the T-stage diagnosis (Figure 5). Table 5 summarizes the performance characteristics, such as the AUC, sensitivity, and specificity. The cut-off values of the PV, PZV, CZV, TA, TV, and the ratio of TV/PV for discrimination of T1 and T2 were 53.63 cm³, 11.60 cm³, 1.97 cm³, 2.30 mm, 0.90 cm³, and 0.03 (AUCs: 0.628, 0.658, 0.610, 0.689, 0.724, and 0.764), respectively. The cut-off values of the TA, TV, and the ratio of TV/PV for discrimination of T2 and T3 were 2.80 mm, 8.29 cm³, and 0.12 (AUCs: 0.769, 0.702, and 0.688), respectively. The cut-off values of the TA, TV, and the ratio of TV/PV for discrimination of T3 and T4 were 4.17 mm, 18.71 cm³, and 0.22 (AUCs: 0.674, 0.709, and 0.729), respectively.

## Discussion

ECE (stage T3a or more) is associated with a higher risk of positive surgical margins, biochemical recurrence (BCR), and metastasis,

and a lower cancer-specific survival rate.[18] Accurate detection of ECE is essential to maintaining urinary continence and sexual ability.[19] Therefore, it is necessary to diagnose the PCa T-stage before surgery correctly. In this study, the authors retrospectively analyzed the relationships between the morphological parameters and PCa T-stage based on 3D reconstructions after manually segmenting the MRI images. The study's results showed that the morphology of the prostate zones and tumors could predict the PCa T-stage.

Previous authors have pointed out that 3D-based scores better define the complexity of tumors and have higher predictive accuracy for postoperative complications than 2D-based ones.[20] However, the potential applications of 3D reconstruction are yet to be fully studied, and the information that can be extracted from 3D virtual models and their refinement has yet to be explored. The au-

thors have identified new morphological and volumetric parameters from the 3D model.

In this study, 46.3% of tumors were only in the PZ. In contrast, 7.4% of tumors were only in the TZ. Yang et al.[21] also reported many more tumors in the PZ than in the TZ, with a high-grade GS of 8 and 9 (38.5% vs. 24.3%). Additionally, Ali et al.[22] suggested that PCa in the TZ had better clinical outcomes than PCa in the PZ and CZ. Similarly, Sato et al.[23] indicated that conservative treatment could be used for PCa in the TZ and that these patients had a better prognosis than those with PCa in the PZ and CZ. The authors hypothesize that this may be related to increased androgen dependency within the PZ, leading to the occurrence and development of PCa in the PZ.[24]

This study found that the PV gradually decreased from stage T1 to T4 ($P < 0.050$), consistent with studies that found that the

**Table 4.** Morphological parameter comparisons among the consequent tumor stages of prostate cancer

|  | T1 (n = 25) | T2 (n = 80) | P | T2 (n = 8 0) | T3 (n = 36) | P | T3 (n = 36) | T4 (n = 34) | P |
|---|---|---|---|---|---|---|---|---|---|
| PV (cm³) | 47.83 ± 18.80 | 38.39 ± 21.64 | 0.001 | 38.39 ± 21.64 | 36.35 ± 28.72 | 0.317 | 53.87 ± 34.06 | 68.04 ± 38.56 | 0.749 |
| PZV (cm³) | 17.42 ± 9.77 | 11.47 ± 5.22 | 0.000 | 11.47 ± 5.22 | 11.57 ± 10.02 | 0.864 | 11.57 ± 10.02 | 12.95 ± 7.29 | 0.808 |
| TZV (cm³) | 25.76 ± 14.39 | 18.41 ± 13.36 | 0.167 | 18.41 ± 13.36 | 22.97 ± 22.14 | 0.173 | 22.97 ± 22.14 | 22.43 ± 18.67 | 0.913 |
| CZV (cm³) | 2.28 ± 1.60 | 1.76 ± 1.53 | 0.121 | 1.76 ± 1.53 | 1.50 ± 1.49 | 0.4 | 1.50 ± 1.49 | 0.94 ± 1.24 | 0.097 |
| AFMSV (cm³) | 2.38 ± 1.13 | 2.53 ± 1.74 | 0.688 | 2.53 ± 1.74 | 2.16 ± 1.73 | 0.294 | 2.16 ± 1.73 | 1.81 ± 1.20 | 0.329 |
| PZV/TZV | 0.89 ± 0.47 | 1.22 ± 2.11 | 0.44 | 1.22 ± 2.11 | 0.77 ± 0.60 | 0.222 | 0.77 ± 0.60 | 0.64 ± 0.60 | 0.398 |
| PZV/PV | 0.38 ± 0.12 | 0.36 ± 0.17 | 0.623 | 0.36 ± 0.17 | 0.35 ± 0.18 | 0.745 | 0.24 ± 0.12 | 0.18 ± 0.10 | 0.93 |
| TZV/PV | 0.50 ± 0.14 | 0.49 ± 0.17 | 0.855 | 0.49 ± 0.17 | 0.53 ± 0.19 | 0.312 | 0.41 ± 0.18 | 0.32 ± 0.16 | 0.921 |
| CZV/PV | 0.05 ± 0.04 | 0.05 ± 0.04 | 0.833 | 0.05 ± 0.04 | 0.05 ± 0.05 | 0.647 | 0.03 ± 0.04 | 0.02 ± 0.03 | 0.292 |
| AFMSV/PV | 0.05 ± 0.03 | 0.07 ± 0.04 | 0.057 | 0.07 ± 0.04 | 0.05 ± 0.04 | 0.130 | 0.05 ± 0.03 | 0.03 ± 0.02 | 0.349 |
| TA (mm) | 1.55 ± 0.84 | 2.23 ± 1.13 | 0.008 | 2.23 ± 1.13 | 3.39 ± 1.25 | 0.000 | 3.39 ± 1.25 | 4.45 ± 1.67 | 0.004 |
| TV (cm³) | 1.91 ± 2.68 | 7.10 ± 14.13 | 0.003 | 7.10 ± 14.13 | 15.52 ± 18.5 | 0.020 | 15.52 ± 18.5 | 29.93 ± 25.14 | 0.010 |
| TV/PV | 47.83 ± 18.80 | 38.39 ± 21.64 | 0.000 | 38.39 ± 21.64 | 36.35 ± 28.72 | 0.005 | 0.25 ± 0.24 | 0.42 ± 0.20 | 0.008 |

P, independent samples t-test. T, tumor; PV, prostate volume; PZV, peripheral zone volume; TZV, transition zone volume; CZV, central zone volume; AFMSV, anterior fibromuscular stroma volume; PZV/TZV, the ratio of PZV and TZV; PZV/PV, the ratio of PZV and PV; TZV/PV, the ratio of TZV and PV; CZV/PV, the ratio of CZV and PV; AFMSV/PV, the ratio of AFMSZV and PV; TA: tumor's major axis; TV, tumor volume; TV/PV, the ratio of TV and PV.
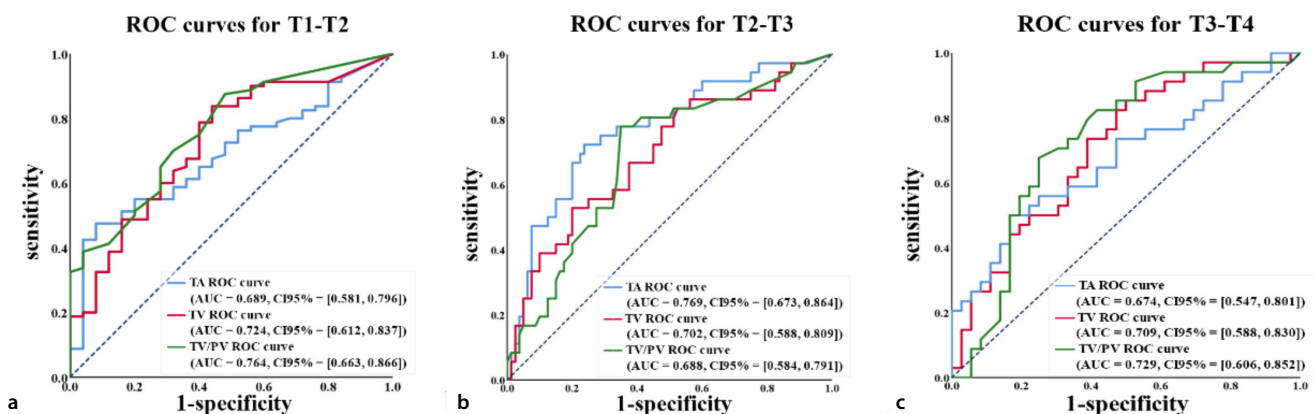


**Figure 5.** Receiver operating characteristic curves of the morphological parameters of the tumors for discrimination of T1 and T2 (**a**), T2 and T3 (**b**), and T3 and T4 (**c**). TA, tumor's major axis; TV, tumor volume; TV/PV, the volume ratio of TV and PV; ROC, receiver operating characteristic; AUC, area under the curve.

**Table 5.** The cut-off values, area under the curve, sensitivity, and specificity for the differentiation of the tumor stages of prostate cancer

|  |  | Cut-off | AUC | Sensitivity | Specificity |
|---|---|---|---|---|---|
| **T1–T2** | PV (cm³) | 53.63 | 0.628 (0.469, 0.787) | 0.579 | 0.789 |
|  | PZV (cm³) | 11.60 | 0.658 (0.530, 0.786) | 0.895 | 0.404 |
|  | CZV (cm³) | 1.97 | 0.610 (0.445, 0.749) | 0.599 | 0.764 |
|  | TA (mm) | 2.30 | 0.689 (0.581, 0.796) | 0.475 | 0.920 |
|  | TV (cm³) | 0.90 | 0.724 (0.612, 0.837) | 0.838 | 0.560 |
|  | TV/PV | 0.03 | 0.764 (0.663, 0.866) | 0.901 | 0.620 |
| **T2–T3** | TA (mm) | 2.80 | 0.769 (0.673, 0.864) | 0.778 | 0.762 |
|  | TV (cm³) | 8.29 | 0.702 (0.588, 0.809) | 0.528 | 0.800 |
|  | TV/PV | 0.12 | 0.688 (0.584, 0.791) | 0.722 | 0.650 |
| **T3–T4** | TA (mm) | 4.17 | 0.674 (0.547, 0.801) | 0.500 | 0.833 |
|  | TV (cm³) | 18.71 | 0.709 (0.588, 0.830) | 0.676 | 0.500 |
|  | TV/PV | 0.22 | 0.729 (0.606, 0.852) | 0.853 | 0.750 |

T, tumor; PV, prostate volume; PZV, peripheral zone volume; CZV, central zone volume; TA, tumor's major axis; TV, tumor volume; TV/PV, the ratio of TV and PV; AUC, area under the curve.

PV negatively correlated with the incidence rate and aggressiveness of PCa.[25-27] Previous histo-anatomical studies showed that TZ growth leads to secondary atrophy and PZ tissue apoptosis and necrosis, which may explain why increased TZV inhibits PCa. However, the authors found no differences among the T-stages for TZV or the TZV/PZV ratio, perhaps due to an insufficient sample size.

The hypothesis that the TV is the most important PCa prognostic indicator remains controversial.[28] Some studies have reported a strong correlation between the TV and BCR, and the authors of these studies thought that the clinical failure (CF) rate of patients with PCa with a TV of less than 0.5 cc is low.[29,30] However, Mayer et al.[31] reported that histology-based TV is related to the GS (r = 0.498, $P = 0.0098$), and Baba et al.[9] suggested that the optimal TV cut-off value for predicting BCR was 2.8 cc (AUC: 0.690). Moreover, Castiglione et al.[32] concluded that for high-risk patients with PCa, a TV >6.29 cc (AUC: 0.722) leads to CF, and Dong et al.[33] reported that the optimal cut-off value for identifying the best maximum standardized uptake value ($SUV_{max}$) for high-risk patients with PCa was 9.61 (AUC: 0.828). Furthermore, Jiao et al.[34] established and prospectively verified that the optimal $SUV_{max}$ cut-off value for discriminating clinically significant PCa from BPH was 5.30, with AUCs of 0.893 in the training and 0.853 in the prospective validation cohorts. However, no prior studies have analyzed the diagnostic value of the TA, TV, and TV/PV for the T-stage diagnoses of PCa.

Finally, the authors assessed the relationships between the tumor's morphological parameters and the T-stage. They found that the TA, TV, and TV/PV gradually increased from stage T1 to T4 ($P < 0.050$), which agreed with Yuk et al.'s[35] study. The authors also found that the higher the T-stage, the greater the cut-off value, indicating that the tumor's morphological parameters are important indicators for the T-stage diagnosis. Therefore, the authors considered that the TA, TV, and TV/PV can predict the T-stage in patients with PCa.

This study has four limitations. First, the study population only included the Asian population, whose PCa incidence rates, mortality rates, and PV are lower than those of Western populations. Therefore, more institutions should be involved in any future study. Second, the authors evaluated the correlations between the morphological parameters in MRI and the T-stage, ignoring the microscopic pathological changes. Thus, further genomics and pathological analysis are needed.[34] Third, manual segmentation is time-consuming and labor-intensive, resulting in a small sample size. In the future, artificial intelligence should be used to assist in segmentation to reduce the segmentation time. Fourth, there are some errors in manual segmentation due to fatigue and personal subjectivity. As a next step, the authors will invite more experts to verify the segmentation in this study.

In conclusion, the morphological parameters of the prostate zones and prostate tumor significantly differed among the T-stages, including the PV, PZ's volume, CZ's volumes, TA, TV, and the TV/PV ratio. Based on MRI 3D reconstruction, the TA, TV, and TV/PV are the key indicators of the PCa T-stage diagnosis, which can help to make accurate diagnoses and lateral treatment decisions.

## References

1. Sung H, Ferlay J, Siegel RL, et al. Global Cancer Statistics 2020: GLOBOCAN estimates of incidence and mortality worldwide for 36 cancers in 185 countries. *CA Cancer J Clin*. 2021;71(3):209-249. [CrossRef]

2. McNeal JE. The zonal anatomy of the prostate. *Prostate*. 1981;2(1):35-49. [CrossRef]

3. Giganti F, Allen C. Imaging quality and prostate MR: it is time to improve. *Br J Radiol*. 2021;94(1118):20200934. [CrossRef]

4. Schoots IG, Roobol MJ, Nieboer D, Bangma CH, Steyerberg EW, Hunink MG. Magnetic resonance imaging-targeted biopsy may enhance the diagnostic accuracy of significant prostate cancer detection compared to standard transrectal ultrasound-guided biopsy: a systematic review and meta-analysis. *Eur Urol*. 2015;68(3):438-450. [CrossRef]

5. No authors listed. Hematuria in adults. *N Engl J Med*. 2021;385:576. [CrossRef]

6. Marenco J, Orczyk C, Collins T, Moore C, Emberton M. Role of MRI in planning radical prostatectomy: what is the added value? *World J Urol*. 2019;37:1289-1292. [CrossRef]

7. Colvin R, Walker D, Hafron J, et al. Which measurement method should be used for prostate volume for PI-RADS? A comparison of ellipsoid and segmentation methods. *Clin Imaging*. 2021;80:454-458. [CrossRef]

8. Hamzaoui D, Montagne S, Granger B, et al. Prostate volume prediction on MRI: tools, accuracy and variability. *Eur Radiol*. 2022;32:4931-4941. [CrossRef]

9. Baba, H, Sakamoto S, Zhao X, et al. Tumor location and a tumor volume over 2.8 cc predict the prognosis for Japanese localized prostate cancer. *Cancers (Basel)*. 2022;14(23):5823. [CrossRef]

10. Tan N, Lin WC, Khoshnoodi P, et al. In-Bore 3-T MR-guided transrectal targeted prostate biopsy: prostate imaging reporting and data system version 2-based diagnostic performance for detection of prostate cancer. *Radiology*. 2017;283(1):130-139. [CrossRef]

11. Hoeks CM, Hambrock T, Yakar D, et al. Transition zone prostate cancer: detection and localization with 3-T multiparametric MR imaging. *Radiology*. 2013;266(1):207-217. [CrossRef]

12. Liang W, Qiubai L, Alberto Hebert V. Prostate MRI anatomical partition. *China J Radiology*. 2020;54:1038-1040. [CrossRef]

13. Turkbey B, Rosenkrantz AB, Haider MA, et al. Prostate imaging reporting and data system version 2.1: 2019 update of prostate imaging reporting and data system version 2. *Eur Urol*. 2019;76:340-351. [CrossRef]

14. Mehralivand S, Shih JH, Harmon S, et al. A grading system for the assessment of risk of extraprostatic extension of prostate cancer at multiparametric MRI. *Radiology*. 2019;290:709-719. [CrossRef]

15. Obuchowski NA, Bullen JA. Receiver operating characteristic (ROC) curves: review of methods with applications in diagnostic medicine. *Phys Med Biol*. 2018;63(7):07TR01. [CrossRef]

16. Nahm FS. Receiver operating characteristic curve: overview and practical use for clinicians. *Korean J Anesthesiol*. 2022;75(1):25-36. [CrossRef]

17. Njor SH, Andersen B, Friis-Hansen L, et al. The optimal cut-off value in fit-based colorectal cancer screening: An observational study. *Cancer Med*. 2021;10(5):1872-1879. [CrossRef]

18. Chang AJ, Autio KA, Roach M 3rd, Scher HI. High-risk prostate cancer-classification and therapy. *Nat Rev Clin Oncol*. 2014;11(6):308-323. [CrossRef]

19. Sighinolfi MC, Assumma S, Cassani A, et al. Pre-operative prediction of extracapsular extension of prostate cancer: first external validation of the PRECE model on an independent dataset. *Int Urol Nephrol*. 2023;55(1):93-97. [CrossRef]

20. Bianchi L, Schiavina R, Bortolani B, et al. Novel volumetric and morphological parameters derived from three-dimensional virtual modeling to improve comprehension of tumor's anatomy in patients with renal cancer. *Eur Urol Focus*. 2022;8(5):1300-1308. [CrossRef]

21. Yang L, Li M, Zhang MN, Yao J, Song B. Association of prostate zonal volume with location and aggressiveness of clinically significant prostate cancer: a multiparametric MRI study according to PI-RADS version 2.1. *Eur J Radiol* 2022;150, 110268. [CrossRef]

22. Ali A, Du Feu A, Oliveira P, Choudhury A, Bristow RG, Baena E. Prostate zones and cancer: lost in transition? *Nat Rev Urol*. 2022;19(2):101-115. [CrossRef]

23. Sato S, Kimura T, Onuma H, Egawa S, Takahashi H. Transition zone prostate cancer is associated with better clinical outcomes than peripheral zone cancer. *BJUI Compass*. 2020;2(3):169-177. [CrossRef]

24. Cancer Genome Atlas Research Network. The molecular taxonomy of primary prostate cancer. *Cell*. 2015;163(4):1011-1025. [CrossRef]

25. Frost JM, Smith LA, Sharma P, de Riese WT. Possible clinical implications of peripheral zone changes depending on prostate size. *Int Urol Nephrol*. 2019;51(10):1721-1726. [CrossRef]

26. Sellers J, Wagstaff RG, Helo N, de Riese WTW. Quantitative measurements of prostatic zones by MRI and their dependence on prostate size: possible clinical implications in prostate cancer. *Ther Adv Urol*. 2021;13:17562872211000852. [CrossRef]

27. Yamashiro JR, de Riese WTW. Any correlation between prostate volume and incidence of prostate cancer: a review of reported data for the last thirty years. *Res Rep Urol*. 2021;13:749-757. [CrossRef]

28. Wolters T, Roobol MJ, van Leeuwen PJ, et al. A critical analysis of the tumor volume threshold for clinically insignificant prostate cancer using a data set of a randomized screening trial. *J Urol*. 2011;185(1):121-125. [CrossRef]

29. Hashimoto Y, Okamoto A, Imai A, et al. Biochemical outcome of small-volume or insignificant prostate cancer treated with radical prostatectomy in Japanese population. *Int J Clin Oncol*. 2012;17(2):119-123. [CrossRef]

30. Reinhardt D, Helfand BT, Cooper PR, Roehl KA, Catalona WJ, Loeb S. Prostate cancer risk alleles are associated with prostate cancer volume and prostate size. *J Urol*. 2014;191(6):1733-1736. [CrossRef]

31. Mayer R, Simone CB, Turkbey B, Choyke P. Prostate tumor eccentricity predicts Gleason score better than prostate tumor volume. *Quant Imaging Med Surg*. 2022;12(2):1096-1108. [CrossRef]

32. Castiglione F, Dell'Oglio P, Tosco L, et al. Tumor volume and clinical failure in high-risk prostate cancer patients treated with radical prostatectomy. *Prostate*. 2017;77(1):3-9. [CrossRef]

33. Dong S, Li Y, Chen J, Li Y, Yang P, Li J. 18F-PSMA-1007 PET/CT-derived semi-quantitative parameters for risk stratification of newly diagnosed prostate cancer. *Front Oncol*. 2022;12:1025930. [CrossRef]

34. Jiao J, Kang F, Zhang J, et al. Establishment and prospective validation of an SUV (max) cutoff value to discriminate clinically significant prostate cancer from benign prostate diseases in patients with suspected prostate cancer by 68Ga-PSMA PET/CT: a real-world study. *Theranostics*. 2021;11(17):8396-8411. [CrossRef]

35. Yuk HD, Byun SS, Hong SK, Lee H. The tumor volume after radical prostatectomy and its clinical impact on the prognosis of patients with localized prostate cancer. *Sci Rep*. 2022;12(1):6003. [CrossRef]

# Comparison of mammography and ultrasound findings in the follow-up of patients with breast cancer treated with segmental mastectomy followed by intraoperative electron radiotherapy versus external whole breast radiotherapy

Burçin Tutar 🆔

Gül Esen İçten 🆔

Ayşe Altınok 🆔

Seda Eröz 🆔

Nuran Beşe 🆔

Cihan Uras 🆔

**PURPOSE**

This study aims to describe imaging findings in patients treated with intraoperative electron radiotherapy and compare them with those detected in patients treated with external whole breast radiotherapy (WBRT).

**METHODS**

The study population consisted of 25 patients who received intraoperative radiotherapy [IORT (21 Gy)] as single-dose radiotherapy and a control group of 25 patients who received WBRT at the same institution. Mammography and ultrasound (US) findings were divided into three groups: minor, intermediate, and advanced. On mammography, mass lesions were considered advanced, and asymmetries or architectural distortions were considered intermediate. Oil cysts, linear scars, and the increase in parenchymal density were considered minor findings. On US, irregular non-mass lesions were considered advanced, and circumscribed hypoechoic lesions or planar irregular scars with shadowing were considered intermediate. Oil cysts, fluid collections, or linear scars were considered minor findings.

**RESULTS**

On mammography, skin thickening ($P = 0.001$), edema ($P < 0.001$), increased parenchymal density ($P < 0.001$), dystrophic calcifications ($P = 0.045$), and scar/distortion ($P = 0.005$) were significantly more common in the WBRT group. On US, irregular non-mass lesions, which made interpretation considerably difficult, were significantly more common in the IORT group ($P = 0.004$). Dominant US findings were fluid collections and postoperative linear or planar scars in the WBRT group. Minor findings were more common in low-density breasts, and major findings (intermediate and advanced) were more common in high-density breasts on both mammographies ($P = 0.011$) and US ($P = 0.027$) in the IORT group.

**CONCLUSION**

Ill-defined non-mass lesions detected on US in the IORT group have not been defined previously. Radiologists should be aware of these lesions because they can be confusing, especially in early follow-up studies. This study has found that minor findings are seen more frequently in low-density breasts, while major findings are more common in high-density breasts in the IORT group. This has not been reported before, and further studies with more cases are needed to verify these results.

**KEYWORDS**

Breast, intraoperative radiotherapy, whole breast radiotherapy, mammography, ultrasonography

From the Clinic of Radiology (B.T. soysalburcin@gmail.com ✉), Acıbadem Maslak Hospital, İstanbul, Turkey; Department of Radiology (G.E.İ.), Acıbadem University, Senology Research Institute, İstanbul, Turkey; Clinic of Radiation Oncology (A.A.), Bahçelievler Medical Park Hospital, İstanbul, Turkey; Clinic of Radiation Oncology (S.E.), Acıbadem Maslak Hospital, İstanbul, Turkey; Department of Radiation Oncology (N.B.), Acıbadem University, Senology Research Institute, İstanbul, Turkey; Department of Breast Surgery (C.U.), Acıbadem Mehmet Ali Aydınlar University, Research Institute of Senology, İstanbul, Turkey.

ntraoperative radiotherapy (IORT) is an adjuvant treatment option for selected cases of early-stage breast cancer. It is applied using either electron beams [intraoperative electron radiotherapy (IOeRT)] or X-ray, and it can be used alone as primary radiotherapy or as a boost followed by external whole breast radiotherapy (WBRT).[1-6] The advantages of IORT include

the direct visualization of the tumor bed, reduced skin doses, and patient convenience.

There are only a few reports on the radiological findings in patients treated with IORT.[7-15] Some of them have reported that postoperative changes in mammography and ultrasound (US) are more pronounced in patients treated with IORT compared with those treated conventionally with WBRT.[7-9,11,13] However, radiological findings, especially sonographic results, after IORT are not well documented. During the radiological follow-up of these patients, some findings were different from those seen in patients treated with WBRT. This study's aim was to describe early and late imaging findings in patients treated with IORT as single-dose radiotherapy and compare them with those detected in a conventionally-treated WBRT group.

## Methods

### Intraoperative radiotherapy group

Between October 2012 and August 2021, 94 patients with breast cancer underwent IOeRT in the clinic. Forty-four of these patients received IOeRT as single-dose radiotherapy (21 Gy). Nineteen patients were excluded from this study either because they received additional WBRT after the operation, had less than six months follow-up, had previous breast surgery, or their radiological images were not available in the picture archiving and communication system. The remaining 25 patients made up the study population. IOeRT was performed using the Sordino IOeRT technologies-LIAC mobile IOeRT device. Electron energies of 12 MeV were given with 80% isodose. Applicators with different diameters (4–8 mm) were selected based on tumor size, breast volume, and flap volume.

<div style="background:#cce0f0;padding:10px">

**Main points**

- Mammography revealed more diffuse changes in the whole breast radiotherapy (WBRT) group as opposed to localized findings in the intraoperative radiotherapy (IORT) group in terms of skin thickening, edema, and the increase in parenchymal density.

- Ultrasound (US) demonstrated more circumscribed masses and suspicious ill-defined non-mass lesions in the IORT group, while fluid collections and linear and planar scars were more typical for WBRT.

- Minor findings were seen significantly more frequently in low-density breasts, while major findings were more common in high-density breasts on both mammography and US in the IORT group.

</div>

In the institution, the patient selection criteria for IOeRT were based on the American Society for Radiation Oncology guidelines, which were published in 2009 and updated in 2017.[16,17] Patients with histologically proven unifocal ductal invasive cancer of <2 cm or non-high grade ductal carcinoma *in situ* of <2.5 cm in size and who were at least 50 years old were chosen. For this group of patients, additional states of (–) lymphovascular invasion, (–) axillary lymph nodes, (–) grade 3 status, (+) estrogen receptor, and >2 mm clean surgical margins were required.

### Whole breast radiotherapy group

The control group consisted of 25 patients with breast cancer who were treated with breast-conserving surgery (BCS) followed by WBRT in the same institution between November 2010 and July 2018. WBRT was applied using a linear accelerator (varian true beam) with a total dose of 50 Gy and a boost dose of 10–16 Gy in 5–8 fractions or with a hypofractionated schedule with a total dose of 42.5 Gy in 16 fractions with a boost dose of 10–12.5 Gy in 4–8 fractions. Patients in the WBRT group were selected in chronological order from the radiation oncology patient list using the same exclusion criteria.

### Evaluation of imaging findings

Follow-up mammography and US images were retrospectively evaluated by two breast radiologists (with 10 and 25 years of experience) in consensus, and they were blinded to the treatment protocol. Digital mammography (Pristina, General Electric, Chicago, Il, United States) and US (Logic S8, General Electric, Wauwatosa, WI, United States) examinations were performed using the same equipment in all patients. At the institution, patients treated with BCS were routinely scheduled for US examination at six-month intervals and mammographic examination at 12-month intervals for follow-up during the first five years and at yearly intervals afterward. All mammography and US images that were available were evaluated sequentially. The examinations performed in the first 24 months were considered short-term follow-ups, while those taken after 24 months were considered long-term follow-ups.

On mammograms, breast density, the presence or absence of masses (Figure 1), asymmetries (Figure 2), oil cysts, postoperative scars, architectural distortion, calcifications (dystrophic or rim-like), edema (minimal, moderate, and advanced), skin thickening (localized or generalized), and the

increase in parenchymal density compared with the contralateral breast (regional or diffuse) were evaluated. Breast density was assessed according to the breast parenchyma types (a–d) stated in the BI-RADS atlas 5th edition of the American College of Radiology.[18] On US images, the presence or absence of fluid collections, ill-defined, non-mass hypoechoic lesions (Figures 3, 4), circumscribed hypoechoic masses (Figure 1), oil cysts, and postoperative linear or planar scars were assessed. Planar scars were defined as irregular scars with shadowing that looked suspicious in one plane but were elongated and changed in shape in the orthogonal plane and usually continuous with skin incision (Figure 5). All focal lesions were measured, and if the patient had sequential examinations, the time of appearance of the findings was recorded.

Mammography and US findings were divided into three groups: minor, intermediate, and advanced, based on the degree to which they made interpretation difficult. On mammography, masses were considered advanced; asymmetries and architectural distortions were considered intermediate; oil cysts, linear postoperative scars, and the increase in parenchymal density were considered minor findings. On US, ill-defined, non-mass hypoechoic lesions were considered advanced; circumscribed hypoechoic lesions or planar irregular scars with shadowing were considered intermediate; oil cysts, fluid collections, or linear postoperative scars were considered minor findings.

The institutional review board granted approval for this retrospective study (ATA-DEK) (decision number: 2020-05/26, date: 09.04.2020), and patient consent was waived.

### Statistical analysis

For statistical purposes, breast parenchyma types A and B were grouped as low density, and types C and D were grouped as high density. Moderate and advanced edema were grouped together as marked edema. Overall findings were dichotomized as minor versus major (intermediate or advanced). The software SPSS v23.0 (IBM Corp., Armonk, NY) was used for data analysis. The Shapiro–Wilk test was used to test the normality of data. Continuous data were presented using mean ± standard deviation for normally distributed data and median (interquartile range: 25%–75%) for non-normally distributed data. Categorical variables were given by n (%) and compared with Pearson's chi-square test and Fisher's exact test. The Mann–Whitney U test
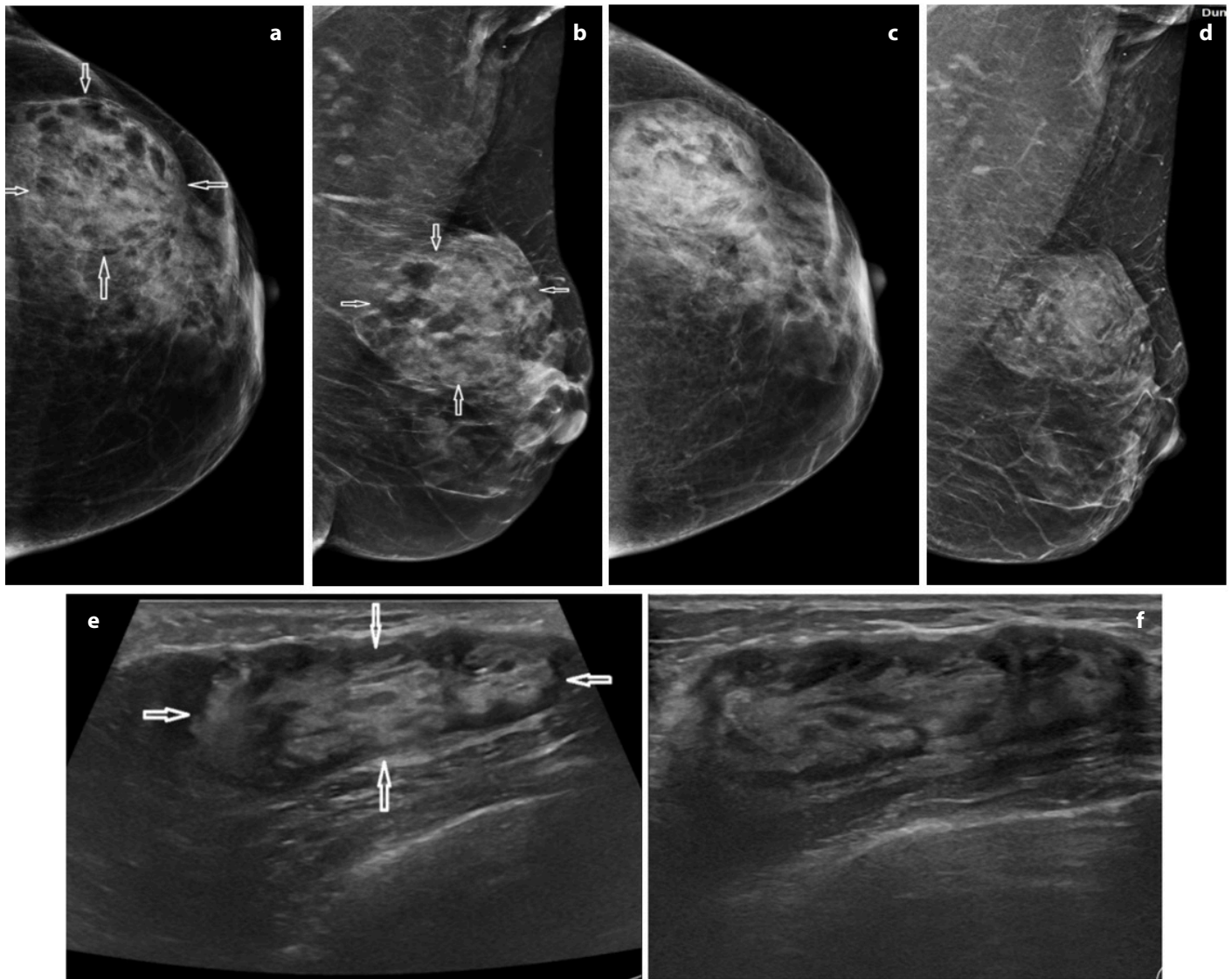
**Figure 1. (a-f)** Mammography and US images of a 54-year-old patient treated with IORT: initial mammograms **(a, b)** show a heterogeneous mass (arrows) in the left breast, which persists without any change on follow-up mammograms **(c, d)** taken three years after therapy. Initial US image of the same patient **(e)** shows a heterogeneous oval circumscribed mass (arrows). This lesion also persists three years after therapy **(f)**. IORT, intraoperative radiotherapy; US, ultrasound.

and the independent t-test were performed for non-parametric and parametric comparisons of continuous data between groups, respectively. A two-sided *P* value of less than 0.05 was considered statistically significant.

## Results

WBRT was given in full doses to 7 patients and was hypofractionated in 18 patients. Patients in the IORT group (mean age: 59.6 ± 6.41) were significantly older than those in the WBRT group (53.36 ± 8.94) (*P* = 0.007), which was expected since only patients older than 50 years of age were eligible for IORT. The most common tumor type was infiltrating ductal carcinoma in both groups, and 24/25 cases treated with IORT and 23/25 cases treated with WBRT were invasive cancers.

Tumors were mostly located in the right breast (IORT: 20/25, WBRT: 15/25) and in the upper outer quadrant (IORT: 14/25, WBRT: 18/25) in both groups. There was no statistically significant difference in tumor size. Follow-up time was significantly shorter in the IORT group (*P* = 0.012) because all eligible and more recent cases were included in this study. Six patients in the IORT group and two patients in the WBRT group had only early follow-ups. None of the patients had any local recurrences or systemic metastases during the follow-up period. Patients' characteristics are described in Table 1.

### Imaging findings

The distribution of each finding, size of the lesions, and development time can be seen in Table 1. The most dominant findings

in the initial examinations can be seen in Table 2. The distribution of minor versus major findings in breasts with low density versus high density can be seen in Table 3.

### Mammographic evaluation

In the initial mammograms obtained after therapy, masses, asymmetries, and oil cysts were more common in the IORT group, while increased parenchymal density, edema, architectural distortion, and postoperative scars were the most dominant findings in the WBRT group (Table 2). Calcifications and some oil cysts appeared later during follow-up.

Statistically, there was a significant difference between the two groups for the following findings: skin thickening (*P* = 0.001), ede-
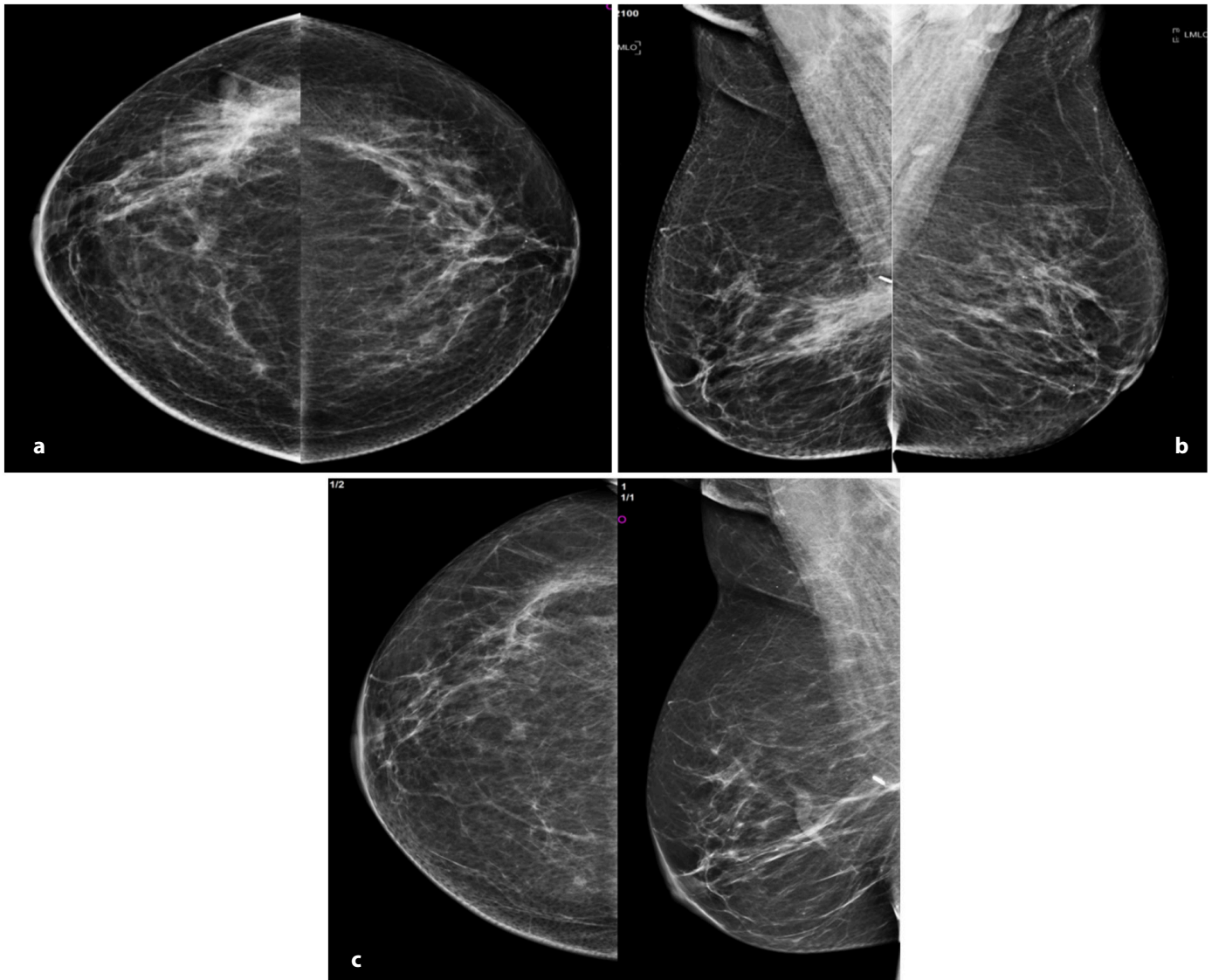
**Figure 2. (a-c)** Craniocaudal **(a)** and mediolateral oblique **(b)** mammograms of a 59-year-old patient treated with IORT show an asymmetry in the right breast. It resolves during follow-up and only a minor linear scar remains four years after therapy **(c)**. IORT, intraoperative radiotherapy.
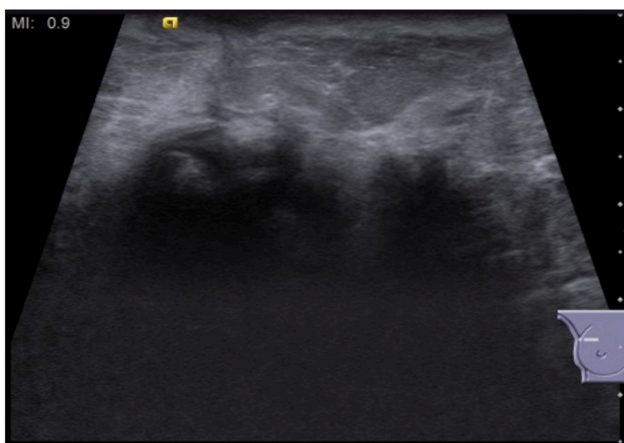


**Figure 3.** Early US image of a patient treated with IORT demonstrates a suspicious-looking ill-defined non-mass hypoechoic lesion at the operation site. IORT, intraoperative radiotherapy; US, ultrasound.

ma ($P < 0.001$), distrophic calcifications ($P = 0.045$), scar/distortion ($P = 0.005$), oil cysts ($P = 0.047$), and increased parenchymal density ($P < 0.001$) (Table 1).

Skin thickening was either not present or localized in most of the patients in the IORT group (8% and 68%, respectively), while generalized skin thickening was much more common (76%) in patients in the WBRT group ($P = 0.001$). Edema was either not present or minimal (84% and 12%, respectively) in patients in the IORT group, while 80% of the patients had edema in the WBRT group, and it was advanced in half of them ($P < 0.001$). The increase in parenchymal density compared with the contralateral breast was significantly more common in patients in the WBRT group (62.5% vs. 40%); it was mostly regional in the IORT group but diffuse in the WBRT group ($P < 0.001$) (Figure 6). Parenchymal distortion or scar formation was more common among patients in the WBRT group (72% vs. 32%) ($P = 0.005$). Dystrophic calcifications were significantly more common in the WBRT group (56% vs. 28%) ($P = 0.045$). Calcifications appeared earlier during follow-up in the IORT group, but the difference was not significant. Oil cysts were significantly more common in the IORT group (62%
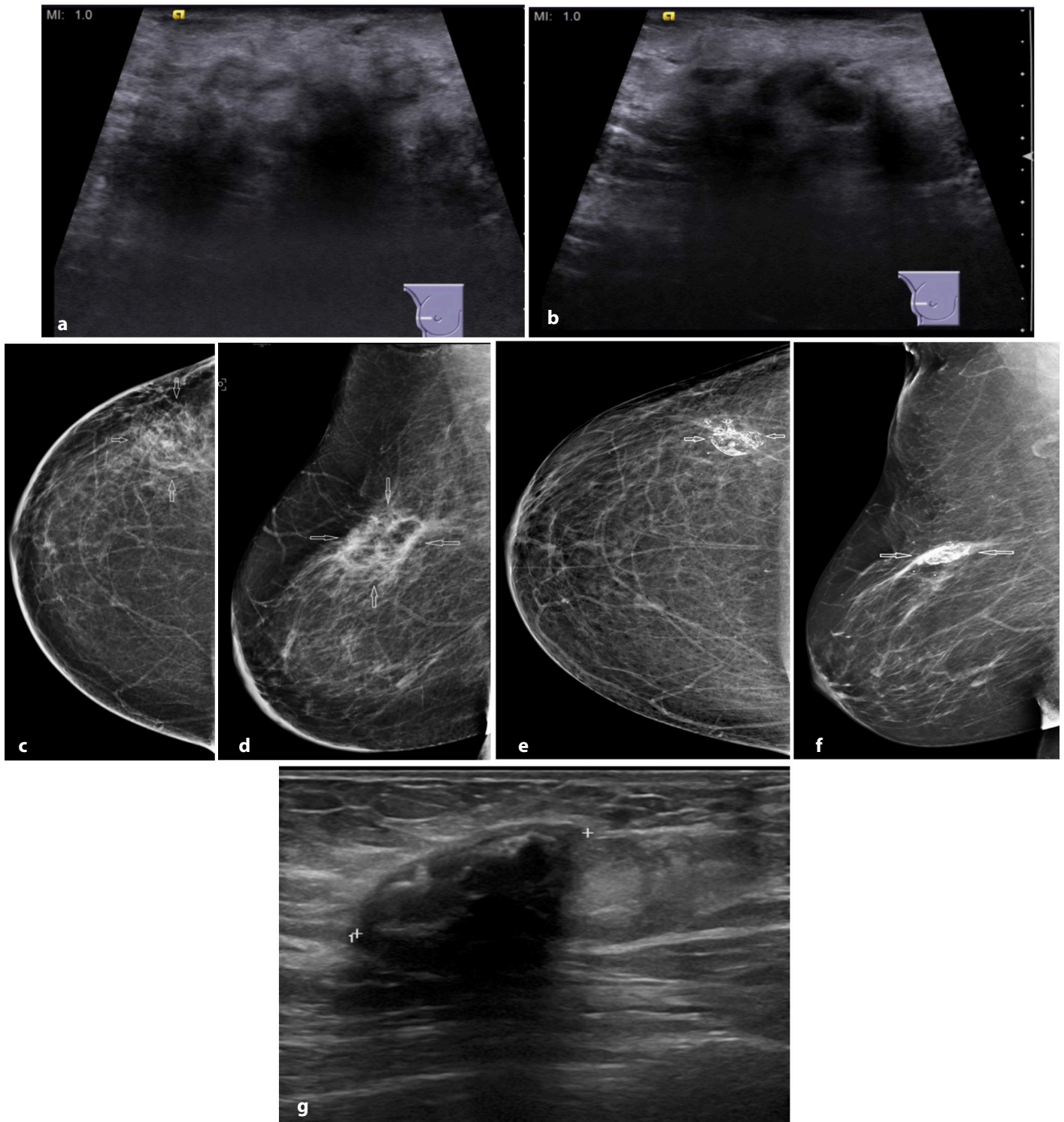
**Figure 4. (a-g)** US images of a 58-year-old patient treated with IORT, which was taken six months **(a)** and one year **(b)** after therapy show a suspicious-looking ill-defined non-mass lesion at the operation site in the right breast. However, mammograms taken at the first follow-up **(c, d)** show only minor changes compatible with fat necrosis (arrows). Mammograms **(e, f)** and US image **(g)** taken five years later show that the lesion turns into a calcified oil cyst on both examinations. IORT, intraoperative radiotherapy; US, ultrasound.

vs. 32%) ($P = 0.047$). Cysts were larger in the IORT group; however, differences between the median size and median time to develop were not significant.

There was no difference in the number of patients with masses or asymmetries. The sizes of both lesions were larger in patients in the IORT group, although the difference between the median sizes was significant only for asymmetries ($P = 0.031$). Minor findings were more common in the WBRT group, while major findings were more common in the IORT group. However, the difference was not significant.

### Ultrasound evaluation

Most dominant findings in the first US examinations obtained after therapy were ill-defined, non-mass hypoechoic lesions and circumscribed hypoechoic masses in the IORT group. Dominant US findings were mostly in the form of fluid collections and

**Figure 5. (a, b)** US images of a 50-year-old patient treated with WBRT show a planar scar. The lesion is irregular with shadowing on one plane **(a)**, but it is elongated on the orthogonal plane **(b)** and is easily diagnosed as a scar. US, ultrasound; WBRT, whole breast radiotherapy.

**Table 1.** Distribution of clinical, histopathological, and radiological findings

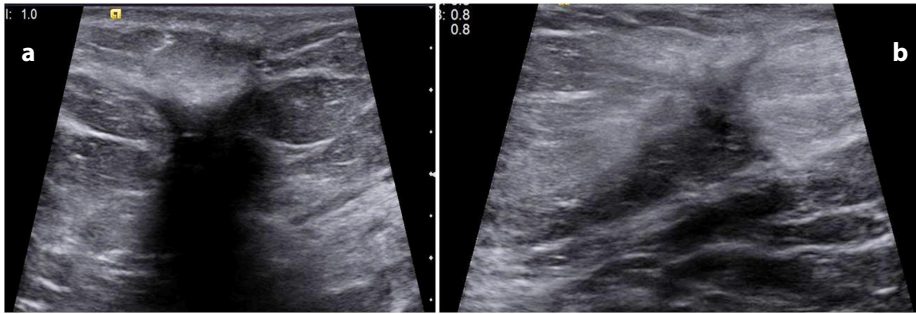| Variables | IORT (n = 25) | WBRT (n = 25) | P value |
|---|---|---|---|
| **Clinical findings** | | | |
| Mean age (years) | 59.6 ± 6.41 | 53.36 ± 8.94 | **0.007** |
| Median tumor size (mm) | 11.5 (8–16.5) | 11 (6–15) | 0.767 |
| **Follow-up** | | | |
| Median follow-up time (months) | 46 (29–72) | 67 (56–74) | **0.012** |
| Median of mammograms | 3 (1–6) | 5 (3–6) | **0.041** |
| Median of US exams | 4 (2–7) | 7 (5–9) | **0.023** |
| **Mammography** | | | |
| Breast parenchyma | | | |
| Low density (type A + B) | 16 (64) | 10 (40) | 0.089 |
| High density (type C + D) | 9 (36) | 15 (60) | |
| Skin thickening | | | |
| None | 2 (8)[a] | 0 (0)[a] | **0.001** |
| Localized | 17 (68)[a] | 6 (24)[b] | |
| Generalized | 6 (24)[a] | 19 (76)[b] | |
| Median skin thickness (mm) | 2.9 (2.4–3.3) | 3.1 (2.6–4.6) | 0.080 |
| Edema | | | |
| None | 21 (84)[a] | 5 (20)[b] | **<0.001** |
| Minimal | 3 (12)[a] | 10 (40)[b] | |
| Advanced | 1 (4)[a] | 10 (40)[b] | |
| Calcifications | | | |
| Patients with calcifications | 13 (52) | 17 (68) | 0.248 |
| Dystrophic | 7 (28) | 14 (56) | **0.045** |
| Rim | 10 (40) | 6 (24) | 0.225 |
| Median time to develop (months) | 20 (19–33) | 30 (20–44) | 0.300 |
| <24 months | 7 (53.8) | 8 (47.1) | 0.713 |
| >24 months | 6 (46.2) | 9 (52.9) | |
| Scar/distortion | 8 (32) | 18 (72) | **0.005** |
| Masses | | | |
| Number of cases | 4 (16) | 1 (4) | 0.349 |
| Median size (mm) | 42.5 (35.5–65.5) | 25 | 0.400 |
| Asymmetry | | | |
| Number of cases | 9 (36) | 7 (28) | 0.544 |
| Median size (mm) | 50 (42–60) | 30 (20–46) | **0.031** |
| Oil cysts | | | |
| Number of cases | 15 (60) | 8 (32) | **0.047** |

postoperative linear or planar scars in the WBRT group. The differences were statistically significant (Table 2).

Ill-defined, non-mass hypoechoic lesions were significantly more common (44% vs. 8%) ($P = 0.004$), and the median size of these lesions was significantly larger (45 mm vs. 16.5 mm) in the IORT group ($P = 0.026$). Circumscribed mass lesions were also more common in the IORT group (28% vs. 4%) ($P = 0.049$). Patients in the IORT group had significantly fewer scars (12% vs. 80%), and planar scars were especially typical in patients in the WBRT group (0% vs. 36%) ($P < 0.001$). Fluid collections were exclusively seen in patients treated with WBRT ($P = 0.049$). There was no difference in the number of cases with oil cysts, but they were significantly larger in the IORT group (26 ± 14.08 mm vs. 15.1 ± 8.9 mm) ($P = 0.043$). Minor findings were significantly more common in the WBRT group, while major findings were significantly more common in the IORT group ($P = 0.014$) (Table 1).

## Overall findings

This study analyzed the relationship between parenchymal density and the rate of minor and major findings. For mammography and US, minor findings were significantly more common in low-density breasts, and major findings were more common in high-density breasts in the IORT group (mammography: $P = 0.011$, US: $P = 0.027$) (Table 3). There was no difference in the WBRT group.

## Follow-up findings

Results were obtained from the follow-up data of major findings. For mammography, 9/10 patients with major findings had a late follow-up in the WBRT group, and all of them turned into minor findings. Furthermore, 11/13 patients with major findings had a late follow-up in the IORT group, and only 6 (54.55%) turned into minor findings. The difference was statistically significant ($P = 0.038$). For US, 11/12 patients in the WBRT group and 18/18 patients in the IORT group with major findings had a late follow-up. They turned into minor findings in seven patients (63.64%) in the WBRT group and in six patients (33.33%) in the IORT group at the end of follow-up. The difference was not statistically significant. Most of the circumscribed masses and ill-defined non-mass lesions persisted as circumscribed masses, which were probably compatible with fat necrosis but not in the typical form of an oil cyst.

| Table 1. Continued | | | |
|---|---|---|---|
| Median size (mm) | 39 (23–45) | 20 (13.5–27.5) | 0.070 |
| Median time to develop (months) | 8 (7–20) | 8.5 (6.5–22.5) | 0.999 |
| <24 months | 12 (85.7) | 6 (75) | 0.602 |
| >24 months | 2 (14.3) | 2 (25) | |
| Increased parenchymal density | | | |
| None | 15 (60)[a] | 9 (37.5)[b] | **<0.001** |
| Regional | 9 (36)[a] | 2 (8.3)[b] | |
| Diffuse | 1 (4)[a] | 13 (54.2)[b] | |
| **Ultrasonography** | | | |
| Non-mass ill-defined lesion | | | |
| Number of cases | 11 (44) | 2(8) | **0.004** |
| Median size (mm) | 45 (36–50) | 16.5 (15–18) | **0.026** |
| Circumscribed mass lesion | | | |
| Number of cases | 7 (28) | 1 (4) | **0.049** |
| Median size (mm) | 45 (30–55) | 35 | 0.750 |
| Scar/distortion | | | |
| None | 22 (88)[a] | 5 (20)[b] | **<0.001** |
| Linear scar/distortion | 3 (12)[a] | 11 (44)[b] | |
| Planar scar | 0 (0)[a] | 9 (36)[b] | |
| Fluid collection | | | |
| Number of cases | 0(0) | 5 (20) | **0.049** |
| Median size (mm) | - | 22 (13–38) | - |
| Oil cysts | | | |
| Number of cases | 14 (56) | 10 (40) | 0.258 |
| Mean size (mm) | 26 ± 14.08 | 15.1 ± 8.9 | **0.043** |
| Median time to develop (months) | 14 (7–43) | 12 (7–19) | 0.437 |
| **Overall findings** | | | |
| Mammography | | | |
| Minor | 12 (48) | 15 (60) | 0.430 |
| Intermediate | 9 (36) | 9 (36) | |
| Advanced | 4 (16) | 1 (4) | |
| Ultrasonography | | | |
| Minor | 7 (28)[a] | 13 (52)[a] | **0.014** |
| Intermediate | 7 (28)[a] | 10 (40)[a] | |
| Advanced | 11 (44)[a] | 2 (8)[b] | |

Values are expressed as means ± standard deviation, median interquartile range, or n (%). The independent t-test, Mann–Whitney U test, Pearson chi-square test, and Fisher's exact test were used. The same letters in a row (a,b) denote the lack of statistically significant differences. IORT, intraoperative radiotherapy; WBRT, whole breast radiotherapy.

## Discussion

This study compared mammography and US findings of breast cancer patients who were treated with IORT with the findings of patients treated with WBRT. It was found that mammography demonstrated significantly more diffuse changes in the form of skin thickening, edema, and increased parenchymal density in patients in the WBRT group. Focal findings such as masses, asymmetries, and oil cysts were more common in patients in the IORT group. On US, irregular non-mass lesions or circumscribed masses were the dominant findings in patients in the IORT group, while postoperative scars and fluid collections were typical for patients in the WBRT group. Major findings, some of which could lead to diagnostic problems, were more common after IORT.

There are only a few articles in the literature about imaging findings in patients treated with IORT.[7-15] Most of these studies are more than 10 years old and have been performed by a few groups involved in the early clinical trials comparing IORT and WBRT. A limited number of findings have been evaluated, and conflicting results were reported. After IORT was implemented in the clinic, ill-defined non-mass hypoechoic lesions with indistinct margins were found in some cases on US examination. This was very different from the findings usually found in patients treated with WBRT. Because most of the previous reports failed to mention such a lesion, it was decided to conduct this study and describe its findings.

In this study, US revealed non-mass irregular lesions in the tumor bed of 11 patients in the IORT group (44%) but in only 2 patients in the WBRT group (8%), and the difference was statistically significant. The differential diagnosis of an irregular lesion at the surgical site included residual or recurrent tumors as well as fat necrosis. Magnetic resonance imaging and/or US-guided core needle biopsy may be needed for the final diagnosis if the lesion seems suspicious. Short-term follow-up was performed instead of biopsy as these lesions were present in the first follow-up examinations, making the timing unlikely for a malignant process. A similar finding has been mentioned only by Della Sala et al.[11] The biopsy revealed fat necrosis in their study, and lesions either persisted or turned into oil cysts over time. In this study, most of these lesions turned into circumscribed masses, probably compatible with fat necrosis. Similar cases were probably categorized as fat necrosis or unorganized scars in other studies.[11,13] Some authors have reported that mammography revealed more distinct changes after IORT and that US can be used as a problem-solving modality.[7-9,11,13] This study found the opposite: US findings were more confusing compared with mammography in many cases, as seen in Figure 4. Furthermore, mammography can help in the differential diagnosis of such cases because it can clearly demonstrate the fatty content of the lesion, enabling the diagnosis of fat necrosis.

Another interesting finding of this study was that minor findings were significantly more common in fatty breasts, and major findings were more common in dense breasts in the IORT group but not in the WBRT group. It is thought that this may be due to the localized and confined nature of fat necrosis in the dense breast tissue, which causes a suspicious appearance, especially in the early follow-up period. Moreover, more diffuse changes or more typical liquefaction may be the dominant findings in the fatty breast tissue, which do not usually lead to diagnostic problems. Another explanation

**Table 2.** Dominant imaging findings in the early mammography and ultrasound examinations

| Findings, n (%) | IORT (n = 25) | WBRT (n = 25) | *P* value |
|---|---|---|---|
| **Dominant findings in early mammograms** | | | |
| Increased density | 1 (4) | 3 (12) | 0.609 |
| Mass-like opacity | 4 (16) | 2 (8) | 0.667 |
| Heterogeneous non-mass opacity | 9 (36) | 6 (24) | 0.355 |
| Oil cysts | 7 (28) | 4 (16) | 0.306 |
| Scar/distortion | 4 (16) | 8 (32) | 0.185 |
| Spiculated scar | 0 (0) | 2 (8) | 0.490 |
| **Dominant findings in early US examinations** | | | |
| Scar/distortion | 1 (4) | 4 (16) | 0.349 |
| Ill-defined non-mass lesion | 11 (44) | 2 (8) | **0.004** |
| Circumscribed mass | 7 (28) | 1 (4) | **0.049** |
| Oil cyst | 6 (24) | 4 (16) | 0.480 |
| Planar scar | 0 (0) | 9 (36) | **0.002** |
| Fluid collection | 0 (0) | 4 (16) | 0.110 |

Pearson chi-square test and Fisher's exact test were used. IORT, intraoperative radiotherapy; WBRT, whole breast radiotherapy; US, ultrasound.

**Table 3.** Distribution of overall imaging findings according to breast density

| Findings, n (%) | Low density | High density | *P* value |
|---|---|---|---|
| **All patients (n = 50)** | | | |
| Mammography | | | |
| Minor | 17 (65.4) | 10 (41.7) | 0.093 |
| Major (intermediate/advanced) | 9 (34.6) | 14 (58.3) | |
| Ultrasound | | | |
| Minor | 14 (53.8) | 6 (25) | **0.038** |
| Major (intermediate/advanced) | 12 (46.2) | 18 (75) | |
| **IORT (n = 25)** | | | |
| Mammography | | | |
| Minor | 11 (68.8) | 1 (11.1) | **0.011** |
| Major (intermediate/advanced) | 5 (31.3) | 8 (88.9) | |
| Ultrasound | | | |
| Minor | 7 (43.8) | 0 (0) | **0.027** |
| Major (intermediate/advanced) | 9 (56.3) | 9 (100) | |
| **WBRT (n = 25)** | | | |
| Mammography | | | |
| Minor | 6 (60) | 9 (60) | 0.999 |
| Major (intermediate/advanced) | 4 (40) | 6 (40) | |
| Ultrasound | | | |
| Minor | 7 (70) | 6 (40) | 0.226 |
| Major (intermediate/advanced) | 3 (30) | 9 (60) | |

Pearson chi-square test and Fisher's exact test were used. IORT, intraoperative radiotherapy; WBRT, whole breast radiotherapy.

may be the difference in vascular support in fatty and dense breasts. Apparently, this difference is only valid for the local effects of IORT and not for the diffuse effects of external WBRT. The correlation between breast density and the type of imaging findings has not been reported previously.

IORT was used with varying indications (as single-dose radiotherapy, as a boost followed by WBRT, or mixed) in different studies. Patients who received IORT as a boost were excluded from this study to achieve more uniform results that are not complicated by the additional effects of WBRT applied after the operation. A study comparing the imaging findings of IORT applied as a boost prior to WBRT with those of WBRT alone reported that more pronounced findings were detected in the IORT group.[7] This shows that the focal effects of IORT in the breast tissue are apparent, even if it is followed by WBRT. In this study, skin thickening, edema, and increased parenchymal density on mammography were significantly more common and more diffuse after WBRT. These early mammographic findings are all related to each other and are as expected since external radiotherapy applied to the whole breast causes more diffuse changes. These results agree with those of Della Sala et al.[11] and Elsberger et al.[15], who have also included only patients who received single-dose IORT in their studies. Other studies where IORT was used as a boost before WBRT have not reported similar findings, probably because both groups demonstrated diffuse changes.

This study detected calcifications in more than half of the patients in both groups, and there was no significant difference in the development time for calcifications. This is similar to the results of Ruch et al.[13] and Elsberger et al.[15], and all calcifications were typically benign. Although some of them seemed non-uniform in the beginning, they developed into typical rim calcifications eventually. Similar to the findings of Ruch et al.[13], dystrophic calcifications were more common in the WBRT group, and rim calcifications were more common in the IORT group. However, other authors have reported that calcifications were significantly more common in the IORT group.[8,11,12] Jalaguier-Coudray et al.[14] have stated that non-uniform calcifications can also be associated with tungsten deposits due to the use of shielding devices composed of this material.

Oil cysts were more common after IORT on both mammography and US, but the difference was significant only for mammography. There were fewer typical oil cysts on US because some of the fat necrosis cases probably appeared as well-circumscribed hypoechoic masses or ill-defined non-mass lesions in early examinations. Circumscribed masses may also represent organized hematoma. Some of these lesions turned into oil cysts during follow-up, while the rest persisted as circumscribed masses. Mammography was superior in diagnosing oil cysts due to its ability to demonstrate inner fatty content. They were larger in the IORT group, but this was not statistically significant. Other studies have also reported more frequent oil cysts and fat necroses as well as larger lesions in patients who received IORT.[8,11,13,15]
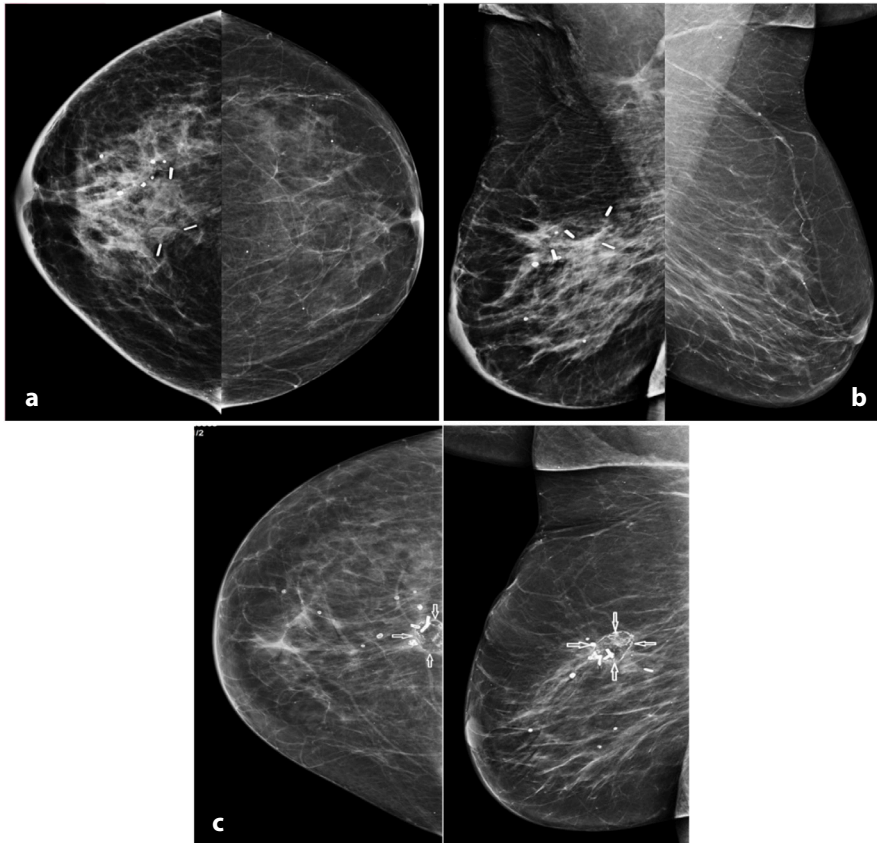
**Figure 6. (a-c)** Early mammograms **(a, b)** of a 46-year-old patient treated with WBRT show generalized skin thickening, diffuse increase in parenchymal density, and marked edema. These findings resolve during follow-up **(c)** and dystrophic and rim-like calcifications (arrows) appear instead. WBRT, whole breast radiotherapy.

In conclusion, mammography revealed more diffuse changes in the WBRT group as opposed to localized findings in the IORT group in terms of skin thickening, edema, and the increase in parenchymal density. US demonstrated significantly more ill-defined non-mass lesions and circumscribed masses in the IORT group, while fluid collections and linear and planar scars were more typical for WBRT. Radiologists should especially be aware of ill-defined non-mass lesions, which are considerably more common in patients who received IORT, because they can be confusing, especially in early follow-up studies. This study found that minor findings were seen more frequently in low-density breasts, while major findings were more common in high-density breasts on both mammography and US in the IORT group. This has not been reported before, and further studies with more cases are needed to verify these results.

## Conflict of interest disclosure

The authors declared no conflicts of interest.

## References

1. Vaidya JS, Tobias JS, Baum M, et al. TARGeted intraoperative radiotherapy (TARGIT): an innovative approach to partial-breast irradiation. Semin Radiat Oncol. 2005;15(2):84-91. [CrossRef]

2. Veronesi U, Orecchia R, Luini A, et al. A preliminary report of intraoperative radiotherapy (IORT) in limited-stage breast cancers that are conservatively treated. *Eur J Cancer*. 2001;37(17):2178-2183. [CrossRef]

3. Reitsamer R, Peintinger F, et al. Intraoperative radiotherapy given as a boost after breast-conserving surgery in breast cancer patients. *Eur J Cancer*. 2002;38(12):1607-1610. [CrossRef]

4. Kraus-Tiefenbacher U, Scheda A, Steil V, et al. Intraoperative radiotherapy (IORT) for breast cancer using the Intrabeam system. *Tumori*. 2005;91(4):339-345. [CrossRef]

5. Gatzemeier W, Orecchia R, Gatti G, Intra M, Veronesi U. Intraoperative strahlentherapie (IORT) in der Behandlung des Mammakarzinoms--eine neue therapeutische Alternative im Rahmen der brusterhaltenden Therapie? Stellenwert und Zukunftsperspektiven. Erfahrungsbericht aus dem European Institute of Oncology (EIO), Mailand [Intraoperative radiotherapy (IORT) in treatment of breast carcinoma--a new therapeutic alternative within the scope of breast-saving therapy? Current status and future prospects. Report of experiences from the European Institute of Oncology (EIO), Mailand]. *Strahlenther Onkol*. 2001;177(7):330-337. [CrossRef]

Scars and distortion were significantly more frequent in the mammograms of patients in the WBRT group in this study, which was contrary to other studies.[8,11,15] On US, fluid collections were more common in the WBRT group, which was in contrast to other studies.[7,11,13] This is probably because the surgeons kept surgical drains longer in patients in the IORT group because more extensive dissection was needed to place the applicator. Linear (44% vs. 12%) or planar scars (36% vs. 0%) were other dominant US findings in the WBRT group. Although planar scars seemed suspicious in one plane because of ill-defined margins and shadowing, they were elongated in the other plane along the incision line and did not cause diagnostic challenges.

This is the only study in the literature where both early and late mammography and US findings were evaluated to determine the changes that take place over time. This study has shown that major focal findings such as masses and ill-defined non-mass lesions tend to persist in the late period in patients in the IORT group, but they usually turn into minor findings in the WBRT group. Furthermore, diffuse changes such as skin thickening, increased parenchymal density, and edema regressed completely or partially in both groups over time.

Major limitations in this study include the small number of patients. In the clinic, IORT was performed in a very selective manner, and only single-dose therapy cases were included. The control group was not homogeneous and consisted of both standard and hypofractionated regimens because hypofractionation has been preferred whenever possible during recent years. Follow-up examinations were not available in every case due to the retrospective design of the study. Furthermore, the classification of radiological findings as "minor or major" was somewhat subjective as there are no standardized criteria for this classification. However, two experienced breast radiologists interpreted the findings in consensus. Although the readers were unaware of the treatment protocol, surgical markers placed at the tumor bed in some patients inevitably indicated WBRT on mammography. Finally, this study did not evaluate the rate of false positive findings leading to magnetic resonance imaging or biopsy.

6.  Intra M, Gatti G, Luini A, et al. Surgical technique of intraoperative radiotherapy in conservative treatment of limited-stage breast cancer. Arch Surg. 2002;137(6):737-740. [CrossRef]

7.  Wasser K, Schoeber C, Kraus-Tiefenbacher U, et al. Early mammographic and sonographic findings after intraoperative radiotherapy (IORT) as a boost in patients with breast cancer. *Eur Radiol*. 2007;17(7):1865-1874. [CrossRef]

8.  Wasser K, Ruch M, Brade J, et al. Do structural changes in the tumour bed after intraoperative radiotherapy (IORT) of breast cancer complicate the evaluation of mammograms in a long-term follow-up?. *Eur J Radiol*. 2012;81(3):e255-e259. [CrossRef]

9.  Wasser K, Ruch M, Brade J, et al. Do structural changes in the tumour bed after intraoperative radiotherapy (IORT) of breast cancer complicate the evaluation of mammograms in a long-term follow-up?. *Eur J Radiol*. 2012;81(3):e255-e259. [CrossRef]

10. Machiels M, Weytjens R, Erven K, et al. Oncological outcome, postoperative complications, and mammographic changes after intraoperative radiotherapy with electrons (IOERT) as a boost in a large single-institution cohort of breast cancer patients. *Breast J*. 2020;26(10):1937-1945. [CrossRef]

11. Della Sala SW, Pellegrini M, Bernardi D, et al. Mammographic and ultrasonographic comparison between intraoperative radiotherapy (IORT) and conventional external radiotherapy (RT) in limited-stage breast cancer, conservatively treated. *Eur J Radiol*. 2006;59(2):222-230. [CrossRef]

12. Engel D, Schnitzer A, Brade J, et al. Are mammographic changes in the tumor bed more pronounced after intraoperative radiotherapy for breast cancer? Subgroup analysis from a randomized trial (TARGIT-A). *Breast J*. 2013;19(1):92-95. [CrossRef]

13. Ruch M, Brade J, Schoeber C, et al. Long-term follow-up-findings in mammography and ultrasound after intraoperative radiotherapy (IORT) for breast cancer. Breast. 2009;18(5):327-334. [CrossRef]

14. Jalaguier-Coudray A, Cohen M, Thomassin-Piana J, et al. Calcifications and tungsten deposits after breast-conserving surgery and intraoperative radiotherapy for breast cancer. *Eur J Radiol*. 2015;84(12):2521-2525. [CrossRef]

15. Elsberger B, Romsauerova A, Vinnicombe S, et al. Comparison of mammographic findings after intraoperative radiotherapy or external beam whole breast radiotherapy. *Eur J Surg Oncol*. 2014;40(2):163-167. [CrossRef]

16. Smith BD, Arthur DW, Buchholz TA, et al. Accelerated partial breast irradiation consensus statement from the American Society for Radiation Oncology (ASTRO). *Int J Radiat Oncol Biol Phys*. 2009 15;74(4):987-1001. [CrossRef]

17. Correa C, Harris EE, Leonardi MC, et al. Accelerated partial breast irradiation: executive summary for the update of an ASTRO evidence-based consensus statement. *Pract Radiat Oncol*. 2017;7(2):73-79. [CrossRef]

18. American College of Radiology. BI-RADS Atlas 5th Edition American College of Radiology, Reston VA; 2013. [CrossRef]

# Nomogram based on clinical characteristics and radiological features for the preoperative prediction of spread through air spaces in patients with clinical stage IA non-small cell lung cancer: a multicenter study

Yun Wang* 🆔
Deng Lyu* 🆔
Di Zhang* 🆔
Lei Hu 🆔
Junhong Wu 🆔
Wenting Tu 🆔
Yi Xiao 🆔
Li Fan 🆔
Shiyuan Liu 🆔

**\*Authors contributed equally to this work.**

From the Department of Radiology (Y.W., D.L., D.Z., W.T., Y.X., L.F. ✉ fanli0930@163.com, S.L. ✉ radiology_cz@163.com), Second Affiliated Hospital of Navy Medical University, Shanghai, China; Department of Radiology Medicine (L.H.), The People's Hospital of Chizhou, Anhui, China; Department of Radiology Medicine (J.W.), The People's Hospital of Guigang, Guangxi, China.

**PURPOSE**

To investigate the value of clinical characteristics and radiological features for predicting spread through air spaces (STAS) in patients with clinical stage IA non-small cell lung cancer (NSCLC).

**METHODS**

A total of 336 patients with NSCLC from our hospital were randomly divided into two groups, i.e., the training cohort (n = 236) and the internal validation cohort (n = 100) (7:3 ratio). Furthermore, 69 patients from two other hospitals were collected as the external validation cohort. Eight clinical patient characteristics were recorded, and 20 tumor radiological features were quantitatively measured and qualitatively analyzed. In the training cohort, the differences in clinical characteristics and radiological features were compared using univariate and multivariate analysis. A nomogram was created, and the predictive efficacy of the model was evaluated in the validation cohorts. The receiver operating characteristic curve and area under the curve (AUC) value were used to evaluate the discriminative ability of the model. In addition, the Hosmer–Lemeshow test and calibration curve were used to evaluate the goodness-of-fit of the model, and the decision curve was used to analyze the model's clinical application value.

**RESULTS**

The best predictors included gender, the carcinoembryonic antigen (CEA), consolidation-to-tumor ratio (CTR), density type, and distal ribbon sign. Among these, the tumor density type [odds ratio (OR): 6.738] and distal ribbon sign (OR: 5.141) were independent risk factors for predicting the STAS status. Moreover, three different STAS prediction models were constructed, i.e., a clinical, radiological, and combined model. The clinical model comprised gender and the CEA, the radiological model included the CTR, density type, and distal ribbon sign, and the combined model comprised the above two models. A DeLong test results revealed that the combined model was superior to the clinical model in all three cohorts and superior to the radiological model in the external validation cohort; the cohort AUC values were 0.874, 0.822, and 0.810, respectively. The results also showed that the combined model had the highest diagnostic efficacy among the models. The Hosmer–Lemeshow test showed that the combined model showed a good fit in all three cohorts, and the calibration curve showed that the predicted probability value of the combined model was in good agreement with the actual STAS status. Finally, the decision curve showed that the combined model had a better clinical application value than the clinical and radiological models.

**CONCLUSION**

The nomogram created in this study, based on clinical characteristics and radiological features, has a high diagnostic efficiency for predicting the STAS status in patients with clinical stage IA NSCLC and may support the creation of personalized treatment strategies before surgery.

**KEYWORDS**

Spread through air spaces, nomogram, radiological, prediction, non-small cell lung cancer

The global cancer incidence statistics for 2020 reported lung cancer as one of the leading causes of cancer-induced death, with non-small cell lung cancer (NS-CLC) accounting for approximately 80–85% of lung cancers.[1] According to the latest National Comprehensive Cancer Network guidelines,[2] lobectomy has been the standard surgical procedure for clinical-stage IA NSCLC; however, sublobar resection, including segmentectomy and wedge resection, is considered acceptable for lower-risk patients in early stages of the disease, such as those with a tumor diameter ≤2 cm, a ground-glass opacity (GGO) component and other standards.[3-5]

In 2015, the World Health Organization (WHO) formally defined "spread through air spaces (STAS)" as tumor cells appearing in the form of micropapillary cell clusters, solid cancer nests, or single tumor cells in the lung tissue surrounding the main tumor. It further identified STAS as the fourth type of invasion mode in lung adenocarcinoma.[6] Recent studies showed that STAS was a prognostic factor of poor outcomes for sublobar resection in patients with clinical or pathological stage IA lung cancer.[7,8] The presence of STAS was an independent risk factor for recurrence in patients with stage IA part-solid adenocarcinoma after sublobar resection.[9] Therefore, the use of relatively radical surgery, such as lobectomy rather than sublobar resection, as well as a wider surgical resection margin may be appropriate in the presence of STAS.[7-10] Effective preoperative evaluation of the STAS status may help to improve patient outcomes.

At present, postoperative pathological section,[6] which does not facilitate preoperative surgical planning, remains the gold standard for STAS diagnosis. However, preoperative puncture and intraoperative frozen pathological examinations are limited by

their low sensitivity, small tissue sample size, and short diagnosis time.[11,12] Therefore, accurate assessment of the STAS status using preoperative imaging methods and other valuable clinical information could significantly impact surgical plans.

Scholar-led studies on the STAS status of lung cancer based on preoperative computed tomography (CT) results revealed a correlation between certain radiological features of lung cancer and the STAS status.[13-19] Through the use of different multiple regression models, these studies showed an association between STAS and larger tumor size,[13,14] larger solid component size,[13-16] a larger ratio of solid component size to total tumor size [consolidation-to-tumor ratio (CTR)],[13,14,16-18] air bronchogram sign,[13] vacuole sign,[15] spiculation sign,[15] lobulation sign,[18] and notch sign.[19] Additionally, Kim et al.[17] found that STAS was absent in pure GG lesions. Most existing studies included lesions in any stage of lung adenocarcinoma;[15-17,19] only two studies included stage IA lung adenocarcinoma,[13,18] and one study included only part-solid nodules.[14] Furthermore, the above-described studies only included histologic adenocarcinoma tumors. However, STAS was reportedly associated with the poor prognosis of other types of lung cancer, such as lung squamous cell carcinoma,[20] lung pleomorphic carcinoma,[21] and lung neuroendocrine tumors.[22] Jia et al.[23] also showed that clinical characteristics, such as age, gender, and the carcinoembryonic antigen (CEA), were predictors of STAS in lung cancer. To the best of the present authors' knowledge, studies focusing on clinical stage IA NSCLC [excluding pure GG nodules (pGGNs)] and incorporating the relevant CT radiological features and valuable clinical information for predicting the STAS status are rare. Therefore, the current study explored the risk factors of STAS in clinical stage IA NSCLC with a focus on clinical characteristics and radiological features. A prediction model was constructed, and a nomogram was produced. The model underwent internal and external validation to provide a basis for accurately assessing the presence or absence of STAS in patients with preoperative clinical stage IA NSCLC.

## Methods

### Patients

The present study was approved by the Ethics Committee of Changzheng Hospital, Naval Medical University (decision number: CZ-20220712-03). Due to the retrospective nature of this study, the need for informed consent was waived.

A retrospective patient analysis was performed; the included patients (1) had a clinical stage IA NSCLC status assessed by postoperative pathology and (2) had undergone a preoperative chest CT examination one week before surgical resection at our hospital and two other hospitals between September 2019 to September 2022. The authors collected 290 patients presenting as pGGNs, none of which were positive for STAS. As reported in the references,[17] these pGGNs were excluded.

The inclusion criteria were as follows: patients with (i) a thin-slice (≤1.5 mm) chest CT with no artifacts within one week before surgery; (ii) complete clinical and pathological data; (iii) clinical stage IA NSCLC (cT1N0M0, with a maximum tumor diameter of ≤3 cm); and (iv) solid or mixed GG nodules (mGGNs).

The exclusion criteria were as follows: patients with (i) poor image quality; (ii) incomplete clinical and pathological data; (iii) a maximum tumor diameter of >3 cm; (iv) tumors with lymph node or distant metastasis; (v) a pathological type other than NSCLC; (vi) a history of preoperative neoadjuvant treatment and chemotherapy; and (vii) pGGNs.

A total of 336 patients from our hospital (hospital 1) were included in the study and randomly divided into two groups, i.e., the training cohort (n = 236) and the internal validation cohort (n = 100) (7:3 ratio). Furthermore, 69 cases from two other hospitals (hospital 2 and hospital 3) were used as the external validation cohort, including 30 patients from hospital 2 and 39 patients from hospital 3. The detailed patient inclusion procedure is shown in Figure 1.

If multiple lesions in the same patient were surgically removed and met the inclusion criteria, the research conducted by Dercle et al.[24] was referred to for the selection of a representative lesion with the largest tumor size for analysis.

### Clinical and pathological data collection

Patient data were collected, including gender, age, clinical symptoms, smoking status, family history of lung cancer, history of malignant tumors, history of multiple primary lung cancer, surgical type, pathological type, and CEA levels.

### Equipment and parameters

Patients from hospital 1 underwent preoperative chest CT examinations with four types of CT machines, including the Toshiba Aquilion16 row, GE Light Speed VCT64 row,

Philips Ingenuity 64 row, and Brilliance iCT 128 row CT machines, from three vendors. In the external cohort, patients from hospital 2 were assessed with the American Light Speed 16, Light Speed VCT64 row, and Dutch Philips iCT 256-row CT machines. Hospital 3 utilized the German SOMATOM Definition Flash and SOMATOM Drive 64-row CT machines. The patients were instructed to lie down during the scan. The scanning range was set from the thoracic inlet to the middle portion of the kidneys; the tube voltage was set to 120 kVp, with a tube current of 150–250 mAs or automatic tube current regulation; the scanning slice thickness and slice increment were 5 mm; the reconstruction slice thickness and slice increment were (1) 1 mm in hospital 1 and hospital 2 and (2) 1.3 mm in hospital 3. The lung or standard algorithm reconstruction was selected, and non-contrast enhanced images were used for analysis.

## Image evaluation

The CT images were imported into software (RadiAnt DICOM Viewer 4.2.1, Medixant, Poland) and analyzed by two independent radiologists with 2 and 10 years of experience, respectively, who were blinded to the pathological information. The lung window [width: 1500 Hounsfield scale (HU), level: −500 HU], mediastinal window (width: 300 HU, level: 50 HU), multiplanar reformation (MPR), and maximal intensity projection were used to analyze the lesion. For quantitative measures, the average measurements of two independent radiologists were used as the final data. For qualitative indicators, disagreements were discussed until a consensus was reached.

First, the longest diameter of the entire tumor and the consolidation part were measured at the lung window on the MPR images, and the proportion of the consolidation part (CTR) was calculated.[13] Clinical T-staging was performed according to the maximum diameter of the solid components of the tumor.[25]

Second, the following qualitative CT radiological features were assessed: the tumor location, density type (solid and mGGN), shape (round and irregular), tumor–lung interface (well-defined and ill-defined), margin (lobulation and spiculation), internal features (vacuole sign and cavity/cystic airspace), and external features (vascular convergence, bronchial change, pleural tags, pleural indentation, halo sign, satellite lesions, distal ribbon sign, and combination with emphysema).

The definitions of CT radiological features are described in Supplementary Table 1, and the CT radiological features are shown in Supplementary Figures 1-4. Most of the definitions concerning the pulmonary nodules' radiological features have previously been reported.[17,26-29]

## Pathological diagnosis

The pathological diagnosis of each patient included in the present study was established, respectively, by two pathologists, a junior pathologist and a senior pathologist with more than 10 years of work experience collectively, based on the 2015 WHO definition of STAS.[6] The classification of lung cancer was based on the WHO's classification of lung cancer (2015 edition),[6] and the clinical and pathological staging was based on the TNM staging standard of lung cancer (8th edition),[25] as the pathological diagnosis was determined as part of routine clinical practice, and the specimens were not reviewed specifically for this study.

## Statistical analysis

The SPSS (v.20.0) and R (v.4.2.2) statistical software programs were used for analyzing all statistical tests. The classified data were represented by the number of cases, and the comparison between the two groups was performed using Pearson's chi-square test, Yate's correction for continuity, or Fisher's exact test. A P value of <0.05 was considered statistically significant in the univariate analysis. Variables with $P < 0.1$ in the univariate analysis were included in the multivariate logistic regression analysis, backward stepwise selection was applied using the likelihood ratio test, with Akaike's information criterion as the stopping rule to select the best combination of variables for building the prediction model in the training cohort, and a corresponding nomogram was constructed. The interobserver agreement of numeric and categorical variables was assessed using intraclass correlation coefficients (ICCs) and κ-statistics, respectively. The receiver operating characteristic (ROC) curve with the
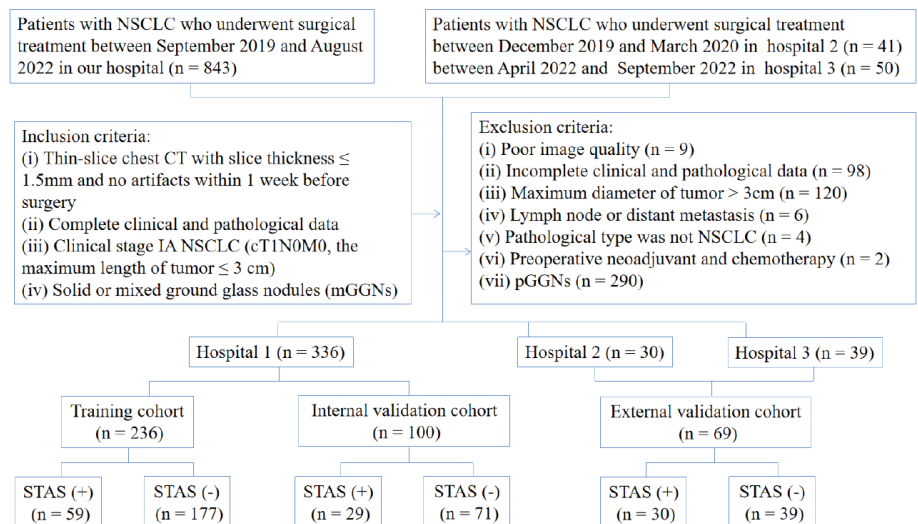


**Figure 1.** The flow chart for patient selection. NSCLC, non-small cell lung cancer; CT, computed tomography; STAS, spread through air spaces.
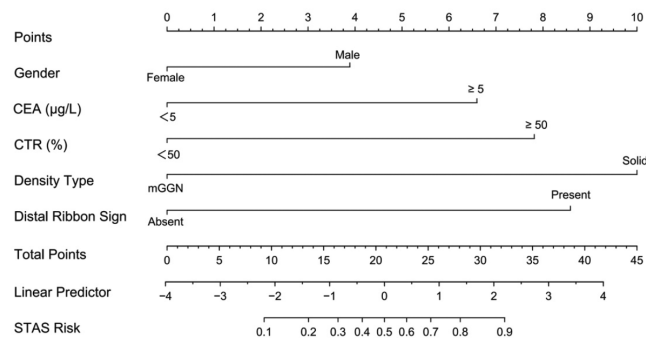


**Figure 2.** The nomogram for the preoperative prediction of the spread through air spaces status based on clinical characteristics and radiological features in clinical stage IA non-small cell lung cancer. CEA, carcinoembryonic antigen; CTR, consolidation-to-tumor ratio; STAS, spread through air spaces, mGGN, mixed ground-glass nodule.

corresponding area under the curve (AUC) value was used to evaluate the discriminative ability of the prediction models for predicting STAS in the training and validation cohorts. The DeLong test was used to assess AUC differences between models. Calibration curves and the Hosmer–Lemeshow test were used to evaluate the goodness-of-fit of the prediction model; a *P* value of >0.05 indicated a high goodness-of-fit. The decision curve analysis (DCA) was used to evaluate the clinical utility of the nomogram. Multivariate binary logistic regression, nomograms, and calibration plots were performed with the "rms" package of the R software. The ROC was performed using the "pROC" package. Validation was performed by the "rms" package. DCA was performed using the "gg.DCA" function.

## Results

### Clinicopathological characteristics of the study cohorts

Of the 405 patients with NSCLC included in the present study, 118 were STAS-positive and 287 were STAS-negative. Statistically significant gender differences were observed in the training and external validation cohorts (*P* < 0.05). Furthermore, the surgical method showed statistically significant differences in the training and internal validation cohorts (*P* < 0.05), whereas smoking status, CEA, and pathological type demonstrated statistically significant differences in the training cohort (*P* < 0.05). Additionally, there were statistically significant differences concerning clinical symptoms in the external validation cohort (*P* < 0.05) (Table 1).

### Univariate and multivariate logistic regression analysis

For radiological features, good consistency was observed in terms of quantitative parameters between two observers (ICC: 0.934–0.935), with a strong consistency in qualitative indicators (Kappa value: 0.852–1.000). The interobserver agreement assessment results of each index are shown in Supplementary Table 2.

In the training cohort, univariate analysis showed statistically significant differences in gender, smoking status, CEA, clinical T-stage, CTR, density type, spiculation, bronchial change, vascular convergence, halo sign, distal ribbon sign, pleural indentation, and pleural tags between the STAS-positive and the STAS-negative groups (*P* < 0.05) (Table 2). No multicollinearity was observed (see Supplementary Table 3). The best combination of variables selected by multivariate logistic regression analysis included gender, the CEA, CTR, density type, and distal ribbon sign, among which the tumor density type [odds ratio (OR): 6.738] and distal ribbon sign (OR: 5.141) were independent risk factors for predicting the STAS status (Table 3).

### Model development and evaluation

Based on the best combination of variables selected by multivariate logistic regression analysis, three different models were constructed: (1) a clinical model comprising gender and the CEA; (2) a radiological model comprising the CTR, density type, and distal ribbon sign; and (3) a combined model including of all the above variables. Then, predictive diagnostic efficacy was compared among the different models. The results indicated that the AUC values in the three cohorts were 0.874, 0.822, and 0.810 in the combined model, 0.862, 0.821, and 0.738 in the radiological model, and 0.639, 0.505, and 0.685 in the clinical model. The predictive efficacy is shown in Table 4, and the ROC curves are shown in Figures 3-5. The DeLong test demonstrated that the combined mod-

el was superior to the clinical model in the three cohorts (Z = 6.315, 4.969, and 2.085; *P* < 0.05) and that the combined model was superior to the radiological model in the external validation cohort (Z = 2.529; *P* < 0.05). The radiological model was superior to the clinical model in the training cohort and the internal validation cohort (Z = 5.065 and 4.306; *P* < 0.05). Based on the regression coefficients of the variables selected by multivariate logistic regression analysis, a nomogram was constructed to evaluate the STAS risk intuitively, as shown in Figure 2. The regression equation was ln (P/1−P) = −3.97 + 0.74 × gender + 1.25 × CEA + 1.49 × CTR + 1.90 × density type + 1.64 × distal ribbon sign, where P represents the probability of predicting the occurrence of STAS. The Hosmer–Lemeshow test showed that the combined model was a good fit in all three cohorts (*P* = 0.22, 0.94, and 0.51, respectively). Moreover, the calibration curve showed that the predicted probabilities of the combined model were in acceptable agreement with the actual probabilities in the three cohorts (Figures 6-8). The DCA showed that the combined model had a better clinical application value than the clinical and radiological models (Figures 9-11).

## Discussion

With the extensive application of low-dose CT screening for lung cancer, the detection and surgical rates of the disease have been continuously improving.[30] STAS is a risk factor for postoperative tumor recurrence and metastasis in patients with early lung cancer, and lobectomy can achieve a better clinical prognosis than sublobectomy.[7,8,31] Therefore, an accurate prediction of the STAS status before surgery has important guiding significance for the selection of the surgical procedure. This study revealed that the tumor density type and distal
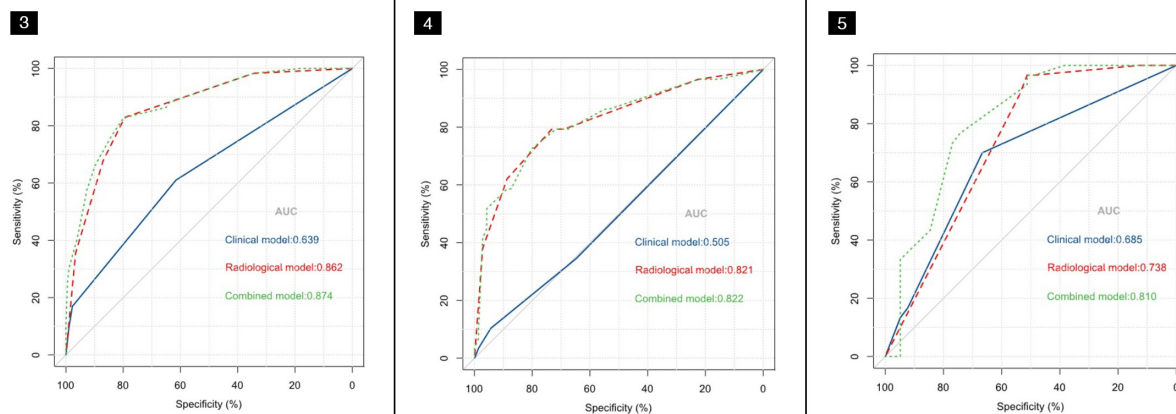


**Figures 3-5.** The receiver operation characteristic curve analysis of the clinical, radiological, and combined models in the three cohorts. **(Figure 3)** The training cohort, **(Figure 4)** the internal validation cohort, and **(Figure 5)** the external validation cohort. AUC, area under the curve.

**Table 1.** The clinical and pathological characteristics of patients in the training cohort and the two validation cohorts

| Characteristics | Training cohort (n = 236) | | | Internal validation cohort (n = 100) | | | External validation cohort (n = 69) | | |
|---|---|---|---|---|---|---|---|---|---|
| | STAS (−) (n = 177) | STAS (+) (n = 59) | P value | STAS (−) (n = 71) | STAS (+) (n = 29) | P value | STAS (−) (n = 39) | STAS (+) (n = 30) | P value |
| **Gender** | | | | | | | | | |
| Male | 66 (37.3%) | 32 (54.2%) | 0.022[a] | 49 (69.0%) | 21 (72.4%) | 0.736[a] | 12 (30.8%) | 20 (66.7%) | 0.003[a] |
| Female | 111 (62.7%) | 27 (45.8%) | | 22 (31.0%) | 8 (27.6%) | | 27 (69.2%) | 10 (33.3%) | |
| **Age (year)** | | | | | | | | | |
| <65 | 125 (70.6%) | 35 (59.3%) | 0.108[a] | 50 (70.4%) | 17 (58.6%) | 0.255[a] | 30 (76.9%) | 19 (63.3%) | 0.217[a] |
| ≥65 | 52 (29.4%) | 24 (40.7%) | | 21 (29.6%) | 12 (41.4%) | | 9 (23.1%) | 11 (36.7%) | |
| **Clinical symptoms** | | | | | | | | | |
| Absent | 124 (70.1%) | 47 (79.7%) | 0.153[a] | 49 (69.0%) | 16 (55.2%) | 0.188[a] | 31 (79.5%) | 17 (56.7%) | 0.041[a] |
| Present | 53 (29.9%) | 12 (20.3%) | | 22 (31.0%) | 13 (44.8%) | | 8 (20.5%) | 13 (43.3%) | |
| **Smoking status** | | | | | | | | | |
| Non-smoker | 151 (85.3%) | 42 (71.2%) | 0.015[a] | 62 (87.3%) | 25 (86.2%) | 1.000[b] | 34 (87.2%) | 21 (70.0%) | 0.079[a] |
| Smoker | 26 (14.7%) | 17 (28.8%) | | 9 (12.7%) | 4 (13.8%) | | 5 (12.8%) | 9 (30.0%) | |
| **Family history of lung cancer** | | | | | | | | | |
| Absent | 164 (92.7%) | 57 (96.6%) | 0.441[b] | 67 (94.4%) | 28 (96.6%) | 1.000[b] | 39 (100.0%) | 30 (100.0%) | N/A |
| Present | 13 (7.3%) | 2 (3.4%) | | 4 (5.6%) | 1 (3.4%) | | 0 (0.0%) | 0 (0.0%) | |
| **History of malignancy** | | | | | | | | | |
| Absent | 151 (85.3%) | 51 (86.4%) | 0.831[a] | 60 (84.5%) | 25 (86.2%) | 1.000[b] | 35 (89.7%) | 29 (96.7%) | 0.528[b] |
| Present | 26 (14.7%) | 8 (13.6%) | | 11 (15.5%) | 4 (13.8%) | | 4 (10.3%) | 1 (3.3%) | |
| **History of multiple primary lung cancer** | | | | | | | | | |
| Absent | 145 (81.9%) | 51 (86.4%) | 0.423[a] | 55 (77.5%) | 25 (86.2%) | 0.321[a] | 32 (82.1%) | 26 (86.7%) | 0.851[b] |
| Present | 32 (18.1%) | 8 (13.6%) | | 16 (22.5%) | 4 (13.8%) | | 7 (17.9%) | 4 (13.3%) | |
| **CEA (μg/L)** | | | | | | | | | |
| <5 | 173 (97.7%) | 49 (83.1%) | <0.001[b] | 67 (94.4%) | 26 (89.7%) | 0.685[b] | 36 (92.3%) | 25 (83.3%) | 0.438[b] |
| ≥5 | 4 (2.3%) | 10 (16.9%) | | 4 (5.6%) | 3 (10.3%) | | 3 (7.7%) | 5 (16.7%) | |
| **Surgery type** | | | | | | | | | |
| Sublobectomy | 80 (45.2%) | 14 (23.7%) | 0.004[a] | 25 (35.2%) | 3 (10.3%) | 0.023[b] | 12 (30.8%) | 3 (10.0%) | 0.075[b] |
| Lobectomy | 97 (54.8%) | 45 (76.3%) | | 46 (64.8%) | 26 (89.7%) | | 27 (69.2%) | 27 (90.0%) | |
| **Pathological type** | | | | | | | | | |
| MIA | 14 (7.9%) | 0 (0.0%) | | 7 (9.9%) | 0 (0.0%) | | 1 (2.6%) | 0 (0.0%) | |
| IA | 154 (87.0%) | 53 (89.8%) | | 64 (90.1%) | 28 (96.6%) | | 37 (94.8%) | 28 (93.3%) | |
| IMA | 5 (2.8%) | 4 (6.8%) | 0.021[c] | 0 (0.0%) | 0 (0.0%) | 0.069[c] | 1 (2.6%) | 0 (0.0%) | 0.588[c] |
| SCC | 3 (1.7%) | 0 (0.0%) | | 0 (0.0%) | 0 (0.0%) | | 0 (0.0%) | 0 (0.0%) | |
| ASC | 1 (0.6%) | 2 (3.4%) | | 0 (0.0%) | 0 (0.0%) | | 0 (0.0%) | 1 (3.4%) | |
| NSCLC-NOS | 0 (0.0%) | 0 (0.0%) | | 0 (0.0%) | 1 (3.4%) | | 0 (0.0%) | 1 (3.4%) | |

The P value represents the univariate analysis; data are presented as n (%). [a], Pearson's chi-square; [b], Yates' correction for continuity; [c], Fisher's exact test; STAS, spread through air spaces; STAS (−), STAS-negative; STAS (+), STAS-positive; CEA, carcinoembryonic antigen; MIA, minimally invasive adenocarcinoma; IMA, invasive mucinous adenocarcinoma; SCC, squamous cell carcinoma; ASC, adenosquamous carcinoma; NSCLC-NOS: non-small cell lung cancer, not otherwise specified.

**Table 2.** Radiological features of the tumor in the training cohort and the two validation cohorts

| Features | Training cohort (n = 236) | | | Internal validation cohort (n = 100) | | | External validation cohort (n = 69) | | |
|---|---|---|---|---|---|---|---|---|---|
| | STAS (−) (n = 177) | STAS (+) (n = 59) | P value | STAS (−) (n = 71) | STAS (+) (n = 29) | P value | STAS (−) (n = 39) | STAS (+) (n = 30) | P value |
| **Clinical T-stage** | | | | | | | | | |
| cT1mi | 17 (9.6%) | 0 (0.0%) | | 5 (7.0%) | 0 (0.0%) | | 1 (2.6%) | 0 (0.0%) | |
| cT1a | 75 (42.4%) | 11 (18.6%) | <0.001[c] | 28 (39.4%) | 1 (3.4%) | <0.001[c] | 11 (28.2%) | 1 (3.3%) | <0.001[c] |
| cT1b | 69 (39.0%) | 22 (37.3%) | | 32 (45.1%) | 9 (31.0%) | | 25 (64.1%) | 18 (60.0%) | |
| cT1c | 16 (9.0%) | 26 (44.1%) | | 6 (8.5%) | 19 (65.6%) | | 2 (5.1%) | 11 (36.7%) | |
| **CTR (%)** | | | | | | | | | |
| <50 | 63 (35.6%) | 2 (3.4%) | <0.001[a] | 19 (26.8%) | 1 (3.4%) | 0.008[a] | 6 (15.4%) | 0 (0.0%) | 0.032[c] |
| ≥50 | 114 (64.4%) | 57 (96.6%) | | 52 (73.2%) | 28 (96.6%) | | 33 (84.6%) | 30 (100.0%) | |
| **Density type** | | | | | | | | | |
| mGGN | 154 (87.0%) | 19 (32.2%) | <0.001[a] | 63 (88.7%) | 11 (37.9%) | <0.001[a] | 21 (53.8%) | 3 (10.0%) | <0.001[b] |
| Solid | 23 (13.0%) | 40 (67.8%) | | 8 (11.3%) | 18 (62.1%) | | 18 (46.2%) | 27 (90.0%) | |
| **Location** | | | | | | | | | |
| RUL | 58 (32.8%) | 12 (20.3%) | | 19 (26.8%) | 11 (37.9%) | | 11 (28.2%) | 8 (26.7%) | |
| RML | 16 (9.0%) | 5 (8.6%) | | 7 (9.9%) | 3 (10.5%) | | 4 (10.3%) | 2 (6.7%) | |
| RLL | 27 (15.3%) | 16 (27.1%) | 0.174[a] | 17 (23.9%) | 5 (17.2%) | 0.783[a] | 7 (17.9%) | 6 (20.0%) | 0.737[a] |
| LUL | 53 (29.9%) | 16 (27.1%) | | 17 (23.9%) | 5 (17.2%) | | 10 (25.7%) | 5 (16.6%) | |
| LLL | 23 (13.0%) | 10 (16.9%) | | 11 (15.5%) | 5 (17.2%) | | 7 (17.9%) | 9 (30.0%) | |
| **Shape** | | | | | | | | | |
| Irregular | 26 (14.7%) | 12 (20.3%) | 0.307[a] | 12 (16.9%) | 5 (17.2%) | 1.000[b] | 20 (51.3%) | 14 (46.7%) | 0.704[a] |
| Round/oval | 151 (85.3%) | 47 (79.7%) | | 59 (83.1%) | 24 (82.8%) | | 19 (48.7%) | 16 (53.3%) | |
| **Tumor-lung interface** | | | | | | | | | |
| Well-defined | 167 (94.4%) | 51 (86.4%) | 0.089[b] | 68 (95.8%) | 23 (79.3%) | 0.026[b] | 34 (87.2%) | 25 (83.3%) | 0.653[a] |
| Ill-defined | 10 (5.6%) | 8 (13.6%) | | 3 (4.2%) | 6 (20.7%) | | 5 (12.8%) | 5 (16.7%) | |
| **Lobulation** | | | | | | | | | |
| Absent | 32 (18.1%) | 6 (10.2%) | 0.152[a] | 18 (25.4%) | 3 (10.3%) | 0.095[a] | 14 (35.9%) | 11 (36.7%) | 0.947[a] |
| Present | 145 (81.9%) | 53 (89.8%) | | 53 (74.6%) | 26 (89.7%) | | 25 (64.1%) | 19 (63.3%) | |
| **Spiculation** | | | | | | | | | |
| Absent | 156 (88.1%) | 34 (57.6%) | <0.001[a] | 64 (90.1%) | 18 (62.1%) | 0.001[a] | 32 (82.1%) | 18 (60.0%) | 0.042[a] |
| Present | 21 (11.9%) | 25 (42.4%) | | 7 (9.9%) | 11 (37.9%) | | 7 (17.9%) | 12 (40.0%) | |
| **Vacuole** | | | | | | | | | |
| Absent | 127 (71.8%) | 38 (64.4%) | 0.287[a] | 49 (69.0%) | 20 (69.0%) | 0.996[a] | 31 (79.5%) | 25 (83.3%) | 0.685[a] |
| Present | 50 (28.2%) | 21 (35.6%) | | 22 (31.0%) | 9 (31.0%) | | 8 (20.5%) | 5 (16.7%) | |
| **Cavity/cystic airspace** | | | | | | | | | |
| Absent | 161 (91.0%) | 52 (88.1%) | 0.526[a] | 66 (93.0%) | 26 (89.7%) | 0.884[b] | 37 (94.9%) | 30 (100.0%) | 0.501[c] |
| Present | 16 (9.0%) | 7 (11.9%) | | 5 (7.0%) | 3 (10.3%) | | 2 (5.1%) | 0 (0.0%) | |
| **Bronchial change** | | | | | | | | | |
| Absent | 84 (47.5%) | 19 (32.2%) | 0.041[a] | 29 (40.8%) | 9 (31.0%) | 0.359[a] | 19 (48.7%) | 16 (53.3%) | 0.704[a] |
| Present | 93 (52.5%) | 40 (67.8%) | | 42 (59.2%) | 20 (69.0%) | | 20 (51.3%) | 14 (46.7%) | |

**Table 2.** Continued

| Features | Training cohort (n = 236) | | | Internal validation cohort (n = 100) | | | External validation cohort (n = 69) | | |
|---|---|---|---|---|---|---|---|---|---|
| | STAS (−) (n = 177) | STAS (+) (n = 59) | P value | STAS (−) (n = 71) | STAS (+) (n = 29) | P value | STAS (−) (n = 39) | STAS (+) (n = 30) | P value |
| **Vascular convergence** | | | | | | | | | |
| Absent | 150 (84.7%) | 43 (72.9%) | 0.041[a] | 53 (74.6%) | 19 (65.5%) | 0.356[a] | 35 (89.7%) | 18 (60.0%) | 0.009[b] |
| Present | 27 (15.3%) | 16 (27.1%) | | 18 (25.4%) | 10 (34.5%) | | 4 (10.3%) | 12 (40.0%) | |
| **Pleural tags** | | | | | | | | | |
| Absent | 97 (54.8%) | 18 (30.5%) | 0.001[a] | 31 (43.7%) | 8 (27.6%) | 0.135[a] | 14 (35.9%) | 11 (36.7%) | 0.947[a] |
| Present | 80 (45.2%) | 41 (69.5%) | | 40 (56.3%) | 21 (72.4%) | | 25 (64.1%) | 19 (63.3%) | |
| **Pleural indentation** | | | | | | | | | |
| Absent | 115 (65.0%) | 23 (39.0%) | <0.001[a] | 38 (53.5%) | 12 (41.4%) | 0.271[a] | 17 (43.6%) | 13 (43.3%) | 0.983[a] |
| Present | 62 (35.0%) | 36 (61.0%) | | 33 (46.5%) | 17 (58.6%) | | 22 (56.4%) | 17 (56.7%) | |
| **Halo sign** | | | | | | | | | |
| Absent | 175 (98.9%) | 54 (91.5%) | 0.015[b] | 70 (98.6%) | 24 (82.8%) | 0.010[b] | 37 (94.9%) | 29 (96.7%) | 1.000[b] |
| Present | 2 (1.1%) | 5 (8.5%) | | 1 (1.4%) | 5 (17.2%) | | 2 (5.1%) | 1 (3.3%) | |
| **Satellite lesions** | | | | | | | | | |
| Absent | 165 (93.2%) | 56 (94.9%) | 0.878[b] | 63 (88.7%) | 23 (79.3%) | 0.360[b] | 34 (87.2%) | 25 (83.3%) | 0.653[a] |
| Present | 12 (6.8%) | 3 (5.1%) | | 8 (11.3%) | 6 (20.7%) | | 5 (12.8%) | 5 (16.7%) | |
| **Distal ribbon sign** | | | | | | | | | |
| Absent | 157 (88.7%) | 29 (49.2%) | <0.001[a] | 55 (77.5%) | 13 (44.8%) | 0.001[a] | 31 (79.5%) | 19 (63.3%) | 0.136[a] |
| Present | 20 (11.3%) | 30 (50.8%) | | 16 (22.5%) | 16 (55.2%) | | 8 (20.5%) | 11 (36.7%) | |
| **ELLC** | | | | | | | | | |
| Absent | 163 (92.1%) | 54 (91.5%) | 1.000[b] | 69 (97.2%) | 27 (93.1%) | 0.702[b] | 38 (97.4%) | 25 (83.3%) | 0.103[b] |
| Present | 14 (7.9%) | 5 (8.5%) | | 2 (2.8%) | 2 (6.9%) | | 1 (2.6%) | 5 (16.7%) | |
| **ERL** | | | | | | | | | |
| Absent | 163 (92.1%) | 54 (91.5%) | 1.000[b] | 70 (98.6%) | 27 (93.1%) | 0.416[b] | 38 (97.4%) | 25 (83.3%) | 0.103[b] |
| Present | 14 (7.9%) | 5 (8.5%) | | 1 (1.4%) | 2 (6.9%) | | 1 (2.6%) | 5 (16.7%) | |

The P value represents the univariate analysis; data are presented as n (%). [a], Pearson's chi-square; [b], Yates' correction for continuity; [c], Fisher's exact test; STAS, spread through air spaces; STAS (−), STAS-negative; STAS (+), STAS-positive; cT1mi, tumor with a solid component size of <0.5 cm and an entire tumor size of <3.0 cm; cT1a, tumor with a solid component size of 0.6–1.0 cm and entire tumor size of 0.6–3.0 cm; cT1b, tumor with a solid component size of 1.1–2.0 cm and entire tumor size of 1.1–3.0 cm; cT1b, tumor with a solid component size of 2.1–3.0 cm and an entire tumor size of 2.1–3.0 cm; CTR, consolidation-to-tumor ratio; mGGN, mixed ground-glass nodule; RLL, right lower lobe; RML, right middle lobe; RUL, right upper lobe; LUL, left upper lobe; LLL, left lower lobe; ELLC, emphysema in the lobe of lung cancer; ERL, emphysema in the remaining lobes.
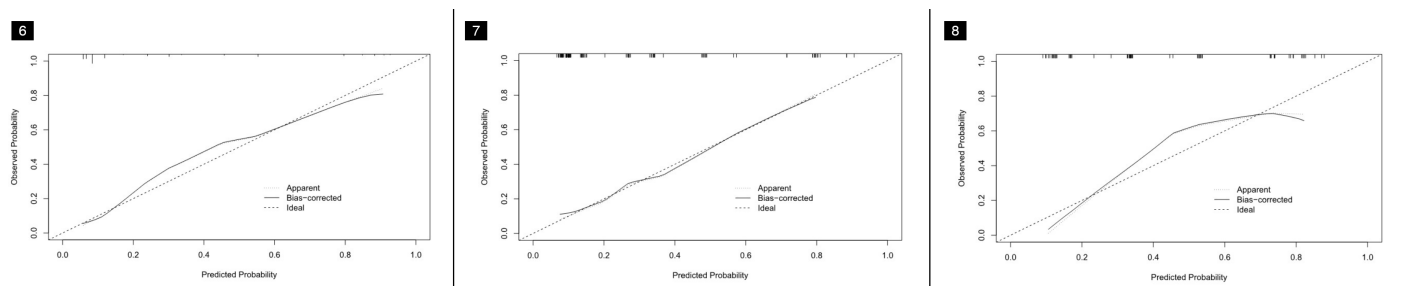


**Figures 6-8.** The calibration curves of the combined model in the three cohorts. (**Figure 6**) The training cohort, (**Figure 7**) the internal validation cohort, and (**Figure 8**) the external validation cohort.

ribbon sign were independent risk factors for predicting the STAS status. The combined model was constructed based on the best combination of variables selected by multivariate logistic regression analysis, including gender, the CEA, CTR, density type, and distal ribbon sign, and had the highest diagnostic efficacy of the models. The AUC values in the training cohort, internal validation cohort, and external validation cohorts were 0.874, 0.822, and 0.810, respectively. The accuracy of the model was 80.51%, 78.00%, and 75.36%, respectively, the sensitivity was 83.05%, 72.41%, and 76.67%, respectively, and the specificity was 79.66%, 80.28%, and 74.36%, respectively.

In the present study, the spiculation sign, pleural indentation sign, and vascular convergence sign were more common in the STAS-positive than in the STAS-negative group; this is consistent with previous lit-
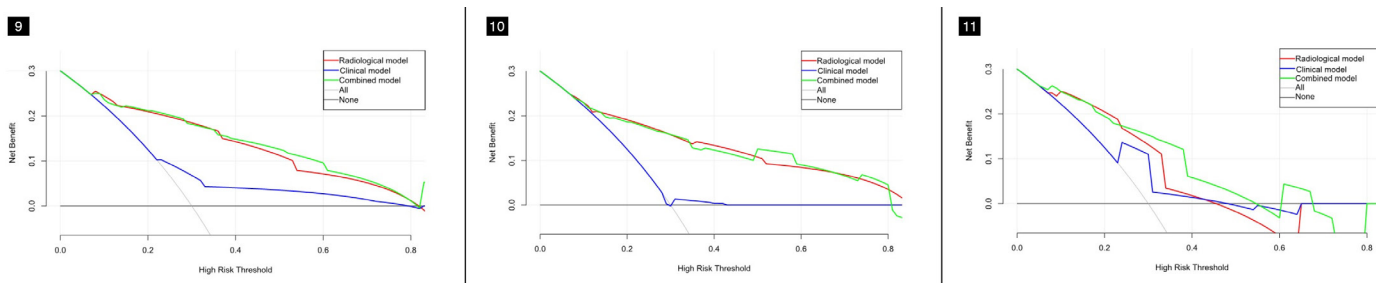


**Figures 9-11.** The decision curve shows that the combined model has better clinical application value than the clinical and radiological models in the three cohorts. **(Figure 9)** The training cohort, **(Figure 10)** the internal validation cohort, and **(Figure 11)** the external validation cohort.

**Table 3.** Univariate and multivariate logistic regression analysis of factors in the training cohort

| Factors | Univariate logistic regression analysis | | Multivariate logistic regression analysis | |
|---|---|---|---|---|
| | OR (95% CI) | P value | OR (95% CI) | P value |
| Gender | 1.993 (1.100–3.638) | 0.023 | 2.100 (0.977–4.585) | 0.058 |
| Smoking status | 2.351 (1.154–4.718) | 0.017 | | |
| CEA | 8.827 (2.821–33.31) | <0.001 | 3.519 (0.826–17.32) | 0.101 |
| Clinical T-stage | 3.576 (2.344–5.684) | <0.001 | | |
| CTR | 15.75 (4.690–98.11) | <0.001 | 4.441 (1.159–29.24) | 0.057 |
| Density type | 14.10 (7.125–29.03) | <0.001 | 6.738 (3.107–15.18) | <0.001 |
| Tumor-lung interface | 2.620 (0.954–6.993) | 0.054 | | |
| Spiculation | 5.462 (2.757–10.99) | <0.001 | | |
| Bronchial change | 1.902 (1.034–3.596) | 0.042 | | |
| Pleural tags | 2.762 (1.493–5.275) | 0.002 | | |
| Pleural indentation | 2.903 (1.592–5.388) | 0.001 | | |
| Vascular convergence | 2.067 (1.007–4.158) | 0.044 | | |
| Halo sign | 8.102 (1.694–57.70) | 0.014 | | |
| Distal ribbon sign | 8.121 (4.114–16.46) | <0.001 | 5.141 (2.272–12.00) | <0.001 |

OR, odds ratio; CI, confidence interval; CEA, carcinoembryonic antigen; CTR, consolidation-to-tumor ratio.

**Table 4.** The predictive efficacy of the clinical, radiological, and combined models in the three cohorts

| Model | Cohort | Cut-off | AUC (95% CI) | Accuracy (%) | Sensitivity (%) | Specificity (%) | PPV (%) | NPV (%) |
|---|---|---|---|---|---|---|---|---|
| Clinical | Training | 0.231 | 0.639 (0.574–0.700) | 61.44% | 61.02% | 61.58% | 34.62% | 82.58% |
| | Internal validation | | 0.505 (0.403–0.607) | 70.00% | 10.34% | 94.37% | 42.86% | 72.04% |
| | External validation | | 0.685 (0.562–0.792) | 68.12% | 70.00% | 66.67% | 61.76% | 74.29% |
| Radiological | Training | 0.113 | 0.862 (0.811–0.903) | 80.08% | 83.05% | 79.10% | 56.98% | 93.33% |
| | Internal validation | | 0.821 (0.731–0.890) | 75.00% | 79.31% | 73.24% | 54.76% | 89.66% |
| | External validation | | 0.738 (0.618–0.836) | 71.01% | 96.67% | 51.28% | 60.42% | 95.24% |
| Combined | Training | 0.264 | 0.874 (0.825–0.914) | 80.51% | 83.05% | 79.66% | 57.65% | 93.37% |
| | Internal validation | | 0.822 (0.733–0.891) | 78.00% | 72.41% | 80.28% | 60.00% | 87.69% |
| | External validation | | 0.810 (0.697–0.894) | 75.36% | 76.67% | 74.36% | 70.00% | 80.56% |

AUC, area under the curve; CI, confidence interval; PPV, positive predictive value; NPV, negative predictive value.

erature reports[19,32] and indicates a possible relation of STAS-positivity to the disease's pathological mechanism. Spiculation is associated with tumor cell infiltration into adjacent blood and lymphatic vessels, suggesting that lung cancer is relatively aggressive;[33] meanwhile, pleural indentation arises from intratumor reactive fibrous hyperplasia, pulling the adjacent pleura and causing deviation from its original position.[34] The vascular convergence sign is also caused by the reactive fibrous hyperplasia of the tumor, which pulls the adjacent pulmonary vessels to converge with the tumor.[35] A relatively high degree of tumor infiltration is associated with serious internal reactive fibroplasia as well as with a higher probability of pleural indenta-tion and vascular convergence, indicating a greater possibility of STAS.

Kim et al.[17] reported that STAS did not exist in the pGGNs of lung adenocarcinoma. The authors of the present study collected 290 patients presenting as pGGNs, none of which were positive for STAS. Therefore, this study excluded patients with pGGNs but included those with mGGNs and solid nodules, which are at potential risk of STAS. The strict inclusion and exclusion criteria promoted an objective prediction efficiency of the model constructed in this study. Yin et al.[36] showed that STAS was more common in lung adenocarcinoma presenting as solid nodules than mGGNs or pGGNs. The results of the present study revealed that the tumor density type was an independent risk factor for predicting STAS. The incidence of STAS in patients with solid nodules showing on CT was 63.4% (85/134), while that of mGGNs was 12.1% (33/271); this is consistent with the results of previous studies.[19,36]

Solid components typically represent the more aggressive part of the tumor.[25] Previous studies have shown a positive correlation between CTR and STAS,[13,14,16,18] and higher CTR values were associated with more aggressive tumors, a higher likelihood of a STAS-positive status, and a worse patient prognosis.[27] In the present study, the STAS-positive rate in the CTR ≥50% group was 36.6% (115/314), and the STAS-positive rate in the CTR <50% group was 3.3% (3/91), indicating a higher STAS incidence in cases with higher solid components showing on CT, which is in agreement with existing research. This study also found that the distal ribbon sign was another independent risk factor for predicting STAS. This can possibly be attributed to tumor cells escaping from the primary lesion, redistributing through the airway, and growing along the surrounding alveolar wall, thus resulting in parenchymal obstruction of the surrounding lung or obstruction of the terminal bronchioles and reducing the gas content in the alveoli.





**Figures 12, 13.** A 58-year-old male patient with lung adenocarcinoma and a positive spread through air spaces status. The sagittal non-contrast computed tomography image shows a solid nodule in the right lower lobe of the lung **(Figure 12)**, consolidation-to-tumor ratio ≥50%, with distal ribbon sign (red arrow), lobulation sign, spiculation sign (yellow arrow), and multiple pleural tags (green arrow). **(Figure 13)** The photomicrograph (hematoxylin and eosin stained, magnification x100) shows detached micropapillary clusters of tumor cells (arrows) in the alveolar beyond the edge (dark line) of the main tumor (star).

Qi et al.[32] proposed for the first time that GG ribbons were an independent risk factor for predicting STAS; a GG ribbon was defined as a band-shaped GGO with a blurred edge emitting from the edge of the nodule and extending into the adjacent lung. This is similar to the distal ribbon sign described in the present study (Figures 12-15). In general, a higher degree of tumor invasion is associated with a higher incidence of STAS, which is indicated by a relatively high proportion of tumor solid components on CT and a relatively high number of malignant radiological features. Lobectomy is recommended for this type of early lung cancer.

The current study found STAS-positivity correlated with gender and the CEA level. Among the patients included in the study, 37.5% (60/160) of male patients and 23.7% (58/245) of female patients were STAS-positive; furthermore, 26.6% (100/376) of patients with CEA <5 μg/L and 62.1% (18/29) of patients with CEA ≥5 μg/L were STAS-positive. The results showed that male patients with lung cancer and CEA ≥5 μg/L had a heightened likelihood of being associated with STAS-positivity; this is similar to the conclusions presented by Jia et al.[23]





**Figures 14, 15.** A 67-year-old female patient with lung adenocarcinoma and a negative spread through air spaces (STAS) status. **(Figure 14)** The axial non-contrast computed tomography image shows a mixed ground-glass nodule in the right lower lobe of the lung, with the longest interface length of the entire tumor and solid component being 1.80 cm and 5.57 mm, respectively; consolidation-to-tumor ratio <50%, with an irregular shape and a well-defined interface. **(Figure 15)** The pathological section indicated a negative STAS status; that is, there were no free tumor cell clusters in the alveolar cavity outside the edge of the main lesion. The photomicrograph (hematoxylin and eosin stained, magnification x40) shows clean alveolar spaces adjacent to the boundary (dashed line) of the tumor (star).

Many previous studies have investigated STAS based on preoperative CT examination;[13-19] however, these studies only included lung adenocarcinoma, and the variables selected to construct the model were mostly based on CT features. The diagnostic efficiency of these models ranged from 0.726 to 0.803, and most of them lacked external validation. Focusing on clinical stage IA NSCLC, this study included a wider spectrum of lung cancer, representing relatively high clinical significance. The best combination of variables selected by multivariate logistic regression analysis included preoperative clinical characteristics and radiological features, and a corresponding clinical model, radiological model, and combined model were constructed, respectively. Moreover, this study adopted a multicenter external dataset, which improved the generalizability of the model. Subsequently, the diagnostic efficacy of the different models was assessed in the three cohorts, indicating that some clinical characteristics and radiological features of patients could be used to predict the STAS status before surgery. The combined model yielded the highest diagnostic efficacy and showed the best clinical application value among the models. Furthermore, a nomogram was drawn to illustrate the complex regression equation of the model in a visual graph, providing an intuitive, easy-to-understand, and convenient method to evaluate patients. The nomogram also guides the accurate judgment of the STAS status before surgery.

The limitations of this study should be acknowledged. First, this research represents a retrospective study, and a degree of selection bias was inevitable. Second, this study only analyzed the clinical characteristics and radiological features of patients, and further studies related to radiomics and artificial intelligence can be performed to explore whether the diagnostic efficiency could be further improved. Third, due to the lack of detailed follow-up data, whether STAS is an independent prognostic factor, as well as its effect on patients undergoing sublobectomy, should be further confirmed; the authors aim to conduct another study in the future when more follow-up data has been collected.

In conclusion, the nomogram presented in this study incorporating clinical characteristics and radiological features allows for the preoperative prediction of the STAS status in patients with clinical stage IA NSCLC and can assist thoracic surgeons in rationally selecting surgical methods.

# References

1. Sung H, Ferlay J, Siegel RL, et al. Global Cancer Statistics 2020: GLOBOCAN estimates of incidence and mortality worldwide for 36 cancers in 185 countries. *CA Cancer J Clin*. 2021;71(3):209-249. [CrossRef]

2. Ettinger DS, Wood DE, Aisner DL, et al. NCCN Guidelines® Insights: non-small cell lung cancer, version 2.2023. *J Natl Compr Canc Netw*. 2023;21(4):340-350. [CrossRef]

3. Saji H, Okada M, Tsuboi M, et al. Segmentectomy versus lobectomy in small-sized peripheral non-small-cell lung cancer (JCOG0802/WJOG4607L): a multicentre, open-label, phase 3, randomised, controlled, non-inferiority trial. *Lancet*. 2022;399(10335):1607-1617. [CrossRef]

4. Suzuki K, Saji H, Aokage K, et al. Comparison of pulmonary segmentectomy and lobectomy: safety results of a randomized trial. *J Thorac Cardiovasc Surg*. 2019;158(3):895-907. [CrossRef]

5. Suzuki K, Watanabe SI, Wakabayashi M, et al. A single-arm study of sublobar resection for ground-glass opacity dominant peripheral lung cancer. *J Thorac Cardiovasc Surg*. 2022;163(1):289-301. [CrossRef]

6. Travis WD, Brambilla E, Nicholson AG, et al. The 2015 World Health Organization Classification of Lung Tumors: Impact of Genetic, Clinical and Radiologic Advances Since the 2004 Classification. *J Thorac Oncol*. 2015;10(9):1243-1260. [CrossRef]

7. Shiono S, Endo M, Suzuki K, Yarimizu K, Hayasaka K, Yanagawa N. Spread through air spaces is a prognostic factor in sublobar resection of non-small cell lung cancer. *Ann Thorac Surg*. 2018;106(2):354-360. [CrossRef]

8. Ren Y, Xie H, Dai C, et al. Prognostic impact of tumor spread through air spaces in sublobar resection for 1A lung adenocarcinoma patients. *Ann Surg Oncol*. 2019;26(6):1901-1908. [CrossRef]

9. Chae M, Jeon JH, Chung JH, et al. Prognostic significance of tumor spread through air spaces in patients with stage IA part-solid lung adenocarcinoma after sublobar resection. *Lung Cancer*. 2021;152:21-26. [CrossRef]

10. Kadota K, Nitadori JI, Sima CS, et al. Tumor spread through air spaces is an important pattern of invasion and impacts the frequency and location of recurrences after limited resection for small stage I lung adenocarcinomas. *J Thorac Oncol*. 2015;10(5):806-814. [CrossRef]

11. Cao L, Jia M, Sun PL, Gao H. Histopathologic features from preoperative biopsies to predict spread through air spaces in early-stage lung adenocarcinoma: a retrospective study. *BMC Cancer*. 2021;21(1):913. [CrossRef]

12. Villalba JA, Shih AR, Sayo TMS, et al. Accuracy and reproducibility of intraoperative assessment on tumor spread through air spaces in stage 1 lung adenocarcinomas. *J Thorac Oncol*. 2021;16(4):619-629. [CrossRef]

13. Zhang Z, Liu Z, Feng H, et al. Predictive value of radiological features on spread through air space in stage cIA lung adenocarcinoma. *J Thorac Dis*. 2020;12(11):6494-6504. [CrossRef]

14. de Margerie-Mellon C, Onken A, Heidinger BH, VanderLaan PA, Bankier AA. CT manifestations of tumor spread through airspaces in pulmonary adenocarcinomas presenting as subsolid nodules. *J Thorac Imaging*. 2018;33(6):402-408. [CrossRef]

15. Qin L, Sun Y, Zhu R, Hu B, Wu J. Clinicopathological and CT features of tumor spread through air space in invasive lung adenocarcinoma. *Front Oncol*. 2022;12:959113. [CrossRef]

16. Li C, Jiang C, Gong J, Wu X, Luo Y, Sun G. A CT-based logistic regression model to predict spread through air space in lung adenocarcinoma. *Quant Imaging Med Surg*. 2020;10(10):1984-1993. [CrossRef]

17. Kim SK, Kim TJ, Chung MJ, et al. Lung adenocarcinoma: CT features associated with spread through air spaces. *Radiology*. 2018;289(3):831-840. [CrossRef]

18. Chen Y, Jiang C, Kang W, et al. Development and validation of a CT-based nomogram to predict spread through air space (STAS) in peripheral stage IA lung adenocarcinoma. *Jpn J Radiol*. 2022;40(6):586-594. [CrossRef]

19. Toyokawa G, Yamada Y, Tagawa T, et al. Computed tomography features of resected lung adenocarcinomas with spread through air spaces. *J Thorac Cardiovasc Surg*. 2018;156(4):1670-1676. [CrossRef]

20. Yanagawa N, Shiono S, Endo M, Ogata SY. Tumor spread through air spaces is a useful predictor of recurrence and prognosis in stage I lung squamous cell carcinoma, but not

in stage II and III. *Lung Cancer*. 2018;120:14-21. [CrossRef]

21. Yokoyama S, Murakami T, Tao H, et al. Tumor spread through air spaces identifies a distinct subgroup with poor prognosis in surgically resected lung pleomorphic carcinoma. *Chest*. 2018;154(4):838-847. [CrossRef]

22. Aly RG, Rekhtman N, Li X, et al. Spread through air spaces (STAS) is prognostic in atypical carcinoid, large cell neuroendocrine carcinoma, and small cell carcinoma of the lung. *J Thorac Oncol*. 2019;14(9):1583-1593. [CrossRef]

23. Jia M, Yu S, Gao H, Sun PL. Spread through air spaces (STAS) in lung cancer: a multiple-perspective and update review. *Cancer Manag Res*. 2020;12:2743-2752. [CrossRef]

24. Dercle L, Fronheiser M, Lu L, et al. Identification of non-small cell lung cancer sensitive to systemic cancer therapies using radiomics. *Clin Cancer Res*. 2020;26(9):2151-2162. [CrossRef]

25. Travis WD, Asamura H, Bankier AA, et al. The IASLC lung cancer staging project: proposals for coding T categories for subsolid nodules and assessment of tumor size in part-solid tumors in the forthcoming eighth edition of the TNM classification of lung cancer. *J Thorac Oncol*. 2016;11(8):1204-1223. [CrossRef]

26. Fan L, Liu SY, Li QC, Yu H, Xiao XS. Multidetector CT features of pulmonary focal ground-glass opacity: differences between benign and malignant. *Br J Radiol*. 2012;85(1015):897-904. [CrossRef]

27. Tu W, Sun G, Fan L, et al. Radiomics signature: a potential and incremental predictor for EGFR mutation status in NSCLC patients, comparison with CT morphology. *Lung Cancer*. 2019;132:28-35. [CrossRef]

28. Hsu JS, Han IT, Tsai TH, et al. Pleural Tags on CT scans to predict visceral pleural invasion of non-small cell lung cancer that does not abut the pleura. *Radiology*. 2016;279(2):590-596. [CrossRef]

29. Kim HJ, Cho JY, Lee YJ, et al. Clinical significance of pleural attachment and indentation of subsolid nodule lung cancer. *Cancer Res Treat*. 2019;51(4):1540-1548. [CrossRef]

30. National Lung Screening Trial Research Team; Church TR, Black WC, et al. Results of initial low-dose computed tomographic screening for lung cancer. *N Engl J Med*. 2013;368(21):1980-1991. [CrossRef]

31. Kadota K, Kushida Y, Kagawa S, et al. Limited resection is associated with a higher risk of locoregional recurrence than lobectomy in stage I lung adenocarcinoma with tumor spread through air spaces. *Am J Surg Pathol*. 2019;43(8):1033-1041. [CrossRef]

32. Qi L, Xue K, Cai Y, Lu J, Li X, Li M. Predictors of CT morphologic features to identify spread through air spaces preoperatively in small-sized lung adenocarcinoma. *Front Oncol*. 2021;10:548430. [CrossRef]

33. Jin C, Cao J, Cai Y, et al. A nomogram for predicting the risk of invasive pulmonary adenocarcinoma for patients with solitary peripheral subsolid nodules. *J Thorac Cardiovasc Surg*. 2017;153(2):462-469. [CrossRef]

34. Gruden JF. What is the significance of pleural tags? *AJR Am J Roentgenol*. 1995;164(2):503-504. [CrossRef]

35. Zhang Y, Qiang JW, Ye JD, Ye XD, Zhang J. High resolution CT in differentiating minimally invasive component in early lung adenocarcinoma. *Lung Cancer*. 2014;84(3):236-241. [CrossRef]

36. Yin Q, Wang H, Cui H, et al. Meta-analysis of association between CT-based features and tumor spread through air spaces in lung adenocarcinoma. *J Cardiothorac Surg*. 2020;15(1):243. [CrossRef]

**Supplementary Table 1.** The definitions of radiological features

| Feature | Definition |
|---|---|
| Tumor size | The longest diameter of the whole tumor at the lung window on the MPR image |
| Solid component size | The longest diameter of the solid component of the tumor at the lung window on the MPR image |
| CTR | The proportion of the solid component part (consolidation-to-tumor ratio, CTR) |
| Location | Lobe of tumor originated from |
| Density | mGGN, presence of ground-glass opacity and solid density component; solid, absence of ground-glass opacity, contains solid density component only |
| Shape | Shape of tumor on the MPR images, including round/oval, irregular shape |
| Tumor-lung interface | Interface of the tumor-lung, including well-defined or ill-defined interface |
| **Marginal characteristics** | |
| Lobulation sign | Petaloid or wavy appearance at the tumor's margins |
| Spiculation sign | Short, thin linear strands radiating around the surface of the tumor without reaching the pleural surface |
| **Internal characteristics** | |
| Vacuole sign | A small air containing space (≤5 mm) in the tumor, referring to lung tissue not invaded by the tumor |
| Cavity or cystic airspace | A larger air containing space (>5 mm) in the tumor because of intratumoral necrosis or represents spared parenchyma, normal or ectatic bronchi, or focal emphysema |
| **External characteristics** | |
| Bronchial change | Air-filled bronchus manifesting as natural, dilated/distorted or cut-off within the lesions, or cut-off at the edge of the lesions |
| Vascular convergence sign | The convergence of pulmonary vessels around the tumor towards the lesion |
| Pleural tags sigh | One or multiple high-density linear strands connecting the tumor margin and the pleura |
| Pleural indentation sigh | The deviation of the pleura from its original position due to tumor traction at the lung window |
| Halo sigh | Ill-defined peripheral ground-glass opacity or consolidation around the tumor, which should be distinguished from the well-defined ground-glass opacity of a part-solid lesion |
| Satellite lesion sigh | Smaller nodules located within 2 cm of the primary tumor |
| Distal ribbon sign | A long, thick ribbon strand extending from the distal part of the tumor into the surrounding lung tissue |
| ELLC | Presence of emphysema in the lobe of lung cancer with visual observation |
| ERL | Presence of emphysema in the remaining lobes with visual observation |

CTR, consolidation-to-tumor ratio; ELLC, emphysema in the lobe of lung cancer; ERL, emphysema in the remaining lobes; MPR, multiplanar reformation.

**Supplementary Table 2.** Consistency analysis of radiological features among observers

| | Kappa (95% CI) | | ICC (95% CI) |
|---|---|---|---|
| Density type | 0.960 (0.931–0.989) | Tumor size (mm) | 0.934 (0.911–0.950) |
| Distal ribbon sign | 0.968 (0.939–0.996) | Solid component size (mm) | 0.935 (0.919–0.947) |
| Shape | 0.887 (0.834–0.941) | | |
| Lobulation | 0.949 (0.912–0.986) | | |
| Spiculation | 0.953 (0.916–0.990) | | |
| Tumor-lung interface | 0.886 (0.803–0.969) | | |
| Bronchial change | 0.925 (0.888–0.962) | | |
| Vacuole sign | 0.963 (0.934–0.992) | | |
| Cavity or cystic airspace | 0.881 (0.800–0.962) | | |
| Vascular convergence | 0.875 (0.817–0.933) | | |
| Halo sign | 0.852 (0.709–0.995) | | |
| Pleural tags | 0.960 (0.933–0.987) | | |
| Pleural indentation | 0.970 (0.947–0.994) | | |
| Satellite lesions | 0.925 (0.859–0.990) | | |
| ELLC | 1.000 | | |
| ERL | 1.000 | | |

CI, confidence interval; ICC, intraclass correlation coefficient; ELLC, emphysema in the lobe of lung cancer; ERL, emphysema in the remaining lobes.

**Supplementary Table 3.** The training cohort included collinearity test of multivariate logistic regression analysis variables

| | Collinearity test statistics | |
|---|---|---|
| | Tolerance | Variance inflation factor |
| Gender | 0.669 | 1.494 |
| Smoking status | 0.664 | 1.505 |
| CEA | 0.873 | 1.146 |
| Clinical T-stage | 0.400 | 2.502 |
| CTR | 0.528 | 1.895 |
| Density type | 0.601 | 1.663 |
| Tumor-lung interface | 0.846 | 1.182 |
| Spiculation | 0.663 | 1.508 |
| Bronchial change | 0.844 | 1.185 |
| Pleural tags | 0.742 | 1.347 |
| Pleural indentation | 0.802 | 1.246 |
| Vascular convergence | 0.758 | 1.319 |
| Halo sign | 0.814 | 1.228 |
| Distal ribbon sign | 0.674 | 1.484 |

CEA, carcinoembryonic antigen; CTR, consolidation-to-tumor ratio.
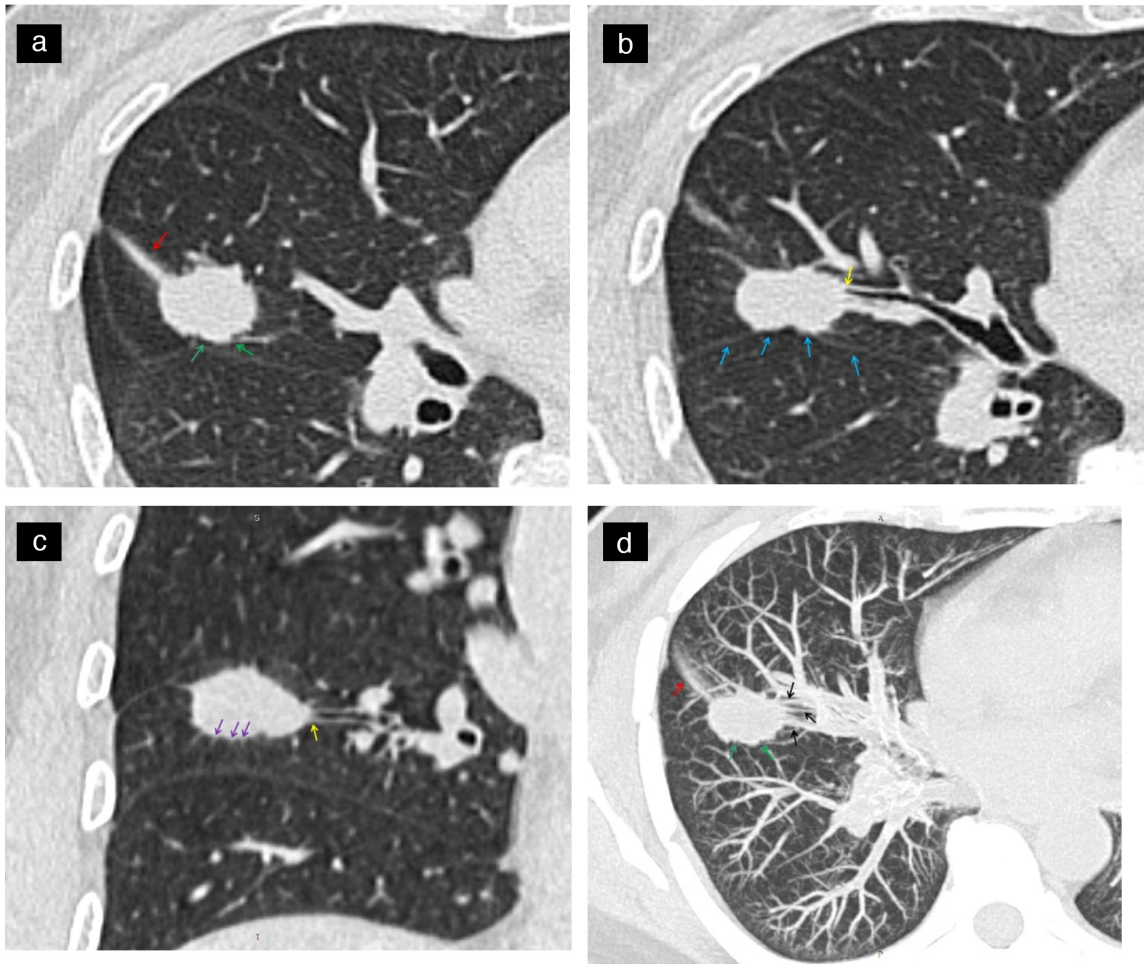
**Supplementary Figure 1.** Show a same patient, a 53-year-old female patient with lung adenocarcinoma and positive STAS status. The axial non-contrast computed tomography shows a solid nodule in the right middle lobe of the lung, CTR ≥50%, with distal ribbon sign (**a**, red arrow), lobulation sigh (**a**, green arrow), interlobar pleura indentation sigh (**b**, blue arrow), bronchial change (**b** and **c**, yellow arrow), spiculation sigh (**c**, purple arrow). The maximal intensity projection **(d)** shows a vascular convergence sign (black arrow), lobulation sigh (green arrow) and distal ribbon sigh (red arrow). STAS, spread through air spaces; CTR, consolidation-to-tumor ratio.
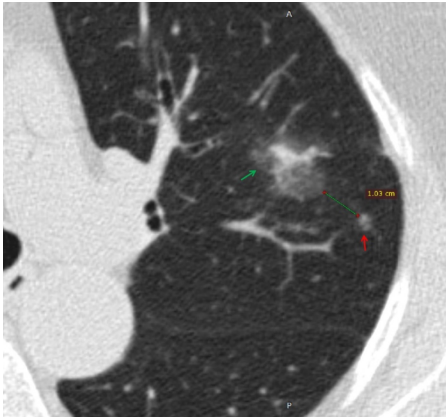
**Supplementary Figure 2.** Shows a 77-year-old female patient with lung adenocarcinoma and negative STAS status. The axial non-contrast computed tomography shows a mixed ground glass nodule in the left upper lobe of the lung (green arrow) with satellite lesion sign (red arrow), the distance between the nodule and the satellite lesion is 1.03 cm. STAS, spread through air spaces.
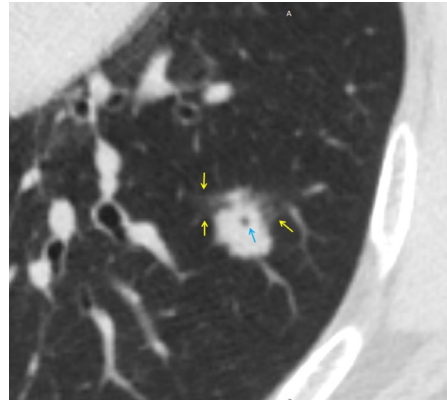
**Supplementary Figure 3.** Shows a 74-year-old male patient with invasive mucinous adenocarcinoma and negative STAS status. The axial non-contrast computed tomography shows a solid nodule in the left lower lobe of the lung with halo sign (yellow arrow) and vacuole sign (blue arrow). STAS, spread through air spaces.
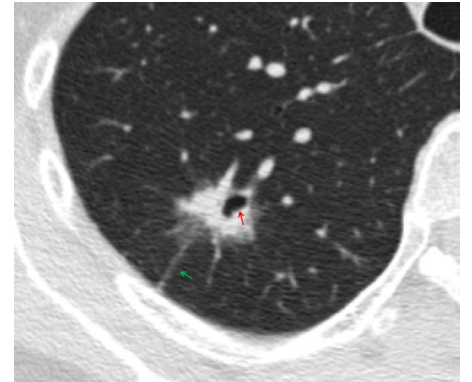
**Supplementary Figure 4.** Shows a 62-year-old female patient with invasive adenocarcinoma and negative STAS status. The axial non-contrast computed tomography shows a mixed ground glass nodule in the right upper lobe of the lung with well-defined interface, pleural tags sigh (green arrow) and cavity or cystic airspace (red arrow). STAS, spread through air spaces.

**HEAD AND NECK IMAGING**

ORIGINAL ARTICLE

# Comparison of image quality and quantitative parameters in intravoxel incoherent motion imaging at 3-T based on turbo spin-echo and echo-planar imaging in patients with oral cancer

Lingjie Yang# 
Xing Wu# 
Yu Wang 
Guangzi Shi 
Huijun Hu* 
Xiaohui Duan* 

**#Lingjie Yang and Xing Wu contributed equally to this work.**

**\*Xiaohui Duan and Huijun Hu are co-corresponding authors and equally contributed to this study.**

From the Department of Radiology (L.Y., X.W., Y.W., G.S., H.H. ✉ huhuijun@mail.sysu.edu.cn, X.D. ✉ duanxh5@mail.sysu.edu.cn), Sun Yat-Sen University, Sun Yat-Sen Memorial Hospital, Guangzhou, China; Guangdong Provincial Key Laboratory of Malignant Tumor Epigenetics and Gene Regulation (G.S., X.D.), Sun Yat-Sen Memorial Hospital, Sun Yat-Sen University, Medical Research Center, Guangzhou, China.

**PURPOSE**

To compare the image quality, apparent diffusion coefficient (ADC), and intravoxel incoherent motion- (IVIM) derived parameters of IVIM imaging based on turbo spin-echo (TSE) and echo-planar imaging (EPI) of patients with oral cancer and to assess the equivalence of the ADC and IVIM-derived parameters.

**METHODS**

Thirty patients with oral cancer underwent TSE-IVIM and EPI-IVIM imaging using a 3.0-T system. The distortion ratio (DR), signal-to-noise ratio (SNR), contrast-to-noise ratio (CNR), qualitative evaluations of image quality, ADC, pure diffusion coefficient (D), pseudo-diffusion coefficient (D*), and perfusion fraction (f) were compared between the two sequences. The consistency of the quantitative parameters in oral cancer between the TSE and EPI sequences was evaluated using a Bland–Altman analysis.

**RESULTS**

TSE-IVIM had a significantly smaller DR than EPI-IVIM ($P < 0.001$). The CNR of EPI-IVIM on most of the anatomical sites was significantly higher than that of TSE-IVIM ($P < 0.05$), while the SNR was not significantly different ($P > 0.05$). TSE-IVIM had significantly higher image quality, less distortion and artifacts, and lower image contrast compared with EPI-IVIM ($P < 0.05$). The lesion-edge sharpness and diagnostic confidence of EPI-IVIM were lower than that of TSE-IVIM, although no significant differences existed ($P > 0.05$). The ADC and D of TSE-IVIM had better reproducibility (intraclass correlation coefficient > 0.9). Although no significant difference existed for the ADC and IVIM-derived parameters of lesions between the two sequences ($P > 0.05$), wide limits of agreement were found in the Bland–Altman plots.

**CONCLUSION**

TSE-IVIM could be used as an alternative technique to EPI-IVIM for patients with oral cancer because of its better image quality. Furthermore, TSE-IVIM can provide more accurate quantitative parameters. However, the quantitative parameters derived from the two IVIM techniques cannot be used as equivalent parameters for patients with oral cancer.

**KEYWORDS**

Echo-planar imaging, image quality, intravoxel incoherent motion imaging, magnetic resonance imaging, oral cancer, quantitative parameters, turbo spin-echo

Oral cancer has become the 16th most common malignancy worldwide, occurring commonly in men of middle or old age in developing countries, with squamous cell carcinomas accounting for more than 90% of cases.[1-3] Diffusion-weighted imaging (DWI) with apparent diffusion coefficient (ADC), which can estimate the diffusion movement of water molecules and reflect the cellular density in tissues,[4-6] has been widely and routinely used in patients with oral cancer.[7,8] However, there is often a failure to distinguish the diffu-

sion of water molecules from the perfusion of capillary blood when using ADC.[9] Multiple *b*-value-based intravoxel incoherent motion (IVIM) is an advanced DWI technique with the parameters of perfusion fraction (*f*), pure diffusion coefficient (D), and pseudo-diffusion coefficient (D*), which can avoid perfusion contamination and evaluate molecular diffusion and blood perfusion effects separately.[10,11] Therefore, IVIM imaging is being increasingly used for tumor detection, diagnosis, differential diagnosis, and prognostic evaluation for oral cancer.[12]

At present, single-shot echo-planar imaging (SS-EPI) is commonly applied for IVIM sequences, with the advantages of a rapid image acquisition speed and a relative insensitivity to motion.[13] Nevertheless, because of the complex structure of many air–bone boundaries and the presence of metallic dental implants in the head and neck, signal loss and geometric distortion are commonly found with SS-EPI due to the susceptibility artifacts and chemical shift artifacts in the phase-encoding direction,[14,15] which may result in a deterioration of image quality and a reduction in the diagnostic confidence of oral lesions. Alternatively, the single-shot turbo spin-echo (SS-TSE) uses multiple radiofrequency (RF) refocusing pulses, resulting in less susceptibility to artifacts and geometric distortions.[16] However, it commonly has the disadvantages of a lower signal-to-noise ratio (SNR) and a longer acquisition time.[17]

Recently, TSE-DWI sequences in 3-T magnetic resonance imaging (MRI) can shorten the scan time and obtain a higher SNR and less blurring through the reduction of echo space with the adoption of an appropriate RF pulse shape.[18] Some studies have reported that TSE-DWI had better image quality than EPI-DWI in breast cancer,[17] pulmonary lesions,[19] and orofacial lesions.[14,20] In addition, a preliminary study compared the image qual-

### Main points

- Turbo spin-echo (TSE)- intravoxel incoherent motion (IVIM) had better image quality in the oral and maxillofacial regions and could be used as an alternative technique to echo-planar imaging (EPI)-IVIM for patients with oral cancer.

- TSE-IVIM can provide more accurate parameter values, especially for the apparent diffusion coefficient and D values.

- The quantitative parameters acquired from TSE-IVIM and EPI-IVIM imaging cannot be used as equivalent parameters for the diagnosis and follow-up of oral cancer.

ity and the quantitative parameters derived from IVIM between the two IVIM sequences in a group of healthy volunteers' head and neck regions.[21] However, to our knowledge, comprehensive evaluation (including quantitative and qualitative) of image quality and comparisons of ADC, D, D*, and *f* between TSE-IVIM and EPI-IVIM in both oral lesions and normal anatomies of the head and neck have not been reported.

Thus, in this study, we evaluated and compared the geometric distortion, SNR, contrast-to-noise ratio (CNR), image quality, and ADC and IVIM-derived parameters in normal anatomies and oral lesions of TSE-IVIM and EPI-IVIM. The purpose of this study was to demonstrate whether TSE-IVIM can become an alternative technique to EPI-IVIM for patients with oral cancer and to determine the equivalence of these quantitative parameters.

## Methods

### Patients

The Ethics Committee of Sun Yat-Sen Memorial Hospital, Sun Yat-Sen University (SY-SEC-KY-KS-2022-029; 2022.01.19) approved this prospective study, and signed informed consent was given by all subjects. Patients with oral cancer requiring MR examination of the head and neck region prior to operation between May 2021 and December 2021 were included in our study. The exclusion criteria were as follows: (1) patients who had undergone a lesion biopsy before MRI; (2) patients who had a resection of the parotid gland, submandibular gland, or tongue; (3) patients who had contraindications for MR examinations that would affect the examination; or (4) patients in the early stage of pregnancy (less than 3 months). Finally, 30 patients, 19 (63.33%) males and 11 (36.67%) females, were included in this study. The mean age was 54 ± 10 years. Among them were 18 (60.00%) tongue carcinomas, 3 (10.00%) oral floor carcinomas, 3 (10.00%) gingiva carcinomas, 2 (6.67%) buccal carcinomas, 2 (6.67%) palate carcinomas, 1 (3.33%) oropharyngeal carcinoma, and 1 (3.33%) tonsil carcinoma.

### Imaging protocol

All patients underwent MR examination using a 3-T MR system (Ingenia Digital Network Architecture 3.0 T, Philips Healthcare, Best, the Netherlands) with a 20-channel head and neck coil. SS-TSE- and SS-EPI-based IVIM sequences were executed consecutively in each examination. We used the same scan-

ning parameters for the two IVIM sequences as far as it was feasible. In addition, 12 b values of 0, 20, 30, 50, 80, 100, 200, 500; 1,000; 1,500; 2,000, and 2,500 s/mm² were applied to the two IVIM sequences. The phase-encoding direction of both sequences was horizontal [left–right (LR)]. The scanning parameters of the two IVIM sequences and T2WI are shown in Table 1.

### Data analysis

#### Image quality

Two experienced radiologists (S.G.Z. and D.X.H., with 6 and 10 years' experience in head and neck radiology, respectively), who were blinded to the scanning sequences and clinical information, independently performed quantitative and qualitative evaluations of the images' quality. The axial images of TSE-IVIM and EPI-IVIM with *b* = 1,000 s/mm² were selected and analyzed.

For the quantitative evaluation of image distortion, we calculated the distortion ratio (DR) at the level of the oral floor on the axial images of two IVIM images in comparison with that of axial TSE-T2WI images. We selected a representative slice level of the oral floor and displayed the TSE-IVIM, EPI-IVIM, and TSE-T2WI images on the same layer. Then, the LR width and anterior–posterior (AP) length of the whole image on transverse sections were measured on these three sequences. The DR was defined as the following equation:

$$DR = \frac{|A-B|}{B} \times 100\% , \qquad (1)$$

where A is the anteroposterior or transverse diameter of the IVIM image and B is the anteroposterior or transverse diameter of the TSE-T2WI image. The DRs in both the LR and AP direction were calculated respectively.

The SNR and CNR were calculated for several normal anatomies and lesions on two kinds of IVIM images. The circular regions of interest (ROI) were placed in the bilateral parotid glands, bilateral submandibular glands, soft palate, tongue, oral floor, buccal mucosa soft tissue, lesion, and the muscles close to each organ, and the size of the ROIs was about 50 pixels. The mean and standard deviation (SD) of the signal intensity (SI) in each ROI were recorded. All ROIs of normal anatomical sites were delineated to avoid blood vessels, gland ducts, and lesions. For the measurements of CNR, adjacent muscles were used as the reference tissue. The SNR and CNR of each ROI were calculated as the following equations:

$$SNR = SI_a/SD_a \, , \qquad (2)$$

$$CNR = |SI_a - SI_{muscle}|/SD_{muscle} \, , \qquad (3)$$

where $SI_a$ and $SD_a$ represent the mean and SD of the SI in the normal anatomies or lesions, and $SI_{muscle}$ and $SD_{muscle}$ represent the mean and SD of the SI in the adjacent muscles.[20,21]

A 5-point scale was applied to qualitatively assess image quality, including image distortion, lesion-edge sharpness, image contrast, artifacts, overall image quality, and diagnostic confidence. Image distortion was recorded as follows: 1 = severe; 2 = obvious; 3 = moderate; 4 = slight; and 5 = no image distortion. Lesion-edge sharpness and image contrast for a normal anatomy were evaluated as follows: 1= unreadable; 2 = doubtful; 3 = moderate; 4 = good; and 5 = obvious. Chemical shift artifacts and susceptibility artifacts were evaluated, respectively, as follows: 1 = artifacts occur in the lesion and affect diagnosis; 2 = artifacts occur in more than three regions but do not affect the diagnosis; 3 = artifacts occur in three regions and do not affect the diagnosis; 4 = artifacts occur in less than three regions and do not affect the diagnosis; and 5 = almost no artifacts. Diagnostic confidence and overall image quality were scored as follows: 1 = not diagnostic; 2 = poor; 3 = moderate; 4 = good; and 5 = excellent.

### ADC and quantitative parameters derived from IVIM

The ADC maps for this study were reconstructed using IntelliSpace Portal (version 9.0, Philips Healthcare), and the IVIM-derived parameter maps were generated by MITK-Diffusion (German Cancer Research Center, Germany).

Two radiologists delineated the ROIs in the bilateral parotid glands, bilateral submandibular glands, soft palate, tongue, oral floor, fat, muscle, and lesions on the ADC, D, D*, and f maps. The ROI of fat was set in the buccal area at the level of the tongue, and the sternocleidomastoid at the same level was designated as the ROI of the muscle. The ROIs were delineated to the maximum possible sizes to avoid blood vessels, gland ducts, and lesions. The ADC values were measured on each ADC parameter map by placing circular regions of multiple anatomical structures and lesions. A biexponential fit model was applied to calculate D, D*, and f according to a previous study.[21]

### Statistical analysis

MedCalc (version 20.0, Mariakerke, Belgium) and SPSS (Version 25.0, IBM Corporation) software were used for all statistical analysis, with $P < 0.05$ representing statistical significance. Normally distributed data are expressed as mean ± SD, non-normally distributed data are displayed as median (minimum–maximum), and categorical variables are presented as frequencies with percentages. The qualitative evaluations and parameters of TSE-IVIM and EPI-IVIM were compared by using a paired Student's t-test and the Wilcoxon signed rank test. Interobserver agreement for continuous variables was estimated using the intraclass correlation coefficient (ICC). The levels of interobserver agreement were assessed as follows: 0–0.50 = poor, 0.51–0.75 = moderate, 0.76–0.90 = good, and 0.91–1.00 = excellent.[11] Additionally, the interobserver agreement of categorical variables was assessed using Kappa statistics: poor (0–0.20), fair (0.21–0.40), moderate (0.41–0.60), good (0.61–0.80), and excellent (0.81–1.00).[18] Furthermore, the consistency of the qualitative parameters of lesions between the two IVIM sequences was evaluated using a Bland–Altman analysis with 95% limits of agreement (LoA).

## Results

### Comparison of distortion ratio

The interobserver agreement of DRs was good ($P < 0.05$). The ICCs of DRs in the direction of LP and AP were 0.819 (TSE-IVIM) and 0.764 (EPI-IVIM), and 0.819 (TSE-IVIM) and 0.779 (EPI-IVIM), respectively. The mean DRs in the LR direction in TSE-IVIM and EPI-IVIM were 11.4% ± 5.1% and 15.1% ± 5.2%, and the mean DRs in the AP direction in TSE-IVIM and EPI-IVIM were 9.93% ± 2.65% and 11.8% ± 2.65%, respectively. Compared with EPI-IVIM, the DRs in both directions were significantly lower in TSE-IVIM ($P < 0.001$) (Figure 1), and the difference was more significant in the direction of LR, which was the phase-encoding direction.

### Comparison of SNR and CNR

The SNR values showed good agreement between the two observers (ICC: 0.825 in TSE-IVIM and 0.829 in EPI-IVIM, $P < 0.05$), and the CNR values showed good to excellent agreement (ICC: 0.962 in TSE-IVIM and 0.873 in EPI-IVIM, $P < 0.05$). As shown in Table 2, no significant differences in SNR existed between the two IVIM sequences ($P > 0.05$) in the normal anatomical sites and the lesions. However, EPI-IVIM had significantly higher CNRs in the tongue, oral floor, buccal mucosa soft tissue, parotid glands, submandibular glands, and lesion compared with TSE-IVIM ($P < 0.05$), while no significant difference of the CNRs in the soft palate was found between the two IVIM techniques ($P = 0.417$).

### Comparison of qualitative evaluations

Moderate to excellent interobserver agreements of the qualitative evaluations were obtained ($P < 0.05$). The Kappa values were 0.783 (TSE-IVIM) and 0.684 (EPI-IVIM) for image distortion, 0.896 (TSE-IVIM) and 0.906 (EPI-IVIM) for lesion-edge sharpness, 0.563 (TSE-IVIM) and 0.604 (EPI-IVIM) for image contrast, 0.851 (TSE-IVIM) and 0.819 (EPI-

**Table 1.** The scanning parameters of T2WI, SS-TSE-IVIM, and SS-EPI-IVIM

|  | T2WI | SS-TSE-IVIM | SS-EPI-IVIM |
|---|---|---|---|
| TR/TE (ms) | 2906/90 | 4488/89 | 5037/81 |
| FOV (mm²) | 230 × 230 | 230 × 230 | 230 × 230 |
| Matrix size | 252 × 160 | 92 × 92 | 92 × 92 |
| Voxel size (mm) | 0.79 × 1.44 | 2.5 × 2.5 | 2.5 × 2.5 |
| Reconstruction voxel size (mm) | 0.53 × 0.53 | 0.96 × 0.96 | 0.8 × 0.8 |
| SENSE factor | / | 3.5 | 3.5 |
| TSE/EPI factor | 20 (TSE) | 53 (TSE) | 23 (EPI) |
| Slice thickness (mm) | 5 | 5 | 5 |
| Interlayer spacing (mm) | 0.5 | 1 | 1 |
| Flip angle | 90° | 90° | 90° |
| Bandwidth (Hz/pixel) | 698.6/0.6 | 652.7/0.7 | 68.0/6.4 |
| NSA | 2 | 2 | 2 |
| Acquisition time | 1 min 38 s | 10 min 55 s | 10 min 19 s |

IVIM, intravoxel incoherent motion; SS-TSE, single-shot turbo spin echo; SS-EPI, SS echo-planar imaging; TR, repetition time; TE, echo time; FOV, field of view; NSA, number of signal averaged.

IVIM) for diagnostic confidence, 0.873 (TSE-IVIM) and 0.907 (EPI-IVIM) for chemical shift artifacts, 0.750 (TSE-IVIM) and 0.634 (EPI-IVIM) for susceptibility artifacts, and 0.561 (TSE-IVIM) and 0.648 (EPI-IVIM) for overall image quality. The mean scores of the qualitative evaluations of image quality on TSE-IVIM and EPI-IVIM are shown in Figure 2. TSE-IVIM had significantly less image distortion, chemical shift artifacts, and susceptibility artifacts than EPI-IVIM ($P < 0.001$). The lesion-edge sharpness and diagnostic confidence of EPI-IVIM were lower than for TSE-IVIM, although no significant differences existed ($P > 0.05$). EPI-IVIM had significantly higher image contrast than TSE-IVIM ($P < 0.05$), although TSE-IVIM had significantly higher overall image quality than EPI-IVIM ($P < 0.001$). Representative IVIM images are presented in Figures 3, 4.

### Comparison of ADC and quantitative parameters derived from IVIM

The ICCs of ADC and IVIM-derived parameters in the normal anatomical sites and lesions on TSE-IVIM and EPI-IVIM are shown in Table 3. Good to excellent interobserver

agreement was found for ADC, and the interobserver agreement for TSE was similar to that for EPI. The interobserver agreement of D was moderate to excellent, and the interobserver agreement of TSE was better than that of EPI. The measurement consistency of D* and $f$ was relatively poor. The interobserver agreement for D* was moderate to good, and no obvious difference existed between TSE and EPI. The interobserver agreement for $f$ was moderate to excellent, and no obvious difference existed between TSE and EPI.

Table 3 summarizes the mean ADC, D, D*, and $f$ values derived from the two IVIMs. No significant differences in the values of ADC, D, D*, and $f$ were found in lesions and fat ($P > 0.05$). The ADC values of the right parotid gland, right submandibular gland, and oral floor were not significantly different between the two sequences ($P > 0.05$). The ADC values of the soft palate in EPI-IVIM were lower than those in TSE-IVIM ($P = 0.033$). In addition, EPI-IVIM had higher ADC values than TSE-IVIM in other parts ($P < 0.05$). The D values of the tongue and oral floor were not significantly different between the two

sequences ($P > 0.05$). The D values of EPI-IVIM were higher than those of TSE-IVIM in other parts except the soft palate, which was lower in EPI-IVIM ($P < 0.05$). The D* values of the parotid glands, soft palate, and muscle in TSE-IVIM and EPI-IVIM were not significantly different ($P > 0.05$). However, in the other parts, D* of EPI-IVIM exhibited higher values than for TSE-IVIM ($P < 0.05$). The $f$ values for the oral floor, submandibular glands, and parotid glands were not significantly different between the two sequences ($P > 0.05$). The $f$ values of the soft palate and tongue were higher for TSE-IVIM than EPI-IVIM, while the $f$ values of muscle were higher for EPI-IVIM ($P < 0.05$).

As shown in Figure 5, the Bland–Altman plots exhibit a consistency in the quantitative parameters for lesions between the two IVIM sequences. The 95% LoAs were −1.12 to 1.53 for ADC, −0.84 to 0.70 for D, −32.0 to 31.7 for D*, and −27.5 to 27.8 for $f$. No fixed biases between the two sequences were found regarding ADC ($P = 0.107$), D ($P = 0.341$), D* ($P = 0.949$), or $f$ ($P = 0.952$) values for lesions. However, the 95% LoAs shown in the plots were wide between TSE-IVIM and EPI-IVIM.

## Discussion

Our results demonstrated that TSE-IVIM had significantly less image distortion, chemical-shift artifacts, and susceptibility artifacts than EPI-IVIM in patients with oral cancer. TSE-IVIM had better lesion-edge sharpness and higher diagnostic confidence than EPI-IVIM, although no statistical differences existed. SNR had no significant differences, while EPI-IVIM had significantly higher CNR on most anatomical structures and lesions in comparison with TSE-IVIM, indicating that EPI-IVIM had significantly higher image contrast than TSE-IVIM. On the whole, TSE-IVIM
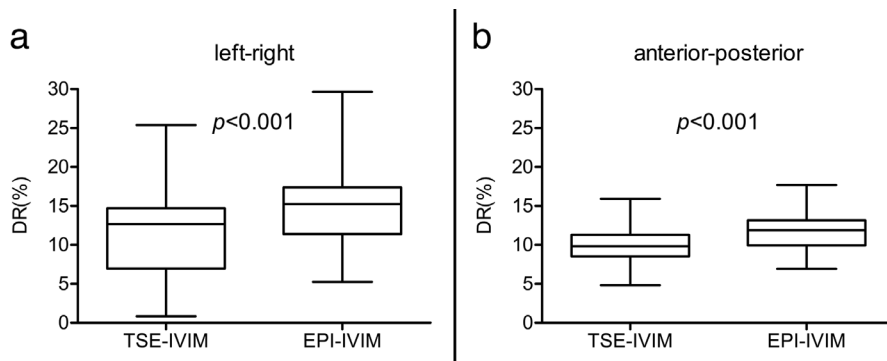


**Figure 1.** Box-and-whisker plots for the distortion ratios (DRs) of turbo spin-echo intravoxel incoherent motion (TSE-IVIM) and echo-planar imaging (EPI) IVIM. The DRs of the **(a)** left–right width and **(b)** anterior–posterior length were significantly lower in the images of TSE-IVIM than in those of EPI-IVIM ($P < 0.001$ by paired Student's t-test).

**Table 2.** The SNR and CNR on TSE-IVIM and EPI-IVIM

| | SNR (n = 30) | | | CNR (n = 30) | | |
|---|---|---|---|---|---|---|
| | TSE-IVIM | EPI-IVIM | P | TSE-IVIM | EPI-IVIM | P |
| Parotid gland (L) | 8.9 (5.3–19.9) | 9.2 (6.2–24.7) | 0.072 | 1.9 (0.3–7.2) | 4.3 (0.2–20.2) | 0.004 |
| Parotid gland (R) | 9.0 (4.4–16.0) | 8.3 (3.8–18.7) | 0.165 | 2.1 (0.1–11.1) | 4.9 (0.3–35.6) | 0.003 |
| Submandibular gland (L) | 9.1 (5.9–19.1) | 8.0 (4.9–19.9) | 0.309 | 4.4 (0.2–17.9) | 7.0 (1.5–29.2) | <0.001 |
| Submandibular gland (R) | 9.8 (5.8–23.2) | 9.4 (5.1–28.2) | 0.673 | 3.4 (0.3–15.5) | 6.4 (0.2–29.5) | <0.001 |
| Soft palate | 6.3 (4.0–12.7) | 7.2 (3.0–12.7) | 0.734 | 5.5 (1.5–12.3) | 4.9 (0.5–14.8) | 0.417 |
| Tongue | 7.7 (4.0–13.1) | 7.8 (3.5–16.4) | 0.098 | 3.1 (0.2–6.9) | 5.0 (1.1–10.8) | 0.002 |
| Oral floor | 8.2 (3.9–15.6) | 6.7 (4.5–10.8) | 0.185 | 1.2 (0.2–7.2) | 3.9 (0.2–25.8) | <0.001 |
| Buccal mucosa soft tissue | 9.0 (3.5–12.7) | 7.6 (3.9–12.5) | 0.199 | 0.8 (0.2–15.5) | 1.3 (0.1–19.8) | 0.047 |
| Lesion | 10.6 (6.9–36.0) | 10.8 (4.1–32.5) | 0.517 | 13.1 (1.5–70.9) | 16.2 (1.5–109.7) | 0.037 |

Data are presented as median (minimum–maximum). IVIM, intravoxel incoherent motion; TSE, turbo spin echo; EPI, echo-planar imaging; SNR, signal-to-noise ratio; CNR, contrast-to-noise ratio.

had better overall image quality than EPI-IVIM. The ADC and D values showed good interobserver agreement, while the measurement consistency of D* and f was poor. Moreover, TSE-IVIM exhibited higher measurement consistency of ADC and D than EPI-IVIM. Additionally, although no fixed bias existed for the ADC, D, D*, and f values of lesions between the two sequences, the Bland–Altman plots showed wide 95% LoAs.

Clinically, SS-EPI is the most commonly used technique for IVIM sequences. However, artifacts and geometric distortions in EPI-IVIM are usually prominent in patients with oral cancer because of the presence of air–tissue interfaces or metallic implants in the oral and maxillofacial region, which may negatively impact on the reproducibility and reliability of IVIM and the derived quantitative parameters.[10] Theoretically, artifacts and geometric distortions in EPI sequences are prone to arise in the phase-encoding direction because of the acquisition of each echo at a different echo time and the accumulation of phase errors caused by rotating protons without RF refocusing pulses. In contrast, TSE sequences acquire multiple echoes at each excitation and apply RF refocusing pulses to reduce magnetic field inhomogeneity and avoid the accumulation of phase errors; hence, TSE sequences usually have less image distortion, chemical shift artifacts, and susceptibility artifacts than EPI sequences.[14,18] In our study, TSE-IVIM showed better image quality on account of lower levels of image distortion and artifacts than EPI-IVIM, which was in agreement with previous studies on the head and neck region[14,20,22] and the whole body.[23] The artifacts within and around the lesions in EPI-IVIM images could reduce the lesion-edge sharpness and diagnostic confidence for oral cancer. Therefore, the reduction of image distortion and artifacts using TSE-IVIM may facilitate a better diagnostic confidence for oral cancer.

As for SNR and CNR, previous studies have shown that TSE-DWI had inherently lower SNR in comparison with EPI-DWI as a result of multiple RF refocusing pulses.[13,22,24] Nevertheless, some studies had opposite results, with significantly higher SNR and CNR occurring in TSE-DWI compared with in EPI-DWI.[20,21] Shorter RF pulses owing to the adjustment of RF pulse shape can contribute to higher SNR and less blurring in TSE-DWI. In the present study, IVIM and EPI-IVIM showed similar SNRs; this is different to the aforementioned studies but consistent with some reports that showed both sequences had comparable SNRs in the lung.[19,25] However, EPI-IVIM had higher CNR in comparison with TSE-IVIM in our study, which was oppositive to the reports in previous studies.[20,21] These differences might have resulted from the higher noise (SD value) of TSE-IVIM in comparison with that of EPI-IVIM in our study. Various parameters of image acquisition, including the voxel size, receiver bandwidth, and number of signal averaged (NSA), can affect image noise.[26,27] In our study, the voxel size and NSA of the two sequences were the same, while the TSE-IVIM sequence had an obviously wider bandwidth (932.4 Hz/pixel) than EPI-IVIM (10.6 Hz/pixel). The wider bandwidth in TSE-IVIM leads to greater image noise.[24] In contrast, the bandwidth of TSE-IVIM in previous studies was smaller than that seen in EPI-IVIM, thus inducing the lower noise of TSE-IVIM.[20,21] According to the formulae of SNR and CNR in our study, the higher SI and the higher level of noise in TSE-IVIM resulted in a similar SNR to that of EPI-IVIM, and the larger amount of noise of the adjacent muscles used as the reference tissue led to a lower CNR in TSE-IVIM.
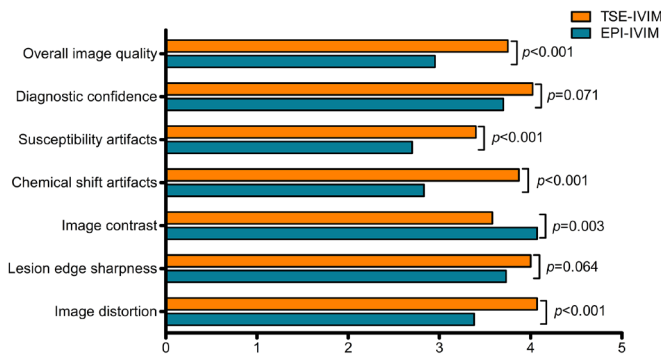


**Figure 2.** Bar chart showing the mean scores of qualitative evaluations of image quality for turbo spin-echo intravoxel incoherent motion (TSE-IVIM) and echo-planar imaging (EPI) IVIM images. The *P* values acquired using Wilcoxon's signed rank test are shown on the right side for comparison of the two sequences.



**Figure 3. (a)** T2WI fat-suppressed, **(b)** turbo spin-echo intravoxel incoherent motion (TSE-IVIM) b1000, and **(c)** echo-planar imaging (EPI) IVIM b1000 of a 58-year-old man with squamous cell carcinoma on the left tongue edge. The lesion on **(b)** TSE-IVIM b1000 is shown in accordance with **(a)** T2WI fat-suppressed. However, obvious geometric distortion of lesion (arrowheads) is seen on **(c)** EPI-IVIM b1000 compared with that on **(b)** TSE-IVIM b1000.
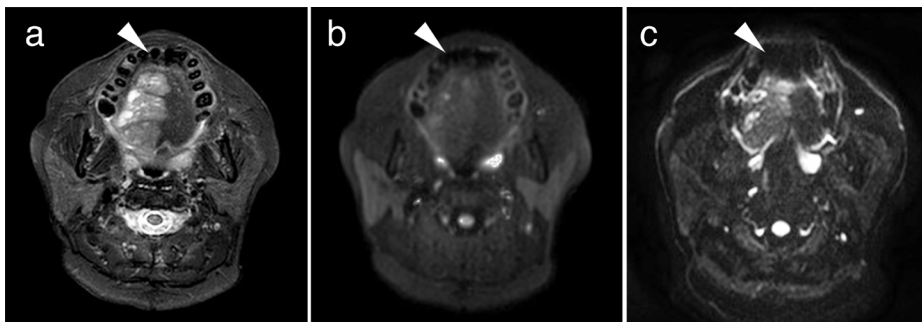


**Figure 4. (a)** T2WI fat-suppressed, **(b)** turbo spin-echo intravoxel incoherent motion (TSE-IVIM) b1000, and **(c)** echo-planar imaging (EPI) IVIM b1000 of a 54-year-old female with squamous cell carcinoma on the right half of the tongue. **(c)** EPI-IVIM b1000 has more susceptibility artifacts (arrowheads), which affect the display of some parts of the lesion, in comparison with **(b)** TSE-IVIM b1000. However, the lesion in **(c)** EPI-IVIM b1000 shows higher contrast than that in **(b)** TSE-IVIM b1000.

**Table 3.** The ADC and IVIM-derived parameters and their ICCs on TSE-IVIM and EPI-IVIM

| | ADC (×10⁻³ mm²/s) (n = 30) | | | D (×10⁻³ mm²/s) (n = 30) | | | D* (×10⁻³ mm²/s) (n = 30) | | | f (%) (n = 30) | | |
|---|---|---|---|---|---|---|---|---|---|---|---|---|
| | TSE-IVIM (ICC) | EPI-IVIM (ICC) | P | TSE-IVIM (ICC) | EPI-IVIM (ICC) | P | TSE-IVIM (ICC) | EPI-IVIM (ICC) | P | TSE-IVIM (ICC) | EPI-IVIM (ICC) | P |
| Parotid gland (L) | 1.38 ± 0.62 (0.990*) | 1.56 ± 0.52 (0.991*) | 0.017 | 0.30 ± 0.13 (0.943*) | 0.45 ± 0.11 (0.678*) | <0.001 | 44.02 ± 13.82 (0.840*) | 40.74 ± 12.95 (0.721*) | 0.262 | 22.49 ± 5.49 (0.751*) | 24.22 ± 5.78 (0.621*) | 0.318 |
| Parotid gland (R) | 1.36 ± 0.67 (0.994*) | 1.78 ± 1.91 (0.995*) | 0.441 | 0.28 ± 0.14 (0.938*) | 0.33 ± 0.14 (0.660*) | 0.001 | 42.62 ± 15.94 (0.745*) | 49.65 ± 18.80 (0.763*) | 0.079 | 25.77 ± 7.84 (0.692*) | 28.37 ± 6.65 (0.732*) | 0.165 |
| Submandibular gland (L) | 1.74 ± 0.62 (0.994*) | 2.01 ± 0.58 (0.987*) | 0.001 | 0.41 ± 0.17 (0.947*) | 0.60 ± 0.26 (0.927*) | <0.001 | 31.76 ± 9.19 (0.835*) | 36.87 ± 11.67 (0.732*) | 0.047 | 34.25 ± 10.46 (0.736*) | 30.91 ± 8.52 (0.812*) | 0.052 |
| Submandibular gland (R) | 1.88 ± 0.67 (0.994*) | 2.01 ± 0.56 (0.997*) | 0.162 | 0.43 ± 0.14 (0.873*) | 0.62 ± 0.18 (0.891*) | <0.001 | 25.73 ± 8.14 (0.751*) | 39.46 ± 16.20 (0.639*) | 0.001 | 35.82 ± 8.16 (0.910*) | 32.36 ± 10.57 (0.692*) | 0.079 |
| Soft palate | 1.41 ± 0.50 (0.996*) | 1.18 ± 0.48 (0.995*) | 0.033 | 0.34 ± 0.12 (0.918*) | 0.30 ± 0.17 (0.927*) | 0.016 | 56.77 ± 19.16 (0.826*) | 57.45 ± 15.36 (0.566*) | 0.959 | 29.31 ± 8.95 (0.730*) | 26.04 ± 8.44 (0.771*) | 0.032 |
| Tongue | 1.04 ± 0.54 (0.977*) | 0.73 ± 0.52 (0.965*) | <0.001 | 0.19 ± 0.12 (0.843*) | 0.16 ± 0.13 (0.896*) | 0.067 | 43.99 ± 15.82 (0.818*) | 60.52 ± 19.05 (0.623*) | <0.001 | 29.67 ± 6.23 (0.751*) | 24.40 ± 8.30 (0.548*) | 0.002 |
| Oral floor | 0.92 ± 0.37 (0.992*) | 1.02 ± 0.46 (0.993*) | 0.178 | 0.14 ± 0.06 (0.936*) | 0.20 ± 0.16 (0.901*) | 0.417 | 40.93 ± 13.74 (0.769*) | 55.03 ± 19.09 (0.869*) | <0.001 | 29.81 ± 6.84 (0.650*) | 27.94 ± 8.40 (0.859*) | 0.159 |
| Fat | 0.19 ± 0.11 (0.978*) | 0.18 ± 0.15 (0.976*) | 0.168 | 0.06 ± 0.02 (0.844*) | 0.08 ± 0.05 (0.672*) | 0.276 | 74.98 ± 11.54 (0.602*) | 72.08 ± 17.79 (0.868*) | 0.719 | 16.39 ± 5.05 (0.662*) | 16.56 ± 7.45 (0.916*) | 0.750 |
| Muscle | 0.39 ± 0.27 (0.922*) | 0.84 ± 0.51 (0.892*) | <0.001 | 0.11 ± 0.08 (0.906*) | 0.21 ± 0.11 (0.772*) | <0.001 | 62.27 ± 17.68 (0.611*) | 60.21 ± 15.90 (0.706*) | 0.644 | 19.69 ± 6.65 (0.722*) | 25.29 ± 5.80 (0.741*) | 0.001 |
| Lesion | 2.37 ± 0.88 (0.983*) | 2.16 ± 0.80 (0.977*) | 0.086 | 0.66 ± 0.19 (0.916*) | 0.73 ± 0.35 (0.595*) | 0.376 | 29.52 ± 14.09 (0.812*) | 29.70 ± 13.83 (0.816*) | 0.894 | 27.07 ± 11.17 (0.762*) | 26.91 ± 10.36 (0.861*) | 0.600 |

*P < 0.05. Data are presented as mean ± standard deviation. ICC, intraclass correlation coefficient; IVIM, intravoxel incoherent motion; TSE, turbo spin echo; EPI, echo-planar imaging; ADC, apparent diffusion coefficients; D, pure diffusion coefficients; D*, pseudo-diffusion coefficient; f, perfusion fraction.

In terms of the reproducibility of ADC, D, D*, and f, we found that the interobserver agreements for ADC and D were satisfactory, indicating that ADC and D were robust parameters in the head and neck region, while D* and f had relatively poor reproducibility and high observer variability based on the lower ICC in both the TSE and EPI sequences, which was in accordance with many previous studies.[28-31] Additionally, in our study, the ADC and D values of TSE-IVIM showed higher measurement consistency than those of EPI-IVIM, especially the D values. This result indicated that TSE-DWI had higher interobserver agreement of ADC and D in comparison to EPI-DWI, similar to some previous studies.[11,32] TSE-IVIM was prone to decreased measurement errors, which may be on account of fewer geometric distortions and susceptibility artifacts, thus impairing interobserver accordance for ADC and D.[11]

In addition, our results showed that the values of D, D*, f, and ADC derived from the two sequences were not completely identical. TSE-IVIM and EPI-IVIM had comparable D, D*, f, and ADC values only in lesions and fat. However, no significant differences of certain parameters in some normal anatomical structures existed between TSE-IVIM and EPI-IVIM, which was in line with a previous study.[21] Furthermore, based on the absence of significant differences for IVIM-derived parameters in lesions between TSE-IVIM and EPI-IVIM, a Bland–Altman analysis of TSE-IVIM and EPI-IVIM was performed in our study; it demonstrated that the parameters of lesions derived from TSE-IVIM and EPI-IVIM had no fixed bias, yet the 95% LoAs were wide, suggesting that the LoAs in lesions between the two sequences were unacceptable, similar to some previous results.[11,21] Wan et al.[11] reported that the 95% LoAs of ADC and D were up to 60% and 62%, respectively, between EPI and TSE in pulmonary neoplasms. Mikayama et al.[21] also found wide 95% LoAs for ADC, D, and f in the normal anatomy of the head and neck. A number of reasons may explain these differences and the wide 95% LoAs between TSE-IVIM and EPI-IVIM. First, the independent ROI delineation of both sequences might result in such differences. Although we attempted to draw the ROIs at the same level with the same size as much as possible, the two ROIs drawn for the two different sequences unavoidably had some differences in terms of size and exact position.[32] Second, geometric distortions caused by susceptibility artifacts observed within the tumor region in the EPI sequence will negatively impact the measurement precision of diffusion parameters.[32] Finally, these parameters can also be influenced by image noise, which may decrease with the increase of image noise.[18] Therefore, D, D*, f, and ADC derived from IVIM based on TSE and EPI cannot be regarded as equivalent parameters for the differential diagnosis and efficacy evaluation of oral cancer.

The present study has some limitations. First, the scanning parameters of the two sequences were not identical; for example, TSE-IVIM and EPI-IVIM used different receiver bandwidths. However, the two se-
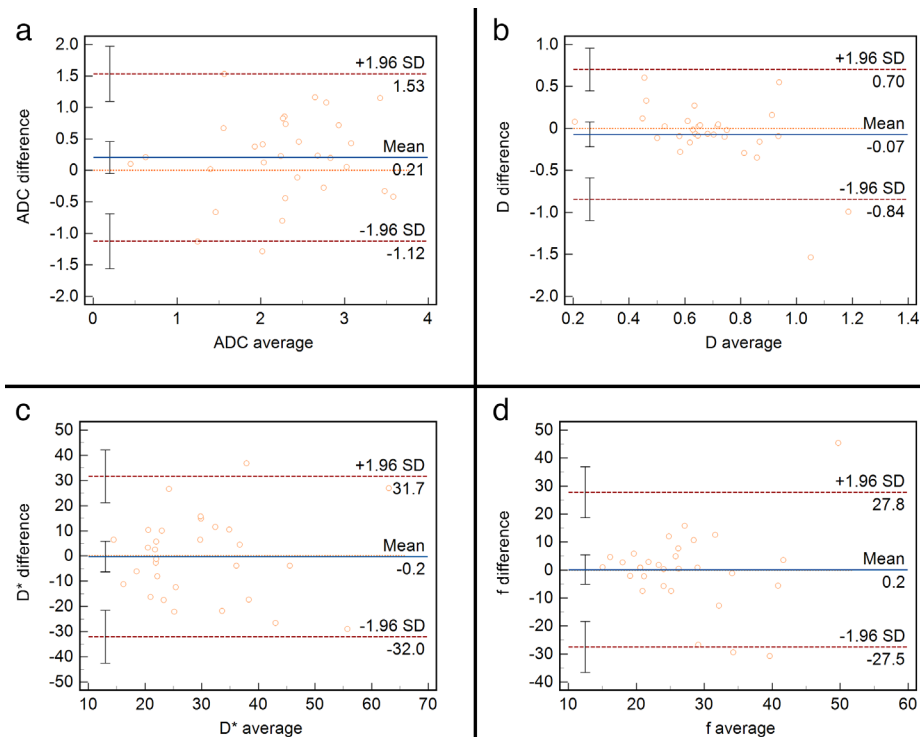
**Figure 5.** Bland–Altman plots for **(a)** apparent diffusion coefficient (ADC), **(b)** diffusion coefficient (D), **(c)** pseudo-diffusion coefficient (D*), and **(d)** perfusion fraction (*f*) of turbo spin-echo intravoxel incoherent motion (TSE-IVIM) and echo-planar imaging IVIM in the lesions. Continuous blue lines indicate mean differences, and dotted red lines indicate 95% limits of agreement (LoA). There were no fixed biases between the two sequences. However, the 95% LoAs were wide.

quences had similar scanning times in our study, although the scanning time for TSE-DWI is longer in clinical practice. Second, the acquisition time was relatively long in this study, lasting more than 10 minutes in both sequences. We used 12 *b* values in both IVIM sequences. In spite of the improvement in accuracy for IVIM-derived parameters using a large number of b values, it significantly prolonged the scanning time, resulting in more motion artifacts, and it is not clinically applicable for limited imaging time. Nevertheless, no obvious motion artifacts were detected for either TSE-IVIM or EPI-IVIM in this study. Third, the data we acquired with a 3-T system cannot be extrapolated to 1.5-T systems. On account of the difference in magnetic field strength, 1.5-T MRI scanners have less magnetic susceptibility artifacts and magnetic field inhomogeneity compared with 3-T scanners.[30] This indicates that the advantage of TSE-DWI having less susceptibility artifacts and geometric distortions may be less significant when used with 1.5-T systems. Accordingly, further research comparing MRI scanners with different magnetic field strengths is necessary.

In conclusion, TSE-IVIM in the oral and maxillofacial regions provides better image quality with less geometric distortion and fewer artifacts than EPI-IVIM. Thus, TSE-IVIM could be used as an alternative technique to EPI-IVIM in patients with oral cancer, especially in those with metallic implants prone to producing artifacts. Furthermore, ADC and D derived from TSE-IVIM have good reproducibility, indicating that TSE-IVIM can provide more accurate parameter values. However, the D, D*, *f*, and ADC values derived from IVIM based on the two sequences cannot be used as equivalent parameters for the diagnosis and follow-up of oral cancer.

### Conflict of interest disclosure

The authors declared no conflicts of interest.

## References

1. Montero PH, Patel SG. Cancer of the oral cavity. *Surg Oncol Clin N Am*. 2015;24(3):491-508. [CrossRef]

2. Warnakulasuriya S, Kerr AR. Oral cancer screening: past, present, and future. *J Dent Res*. 2021;100(12):1313-1320. [CrossRef]

3. D'souza S, Addepalli V. Preventive measures in oral cancer: an overview. *Biomed Pharmacother*. 2018;107:72-80. [CrossRef]

4. Connolly M, Srinivasan A. Diffusion-weighted imaging in head and neck cancer: technique, limitations, and applications. *Magn Reson Imaging Clin N Am*. 2018;26(1):121-133. [CrossRef]

5. Widmann G, Henninger B, Kremser C, Jaschke W. MRI sequences in head & neck radiology - state of the art. *Rofo*. 2017;189(5):413-422. [CrossRef]

6. Iima M, Yamamoto A, Kataoka M, et al. Time-dependent diffusion MRI to distinguish malignant from benign head and neck tumors. *J Magn Reson Imaging*. 2019;50(1):88-95. [CrossRef]

7. Koontz NA, Wiggins RH. Differentiation of benign and malignant head and neck lesions with diffusion tensor imaging and DWI. *AJR Am J Roentgenol*. 2017;208(5):1110-1115. [CrossRef]

8. Norris CD, Quick SE, Parker JG, Koontz NA. Diffusion MR imaging in the head and neck: principles and applications. *Neuroimaging Clin N Am*. 2020;30(3):261-282. [CrossRef]

9. Payabvash S. Quantitative diffusion magnetic resonance imaging in head and neck tumors. *Quant Imaging Med Surg*. 2018;8(10):1052-1065. [CrossRef]

10. Kamimura K, Nakajo M, Yoneyama T, et al. Assessment of microvessel perfusion of pituitary adenomas: a feasibility study using turbo spin-echo-based intravoxel incoherent motion imaging. *Eur Radiol*. 2020;30(4):1908-1917. [CrossRef]

11. Wan Q, Lei Q, Wang P, et al. Intravoxel incoherent motion diffusion-weighted imaging of lung cancer: comparison between turbo spin-echo and echo-planar imaging. *J Comput Assist Tomogr*. 2020;44(3):334-340. [CrossRef]

12. Noij DP, Martens RM, Marcus JT, et al. Intravoxel incoherent motion magnetic resonance imaging in head and neck cancer: a systematic review of the diagnostic and prognostic value. *Oral Oncol*. 2017;68:81-91. [CrossRef]

13. Dudau C, Draper A, Gkagkanasiou M, Charles-Edwards G, Pai I, Connor S. Cholesteatoma: multishot echo-planar vs non echo-planar diffusion-weighted MRI for the prediction of middle ear and mastoid cholesteatoma. *BJR Open*. 2019;1(1):20180015. [CrossRef]

14. Hirata K, Nakaura T, Okuaki T, et al. Comparison of the image quality of turbo spin echo- and echo-planar diffusion-weighted images of the oral cavity. *Medicine (Baltimore)*. 2018;97(19):e0447. [CrossRef]

15. Riffel P, Michaely HJ, Morelli JN, et al. Zoomed EPI-DWI of the head and neck with two-dimensional, spatially-selective radiofrequency excitation pulses. *Eur Radiol*. 2014;24(10):2507-2512. [CrossRef]

16. Wiesmueller M, Wuest W, May MS, et al. Comparison of readout-segmented echo-planar imaging and single-shot TSE DWI for cholesteatoma diagnostics. *AJNR*

*Am J Neuroradiol*. 2021;42(7):1305-1312. [CrossRef]

17. Mori N, Mugikura S, Miyashita M, et al. Turbo Spin-echo diffusion-weighted imaging compared with single-shot echo-planar diffusion-weighted imaging: image quality and diagnostic performance when differentiating between ductal carcinoma in situ and invasive ductal carcinoma. *Magn Reson Med Sci*. 2021;20(1):60-68. [CrossRef]

18. Yoshizako T, Yoshida R, Asou H, Nakamura M, Kitagaki H. Comparison between turbo spin-echo and echo planar diffusion-weighted imaging of the female pelvis with 3T MRI. *Acta Radiol Open*. 2021;10(2):2058460121994737. [CrossRef]

19. Lei Q, Wan Q, Liu L, et al. Values of apparent diffusion coefficient and lesion-to-spinal cord signal intensity in diagnosing solitary pulmonary lesions: turbo spin-echo versus echo-planar imaging diffusion-weighted imaging. *Biomed Res Int*. 2021;3345953. [CrossRef]

20. Panyarak W, Chikui T, Yamashita Y, Kamitani T, Yoshiura K. Image quality and ADC assessment in turbo spin-echo and echo-planar diffusion-weighted mr imaging of tumors of the head and neck. *Acad Radiol*. 2019;26(10):e305-e316. [CrossRef]

21. Mikayama R, Yabuuchi H, Sonoda S, et al. Comparison of intravoxel incoherent motion diffusion-weighted imaging between turbo spin-echo and echo-planar imaging of the head and neck. *Eur Radiol*. 2018;28(1):316-324. [CrossRef]

22. Baltzer PA, Renz DM, Herrmann KH, et al. Diffusion-weighted imaging (DWI) in MR mammography (MRM): clinical comparison of echo planar imaging (EPI) and half-Fourier single-shot turbo spin echo (HASTE) diffusion techniques. *Eur Radiol*. 2009;19(7):1612-1620. [CrossRef]

23. Suzuki M, Morita S, Goto Y, et al. Artifact-robust diffusion-weighted whole-body imaging with background suppression at 3 T using improved turbo spin-echo diffusion-weighted imaging. *Br J Radiol*. 2019;92(1094):20180489. [CrossRef]

24. Sakamoto J, Sasaki Y, Otonari-Yamamoto M, Nishikawa K, Sano T. Diffusion-weighted imaging of the head and neck with HASTE: influence of imaging parameters on image quality. *Oral Radiology*. 2012;28(2);87-94. [CrossRef]

25. Tyagi N, Cloutier M, Zakian K, Deasy JO, Hunt M, Rimner A. Diffusion-weighted MRI of the lung at 3T evaluated using echo-planar-based and single-shot turbo spin-echo-based acquisition techniques for radiotherapy applications. *J Appl Clin Med Phys*. 2019;20(1):284-292. [CrossRef]

26. Edelstein WA, Glover GH, Hardy CJ, Redington RW. The intrinsic signal-to-noise ratio in NMR imaging. *Magn Reson Med*. 1986;3(4):604-618. [CrossRef]

27. Heverhagen JT. Noise measurement and estimation in MR imaging experiments. *Radiology*. 2007;245(3):638-639. [CrossRef]

28. Marzi S, Piludu F, Vidiri A. Assessment of diffusion parameters by intravoxel incoherent motion MRI in head and neck squamous cell carcinoma. *NMR Biomed*. 2013;26(12):1806-1814. [CrossRef]

29. Hilbert F, Wech T, Neubauer H, Veldhoen S, Bley TA, Köstler H. Comparison of Turbo Spin Echo and Echo Planar Imaging for intravoxel incoherent motion and diffusion tensor imaging of the kidney at 3Tesla. *Z Med Phys*. 2017;27(3):193-201. [CrossRef]

30. Jiang J, Yin J, Cui L, et al. Lung Cancer: Short-Term Reproducibility of Intravoxel Incoherent Motion Parameters and Apparent Diffusion Coefficient at 3T. *J Magn Reson Imaging*. 2018;47(4):1003-1012. [CrossRef]

31. Lecler A, Savatovsky J, Balvay D, et al. Repeatability of apparent diffusion coefficient and intravoxel incoherent motion parameters at 3.0 Tesla in orbital lesions. *Eur Radiol*. 2017;27(12):5094-5103. [CrossRef]

32. Verhappen MH, Pouwels PJ, Ljumanovic R, et al. A. Diffusion-weighted MR imaging in head and neck cancer: comparison between half-fourier acquired single-shot turbo spin-echo and EPI techniques. *AJNR Am J Neuroradiol*. 2012;33(7):1239-1246. [CrossRef]

# Mechanical thrombectomy is associated with shorter length of hospital stay and lower readmission rates compared with conservative therapy for acute submassive pulmonary embolism: a propensity-matched analysis

Zain M. Khazi 
Justin Pierce 
Shahrzad Azizaddini 
Ryan Davis 
Ambarish P. Bhat 

**PURPOSE**

To determine if mechanical thrombectomy (MT) for submassive pulmonary embolism (PE) positively impacts length of hospital stay (LOS), intensive care unit stay (ICU LOS), readmission rate, and in-hospital mortality compared with conservative therapy.

**METHODS**

This was a retrospective review of all patients with submassive PE who either underwent MT or conservative therapy (systemic anticoagulation and/or inferior vena cava filter) between November 2019 and October 2021. Pediatric patients (age <18) and those with low-risk and massive PEs were excluded from the study. Patient characteristics, comorbidities, vitals, laboratory values (cardiac biomarkers, hospital course, readmission rates, and in-hospital mortality) were recorded. A 2:1 propensity score match was performed on the conservative and MT cohorts based on age and the PE severity index (PESI) classification. Fischer's exact test, Pearson's $\chi^2$ test, and Student's t-tests were used to compare patient demographics, comorbidities, LOS, ICU LOS, readmission rates, and mortality rates, with statistical significance defined as $P < 0.05$. Additionally, a subgroup analysis based on PESI scores was assessed.

**RESULTS**

After matching, 123 patients were analyzed in the study, 41 in the MT cohort and 82 in the conservative therapy cohort. There was no significant difference in patient demographics, comorbidities, or PESI classification between the cohorts, except for increased incidence of obesity in the MT cohort ($P = 0.013$). Patients in the MT cohort had a significantly shorter LOS compared with the conservative therapy cohort (5.37 ± 3.93 vs. 7.76 ± 9.53 days, $P = 0.028$). However, ICU LOS was not significantly different between the cohorts (2.34 ± 2.25 vs. 3.33 ± 4.49, $P = 0.059$). There was no significant difference for in-hospital mortality (7.31% vs. 12.2%, $P = 0.411$). Of those that were discharged from the hospital, there was significantly lower incidence of 30-day readmission in the MT cohort (5.26% vs. 26.4%, $P < 0.001$). A subgroup analysis did not demonstrate that the PESI score had a significant impact on LOS, ICU LOS, readmission, or in-hospital mortality rates.

**CONCLUSION**

MT for submassive PE can reduce the total LOS and 30-day readmission rates compared with conservative therapy. However, in-hospital mortality and ICU LOS were not significantly different between the two groups.

**KEYWORDS**

Embolectomy, lung, pulmonary, pulmonary embolism, submassive, thrombectomy

The incidence of pulmonary embolism (PE) is estimated at 117 per 100,000 persons in the United States, with approximately 300,000 deaths attributed to PE annually.[1,2] Approximately 55% of patients with PE are at low mortality risk and can be managed with out-

patient anticoagulation, whereas those with massive PE require treatment in an intensive care unit (ICU).[3-5] However, the management of patients with submassive PE is controversial. Unlike patients with massive PE, those with submassive PE are characterized as being hemodynamically stable but demonstrating signs of right heart strain on imaging and/or in laboratory values. Historically, the management of submassive PE has been systemic anticoagulation; however, management with systemic anticoagulation alone is associated with moderate self-reported functional impairment at 1 year after diagnosis of submassive PE.[6] With advancements in endovascular-based interventions, catheter-based thrombolysis with tissue plasminogen (tPA) or mechanical thrombectomy (MT) are often employed. Catheter-directed tPA has been successfully used in the past to treat submassive PE and prevent clinical and hemodynamic deterioration; however, it is associated with increased risk of hemorrhagic stroke and bleeding.[7-10] As a result, MT has gained popularity in recent years because of its ability to rapidly re-perfuse pulmonary circulation without the need for tPA or ICU admission.

An accurate risk stratification of patients with acute submassive PE can help guide the management and level of care. In the current climate of ballooning healthcare costs, the appropriate stratification and treatment of submassive PE can help appropriately allocate intensive care and maximize healthcare cost-effectiveness through efficacious treatment for patients. The PE severity index (PESI) is a validated tool to help stratify patients with acute PE based on the risk of 30-day mortality.[11]

Recent data suggest that MT for PE is safe and effective.[12-14] However, the impact of MT compared with that of conservative therapy for submassive PE has not been well studied. Therefore, the purpose of the current study was to determine the impact of MT using the FlowTriever device (INARI Medical, Irvine, CA, USA) for submassive PE on length of hospital stay (LOS), ICU stay (ICU LOS), readmission rates, and in-hospital mortality rates compared with anticoagulation therapy alone.

## Methods

### Patient selection

After obtaining Institutional Review Board (IRB) approval (2004777), a detailed retrospective review of patients with PE who underwent MT between November 2019 and October 2021was performed. Similarly, patients who were treated conservatively [systemic therapy with/without an inferior vena cava (IVC) filter] between June 2017 and October 2021were retrospectively reviewed for comparison. Patients with massive PE, low-risk PE, pediatric patients (age <18 years), and those that had undergone catheter-directed or systemic thrombolysis with tPA were excluded from both groups (Figure 1). The remaining patients were categorized as an MT cohort (those treated with MT) and conservative therapy cohort (those treated with systemic anticoagulation).

### Variables assessed

Basic patient demographics and comorbidities such as a history of diabetes mellitus, hypertension, coronary artery disease, congestive heart failure, chronic lung disease, obstructive sleep apnea, asthma, smoking, coronavirus disease, and malignant neoplastic disease were recorded. Patient vitals and laboratory values including cardiac biomarkers such as troponin and/or brain natriuretic peptide (BNP) at the time of the PE diagnosis were collected. Patients were determined to have right heart strain/injury based on imaging or biomarker (elevated troponin or BNP compared with baseline) elevation. For all hemodynamically stable patients with a diagnosis of PE, the right ventricle to left ventricle ratio (RV:LV) and maximum pulmonary artery (PA) distance was measured by the primary authors and senior author. Patients with an RV:LV >0.9 and/or echocardiogram evidence of moderate-to-severe right heart strain were determined to have a submassive PE and were included in the study. Finally, PESI was calculated for each patient and stratified into five categories as described by Aujesky et al.[11]

The primary endpoints of the current study were to compare the LOS and mortality rate between the conservative therapy cohort and MT cohort. Therefore, the total LOS and ICU LOS was calculated for each patient. Finally, the incidence of 30 day readmission rates was also determined for both cohorts.

### Mechanical thrombectomy procedure

At the time of PE diagnosis, systemic anticoagulation was started in all patients prior to performing MT. The FlowTriever device is the first MT device approved by the US Food and Drug Administration for the treatment of

<div style="border:1px solid #ccc; padding:8px;">

**Main points**

- Pulmonary embolism (PE) thrombectomy is a safe and effective therapy for the management of acute submassive PEs.

- PE thrombectomy can provide prompt reperfusion of the pulmonary vasculature and have an immediate clinical benefit.

- PE thrombectomy reduces length of hospital stay compared with anticoagulation therapy.

- PE thrombectomy reduces 30-day readmission rates compared with anticoagulation therapy.

</div>
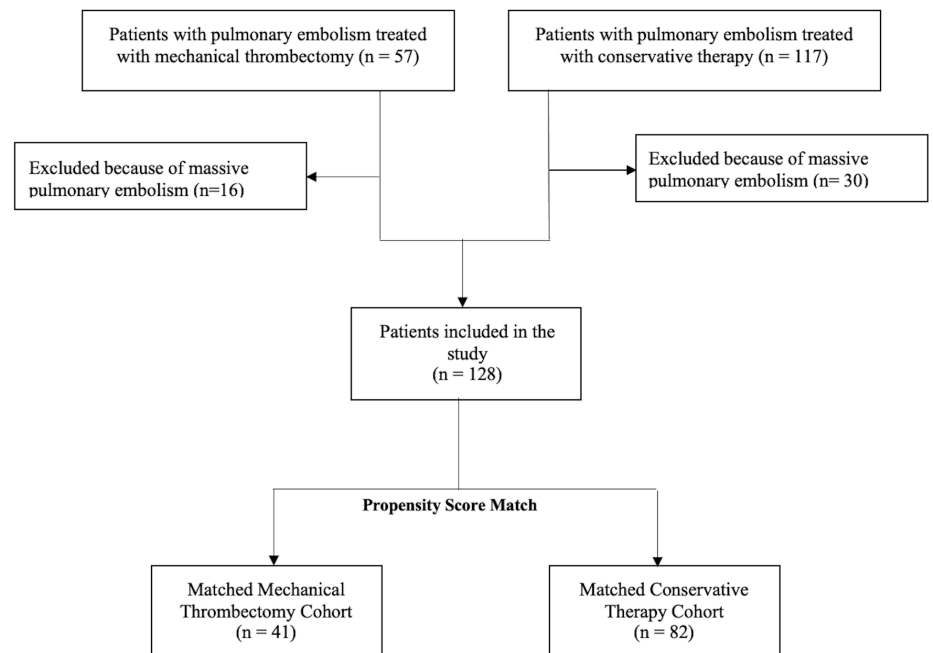


**Figure 1.** Flowchart of inclusion and exclusion criteria.

acute PE and was thus used to perform MT on all acute submassive PEs included in the study (Figure 2a). The technical procedure for MT has been previously described by Yasin et al.[14] Briefly, the right common femoral vein was accessed in all cases. A 5F angled pigtail catheter was advanced through the right heart and was used to select the pulmonary trunk. Baseline main PA pressures were measured, and an initial pulmonary angiogram was performed through the catheter to identify the extent and location of the PE (Figure 2b). Subsequently, 20/24F FlowTriever devices were used for aspiration thrombectomy. The procedure endpoint was decided based on a combination of post-procedure PA angiograms (Figure 2c), PA pressures, and the response of the patient's clinical status following aspiration thrombectomy. The access site was closed with a purse-string suture. Throughout the procedure, additional heparin boluses were administered to maintain the activated clotting time of approximately 250 s.

### Research ethics standards compliance

This original research was completed under an IRB approved protocol. Due to the retrospective nature of the study, informed consent was not required. The IRB number is 2004777. All procedures performed were in accordance with the ethical standards of the institutional and/or national research committee and with the 1964 Helsinki Declaration and its later amendments or comparable ethical standards.

### Statistical analysis

Retrospective analysis can be confounded by selection bias; therefore, a propensity score matching algorithm was used to create similar groups for the conservative therapy and MT cohorts. In this study, a 2:1 propensity score match was used based on age and PESI classification. The matched cohorts were compared for patient demographics, comorbidities, vitals, cardiac biochemical markers, radiographic features of right heart strain (through computed tomography scan or echocardiography), PESI classification, LOS, ICU LOS, mortality rate, and readmission rates using Fisher's exact test or Pearson's $\chi^2$ test for categorical variables and Student's t-tests for continuous variables. All statistical analyses were performed using the R program (r-project.org), with statistical significance set at $P < 0.05$.

## Results

### Patient characteristics

After matching based on PESI classification and age, 123 patients were analyzed in the study, with 82 in the conservative therapy cohort and 41 in the MT cohort. The patient characteristics, imaging findings of right heart strain, elevated cardiac biochemical markers, and PESI classifications are outlined for both cohorts in Table 1. There was no significant difference in patient demographics, comorbidities, or imaging findings of right heart strain between the two cohorts except an increased incidence of obesity in the MT cohort ($P = 0.013$) and hypertension in the conservative therapy cohort ($P = $

0.024). The incidence of elevated cardiac biochemical markers from baseline was higher in patients who underwent MT (100% vs. 72%, $P < 0.001$). There was no difference in IVC filter placement during hospital stay and PESI classification between the cohorts.

### Outcomes assessed

Patients in the MT cohort had a significantly shorter LOS compared with the conservative therapy cohort (5.37 ± 3.93 vs. 7.76 ± 9.53 days, $P = 0.029$; Table 2). However, ICU LOS was not significantly different between the cohorts (2.34 ± 2.25 vs. 3.33 ± 4.49 , $P = 0.062$; Table 2). There was no significant difference for in-hospital mortality (7.31% vs. 12.2%, $P = 0.411$; Table 2). Of those that were discharged from the hospital, there was significantly lower incidence of 30-day readmission in the MT cohort (5.26% vs. 26.4%, $P < 0.001$; Table 2). A subgroup analysis of PESI classifications revealed that PESI scores had no significant impact on LOS, ICU LOS, readmission, or in-hospital mortality rates.

## Discussion

This retrospective study utilized a propensity scoring algorithm to compare MT with conservative therapy for patients with submassive PE with regards to LOS, in-hospital mortality rates, and 30-day readmission rates. The study found that patients treated with MT had a significantly shorter overall LOS and decreased incidence of 30-day readmission compared with conservative therapy. However, there was no significant difference in ICU LOS or in-hospital mortality rates. Notably, the study did not find a correlation
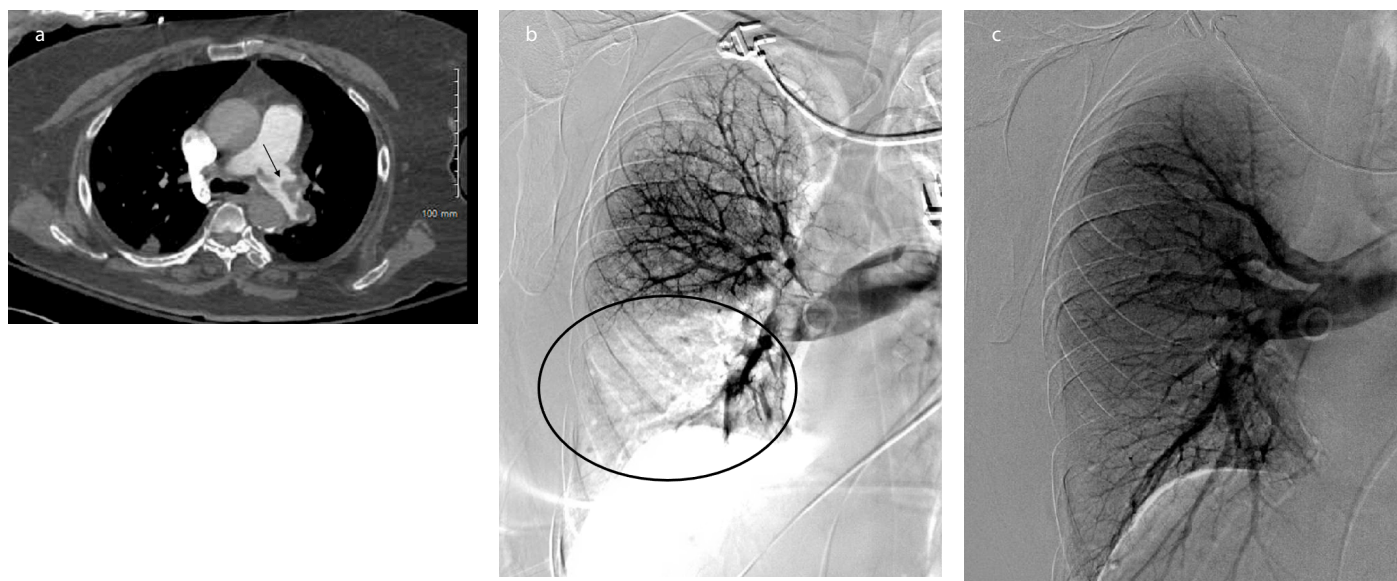


**Figure 2 (a)** Helical computed tomography scan of the pulmonary arteries, demonstrating a large clot burden within the left pulmonary artery (black arrow). **(b)** Pulmonary angiogram revealing a large filling defect within the right lower lobar pulmonary artery (black oval). **(c)** Post mechanical thrombectomy pulmonary angiogram demonstrating. the complete opacification of the right lower lobar pulmonary artery.

between PESI classifications and LOS, ICU LOS, 30-day readmission rates, or in-hospital mortality rates for acute submassive PE.

Venous thromboembolism (VTE) is a major healthcare burden worldwide and is responsible for significant healthcare resource utilization. Acute PE is one of the most feared entities of VTE and is associated with increased patient mortality, long-term morbidity, and healthcare costs.[15,16] Recently, Shalaby et al.[15] queried the National Inpatient Sample database and determined that patients with acute PE had an in-hospital charge of approximately US$ 30,000. Similarly, PE is associated with decreased aerobic functional capacity in half the patients 1 year after their PE diagnosis and has a negative impact on quality of life.[6,17] Current guidelines regarding the management of acute submassive PE recommend anticoagulation therapy with observation and/or the escalation of care based on hemodynamic instability.[18] In addition to conservative therapy with anticoagulation, catheter-based thrombolysis has been shown to be efficacious but is associated with an increased risk of bleeding.[7,9,10] As a result, patients undergoing catheter-based thrombolysis require ICU admission for close monitoring, which can substantially increase healthcare costs. Additionally, about 30% of patients with PE have an absolute or relative contraindication to systemic or catheter-directed thrombolysis.[18,19] However, MT provides a unique opportunity to evacuate the PE with immediate patient benefits as a result of prompt reperfusion.[14] Consequently, the current study sought to compare the clinical benefits to patients of MT with conservative treatment with anticoagulation therapy.

A diagnosis of PE often increases the complexity of care, leading to an increase in LOS, and it can be a barrier to timely discharge. Therefore, prompt diagnosis and the appropriate management of PE is crucial to ensure optimal patient outcomes in a timely manner. However, the appropriate management for submassive PE in not well established. The current study compared MT and conservative therapy for submassive PE and determined that patients undergoing MT for submassive PE had a significantly shorter LOS compared with conservative therapy (5.4 vs. 7.8 days, $P = 0.026$). However, the current study did not identify any difference in the length of ICU stay between the cohorts. Recently, Buckley and Wible[13] compared patients with PESI classification 4 or 5 who underwent MT with those receiving conservative therapy and found that patients who underwent MT had a shorter ICU LOS with no significant impact on overall LOS. This discrepancy in findings regarding ICU stay may be because of the difference in institutional protocols following MT. In our institution, patients who are admitted to the ICU or a

**Table 1.** Adjusted comparison of patient characteristics between mechanical thrombectomy and conservative therapy

| Patient characteristics | Mechanical thrombectomy, n = 41, (%) | Conservative therapy, n = 82, (%) | Adjusted $P$ value |
|---|---|---|---|
| Age, years (SD) | 58.58 ± 14.18 | 59.28 ± 16.24 | 0.762 |
| Sex, male | 16 (39) | 47 (57.3) | 0.066 |
| Obesity | 30 (73.2) | 41 (50) | 0.013* |
| Diabetes mellitus | 9 (21.9) | 26 (19.2) | 0.259 |
| Hypertension | 15 (36.6) | 48 (58.5) | 0.024* |
| Congestive heart failure | 4 (9.8) | 6 (7.3) | 0.644 |
| Coronary artery disease | 4 (9.8) | 11 (13.4) | 0.558 |
| Chronic lung disease | 3 (7.3) | 16 (19.5) | 0.081 |
| Obstructive sleep apnea | 6 (14.6) | 14 (17.1) | 0.731 |
| History of cancer | 11 (26.8) | 19 (23.1) | 0.659 |
| Tobacco use | 10 (24.4) | 34 (41.5) | 0.064 |
| SARS-CoV-2 infection | 5 (12.2) | 3 (3.7) | 0.071 |
| **Imaging and laboratory characteristics of submassive pulmonary embolism** | | | |
| RV:LV ratio | 1.55 ± 0.39 | 1.51 ± 0.58 | 0.672 |
| Main pulmonary artery distance, mm | 32.73 ± 5.89 | 31.28 ± 4.61 | 0.168 |
| Evidence of right heart strain in CT scan | 39 (95.1) | 70 (85.4) | 0.113 |
| Elevated troponin or BNP from baseline | 41 (100) | 59 (71.9) | <0.001* |
| IVC filter placement during hospital stay | 4 (9.8) | 16 (19.5) | 0.174 |
| **PESI category** | | | |
| PESI 1 | 5 (12.2) | 11 (13.4) | 0.842 |
| PESI 2 | 5 (12.2) | 10 (12.2) | 1.000 |
| PESI 3 | 9 (22) | 15 (18.3) | 0.631 |
| PESI 4 | 9 (22) | 13 (15.6) | 0.412 |
| PESI 5 | 13 (31.7) | 33 (40.2) | 0.363 |

*Signifies statistically significant finding; SD, standard deviation; SARS, severe acute respiratory syndrome; CoV-2, coronavirus 2; RV:LV, right ventricle to left ventricle ratio; CT, computed tomography; BNP, brain natriuretic peptide; PESI, pulmonary embolism severity index.

step-down unit are readmitted to ICU care after the MT before the de-escalation of care is considered by the primary team.

With the transition from fee-for-service to bundled payments, there is increasing institutional pressure to reduce the risk of readmissions in patients admitted for elective or urgent procedures. Readmission within 30 days is often a major contributor to healthcare costs, and factors that can reduce the risk of short-term readmissions are being studied across many medical specialties. The diagnosis of VTE, especially PE, has been shown to dramatically increase the risk of increasing short-term readmission rates.[20-22] In a European VTE registry, the readmission rate within 1 year of VTE diagnosis was approximately 25%.[23] Similarly, Chen et al.[24] determined that a perioperative diagnosis of PE following major respiratory, cardiovascular, or musculoskeletal surgery was associated with an increased risk of 30-day readmission compared with a diagnosis of perioperative PE. Therefore, optimizing care for patients with PE is of paramount importance for improving patient outcomes and reducing readmission rates. In the current study, the management of acute submassive PE with MT was associated with lower readmission rates compared with conservative management alone. This is in contrast to the findings of Buckley and Wible[13], who did not identify a significant difference in readmission rates between MT and conservative therapy cohorts. Finally, the present study did not find a statistically significant difference in in-hospital mortality rates between the two cohorts but identified a trend toward decreased risk of mortality in the MT cohort ($P = 0.059$). This finding is consistent with that of Buckley and Wible[13], who demonstrated a significantly reduced mortality rate for patients that underwent MT compared with conservative therapy. Notably, however, the study conducted by Buckley and Wible[13] did not match patients in the two cohorts, and a few patients in the conservative therapy cohort underwent systemic or catheter-based thrombolysis, which adds heterogeneity to the data.

There are several notable limitations to the present study that should be considered when interpreting the findings. Although the present study is the only moderately sized study with robust propensity score matching between cohorts, there likely exists variables that were not controlled for. Despite matching, only a few variables were not equal between the two cohorts, such as elevated biomarkers, which could impact the findings of our study. Additionally, due to the retrospective nature of the study, the findings are limited to shorter LOS and decreased readmission rates with MT compared with conservative therapy as opposed to establishing a cause-and-effect relationship. The lack of mortality benefits with MT compared with conservative therapy may be because of the relatively small sample size. In addition, the study did not evaluate the time interval from PE diagnosis to when thrombectomy was performed, which might have affected the potential benefits of MT for the inclusion of patients who presented early versus those who presented later for thrombectomy.

Finally, for the purposes of this study, a propensity score analysis was utilized to match patients in both cohorts by age and PESI classification, and independent statistical analyses were utilized to compare differences in baseline characteristics and outcomes. There is a lack of consensus regarding the appropriate use of statistical analysis for estimating the treatment effect in propensity-matched groups. It has been suggested that outcomes can be directly compared between propensity-matched cohorts using independent statistical analysis.[25] Therefore, in the current study, a Pearson's $\chi^2$ test and Student's t-tests were performed to compare outcomes between propensity-matched MT and conservative therapy cohorts for submassive PEs.

In conclusion, MT for submassive PE can reduce total LOS and 30-day readmission rates compared with conservative therapy. However, in this study, in-hospital mortality and ICU LOS were not significantly different between the two groups.

## Conflict of interest disclosure

The authors declared no conflicts of interest.

## References

1. Anderson FA Jr, Zayaruzny M, Heit JA, Fidan D, Cohen AT. Estimated annual numbers of US acute-care hospital patients at risk for venous thromboembolism. *Am J Hematol.* 2007;82(9):777-782. [CrossRef]

2. Silverstein MD, Heit JA, Mohr DN, Petterson TM, O'Fallon WM, Melton LJ 3rd. Trends in the incidence of deep vein thrombosis and pulmonary embolism: a 25-year population-based study. *Arch Intern Med.* 1998;158(6):585-593. [CrossRef]

3. Singer AJ, Thode HC Jr, Peacock WF 4th. Admission rates for emergency department patients with venous thromboembolism and estimation of the proportion of low risk pulmonary embolism patients: a US perspective. *Clin Exp Emerg Med.* 2016;3(3):126-131. [CrossRef]

4. Fang MC, Fan D, Sung SH, et al. Outcomes in adults with acute pulmonary embolism who are discharged from emergency departments: the Cardiovascular Research Network Venous Thromboembolism study. *JAMA Intern Med.* 2015;175(6):1060-1062. [CrossRef]

5. Konstantinides SV, Torbicki A, Agnelli G, et al. 2014 ESC guidelines on the diagnosis and management of acute pulmonary embolism. *Eur Heart J.* 2014;35(43):3033-3069, 3069a-3069k. [CrossRef]

6. Kahn SR, Hirsch AM, Akaberi A, et al. Functional and exercise limitations after a first episode of pulmonary embolism: results of the ELOPE prospective cohort study. *Chest.* 2017;151(5):1058-1068. [CrossRef]

7. Nakamura S, Takano H, Kubota Y, Asai K, Shimizu W. Impact of the efficacy of thrombolytic therapy on the mortality of patients with acute submassive pulmonary embolism: a meta-analysis. *J Thromb Haemost.* 2014;12(7):1086-1095. [CrossRef]

8. Meyer G, Vicaut E, Danays T, et al. Fibrinolysis for patients with intermediate-risk pulmonary embolism. *N Engl J Med.* 2014;370(15):1402-1411. [CrossRef]

9. Kucher N, Boekstegers P, Müller OJ, et al. Randomized, controlled trial of ultrasound-assisted catheter-directed thrombolysis for acute intermediate-risk pulmonary embolism. *Circulation.* 2014;129(4):479-486. [CrossRef]

10. Stein PD, Matta F. Thrombolytic therapy in unstable patients with acute pulmonary embolism: saves lives but underused. *Am J Med.* 2012;125(5):465-470. Erratum in: *Am J Med.* 2012;125(7):e13. [CrossRef]

11. Aujesky D, Obrosky DS, Stone RA, et al. Derivation and validation of a prognostic model for pulmonary embolism. *Am J Respir Crit Care Med.* 2005;172(8):1041-1046. [CrossRef]

**Table 2.** Adjusted comparison of primary outcomes between mechanical thrombectomy and conservative therapy

| Outcomes | Mechanical thrombectomy | Conservative therapy | Adjusted *P* value |
|---|---|---|---|
| Readmission rate | 2 | 19 | **<0.001\*** |
| In-hospital mortality | 3 | 10 | **0.411** |
| ICU stay | 2.34 ± 2.25 | 3.33 ± 4.49 | **0.062** |
| LOS stay | 5.37 ± 3.93 | 7.76 ± 9.53 | **0.029\*** |

*Signifies statistically significant finding; ICU, intensive care unit; LOS, length of hospital stay.

12. Ballas ER, Sanders CD, Hoskins JD. Large-bore mechanical thrombectomy of acute pulmonary embolism at a community-based hospital: a case series. *Mil Med.* 2022:usac046. [CrossRef]

13. Buckley JR, Wible BC. In-hospital mortality and related outcomes for elevated risk acute pulmonary embolism treated with mechanical thrombectomy versus routine care. *J Intensive Care Med.* 2022;37(7):877-882. [CrossRef]

14. Yasin JT, Davis R, Saemi A, et al. Technical efficiency, short-term clinical results and safety of a large-bore aspiration catheter in acute pulmonary embolism - a retrospective case study. *Lung India.* 2020;37(6):485-490. [CrossRef]

15. Shalaby K, Kahn A, Silver ES, Kim MJ, Balakumaran K, Kim AS. Outcomes of acute pulmonary embolism in hospitalized patients with cancer. *BMC Pulm Med.* 2022;22(1):11. [CrossRef]

16. Spyropoulos AC, Lin J. Direct medical costs of venous thromboembolism and subsequent hospital readmission rates: an administrative claims analysis from 30 managed care organizations. *J Manag Care Pharm.* 2007;13(6):475-486. [CrossRef]

17. Andersson T, Soderberg S. Incidence of acute pulmonary embolism, related comorbidities and survival; analysis of a Swedish national cohort. *BMC Cardiovasc Disord.* 2017;17(1):155. [CrossRef]

18. Moore K, Kunin J, Alnijoumi M, Nagpal P, Bhat AP. Current endovascular treatment options in acute pulmonary embolism. *J Clin Imaging Sci.* 2021;11:5. [CrossRef]

19. Brown KN, Devarapally SR, Lee LS, Gupta N. Catheter directed thrombolysis of pulmonary embolism. In: *StatPearls. Treasure Island (FL):StatPearls Publishing;* 2022. [CrossRef]

20. Mallick S, Aiken T, Varley P, et al. Readmissions from venous thromboembolism after complex cancer surgery. *JAMA Surg.* 2022;157:312-320. [CrossRef]

21. Zuke WA, Chughtai M, Emara AK, et al. What are drivers of readmission for readmission-requiring venous thromboembolic events after primary total hip arthroplasty? An analysis of 544,443 cases. *J Arthroplasty.* 2022;37:958-965.e3. [CrossRef]

22. Singh V, Muthusamy N, Ikwuazom CP, Sicat CS, Schwarzkopf R, Rozell JC. Postoperative venous thromboembolism event increases risk of readmissions and reoperation following total joint arthroplasty: a propensity-matched cohort study. *Eur J Orthop Surg Traumatol.* 2022;32(6):1055-1061. [CrossRef]

23. Cohen AT, Gitt AK, Bauersachs R, et al. The management of acute venous thromboembolism in clinical practice. Results from the European PREFER in VTE Registry. *Thromb Haemost.* 2017;117(7):1326-1337. [CrossRef]

24. Chen T, Chen Q, Xu W, Guo J, He J. Risks and outcomes of perioperative pulmonary embolism in major surgeries: a population-based study. *Clin Ther.* 2021;43(11):1957-1968.e10. [CrossRef]

25. Schafer JL, Kang J. Average causal effects from nonrandomized studies: a practical guide and simulated example. *Psychol Methods.* 2008;13(4):279-313. [CrossRef]

INTERVENTIONAL RADIOLOGY

ORIGINAL ARTICLE

# Diagnostic accuracy of percutaneous core biopsy before cryoablation for small-sized renal cell carcinoma

Yasuhiro Ushijima
Akihiro Nishie
Nobuhiro Fujita
Yuichiro Kubo
Keisuke Ishimatsu
Kousei Ishigami

**PURPOSE**

To retrospectively determine the diagnostic accuracy of a percutaneous core biopsy performed before cryoablation for small-sized renal cell carcinoma.

**METHODS**

In this study, 216 patients underwent a percutaneous core biopsy for 242 renal lesions suspected to be renal cell carcinoma on image findings before cryoablation at Kyushu University Hospital. We calculated the success rate of the histological diagnosis and investigated factors that may have contributed to the diagnostic success. Complications caused by the biopsy procedure were also evaluated.

**RESULTS**

The histological diagnosis was successful in 203 lesions (82.8%). The success rate of the histological diagnosis was 65.4% (34/52 cases) for tumors with a diameter of ≤15 mm and 88.9% (169/190 cases) for those >15 mm. Therefore, tumor diameter was a factor contributing to the histological diagnosis success rate in both univariate and multivariable analyses ($P < 0.001$). For lesions with a tumor diameter ≤15 mm, the histological diagnosis success rates increased from 50.0% to 76.2% in the presence of pre-lipiodol marking and to 85.7% when the biopsy procedure was performed separately from cryoablation; the latter was statistically significant ($P = 0.039$). Major complications that may have been caused by the biopsy procedure were grade 3 bleeding and tract seeding (one case each).

**CONCLUSION**

Percutaneous core biopsy in cryoablation for small-sized renal cell carcinoma had a high diagnostic rate and was safely performed. For lesions with a tumor diameter ≤15 mm, a separate biopsy procedure and pre-lipiodol marking may improve the diagnostic accuracy.

**KEYWORDS**

Ablation, biopsy, cryotherapy, CT, malignancy, renal

From the Department of Clinical Radiology (Y.U.
✉ ushijima.yasuhiro.538@m.kyushu-u.ac.jp, A.N., N.F.,
Y.K., K.I., K.I.) Kyushu University, Graduate School of
Medical Sciences, Fukuoka, Japan.

Cryoablation for renal cell carcinoma is a minimally invasive treatment that has become well established in recent years. Studies report that it provides a high degree of local control, preserves renal function comparable to surgical resection, and is suitable for elderly patients and patients with comorbidities or multiple lesions.[1-3] With the development of diagnostic imaging equipment, the incidental detection of small-sized renal cell carcinoma is increasing,[4,5] and cryoablation as a minimally invasive treatment for this small-diameter renal cell carcinoma is considered useful.

Prior to cryoablation for renal cell carcinoma, obtaining a histological diagnosis to clarify the medical evidence for the application of this technique is desirable. Most imaging diagnoses are accurate but not complete, and benign lesions may be present, although not frequently.[6,7]

Percutaneous biopsy is necessary to obtain a histological diagnosis, but biopsy is not always easy. The level of difficulty varies depending on the size and location of the lesion, and there is a risk of complications such as bleeding and seeding.[8,9] In addition, the protocol for percutaneous biopsy in cryoablation has not been fully established, such as when to perform the biopsy, whether to perform it at the same time as cryoablation or separately, and the relationship with lipiodol marking, which is widely performed in Japan before cryoablation to improve the visibility of the lesion in computed tomography (CT) fluoroscopic images.[10,11]

Therefore, the purpose of this study is to retrospectively evaluate the diagnostic accuracy of percutaneous biopsy performed before cryoablation for renal cell carcinoma.

## Methods

All the procedures performed in this study were in accordance with the ethical standards of the institutional and/or national research committee and with the 1964 Declaration of Helsinki and its later amendments or comparable ethical standards. This study has obtained approval from the Institutional Review Board of Kyushu University Hospital (no: 21109-00), and the need for informed consent was waived.

### Participants

At our institution, 258 renal lesions of 221 patients were subjected to cryoablation between April 2014 and September 2019. All patients were given information about the indications for treatment by both our team and a urologist from our institution or elsewhere before agreeing to the cryoablation treatment. Percutaneous biopsies for histological diagnosis were performed on 216 patients with 242 lesions, excluding those with multiple lesions or patients who refused biopsy. The patient demographic data and lesion characteristics are detailed in Table 1.

### Flow of the procedure for biopsy, cryoablation, and lipiodol marking

This study had three different procedural flows. One hundred and twenty-eight lesions underwent biopsy and cryoablation in a single session, and 68 lesions were subjected to lipiodol marking as a pretreatment and underwent biopsy and cryoablation in the same session the next day. In 48 cases, the biopsy was performed the day before, with cryoablation performed separately. In 37 of these cases, lipiodol marking was performed after the biopsy. These processes are summarized in Figure 1.

### Percutaneous core biopsy

All percutaneous biopsy procedures were performed under local anesthesia and CT fluoroscopy using an interventional radiology (IVR)-CT system (Aquilion One, Canon, Tokyo, Japan) while the patient was in a prone or oblique-prone position. An 18-gauge (G) core biopsy needle using a 17-G introducer (TEMNO evolution, Merit Medical, Tokyo, Japan) was inserted into the renal lesion, and the tissue was evaluated by an experienced histopathologist for histological diagnosis.

### Cryoablation

All cryoablation procedures were performed with the patient under local anesthesia and in a prone or oblique-prone position using the cryoablation (CryoHit, Galil Medical, MN, USA) and IVR-CT systems. Subsequently, 17-G cryoprobes (IceRod, IceSeed, Galil Medical, MN, USA) were inserted into the tumors using CT fluoroscopy to surround them. The tumors were frozen twice for 10 min by passing argon gas through the probes with a 5-min interval for thawing between the two 10-min freezing periods. Unenhanced CT was obtained to confirm the extension of the ablation area, the so-called "ice ball," at least 5 mm beyond the tumor margin.

### Transarterial lipiodol marking

Transarterial lipiodol marking was performed before cryoablation to improve the contrast between the tumor and normal parenchyma during the CT-guided procedure. Digital subtraction and CT angiography of the renal artery and branches were obtained to identify the tumor through a transfemoral approach using a 3–4F sheath (Super sheath, Medikit, Tokyo, Japan). Selective catheterization of the tumor's feeding artery, injection of lipiodol (Guerbet, Paris, France), and embolization with a small gelatin sponge (Serescue, Nihon Kayaku, Tokyo, Japan) were then performed. Unenhanced CT was obtained to confirm the deposition of lipiodol throughout the tumor.

### Statistical analysis

First, the biopsy results and diagnostic success rate were evaluated. We considered those with a specific histological diagnosis, such as clear cell carcinoma, papillary renal carcinoma, angiomyolipoma, and oncocytoma, to be diagnostic, whereas those with no malignant tissue or with atypical cells were considered non-diagnostic. Second, risk factors associated with histological diagnosis were analyzed. These included age, sex, tumor size, tumor location, biopsy procedure, and pre-lipiodol marking. Continuous variables (e.g., age, tumor size) were compared between diagnostic and non-diagnostic groups using the Student's $t$-test and categorical variables (e.g., sex, tumor size divided

### Main points

- Tumor diameter was a factor contributing to the diagnostic accuracy of a percutaneous core biopsy performed before cryoablation for small-sized renal cell carcinoma.

- A biopsy performed in a separate session from cryoablation elevated the histological diagnostic rate for tumors <15 mm.

- Pre-lipiodol marking also improved the histological diagnostic rate of tumors <15 mm.

**Table 1.** Demographic data and lesion characteristics in all patients undergoing a percutaneous core biopsy for suspected renal cell carcinoma

| Patient characteristics (n = 216) | |
| --- | --- |
| Age, years, median (minimum–maximum) | 71 (30–91) |
| Sex, n (%) | |
| Male/female | 160 (74.1)/56 (25.9) |
| Number of lesions, n (%) | |
| 1/2/3/4 | 195 (90.2)/17 (7.9)/3 (1.4)/1 (0.4) |
| Lesion characteristics (n = 242) | |
| Size, mm, mean ± SD (minimum–maximum) | 23.2 ± 7.98 (8–40) ≤15 (n = 52)/>15 (n = 190) |
| Location, n (%) | |
| Exophytic/endophytic/hilum | 122 (50.4)/103 (42.6)/17 (7.0) |
| Upper/middle/lower | 71 (29.3)/111 (45.9)/60 (24.8) |
| Anterior/posterior/X | 96 (39.7)/120 (49.6)/26 (10.7) |
| SD, standard deviation. | |

into two groups with a 15 mm diameter, tumor location, biopsy procedure, and pre-lipiodol marking) were compared using the chi-square test. Significant differences identified by univariate analysis were then analyzed through multivariate analysis using logistic regression with forward selection. Variables assessed to be $P < 0.10$ in the univariate analysis were entered into a multivariable logistic regression analysis. A comparison of the diagnostic rates from the different procedures was performed for large and small tumor sizes using the chi-square test, with $P < 0.05$ considered a statistically significant difference. Complications were graded according to the Common Terminology Criteria for Adverse Events (version 5), published by the National Cancer Institute in 2017, and complications of grade 3 or higher were examined. All statistical analyses were performed using JMP Pro (version 14; SAS Institute). Descriptive statistics are presented as mean ± standard deviation and frequencies are presented as percentages.

## Results

The results of the biopsy and diagnosis rate assessments are presented in Table 2. The most common type was clear cell carcinoma (179 cases), followed by papillary carcinoma (16 cases). A small number of benign lesions such as oncocytoma and angiomyolipoma were also identified. The overall diagnostic rate was 82.8%. In the analysis of risk factors involved in histological diagnosis, there was a significant difference in the diagnostic rates according to tumor size in the univariate analysis ($P < 0.001$). A significant difference in the diagnostic rate for tumor size ≤15 or >15 mm ($P < 0.001$) was also detected. No significant difference was observed in tumor location (exophytic/endophytic/hilum: $P = 0.336$; upper/middle/lower: $P = 0.078$; anterior/posterior/X: $P = 0.575$) (Table 3). A multivariable analysis was performed on factors achieving $P$ values < 0.1 in the univariate analysis, and in this analysis, a significant difference was observed for tumor size ≤15 and >15 mm ($P < 0.001$) (Table 4).

In the comparison of diagnostic rates according to procedures, the diagnostic rate of the biopsy increased with the addition of pre-lipiodol marking compared with simultaneous biopsy and cryoablation; the diagnostic rates increased further by performing biopsy and cryoablation in separate sessions. This was more pronounced for tumors <15 mm in diameter, for which the diagnostic rate was only 50% in cases where biopsy and cryoablation were performed simultaneously but increased to 76.2% when pre-lipiodol marking was performed; it increased significantly to 85.7% when biopsy and cryoablation were performed in separate sessions ($P = 0.039$) (Figure 2).

The only grade 3 or higher complications were one case of hemorrhage and one of seeding of the puncture site.

## Discussion

Percutaneous biopsy of renal tumors is a well-established technique that has been reported extensively.[8,9,12] However, biopsy of small renal cell carcinoma, which is an indication for cryoablation, is often difficult because of tumor size and location. In addition, it is difficult to determine when to perform a biopsy in cryoablation, and this has not been established. Therefore, we investigated the diagnostic performance of percutaneous biopsy in the cryoablation of renal cell carcinoma.

In the present study, the overall diagnostic rate of biopsy was 82.8%, and the diagnostic rate was higher when cryoablation and biopsy were performed in separate sessions than when they were performed simultaneously. Other authors have reported that the diagnostic rate of biopsy for renal masses is generally around 90%[8,9,12,13] and that the diagnostic performance of radiofrequency ablation and biopsy for renal cell carcinoma is 68%.[14] These suggest that performing a biopsy at the same time as cryoablation decreases the histological diagnostic performance of the biopsy. The reason may be that when a biopsy is performed in the same session as cryoablation, the priority is inevitably given to cryoablation as the treatment, and the biopsy and diagnosis are neglected. In addition, if a biopsy is performed with a cryoprobe inserted into the lesion, the recognition and identification of the lesion may be inadequate because of the artifacts caused by the cryoprobes, thereby affecting the diagnostic performance of the biopsy.

The risk factor involved in the histological diagnostic rate is tumor size. In this
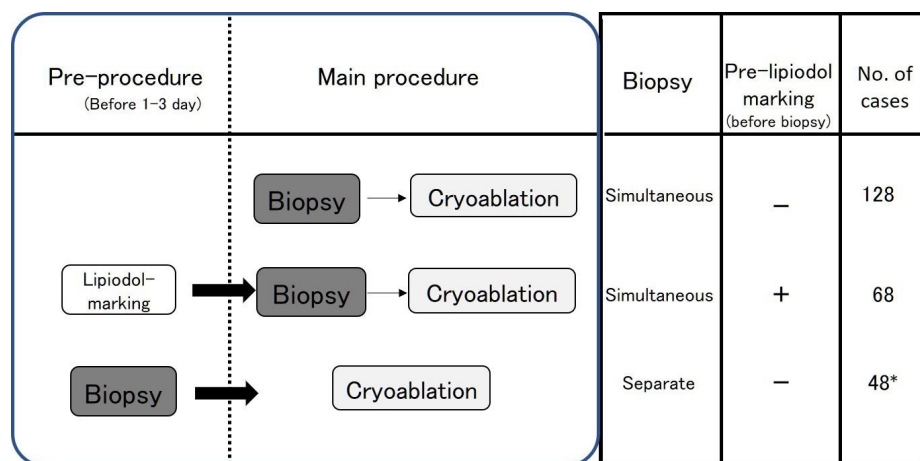


**Figure 1.** Flow of the procedure for biopsy, cryoablation, and lipiodol marking. *Lipiodol marking was performed immediately after the biopsy in 37 of the 48 cases.

**Table 2.** Biopsy results and diagnostic rates

| Biopsy results | | No of cases (%) |
|---|---|---|
| Diagnostic | Clear cell carcinoma | 179 (74.0) |
| | Papillary carcinoma | 16 (6.6) |
| | Chromophobe carcinoma | 1 (0.4) |
| | Metastatic carcinoma | 1 (0.4) |
| | Oncocytoma | 4 (1.7) |
| | Angiomyolipoma | 2 (0.8) |
| | Total | 203 (82.8) |
| Non-diagnostic | No malignant tissue | 25 (10.3) |
| | Atypical cell | 14 (5.8) |
| | Total | 39 (17.2) |

**Table 3.** Univariate analysis of the risk factors associated with histological diagnosis

| Factor | | Diagnostic (n = 203) | Non-diagnostic (n = 39) | P value |
|---|---|---|---|---|
| Age, years | Mean ± SD | 69.9 ± 11.9 | 67.1 ± 15.1 | 0.101 |
| Sex, n (%) | Male/female | 135/51 (82.1/91.1) | 29/5 (17.9/8.9) | 0.212 |
| Size, mm | Mean ± SD | 24.0 ± 7.75 | 19.0 ± 7.98 | <0.001 |
| n (%) | >15 mm | 169 (88.9) | 21 (11.1) | <0.001 |
| | ≤15 mm | 34 (65.4) | 18 (34.6) | |
| Location, n (%) | Exophytic/endophytic/hilum | 99/88/16 (81.1/79.3/94.1) | 23/15/1 (18.9/20.7/5.9) | 0.336 |
| | Upper/middle/lower | 60/98/45 (84.5/88.3/75.0) | 11/13/15 (15.5/11.7/25.0) | 0.078 |
| | Anterior/posterior/X | 82/101/20 (85.4/87.8/76.9) | 14/19/6 (14.6/12.1/23.1) | 0.575 |
| Biopsy procedure, n (%) | Simultaneous/separate | 161/42 (82.1/91.3) | 35/4 (17.9/8.7) | 0.128 |
| Pre-lipiodol marking, n (%) | +/− | 59/144 (86.8/82.8) | 9/30 (13.2/17.2) | 0.446 |

SD, standard deviation.

**Table 4.** Multivariable logistic analysis of the risk factors associated with histological diagnosis

| Factor | | Odds ratio | 95% Confidence interval | P value |
|---|---|---|---|---|
| Size | ≤15 mm/>15 mm (reference) | 4.04 | 1.92, 8.50 | <0.001 |
| Location | Upper/middle/lower (reference) | 0.70 | 0.28, 1.73 | 0.192 |
| | | 0.45 | 0.19, 1.10 | |

Factors with P values <0.1 in the univariate analysis (Table 3) were extracted and subjected to multivariable logistic analysis. P value of the entire logistic model was <0.001. McFaden R-squared was 0.121.
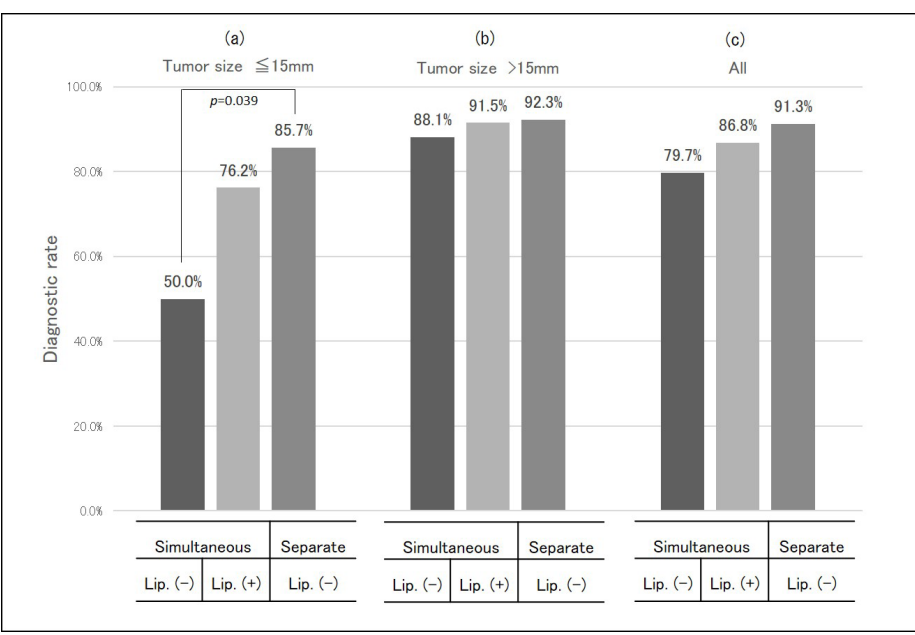


**Figure 2.** Comparison of the diagnostic rates of the biopsies between procedures by tumor size. (a) The diagnostic rate of the biopsy for the tumors with a diameter ≤15 mm increased from 50.0% to 76.2% in the presence of pre-lipiodol-marking and to 85.7% with a biopsy procedure performed separately from the cryoablation, with the latter being statistically significant (P < 0.05, chi-square test). There was a similar but not statistically significant difference in the diagnostic rates for tumors >15 mm (b) and all tumors **(c)**. Lip, pre-lipiodol marking.

study, for tumors <15 mm in diameter, the diagnostic rate was 50% when the biopsy was performed at the same time as cryoablation, increasing to 76.2% when lipiodol marking was performed the day before and further to 85.7 % when the biopsy and cryoablation were performed in separate sessions. This suggests that pre-lipiodol marking and separate sessions of biopsy and cryoablation may be useful for increasing the histological diagnostic rate of lesions with small tumor sizes. Pre-lipiodol marking certainly increases the visibility of the lesion; in addition, performing cryoablation and a biopsy in separate sessions improves the operator's concentration during each procedure (Figures 3, 4). In the present study, pre-lipiodol marking followed by cryoablation and biopsy was not performed in separate sessions, but it is highly likely that this would further increase the histological diagnostic rate.

In the present study, the location of the lesion did not affect the histological diagnostic rate. Studies have reported that exophytic lesions have a high diagnostic rate[15] and that lesions in the hilar region of the kidney also have a high diagnostic rate;[16] thus, the effect of the location of the lesion on the histological diagnostic rate of biopsy is uncertain. At this stage, there is no need to change the biopsy procedure according to the location of the lesion.

Serious complications were not frequent, with one case of hemorrhage and one of seeding of the puncture site; these complications are similar to those previously reported in biopsy and cryoablation studies.[1,2,9] Percutaneous biopsies for renal lesions, including cryoablation and lipiodol marking performed concurrently or in separate sessions, seem to be well tolerated.

In the present study, the imaging modality used for the biopsy of renal lesions was CT. In other imaging modalities, ultrasound allows convenient biopsy from any angle, and magnetic resonance imaging provides better soft-tissue resolution and recognition of target lesions. However, the diagnostic rate of biopsies for renal lesions with these imaging modalities is comparable to that of CT usage in this study, and the incidence of complications is low with each modality.[12,17] Therefore, many options for imaging modalities for renal biopsy are available, and the physician should select an imaging modality based on the facility's equipment and the concurrent treatment, such as image-guided cryoablation.
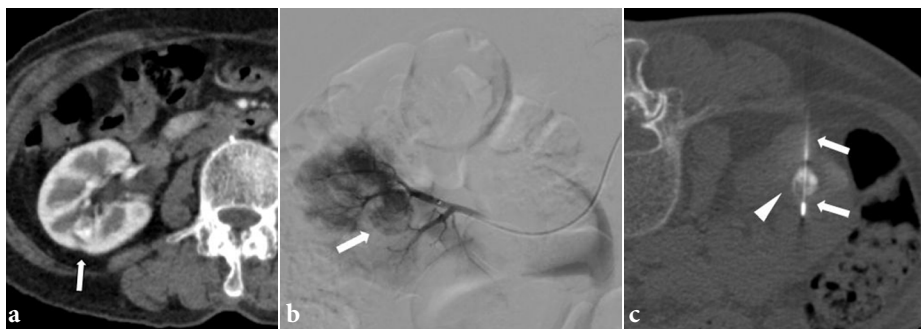
**Figure 3.** Simultaneous computed tomography (CT)-guided biopsy and cryoablation of renal cell carcinoma in a 76-year-old woman in the presence of lipiodol deposition. (a) Contrast-enhanced CT showed an endophytic lesion with an 11 mm diameter in the central part of the right kidney (arrow). (b) Lipiodol was deposited into the lesion (arrow) using a transarterial approach the day before to improve the visibility of the lesion. (c) Biopsy and cryoablation using a cryoprobe (arrow) were performed on the lipiodol-deposited tumor (arrowhead) in the same session the next day. The histological diagnosis was clear cell carcinoma with no severe complications during or after the procedure.
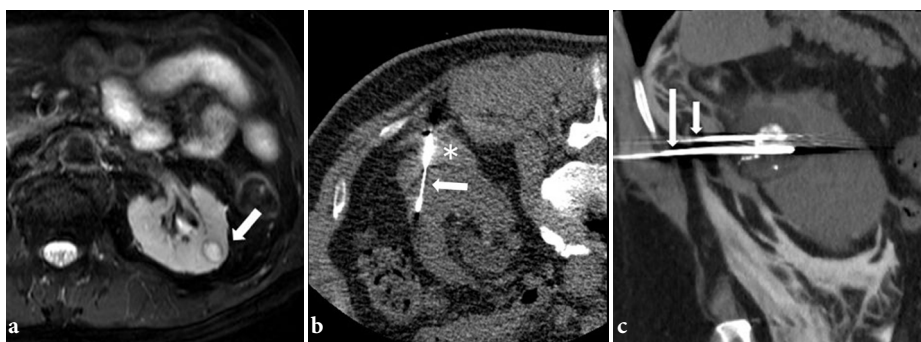


**Figure 4.** Computed tomography-guided biopsy separated from cryoablation of renal cell carcinoma in a 76-year-old man. (a) T2-weighted magnetic resonance image revealed an endophytic lesion with a diameter of 15 mm in the left central kidney that was suspected to be renal cell carcinoma (arrow). **(b)** A biopsy was performed using a biopsy needle (arrow), followed by lipiodol marking using a transarterial approach the day before cryoablation. (c) Cryoablation was performed using cryoprobes (arrow) the next day. The histological diagnosis was clear cell carcinoma. A perirenal hematoma (grade 1) was observed (b, asterisk), but no severe complications were detected during or after the procedures.

Limitations include the fact that the study was not randomized, that some complications were not strictly distinguishable in biopsy or cryoablation, and that non-neoplastic lesions may be considered undiagnosed. For tumors <15 mm, the histological diagnostic rate was higher in patients with separate sessions or pre-lipiodol marking. A future study is needed because both separate sessions and pre-lipiodol marking may increase the success rate of histological diagnosis.

In conclusion, for renal lesions with small tumor diameters, a biopsy performed in a separate session from cryoablation and using pre-lipiodol marking may improve the histological diagnostic rate.

### Conflict of interest

The authors declare that they have no conflicts of interest.

# References

1. Thompson RH, Atwell T, Schmit G, et al. Comparison of partial nephrectomy and percutaneous ablation for cT1 renal masses. *Eur Urol.* 2015;67(2):252-259. [CrossRef]

2. Uhlig J, Strauss A, Rücker G, et al. Partial nephrectomy versus ablative techniques for small renal masses: a systematic review and network meta-analysis. *Eur Radiol.* 2019;29(3):1293-1307. [CrossRef]

3. Yoshimatsu R, Yamagami T, Nishimori M, et al. Time-Dependent Effects of Cryoablation for Renal Tumor on Overall and Split Renal Function. *J Vasc Interv Radiol.* 2019;30(3):460-465. [CrossRef]

4. Kane CJ, Mallin K, Ritchey J, Cooperberg MR, Carroll PR. Renal cell cancer stage migration: analysis of the National Cancer Data Base. *Cancer.* 2008;113(1):78-83. [CrossRef]

5. Gill IS, Aron M, Gervais DA, Jewett MA. Clinical practice. Small renal mass. *N Engl J Med.* 2010;362(7):624-634. [CrossRef]

6. Rioux-Leclercq N, Karakiewicz PI, Trinh QD, et al. Prognostic ability of simplified nuclear grading of renal cell carcinoma. *Cancer.* 2007;109(5):868-874. [CrossRef]

7. Frank I, Blute ML, Cheville JC, Lohse CM, Weaver AL, Zincke H. Solid renal tumors: an analysis of pathological features related to tumor size. *J Urol.* 2003;170(6 Pt 1):2217-2220. [CrossRef]

8. Beland MD, Mayo-Smith WW, Dupuy DE, Cronan JJ, DeLellis RA. Diagnostic yield of 58 consecutive imaging-guided biopsies of solid renal masses: should we biopsy all that are indeterminate? *AJR Am J Roentgenol.* 2007;188(3):792-797. [CrossRef]

9. Marconi L, Dabestani S, Lam TB, et al. Systematic review and meta-analysis of diagnostic accuracy of percutaneous renal tumour biopsy. *Eur Urol.* 2016;69(4):660-673. [CrossRef]

10. Kajiwara K, Yoshimatsu R, Nishimori M, et al. Efficacy of arterial infusion of iodized oil on CT-guided cryoablation for renal cell carcinoma. *Minim Invasive Ther Allied Technol.* 2021;30(6):327-333. [CrossRef]

11. Hongo F, Yamada Y, Ueda T, et al. Preoperative lipiodol marking and its role on survival and complication rates of CT-guided cryoablation for small renal masses. *BMC Urol.* 2017;17(1):10. [CrossRef]

12. Cazzato RL, De Marini P, Auloge P, et al. Diagnostic accuracy and safety of percutaneous MRI-guided biopsy of solid renal masses: single-center results after 4.5 years. *Eur Radiol.* 2021;31(2):580-590. [CrossRef]

13. Jeon HG, Seo SI, Jeong BC, et al. Percutaneous kidney biopsy for a small renal mass: a critical appraisal of results. *J Urol.* 2016;195(3):568-573. [CrossRef]

14. Iguchi T, Hiraki T, Tomita K, et al. Simultaneous biopsy and radiofrequency ablation of T1a renal cell carcinoma. *Diagn Interv Imaging.* 2016;97(11):1159-1164. [CrossRef]

15. Richard PO, Jewett MA, Bhatt JR, et al. Renal tumor biopsy for small renal masses: a single-center 13-year experience. *Eur Urol.* 2015;68(6):1007-1013. [CrossRef]

16. Cooper S, Flood TA, Khodary ME, et al. Diagnostic yield and complication rate in percutaneous needle biopsy of renal hilar masses with comparison with renal cortical mass biopsies in a cohort of 195 patients. *AJR Am J Roentgenol.* 2019;212(3):570-575. [CrossRef]

17. Park SY, Park BK, Kim CK, Kwon GY. Ultrasound-guided core biopsy of small renal masses: diagnostic rate and limitations. *J Vasc Interv Radiol.* 2013;24(1):90-96. [CrossRef]

# Combination transarterial chemoembolization and microwave ablation vs. microwave ablation monotherapy for hepatocellular carcinomas greater than 3 cm: a comparative study

Jason Chiang 🄳

Pradeep S. Rajendran 🄳

Frank Hao 🄳

James Sayre 🄳

Steven S. Raman 🄳

David S. K. Lu 🄳

Justin P. McWilliams 🄳

**PURPOSE**

To evaluate the efficacy of combination therapy using transarterial chemoembolization with microwave ablation (MWA) therapy vs. MWA monotherapy for hepatocellular carcinomas (HCCs) >3 cm in size.

**METHODS**

This two-arm retrospective observational study included patients with HCCs >3 cm who underwent either combination therapy (29 patients) or MWA monotherapy (35 patients) between 2014 and 2020. The treatment outcomes related to primary treatment efficacy, local tumor progression (LTP), tumor control rate, and overall survival were compared between each cohort.

**RESULTS**

The technical success and primary efficacy were 96.56% and 100.00% in the combination therapy cohort, and 91.42% and 100.00% in the MWA cohort, respectively, over a mean follow-up period of 27.6 months. The 1- and 3-year rates of LTP-free survival were 78.57% and 69.56% in the combination therapy cohort, vs. 72.45% and 35.44% in the MWA cohort, respectively ($P = 0.001$). The overall progression-free survival was longer in the combination therapy cohort compared with the MWA cohort (median: 56.0 vs. 13.0 months; $P = 0.017$). With the incorporation of additional locoregional therapy, the overall survival rates were not significantly different, with 1- and 3-year overall survival rates of 100.00% and 88.71% in the combination therapy cohort and rates of 90.15% and 82.76% in the MWA cohort, respectively ($P = 0.235$).

**CONCLUSION**

The combination therapy provided significantly longer upfront LTP-free survival in HCCs >3 cm when compared with the MWA treatment alone, albeit with similar local tumor control and overall survival rates when accounting for additional locoregional therapies.

**KEYWORDS**

Combination therapy, hepatocellular carcinoma, liver, transarterial chemoembolization, tumor ablation, combined therapy, comparative study

From the Department of Radiology (J.C. cjchiang@
mednet.ucla.edu ✉, P.S.R., F.H., J.S., S.S.R., D.S.K.,L., J.P.M.),
Ronald Reagan UCLA Medical Center, Los Angeles,
California, USA

Hepatocellular carcinoma (HCC) is the most common form of primary liver cancer worldwide and continues to rise in incidence in the United States due to non-alcoholic steatohepatitis.[1] The Barcelona Clinic Liver Cancer (BCLC) staging system provides a framework for addressing the treatment of HCC based on liver function, tumor burden, macrovascular invasion, extrahepatic spread, and performance status.[2] For very early and early-stage HCC, surgery and thermal ablation are utilized with curative intent. Thermal ablation techniques have improved over the past 20 years to become the standard of care for

the treatment of unresectable HCCs <3 cm in diameter, with efficacy and survival rates approaching that of surgical resection at centers of excellence.[3]

Microwave ablation (MWA) has supplanted traditional radiofrequency ablation (RFA) as the preferred thermal ablation modality for HCC due to its ability to create larger and more homogeneous ablation zones with less heat-sink effects compared with RFA.[4] These heating advantages have led to its rapid adoption for HCC treatments, especially for HCC lesions >3 cm in diameter. The use of the latest generation MWA devices, including high-powered gas-cooled MWA devices, while the integration of multiple antennas simultaneously enables the safe and effective treatment of HCCs of up to 5 cm in diameter, with a treatment efficacy approaching that achieved with smaller HCCs.[5]

There has also been interest in exploiting the dual synergy between transarterial chemoembolization (TACE) therapy in conjunction with MWA to treat large tumors more effectively. First, TACE decreases the arterial blood flow to HCC lesions, mitigating the heat-sink effects and amplifying the heating capabilities of MWA, leading to larger ablation zones.[6] Second, TACE also delivers cytotoxic drugs to segmental or subsegmental regions of the tumor-bearing liver, thereby treating imaging-occult, microscopic satellite HCCs that are associated with larger HCC lesions.[7] These dual synergies (combination therapy) of TACE and MWA have led to overall improved primary efficacy and progression-free survival in larger tumor cases when compared with monotherapy TACE.[8] However, this treatment strategy requires two interventional procedures to be delivered upfront instead of one.

---

**Main points**

- The combination transarterial chemoembolization–microwave ablation (MWA) therapy provided significantly longer overall progression-free survival compared with MWA monotherapy alone (56 vs. 13 months, $P$ = 0.017) in hepatocellular carcinomas >3 cm.

- The local tumor control rates, which incorporated additional locoregional therapies based on a strict follow-up protocol, were not significantly different between the treatment cohorts. However, the combination therapy still required, on average, significantly more interventional sessions to achieve the equivalent local tumor control.

- The overall survival rates were not significantly different between the combination therapy and MWA monotherapy cohorts.

---

While combination therapy and MWA monotherapy have both demonstrated efficacy in treating large solitary tumors, there have been limited studies comparing the two treatment strategies.[9-11] The present study aimed to evaluate the efficacy of TACE–MWA combination therapy vs. MWA monotherapy in patients with HCCs >3 cm in size.

## Methods

This two-arm retrospective observational study was approved by the Ronald Reagan UCLA Medical Center Institutional Review Board, and the need for patient consent was waived (UCLA IRB, IRB#19-001363; approved 9/6/2019). The study comprised patients with HCC lesions >3 cm with Childs–Pugh A/B liver function who underwent MWA or combination therapy between 2014 and 2020 at a single, high-volume tertiary medical center. All patients with vascular invasion or portal vein thrombosis, inadequate follow-up imaging, or prior treatment (including liver transplant) were excluded (Figure 1). The HCC was confirmed using multiphasic computed tomography (CT) or magnetic resonance imaging (MRI) criteria and was stratified according to the Liver Reporting and Data System classification method within 90 days of treatment. The patients were presented to a multidisciplinary board with recommendations for locoregional therapy for curative intent or a bridge to transplant.

### Combination transarterial chemoembolization–microwave ablation procedure

The TACE procedures were performed by two board-certified interventional radiologists (J.P.M., F.H.) with 3–12 years of experience in intra-arterial therapies. The procedures were performed under moderate sedation in an angiography suite with cone-beam CT capabilities. Arterial access was obtained via ultrasound-guided femoral or radial arterial puncture. Visceral and hepatic angiography was performed, with most treatments delivered superselectively. Once an appropriate catheter position was obtained, TACE was performed. Drug-eluting beads (DEBs) were utilized in 19 (65.52%) of the cases, with a mean dose of 58.67 ± 23.34 mg of doxorubicin incubated on either 100–300 μm low-compression beads (LC Bead™, Boston Scientific, USA) (n = 12) or 75 μm oncozene beads (Varian Medical Systems, USA) (n = 5), or a combination of 75 μm oncozene with 300–500 μm LC beads (n = 2), and administered under fluoroscopic guidance until stasis in the tumor-bearing branches was achieved. Depending on user preference, in

some cases, additional bland embolic material, such as Gelfoam® (n = 3) or 100–300 μm embospheres (Merit Medical Systems, USA) (n = 5) were administered after DEBs were delivered.

Conventional TACE was performed in 10 (34.48%) cases, using a mean dose of 30.80 ± 15.25 doxorubicin mixed with lipiodol (Guerbet, LLC, USA) in a 1:2 ratio, and was administered under fluoroscopic guidance until stasis in the tumor-bearing branches was achieved. Additional bland embolization was administered in some cases, which included gelfoam (n = 3), 100–300 μm embospheres (n = 1), and 40–120 μm embospheres (n = 1). Within 4 weeks (14 ± 7 days) after the TACE procedure, MWA was performed using the protocol described above.

### Microwave ablation procedure

Percutaneous MWA in an outpatient setting was performed by one of four interventional radiologists (D.S.K.L., S.R.R., J.P.M, F.H.) with 3–27 years of experience with liver tumor ablation using combined ultrasound and CT guidance. All patients underwent monitored or general anesthesia, administered by an anesthesiologist. For all included cases, a 2.45 GHz MWA device (Neuwave Medical, USA) was used. The number of antennas, ablation stations, and the ablation power and time were determined by the attending physician with the goal of a 5 mm minimum ablation margin (Table 1). Hydrodissection was utilized for subcapsular tumor locations when needed to minimize the risk to adjacent sensitive organs such as the diaphragm or bowel.

### Assessment of treatment response

The standard imaging protocol included contrast-enhanced CT at the conclusion of the procedure, or same-day MRI prior to discharge. In some cases, post-ablation MRI was performed in an outpatient capacity in the days following the ablation. Surveillance imaging was performed at 1, 3, 6, 9, and 12 months after ablation and every 3–6 months thereafter. The definitions of treatment response were based on the Society of Interventional Radiology (SIR) Standardization of Terminology and Reporting.[12] Technical success was defined as complete tumor coverage by the ablation zone on the first post-ablation multiphasic contrast-enhanced CT or MRI. An ablation treatment course was defined as all ablation sessions performed per nodule based on surveillance imaging for up to 3 months. Primary technique efficacy was

**Table 1.** Patient and tumor characteristics

| Characteristics | MWA (n = 35) | TACE + MWA (n = 29) | P value |
|---|---|---|---|
| Age (year) | 67.26 ± 8.86 | 65.13 ± 9.19 | 0.443 |
| Male sex, % | 29 (82.86) | 23 (79.31) | 0.717 |
| BMI (kg/m³) | 27.35 ± 6.67 | 27.83 ± 5.74 | 0.586 |
| **ECOG performance status, %** | | | 0.624 |
| 0 | 19 (54.28) | 20 (68.97) | |
| 1 | 12 (34.29) | 8 (27.59) | |
| 2 | 3 (8.57) | 1 (3.45) | |
| 3 | 1 (2.86) | 0 (0.00) | |
| **Child–Pugh class, %** | | | 0.835 |
| A | 27 (77.14) | 23 (79.31) | |
| B | 8 (22.86) | 6 (20/69) | |
| **Etiology of liver disease, %** | | | |
| HBV | 13 (37.14) | 2 (6.90) | 0.005 |
| HCV | 11 (31.43) | 17 (58.62) | 0.029 |
| Alcohol | 2 (5.71) | 4 (13.79) | 0.397 |
| NASH | 3 (8.57) | 2 (6.90) | 1.000 |
| PSC | 0 (0.00) | 1 (3.45) | 0.453 |
| HCV/Alcohol | 4 (11.43) | 2 (6.90) | 0.681 |
| HCV/NASH | 2 (5.71) | 0 (0.00) | 0.497 |
| Other | 0 (0.00) | 1 (3.45) | 0.453 |
| Multifocal, % | 10 (28.57) | 6 (20.69) | 0.469 |
| AFP (ng/mL) | 13.60 (4.55–50.25) | 11.70 (4.60–159.88) | 0.852 |
| Tumor size (cm) | 3.69 ± 0.62 | 4.18 ± 0.85 | 0.009 |
| **Tumor lobe, %** | | | 0.717 |
| Left | 6 (17.14) | 6 (20.69) | |
| Right | 29 (82.86) | 23 (79.31) | |
| Well-circumscribed margin, % | 23 (65.71) | 19 (65.52) | 0.987 |
| Subcapsular location, % | 29 (82.86) | 19 (65.52) | 0.111 |
| Peribiliary location, % | 4 (11.43) | 10 (34.48) | 0.026 |
| Perivascular location, % | 10 (28.57) | 18 (62.07) | 0.007 |
| **Organ at risk, %** | | | |
| Heart | 0 (0.00) | 3 (10.34) | 0.088 |
| Esophagus | 1 (2.86) | 0 (0.00) | 1.000 |
| Stomach | 1 (2.86) | 1 (3.45) | 1.000 |
| Diaphragm | 13 (37.14) | 8 (27.59) | 0.418 |
| Gallbladder/bile duct | 0 (0.00) | 1 (3.45) | 0.453 |
| Colon | 4 (11.43) | 1 (3.45) | 0.366 |
| Adrenal/kidney | 2 (5.71) | 2 (6.90) | 1.000 |
| Varix | 0 (0.00) | 1 (3.45) | 0.453 |

Demographic and baseline clinical characteristics of the study groups. Continuous variables with normal distribution were expressed as mean ± standard deviation; those with non-normal distributions were expressed as median (interquartile range). BMI, body mass index; HBV, hepatitis B; HCV, hepatitis C; ECOG, Eastern Cooperative Oncology Group; MWA, microwave ablation; NASH, non-alcoholic steatohepatitis; TACE, transarterial chemoembolization; PSC, primary sclerosing cholangitis; AFP: alpha fetal protein.

symptoms, imaging results, and laboratory evaluations after treatment and stratified according to SIR standard classification.[13]

The median follow-up period was 14 months [interquartile range (IQR): 9.50–19.25 months] in the combination therapy cohort and 18 months (IQR: 11.50–29.50 months) in the MWA cohort. The primary endpoints of this study were overall survival and primary technique efficacy. The secondary endpoints included local tumor control rate and safety.

### Statistical analysis

The follow-up period ended at the time of death, liver transplantation, or the final clinical follow-up evaluation. The differences among the treatment groups were analyzed using a t-test for normally distributed variables (confirmed by a Kolmogorov–Smirnov test) or a Mann–Whitney U test for non-normally distributed continuous variables. Fisher's exact test or the Fisher–Freeman–Halton exact test, as well as Pearson's chi-squared test, were performed for all categorical variables. The descriptive statistics were described as mean ± standard deviation for normally distributed numeric variables and as median (IQR) for non-normally distributed numeric variables. The descriptive term, n (%), was used for all categorical variables. Kaplan–Meier analysis using the Fleming–Harrington test was utilized to identify differences in survival times.[14] The Fleming–Harrington test was selected rather than the traditional log-rank test since the survival curves overlapped on the later follow-up studies, and our intention was to highlight the longer-term effects of the interventions.[15,16] The follow-up time for the Kaplan–Meier curves was reported as mean ± standard error of the mean, as well as the median when available. For the LTP analysis, the patients were censored at the time of death, liver transplant, or loss to follow-up. Fisher's exact test was used to compare the local tumor control rates and primary technique efficacy. A P value of <0.050 was considered statistically significant. The entire statistical analysis was performed using GraphPad Prism v.9 (GraphPad Software Inc.) and Stata Statistical Software v.15 (StataCorp LLC).

## Results

### Baseline patient characteristics

The overall study group comprised 29 patients (23 men, 6 women) in the combination therapy group and 35 (29 men, 6 women) in the MWA group. The tumor diameter in the combination and MWA cohorts was 4.18 ± 0.85 and 3.69 ± 0.62 cm (P = 0.009),

defined as no evidence of residual tumor at the ablation site at the conclusion of the initial ablation treatment course. Local tumor progression (LTP) could be re-treated with ablative therapy for continued local tumor control and the patient would still be considered locally disease-free.[5] Adverse events were determined according to the clinical

**Table 2.** Ablation parameters

| Parameter | MWA (n = 35) | TACE+MWA (n = 29) | P value |
|---|---|---|---|
| **MWA** | | | |
| No. ablation positions | 1.00 (1.00–2.00) | 2.00 (1.00–2.00) | 0.307 |
| No. probes | 2.14 ± 0.47 | 2.05 ± 0.52 | 0.303 |
| Duration (min) | 11.57 ± 6.10 | 11.75 ± 5.74 | 0.867 |
| Energy (W) | 70.06 ± 11.87 | 68.06 ± 8.93 | 0.541 |
| Technical success, % | 32 (91.43) | 28 (96.55) | 0.620 |

Ablation parameters in the monotherapy microwave ablation and combination therapy group. Continuous variables with normal distribution were expressed as mean ± standard deviation; those with non-normal distributions were expressed as median (interquartile range). Technical success for MWA was defined as complete tumor coverage by ablation zone on the first follow-up imaging performed within 1 month after ablation. MWA, microwave ablation; TACE, transarterial chemoembolization.
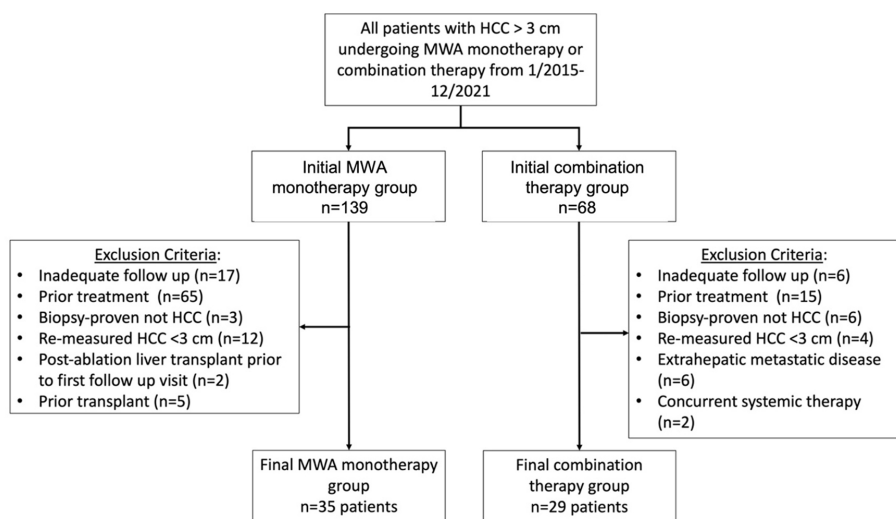


**Figure 1.** Comparative flow chart showing the participant selection and exclusion criteria. MWA, microwave ablation; HCC, hepatocellular carcinoma.
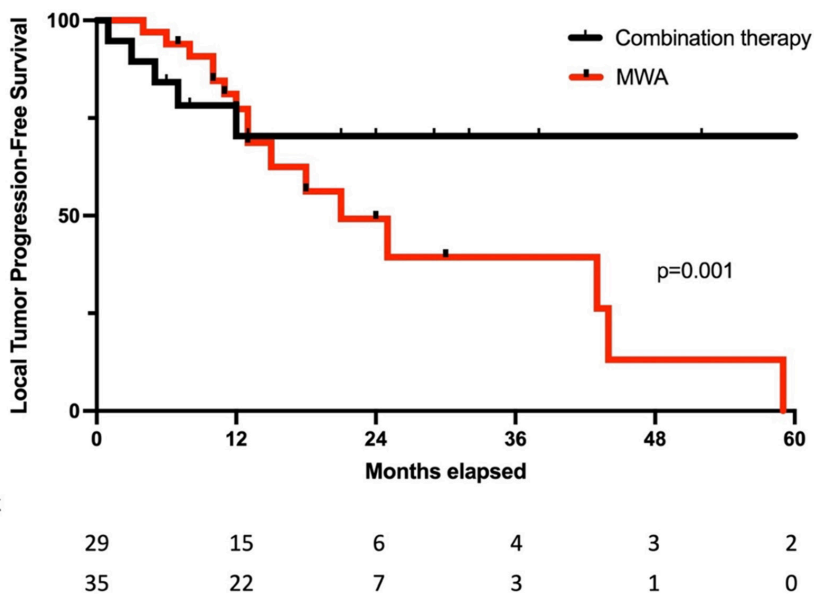


**Figure 2.** Local tumor progression (LTP)-free survival in the patient groups over 5 years. Significantly longer LTP-free survival was demonstrated (Fleming–Harrington test) in the combination therapy group compared with the microwave ablation-only group (P = 0.001). MWA, microwave ablation.

respectively, with a higher proportion of HCC lesions in the combination cohort being perivascular (62.07% vs. 28.57%; P = 0.007) in location. There were significantly more patients with hepatitis C in the combination therapy group (58.62% vs. 31.43%; P = 0.029), while there were significantly more patients with hepatitis B in the MWA group (37.14% vs. 6.90%, P = 0.005). The patient demographics, underlying causes of HCC, and tumor characteristics are presented in Table 1.

## Technical success and primary technique efficacy rate

In the 29-patient combination therapy cohort, one patient (3.45%) presented with imaging-based residual disease within 3 months post-therapy, resulting in a technical success rate of (28) 96.55%. After retreatment with MWA, there were no additional patients with residual diseases at the 3 month time point, resulting in a primary technical efficacy rate of (29) 100.00%.

In the 35-patient MWA therapy cohort, three patients (8.57%) presented with an imaging-based residual disease following ablation within 3 months, resulting in a technical success rate of (32) 91.43%. After successful retreatment with MWA, there was no demonstrable residual disease at the 3-month time point, resulting in a primary technique efficacy of (35) 100.00%. Ablation parameters in each cohort are shown in Table 2.

## Local tumor progression and local tumor control rate

The overall rate of LTP was significantly lower in the combination therapy cohort (8%, 27.59%) compared with the MWA therapy cohort (19%, 54.29%) (P = 0.031). The 1- and 3-year LTP-free survival rates were 78.57% and 69.56% in the combination therapy cohort and 72.45% and 35.44% in the MWA therapy cohort. Compared with the MWA cohort, the combination therapy cohort had significantly longer LTP-free survival times according to Kaplan–Meier analysis [47.75 ± 5.44 (median not reached) vs. 22.82 ± 3.13 months (median: 13.00 months); P = 0.001] (Figure 2). In the combination therapy cohort, the LTP in six tumors was successfully re-treated via MWA, leading to a local tumor control rate of (27) 93.10%. The other two patients were treated palliatively with systemic therapies. In the MWA cohort, the LTP in 15 tumors was successfully re-treated via additional MWA, yielding a local tumor control rate of (31) 88.57%. Overall, there was

no significant difference in the combination cohort compared with the MWA cohort in terms of local tumor control rate [58.02 ± 5.98 (median not reached) vs. 62.33 ± 5.98 months (median: 72.00 months); P = 0.377] (Figure 3). The remaining patients were not retreated due to medical comorbidities or were treated palliatively with TACE, radioembolization, or systemic therapies. A summary of the follow-up time, rate of tumor progression, rate of transplant, and additional therapies are presented in Table 3.

## Extra-segmental progression and overall progression-free survival

The rate of extra-segmental progression over the study period was significantly lower in the combination therapy cohort than in the MWA therapy cohort (8%, 27.58% vs. 20%, 57.14%; P = 0.018). There was also a smaller rate for extrahepatic metastasis in the combination therapy group (2%, 6.90% vs. 6%, 17.14%; P = 0.275), albeit not significantly so. The 1- and 3-year rates of total tumor progression-free survival were 68.28%

and 51.21% for the combination therapy cohort and 68.57% and 11.15% for the MWA therapy cohort. The overall progression-free survival was observably longer in the combination therapy cohort than in the MWA cohort [33.35 ± 5.57 (median: 56.00 months) vs. 14.11 ± 1.65 months (median: 13.00 months)] according to the Kaplan–Meier analysis (P = 0.017) (Figure 4).

## Overall survival and transplant rates

Within the follow-up period, three patients in the combination therapy group and four in the MWA therapy cohort died. Six of the seven patients died from HCC progression, and one patient in the MWA cohort died from renal failure. The 1- and 3-year overall survival rates were 100.00% and 88.71% in the combination therapy cohort, and 90.15% and 82.76% in the MWA therapy cohort, with an overall survival of 58.24 ± 4.15 months (median not reached) and 61.21 ± 5.02 months (median not reached), respectively (P = 0.235) (Figure 5).

## Total number of treatment sessions

Overall, additional locoregional therapies were performed more frequently for the MWA monotherapy patients compared with the combination therapy group to achieve the aforementioned local tumor control and overall survival rates (Table 3). However, considering that the combination therapy comprised two interventional procedures upfront, the median number of procedures per patient over the lifetime of the patient's treatment was 1.00 (1.00–2.00) in the monotherapy group and 2.00 (2.00–2.50) in the combination therapy group (P < 0.001).

## Adverse events

There was one severe adverse event (AE) in the combination therapy cohort, which was an unexpected elevation in serum bilirubin due to biliary stricture following the ablation procedure. This stricture required the placement of an external biliary drain for decompression, which was subsequently converted to an internal–external biliary drain.[17] There were also two moderate AEs among the patients in the combination therapy cohort, including one patient who developed hepatic encephalopathy requiring the initiation of lactulose and another who had slight asymptomatic intracapsular bleeding during placement of the microwave antenna, which was resolved with subsequent thermal coagulation using the MWA probe. To minimize the risk of infection, the hematoma was aspirated with an 8 French pigtail
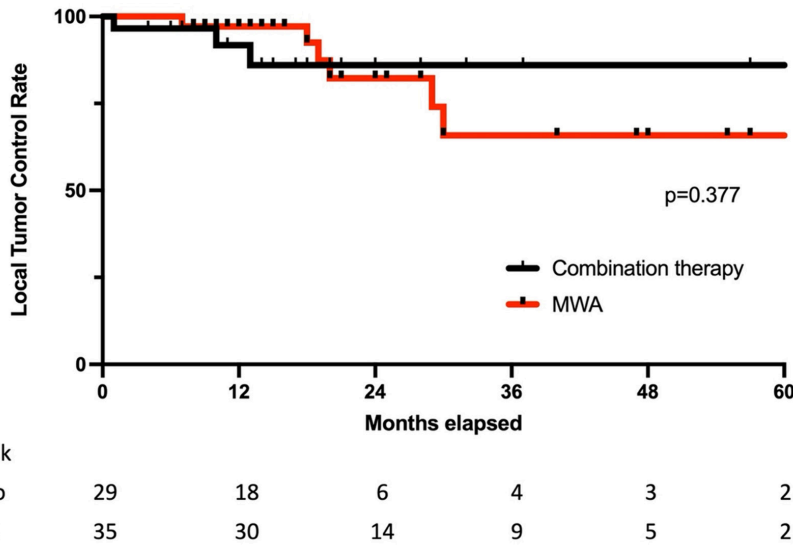


**Figure 3.** Local tumor control rate in the patient groups, which included additional locoregional therapy, over 5 years. There was an equivalent local tumor control rate (Fleming–Harrington test) in the combination therapy group compared with the MWA-only group (P = 0.377). MWA, microwave ablation.

| Table 3. Follow-up and disease progression | | | |
|---|---|---|---|
| | MWA (n = 35) | TACE+MWA (n = 29) | P value |
| Follow-up time (months) | 14 (9.50–19.25) | 18 (11.50–29.50) | 0.295 |
| **Disease progression, %** | | | |
| Local recurrence | 19 (54.43) | 8 (27.59) | 0.031 |
| Extra-segmental progression | 20 (57.14) | 8 (27.59) | 0.018 |
| Extrahepatic metastases | 6 (17.14) | 2 (6.90) | 0.275 |
| Transplant, % | 6 (17.14) | 6 (20.69) | 0.717 |
| Death, % | 4 (11.43) | 3 (10.34) | 1.000 |
| **Additional locoregional therapies to achieve local control, %** | | | |
| MWA | 16 (45.71) | 6 (20.69) | 0.036 |
| TACE | 5 (14.29) | 0 (0.00) | 0.058 |
| Y-90 | 3 (8.57) | 0 (0.00) | 0.243 |
| Systemic therapy, % | 3(8.57) | 3 (10.34) | 1.000 |
| Total number of locoregional therapies per patient to achieve local control | 1.00 (1.00–2.00) | 2.00 (2.00–2.50) | <0.001 |

Clinical follow-up from monotherapy microwave ablation and combination therapy group. Continuous variables with non-normal distributions were expressed as median (interquartile range). Additional locoregional therapies include those performed as part of the initial course of ablation therapy. The total number of locoregional therapies includes every interventional procedure over the lifetime of the patient's treatment for HCC. MWA, microwave ablation; TACE, transarterial chemoembolization; Y-90, Yttrium-90.
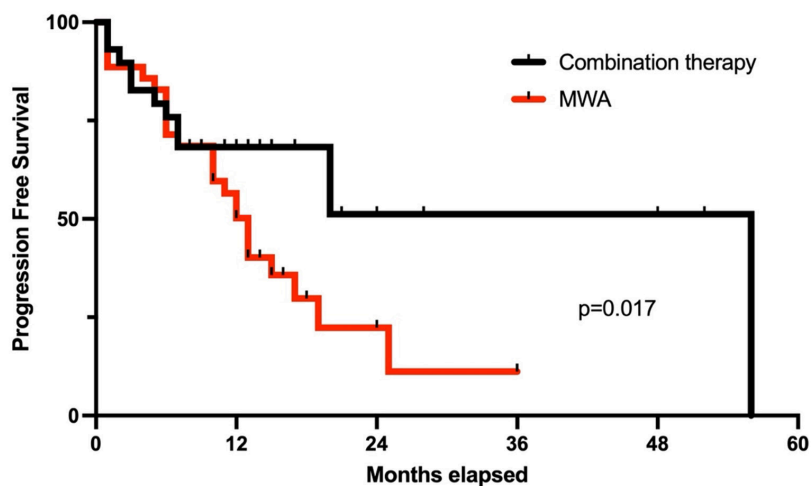
**Figure 4.** Overall progression-free survival in the patient groups over 5 years. The Fleming–Harrington test indicated longer overall progression-free survival in the combination therapy group compared with the MWA-only group (*P* = 0.017). MWA, microwave ablation.
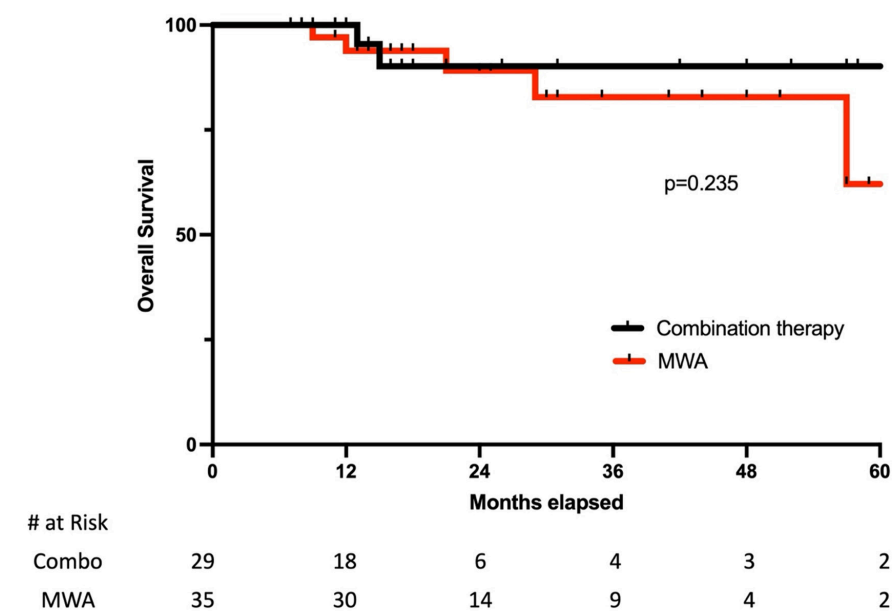


**Figure 5.** Overall survival over 5 years. The Fleming–Harrington test indicated an equivalent survival rate in the combination therapy group compared with the MWA-only group (*P* = 0.235). MWA, microwave ablation.

drain and the drain was removed at the end of the treatment without further sequelae. There were two mild AEs in the MWA cohort, both of which were asymptomatic hepatic dysfunction based on abnormal laboratory values. Both patients were followed closely, and their hepatic dysfunction was resolved without any further therapy. The rate of fever was (12) 41.38% and (3) 8.57% (*P* = 0.003) in the combination and MWA therapy cohorts, respectively, but without significant differences in the rates of post-procedural abdominal pain, chest pain, nausea/vomiting, fatigue, or confusion (Table 4).

## Discussion

This study demonstrated that combination therapy is associated with significantly longer initial LTP-free and total progression-free survival rates compared with MWA therapy alone for HCC lesions >3 cm, while the overall survival rates at 5 years and the progression to liver transplantation rates were similar. The local tumor control rates, which incorporated additional locoregional therapies, based on a strict follow-up protocol, were not significantly different between the treatment cohorts. However, on average, the combination therapy required significantly more interventional sessions to achieve the equivalent local tumor control rate.

The efficacy of combination therapy compared with ablation monotherapy remains under active investigation. While prior studies have focused more on comparing combination therapy with RFA, more recent research evaluated the utility of MWA, with most outcomes supporting combination therapy over MWA alone. Recently, a randomized controlled three-arm trial compared the efficacy of MWA with TACE and combination therapy for HCCs of 3–5 cm in size. The trial results indicated that combination therapy achieved a complete response in 86.5% of the patients, while monotherapy using TACE achieved a complete response in 54.8% and MWA in 56.5%. The recurrence rate after 1 year was significantly lower in the combination group (22.5%) compared with the MWA-only (51.1%) and TACE-only (60.7%) groups. There was also a significantly higher rate of median survival in the combination group than in the TACE and MWA groups (24 months vs. 19 and 21 months, respectively).[9] Another single-center retrospective study looked at propensity-matched BCLC stage B patients with HCC who had undergone either combination therapy or TACE monotherapy for tumors <7 cm.[10] In the above study, the combination therapy significantly improved progression-free survival and overall survival compared with TACE only, with the former returning a tumor control rate of 74.0% and 47.8% at 6 months and 1 year and the latter returning rates of 55.5% and 37.3%. The median survival time of the combination therapy cohort was 18.5 months compared with 14.8 months in the TACE monotherapy cohort. Similarly, in a study of 3–5-cm HCCs, Smolock et al.[18] reported that TACE–MWA combination therapy was associated with a lower rate of LTP compared with TACE monotherapy (34.8% vs. 62.5%) and longer median progression-free survival (22.3 vs. 4.2 months). Conversely, a recent retrospective study with propensity matching did not report any therapeutic superiority in combination vs. MWA therapy for 150 patients in BCLC stage B with a mean tumor diameter >6 cm.[11] However, a sub-cohort analysis of the above study found that tumor number and size were independent risk factors for long-term outcomes, with better LTP and survival rates indicated for combination therapy in tumors >7 cm.

The improved efficacy of combination therapy may be related to the dual syner-

**Table 4.** Post-procedural complications

|  | MWA (n = 35) | TACE + MWA (n = 29) | *P* value |
|---|---|---|---|
| Procedural site pain, % | 1 (2.86) | 2 (6.90) | 0.586 |
| Chest pain, % | 1 (2.86) | 0 (0.00) | 1.000 |
| Shortness of breath, % | 1 (2.86) | 3 (10.34) | 0.321 |
| Fever, % | 3 (8.57) | 12 (41.38) | 0.002 |
| Nausea/vomiting, % | 0 (0.00) | 3 (10.34) | 0.088 |
| Confusion, % | 4 (11.43) | 5 (17.24) | 0.720 |
| Fatigue, % | 0 (0.00) | 1 (3.45) | 0.453 |
| Lower extremity edema, % | 1 (2.86) | 0 (0.00) | 1.000 |
| Acute kidney injury, % | 0 (0.00) | 1 (3.45) | 0.453 |
| Urinary retention, % | 0 (0.00) | 1 (3.45) | 0.453 |

Post-procedural complications from the microwave ablation (MWA) and combination therapy group [transarterial chemoembolization (TACE) + MWA].

gistic effect of TACE and MWA. In this study, TACE preceded MWA by an average of 14 days. The TACE procedure is known to have an embolic effect on the tumor microvasculature of HCCs, decreasing the blood flow to minimize the heat-sink effect and resulting in larger, more homogeneous ablation zones.[19-21] However, if too much time elapses after embolization, as a growing body of literature suggests, the region may become hypoxic, potentially imparting pro-tumorigenic pathways.[22] Thus, the amount of time that elapses between TACE and ablation is important for maximizing the therapeutic response, although there is only limited evidence supporting an optimal timepoint.[23] The intra-arterial nature of TACE also allows therapeutic agents to be delivered to an entire liver segment or sub-segment, potentially treating imaging-occult satellite lesions surrounding an index tumor that may be located outside of the tumor capsule.[7] While the primary technical efficacy rate of MWA monotherapy may be compromised by the presence of nearby satellite lesions, combination therapy with prior TACE could effectively treat microscopic diseases, maximize MWA efficacy, and minimize the risk of incomplete treatment.

There are aspects of this study that may limit the comparisons and generalizability to a broader patient population. First, the MWA cohort had a smaller mean tumor size than the combination therapy cohort. Larger tumors may be more resistant to locoregional therapy and are generally associated with higher rates of tumor progression and poorer overall survival rates. Second, there was a heterogenous institutional protocol for embolization, with most patients receiving DEB–TACE, but a non-negligible number

of patients receiving conventional TACE. Furthermore, there were significantly higher proportions of patients with hepatitis B in the MWA-only group and hepatitis C in the combination therapy group, which may have confounded the study endpoints. The baseline patient population in each study cohort was otherwise well-matched; however, the restrictive tumor size and liver function criteria led to a small study population that made it difficult to perform further sub-group analysis.

In conclusion, this study confirms that combination therapy can achieve significantly higher initial upfront local tumor control rates compared with MWA therapy alone for HCCs >3 cm without increased rates of adverse events. While the combination therapy cohort had a larger mean tumor size compared with the MWA cohort, the combination therapy patients required, on average, a higher number of total procedures due to the upfront performance of two separate interventions. The overall survival and major complication rates were comparable between the two groups when a strict follow-up protocol and additional necessary treatments were incorporated into the overall treatment strategy. A prospective trial is warranted for providing better evidence and an understanding of how to stratify patients into combination vs. MWA therapy for intermediate-to-large-size HCCs.

### Conflict of interest disclosure

J.P.M., D.S.K.L., S.S.R. has received speaker fees from Neuwave Medical Inc.  D.S.K.L and S.S.R. has received speaker fees from Covidien.

## References

1. Llovet JM, Kelley RK, Villanueva A, et al. Hepatocellular carcinoma. *Nat Rev Dis Primers*. 2021;7(1):6. [CrossRef]

2. Reig M, Forner A, Rimola J, et al. BCLC strategy for prognosis prediction and treatment recommendation: The 2022 update. *J Hepatol*. 2022;76(3):681-693. [CrossRef]

3. Lai ECH, Tang CN. Radiofrequency ablation versus hepatic resection for hepatocellular carcinoma within the Milan criteria--a comparative study. *Int J Surg*. 2013;11(1):77-80. [CrossRef]

4. Brace CL. Microwave tissue ablation: biophysics, technology, and applications. *Crit Rev Biomed Eng*. 2010;38(1):65-78. [CrossRef]

5. Thamtorawat S, Hicks RM, Yu J, et al. Preliminary outcome of microwave ablation of hepatocellular carcinoma: breaking the 3-cm barrier? *J Vasc Interv Radiol*. 2016;27(5):623-630. [CrossRef]

6. de Baere T, Arai Y, Lencioni R, et al. Treatment of Liver Tumors with Lipiodol TACE: technical recommendations from experts opinion. *Cardiovasc Intervent Radiol*. 2016;39(3):334-343. [CrossRef]

7. Wang W, Guo Y, Zhong J, et al. The clinical significance of microvascular invasion in the surgical planning and postoperative sequential treatment in hepatocellular carcinoma. *Sci Rep*. 2021;11(1):2415. [CrossRef]

8. English K, Brodin NP, Shankar V, et al. Association of addition of ablative therapy following transarterial chemoembolization with survival rates in patients with hepatocellular carcinoma. *JAMA Netw Open*. 2020;3(11):e2023942. [CrossRef]

9. Zaitoun MMA, Elsayed SB, Zaitoun NA, et al. Combined therapy with conventional transarterial chemoembolization (cTACE) and microwave ablation (MWA) for hepatocellular carcinoma >3–<5 cm. *Int J Hyperthermia*. 2021;38(1):248-256. [CrossRef]

10. Zhang R, Shen L, Zhao L, Guan Z, Chen Q, Li W. Combined transarterial chemoembolization and microwave ablation versus transarterial chemoembolization in BCLC stage B hepatocellular carcinoma. *Diagn Interv Radiol*. 2018;24(4):219-224. [CrossRef]

11. Li X, Chen B, An C, et al. Transarterial chemoembolization combined with microwave ablation versus microwave ablation only for Barcelona Clinic Liver Cancer Stage B hepatocellular carcinoma: a propensity score matching study. *J Cancer Res Ther*. 2020;16(5):1027-1037. [CrossRef]

12. Ahmed M; Technology Assessment Committee of the Society of Interventional Radiology. Image-guided tumor ablation: standardization of terminology and reporting criteria--a 10-year update: supplement to the

consensus document. *J Vasc Interv Radiol*. 2014;25(11):1706-1708. [CrossRef]

13. Khalilzadeh O, Baerlocher MO, Shyn PB, et al. Proposal of a new adverse event classification by the society of interventional radiology standards of practice committee. *J Vasc Interv Radiol*. 2017;28(10):1432-1437. [CrossRef]

14. Harrington DP, Fleming TR. A class of rank test procedures for censored survival data. *Biometrika*. 1982;69(3):553-566. [CrossRef]

15. Garès V, Andrieu S, Dupuy JF, Savy N. On the Fleming-Harrington test for late effects in prevention randomized controlled trials. *J Stat Theory Pract*. 2017;11(3):418-435. [CrossRef]

16. Li H, Han D, Hou Y, Chen H, Chen Z. Statistical Inference methods for two crossing survival curves: a comparison of methods. *PLoS One*. 2015;10(1):e0116774. [CrossRef]

17. Sacks D, McClenny TE, Cardella JF, Lewis CA. Society of interventional radiology clinical practice guidelines. *J Vasc Interv Radiol*. 2003;14(9):199-202. [CrossRef]

18. Smolock AR, Cristescu MM, Hinshaw A, et al. Combination transarterial chemoembolization and microwave ablation improves local tumor control for 3- to 5-cm hepatocellular carcinoma when compared with transarterial chemoembolization alone. *Abdom Radiol* (NY). 2018;43(9):2497-2504. [CrossRef]

19. Weis S, Franke A, Mössner J, Jakobsen JC, Schoppmeyer K. Radiofrequency (thermal) ablation versus no intervention or other interventions for hepatocellular carcinoma. *Cochrane Database Syst Rev*. 2013;12:CD003046. [CrossRef]

20. Kan Z, Wallace S. Sinusoidal embolization: impact of iodized oil on hepatic microcirculation. *J Vasc Interv Radiol*. 1994;5(6):881-886. [CrossRef]

21. Lammer J, Malagari K, Vogl T, et al. Prospective randomized study of doxorubicin-eluting-bead embolization in the treatment of hepatocellular carcinoma: results of the PRECISION V study. *Cardiovasc Intervent Radiol*. 2010;33(1):41-52. [CrossRef]

22. Lai JP, Conley A, Knudsen BS, Guindi M. Hypoxia after transarterial chemoembolization may trigger a progenitor cell phenotype in hepatocellular carcinoma. *Histopathology*. 2015;67(4):442-450. [CrossRef]

23. Feng Y, Wang X, Wang L, et al. Efficacy and safety of combination therapy of chemoembolization and radiofrequency ablation with different time intervals for hepatocellular carcinoma patients. *Surg Oncol*. 2017;26(3):236-241. [CrossRef]

# Percutaneous radiologic gastrostomy with single gastropexy using balloon-assisted tract dilatation: comparison with peel-away sheath

Ji Su Lim
Gyoo Sik Jung
Kyung Seung Oh
Kyung Won Seo
Kyoungwon Jung
Jong Hyouk Yun

**PURPOSE**

To evaluate the safety and efficacy of percutaneous radiologic gastrostomy (PRG) with balloon-assisted tract dilatation (BATD) using a single gastropexy.

**METHODS**

This retrospective study was approved by the institutional review board. From August 2018 to October 2022, 61 patients (53 male and 8 female, mean age 67 years, age range 27–90 years) underwent PRG with balloon-retained tubes for enteral nutrition. Single gastropexy was performed in all cases. Patients were divided into two groups based on the tract dilatation technique used. In the first group, BATD (n = 48) was performed. In the second group, a 24-Fr peel-away sheath (PAS) was used for tract dilatation (n = 13). Patient demographics, technical success rate, clinical success rate, fluoroscopy time, cumulative radiation dose, and complications were retrospectively evaluated. The Mann–Whitney U test for continuous variables and Fisher's exact test for categorical variables were performed to compare the two groups.

**RESULTS**

All procedures were successfully performed with 100% technical and clinical success rates in both groups. The mean fluoroscopy time for the BATD group vs. the PAS group (1.68 ± 0.93 min vs. 3.56 ± 2.41 min, $P < 0.001$) and mean cumulative radiation dose (12.98 ± 9.28 mGy vs. 33.01 ± 15.14 mGy, $P < 0.001$) were significantly lower in the BATD group compared with the PAS group. There was one major complication of peritonitis that led to death in the PAS group (1/13, 7.7%) and no major complications in the BATD group. Minor complications such as pneumoperitoneum, abdominal pain, leakage, and balloon deflation occurred in 16 patients: 12 (12/48, 25.0%) patients in the BATD group and 4 (4/13, 38.5%) patients in the PAS group. The overall rate of major and minor complications was higher in the PAS group but did not show statistically significant differences (odds ratio: 1.875, 95%; confidence interval: 0.514–6.841, $P = 0.486$).

**CONCLUSION**

BATD using a single gastropexy is a safe and effective technique for PRG.

**KEYWORDS**

Fluoroscopy, gastropexy, gastrostomy, radiology, interventional, stomach

From the Department of Radiology (J.S.L., K.S.O., J.H.Y. ✉ xell1015@naver.com), Kosin University Gospel Hospital, Busan, Korea; Department of Radiology (G.S.J.), Ulsan Hospital, Ulsan, Korea; Department of Surgery (K.W.S.), Kosin University Gospel Hospital, Busan, Korea; Department of Internal Medicine (K.J.), Kosin University Gospel Hospital, Busan, Korea.

Percutaneous radiologic gastrostomy (PRG) is an enteral nutrition method widely performed in patients in whom oral intake is unsafe or impossible and is now widely recognized as a safe procedure with low complication rates.[1,2] Since Preshaw[3] first performed PRG in 1981, the procedure's anchor technique and method of tract dilatation have undergone several modifications.

A previous study reported that PRG with a single gastropexy using a tract separate from the one used for tube placement is technically feasible and has a low complication rate.[4] However, the study only placed 12- or 14-Fr pigtail-retained catheters, which are not currently

available in Korea, and used dilators for tract dilatation. In addition, several researchers have reported that small-bore gastrostomy tubes are more prone to tube dysfunction, and large-bore tubes perform better in terms of the time it takes to achieve the feeding goal.[5,6] Another study reported on the safety and effectiveness of large-bore gastrostomy catheter placement using balloon-assisted tract dilatation (BATD), but the study used three gastropexy T-fasteners for stomach fixation.[7]

To date, there is no report of PRG with a single gastropexy using BATD. The aim of this study was to compare this technique to conventional methods using a peel-away sheath (PAS) and assess BATD's technical feasibility and overall complication rate.

# Methods

## Patients

This is a retrospective study that was approved by the Kosin University Gospel Hospital (KUGH 2022-08-014, 25/08/2022). Due to the retrospective nature of the study, informed consent of the patients was not required.

From August 2018 to October 2022, 61 patients who underwent PRG with balloon-retained tubes for enteral nutrition were included in this study. The mean age of the patients was 67 (range: 27–90) years, and there were 53 males and 8 females. Underlying diseases included head and neck cancer (n = 29), esophageal cancer (n = 14), cerebrovascular disease (n = 10), dysphagia (n = 4), Parkinson's disease (n = 2), benign esophageal stricture (n = 1), and tracheostomy state (n = 1). Patients were divided into two groups based on the types of tract dilatation techniques used. In the first group, the authors used the BATD technique (n = 48, 78.7%). In the second group, tract dilatation was performed using a 24-Fr PAS (n = 13, 21.3%).

### Main points

- Percutaneous radiologic gastrostomy (PRG) is a procedure widely performed in patients with conditions that make oral intake unsafe or impossible.

- There have been several modifications of the PRG procedure in anchor technique and method of tract dilatation.

- PRG with a single gastropexy using balloon-assisted tract dilatation appears to be a safe and effective technique.

The baseline characteristics of all patients are presented in Table 1.

## Technique

All procedures were performed by two board-certified interventional radiologists at our hospital. Gastrostomy procedures were performed under fluoroscopic guidance using local anesthesia without intravenous sedation, and all patients received balloon-retained catheters.

Patients fasted for at least 24 hours before the procedure and received 20 mg of butylscopolamine just before the procedure. The abdomen was prepped and draped in a sterile fashion. Through an indwelling nasogastric tube, the stomach was inflated with approximately 500 mL of air. Under fluoroscopic and ultrasound guidance, a site for gastrostomy placement was selected and marked in the epigastric region, avoiding the transverse colon and left lobe of the liver. Local anesthesia was administered at the selected site for gastropexy and gastrostomy. In this region, an incision of approximately 5 mm was made in the skin, and a 17-gauge introducer needle preloaded with an anchor (Cope Gastrointestinal Suture Anchor Set, Cook, Bloomington, IN, USA) was used to access the insufflated stomach. Then, a single suture anchor was deployed and pulled tight to fix the anterior stomach wall against the abdominal wall. After using fluoroscopy to confirm its location within the stomach, a 0.035-inch guidewire was passed into the stomach, and a small dilator (8-Fr) was introduced over the guidewire.

In the BATD group, an Amplatz Super Stiff Guidewire (Boston Scientific, Marlborough,

MA, USA) was also inserted into the stomach through the dilator, and the gastrostomy tube (Entuit Gastrostomy BR Balloon Retention Feeding Tube, Cook, Bloomington, IN, USA) was preloaded on the shaft of a high-pressure balloon. Depending on the diameter of the tube, different balloon sizes were used: 8 mm for the 20-Fr tube, 7 mm for the 18- and 16-Fr tubes, and 6 mm for the 14-Fr tube. The inflation time for ballooning was approximately 30 seconds. As the balloon was deflated, the gastrostomy tube and balloon catheter were advanced together over the wire into the stomach. After removal of the balloon catheter, the retention balloon of the gastrostomy tube was then inflated with a contrast–saline mixture. A contrast medium injection was used to confirm the gastrostomy tube was in the appropriate location. The anchor was then sutured to the abdominal wall, and the gastrostomy tube was fixed to the skin (Figure 1).

In the PAS group, the tract was dilated using a telescoping serial dilator with a 24-Fr peel-away introducer sheath (Peel-away Introducer Set, Cook, Bloomington, IN, USA), and the gastrostomy tube was inserted into the stomach through the PAS. The sheath was then removed, and the retention balloon was inflated with a contrast–saline mixture. After confirming the location of the gastrostomy tube using contrast injection, a suture anchor was sutured to the skin with a small plastic disk. Suture was released 7-10 days after procedure. The sheath was then removed, and the retention balloon was inflated with a contrast–saline mixture (Figure 2).

After the procedure, patients were evaluated for pneumoperitoneum by radiograph and observance of clinical symptoms, such as abdominal pain and fever. If no abnor-

**Table 1.** Characteristics of all patients

|  | Overall (n = 61) | BATD group (n = 48) | PAS group (n = 13) |
|---|---|---|---|
| Mean age (range) | 67 (27–90) | 68 (27–90) | 62 (49–74) |
| **Sex** | | | |
| Male | 53 | 41 | 12 |
| Female | 8 | 7 | 1 |
| **Underlying disease** | | | |
| Head and neck cancer | 29 | 20 | 9 |
| Esophageal cancer | 14 | 12 | 2 |
| Cerebrovascular disease | 10 | 8 | 2 |
| Dysphagia | 4 | 4 | 0 |
| Parkinson's disease | 2 | 2 | 0 |
| Benign esophageal stricture | 1 | 1 | 0 |
| Tracheostomy state | 1 | 1 | 0 |

BATD, balloon-assisted tract dilatation; PAS, peel-away sheath.

malities were present, patients were administered 100 cc of water three times through the gastrostomy tube the day after the procedure, and if there were still no abnormal symptoms, liquid intake was initiated.

### Data collection and definition

Data from all patients were collected, reviewed, and recorded, including the radiology information system and electronic medical record (EMR).

Technical success was defined as when the gastrostomy tube was effectively placed into the stomach, and clinical success was defined as when the feeding tube functioned correctly. The follow-up period was determined as days of hospitalization after the procedure. Data on fluoroscopy time and radiation dose during the procedure were also collected. Complications were categorized as major and minor according to the Society of Interventional Radiology.[8] Major complications were defined as conditions that were life-threatening, causing gastrostomy malfunction, or requiring additional intervention. Minor complications were defined as conditions requiring only minimal medical management or local wound care.

### Statistical analysis

Univariable analyses were performed using the Mann–Whitney U test and the Fisher's exact test for continuous data and categorical data, respectively. The following data were evaluated: age, sex, underlying disease for PRG, technical and clinical success, and major or minor complications, and $P < 0.05$ was considered to indicate a statistically significant difference. All statistical analyses were performed using IBM SPSS Statistics for Windows (version 28.0. Armonk, NY: IBM Corp).

## Results

In 48 patients (78.7%), BATD was used, and the 24-Fr PAS was used in 13 patients (21.3%). A single gastropexy was performed in all cases.

In the BATD group, the mean age was 68.5 years, and in the PAS group, the mean age was 62 years. There were 7 females and 41 males in the BATD group and 1 female and 12 males in the PAS group. There was no statistical difference in the age ($P = 0.976$) and sex ($P = 0.453$) between the two groups.

The technical success rate using a single gastropexy under fluoroscopic guidance was 100% in both groups, and the clinical success rate was 100% in both groups. The mean follow-up time was 24 days (range: 1–209 days).

The diameters of the placed tubes were varied in the BATD group: 20-Fr tubes in 10 patients, 18-Fr tubes in 12 patients, 16-Fr tubes in 21 patients, and 14-Fr tubes in 5 patients. In the PAS group, all patients received a 24-Fr tube.

The mean fluoroscopy time in the BATD group was 1.68 ± 0.93 min (range: 0.68–5.93 min) and in the PAS group was 3.56 ± 2.41 min (range: 1.62–11.35 min) ($P < 0.001$). The mean radiation dose in the BATD group was 12.98 ± 9.28 mGy (range: 2.6–46.8 mGy) and in the PAS group was 33.01 ± 15.14 mGy (range: 19.0–71.0 mGy) ($P < 0.001$) (Table 2).
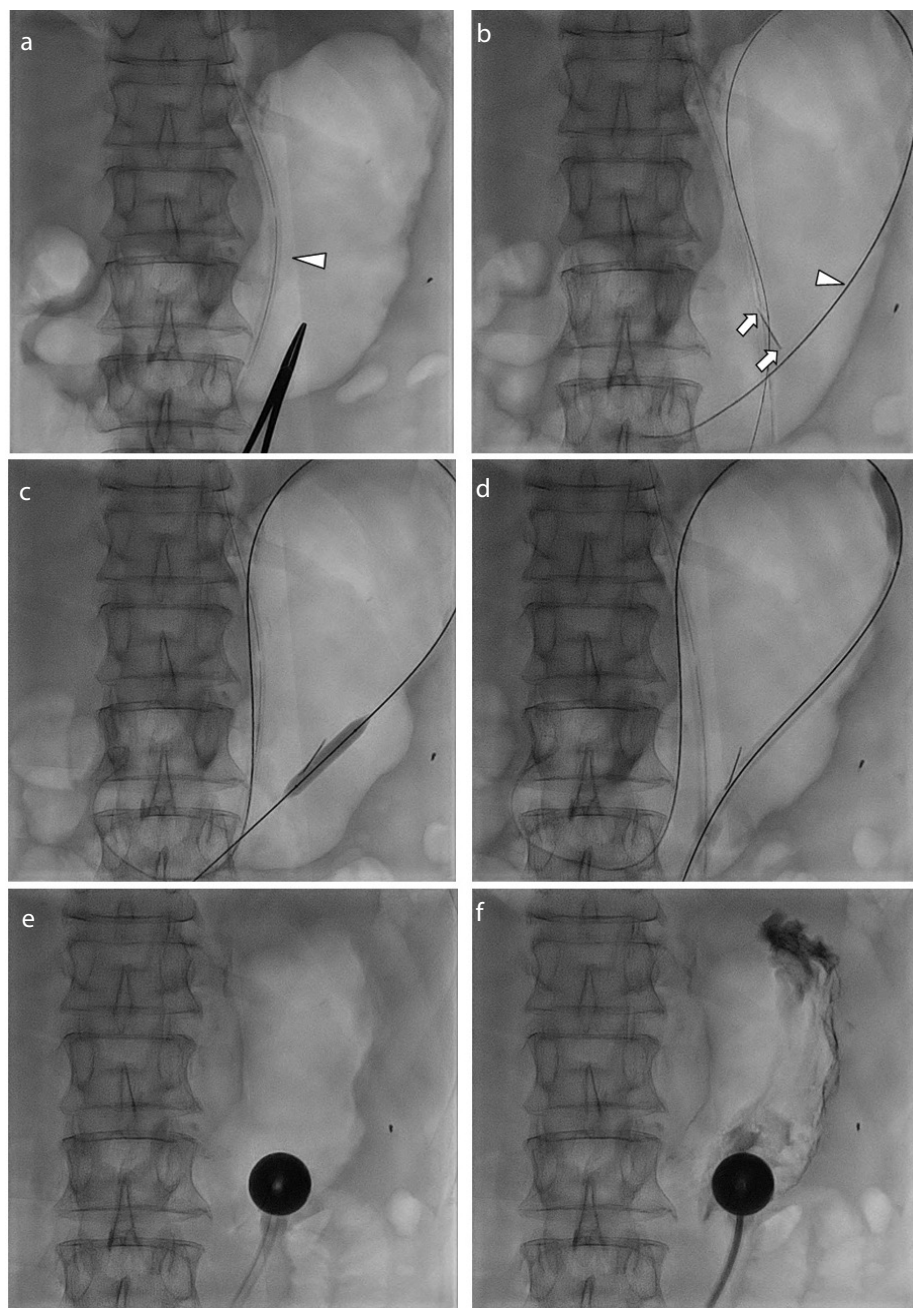


**Figure 1.** Successful percutaneous radiologic gastrostomy in patient with a single gastropexy using balloon-assisted dilatation. **(a)** Stomach insufflated with 500 mL of air through a nasogastric tube (arrowhead). Scissor indicates a site for gastrostomy placement. **(b)** After introducer needle advanced into the inflated stomach, suture anchor (arrow) was deployed into the stomach. A stiff guidewire (arrowhead) was inserted into the stomach through the needle. **(c)** The gastrostomy tube was preloaded on the shaft of a high-pressure balloon, and the balloon was inflated for 30 seconds. **(d)** As the balloon was deflated, the gastrostomy tube and balloon catheter were advanced together over the wire into the stomach. **(e)** The gastrostomy tube was secured in place by inflation with a contrast–saline mixture. **(f)** Finally, a contrast medium was injected through the gastrostomy tube to fluoroscopically confirm the intragastric location.

Major complications (such as peritonitis, migration, bleeding, and pneumonia) occurred in one patient from the PAS group. The patient underwent PRG for esophageal cancer and had no acute symptoms, and the abdominal radiograph the day after the procedure did not indicate pneumoperitoneum. He routinely tried 100 kcal of feeding liquids two days after the procedure, after which the patient complained of severe abdominal pain, and an abdominal radiograph revealed pneumoperitoneum. When subsequent computed tomography indicated that the gastrostomy tube had exited the stomach and migrated to the abdominal cavity, the tube was immediately removed, and the patient received supportive treatment, such as antibiotics and total parenteral nutrition. However, he died 11 days after the procedure.

Possible minor complications included pneumoperitoneum, abdominal pain, skin infection, leakage, and balloon deflation. In the BATD group, 12 patients (25.0%) reported minor complications, including pneumoperitoneum (9/46, 19.6%), abdominal pain (4/46, 8.7%), and leakage (1/46, 2.2%), and two of those patients complained of both pneumoperitoneum and abdominal pain. In the PAS group, four patients (38.5%) reported minor complications, including pneumoperitoneum (2/13, 15.4%), abdominal pain (2/13, 15.4%), and balloon deflation (1/13, 7.7%), and one of those patients complained of both pneumoperitoneum and abdominal pain.

The overall complication rate was higher in the PAS group; however, the difference was statistically non-significant [odds ratio (OR): 1.875, 95%; confidence interval (CI): 0.514, 6.841; $P = 0.486$)] (Table 3).

Twenty-two patients in the BATD group and 13 patients in the PAS group received a large-bore (18- or 20-Fr) gastrostomy tube. Four of these patients in the BATD group (4/22, 18.2%) experienced minor complications: pneumoperitoneum and abdominal pain were reported in three patients and one patient, respectively. Five patients in the PAS group (5/13, 38.5%) who received 20-Fr tubes experienced complications, including one major complication. The overall rate of large-bore tube insertion complications was higher in the PAS group; however, the difference was statistically non-significant (OR: 2.813, 95%; CI: 0.593, 13.336; $P = 0.243$) (Table 4).

## Discussion

There are various ways to perform PRG. Usually, PRG is performed by puncturing the stomach and inserting a gastrostomy tube, either a balloon-retained or pigtail-retained catheter. Pigtail-retained catheters have been widely used because they are easy to insert,[9,10] but they are currently not available in Korea. Several radiologists have placed catheters via the oropharynx using a mushroom-retained catheter and reported that this method was less prone to tube dysfunction and resulted in lower complication rates.[6,11] However, considering that half of the patients in this study were head and neck cancer patients, a mushroom-retained catheter was inappropriate because the catheter must pass through the mouth. Therefore, in the present study, a balloon-retained catheter was used for the gastrostomy procedure.

The PRG procedure has become safer and more effective through several modifications in the anchor technique.[4,12,13] Gastropexy devices provide stabilization of the stomach to the anterior abdominal wall, especially when large-bore catheters are used.[13,14] One prospective randomized study suggested routine performing of T-fastener gastropexy for all PRG procedures.[15] Another retrospective study found that the use of gastropexy is superior to non-gastropexy gastrostomy in terms of preventing leakage.[16] However, gastropexy-related complications, such as suture-related pain, suture rupture, migration, or wound infection, can occur.[17,18] Although removing the T-fasteners can resolve gastropexy-related complications,[15] using more anchors can increase complications such as bleeding and infection.[19] Therefore, many surgeons have tried to minimize the number of suture anchors while allowing safe and easy maneuvering of catheters.[4,20,21] Milovanovic et al.[22] reported one major complication (1.4%) and three minor complications (4.3%) in 69 patients using a single-puncture, multi-anchor technique. Although the complication rate was lower than in the current study, most gastrostomy tubes had a diameter of 12-Fr (86.9%), and there was only one tube larger than 18-Fr.[22] The difference in tube diameter makes it difficult to compare the complication rates. This study shows a safe and effective procedure to ensure the fixation of large-diameter gastrostomy tubes using a single gastropexy. While inserting the balloon dilatation catheter through the guidewire, the surgeon should pull the anchor to attach the anterior stomach wall to the abdominal wall. At the same time, this

**Table 2.** Statistical analysis of fluoroscopy time and radiation dose

|  | Overall (n = 61) | BATD group (n = 48) | PAS group (n = 13) | P value |
|---|---|---|---|---|
| Fluoroscopy time (min) | 2.05 ± 1.36 | 1.68 ± 0.93 | 3.56 ± 2.41 | <0.001 |
| Radiation dose (mGy) | 17.39 ± 13.66 | 12.98 ± 9.28 | 33.01 ± 15.14 | <0.001 |

Data are presented as mean ± standard deviation. BATD, balloon-assisted tract dilatation; PAS, peel-away sheath.

**Table 3.** Postprocedural complications

|  | Overall (n = 61) | BATD group (n = 48) | PAS group (n = 13) | P value |
|---|---|---|---|---|
| Overall complications | 17 (27.9%) | 12 (25.0%) | 5 (38.5%) | 0.486 |
| Major complications | 1 (1.6%) | 0 | 1 (7.7%) | |
| Minor complications | 16 (26.3%) | 12 (25.0%) | 4 (30.8%) | |
| Pneumoperitoneum | 11 (18.0%) | 9 (19.6%) | 2 (15.4%) | |
| Abdominal pain | 6 (9.8%) | 4 (8.7%) | 2 (15.4%) | |
| Skin infection | 0 | 0 | 0 | |
| Leakage | 1 (1.6%) | 1 (2.2%) | 0 | |
| Balloon deflation | 1 (1.6%) | 0 | 1 (7.7%) | |

Data are presented as mean ± standard deviation. BATD, balloon-assisted tract dilatation; PAS, peel-away sheath.

**Table 4.** Complications of large-bore gastrostomy tube in two groups

|  | BATD group with large-bore tube[a] (n = 22) | PAS group (n = 13) | P value |
|---|---|---|---|
| Complications | 4 (18.2%) | 5 (38.5%) | 0.243 |
| No complications | 18 (81.8%) | 8 (61.5%) | |

Data are presented as number (percent). [a]Large-bore tube includes 20- and 18-Fr gastrostomy tubes. BATD, balloon-assisted tract dilatation; PAS, peel-away sheath.

technique should be performed gently, as applying too much tension can cause damage to the stomach wall or break the anchor itself.

There are two reports for the placement of gastrostomy tubes using BATD.[7,23] Research indicates that BATD allows for rapid dilatation of the gastrostomy tract, and insertion of the tube can be performed in a single step, which reduces procedural time.[7] In the study, fluoroscopy time and cumulative radiation dose were significantly lower in the BATD group compared with the PAS group ($P < 0.001$). This suggests that BATD is more effective than using a PAS, with the benefit that it lessens radiation exposure for both surgeons and patients, in line with the principle of reducing radiation doses to "as low as reasonably achievable."[24] Complication rates also show consistent results. Major complications did not occur in the BATD group, whereas one patient in the PAS group experienced a major complication (peritonitis). Patients in each group experienced minor complications: 25% (12/48) for the BATD group and 38.5% (5/13) for the PAS group. Complication rates were lower in the BATD group, but there was no statistical difference between the two groups ($P = 0.486$). The PAS group used a 24-Fr PAS, and considering that the gastrostomy tube is 20-Fr, the PAS expands the gastrostomy tract more than necessary. In contrast, using BATD, the gastrostomy tract can be expanded appropriately to the diameter of the tube, thereby lessening the probability of complications.

Maroun et al.[7] investigated the efficiency and safety of balloon-assisted gastrostomy. The previous study used three gastropexy T-fasteners, a 9–10 mm balloon for a 20-Fr tube, and 1–2 minutes for balloon inflation. In the current study, the authors used a single gastropexy for stomach fixation, a 6–8 mm balloon for a 14- to 20-Fr tube, and approximately 30 seconds for balloon inflation. Compared with the previous study, the balloon capacity was smaller, and the inflation time was shorter. The authors tried to minimize the tract dilatation, resulting in no migration and a low leakage rate (2.2%) in the BATD group.

It may be argued that differences between tube diameters could affect the complication rates. In the BATD group, tubes of various diameters from 14-Fr to 20-Fr were used, but in the PAS group, only 20-Fr tubes were used. Therefore, it may be thought that many complications in the PAS group occurred because larger-diameter tubes were used. However, the overall rate of large-bore tube (18 or 20-Fr) insertion complications was more than two times higher in the PAS group (5/13, 38.5%) than those in the BATD group with a large-bore tube (4/22, 18.2%). Therefore, rather than the diameter of the tube, the method of tract dilatation seems to be more related to the complication rate, but statistical significance was not found ($P = 0.243$).

There were several limitations of the present study. First, it was a small study population from a single institution, and, therefore, institutional bias may make it difficult to generalize the results of this study. Second, the number of patients who underwent PRG with the PAS technique was much smaller compared to the number of patients who underwent PRG with the BATD technique, and the disproportionate number of the two groups may exaggerate or reduce the differences between them. Third, it is possible that complications went unreported because this information was retrospectively collected by review of EMRs. Thus, if post-procedural complications were not included in these records, the presence of complications could not be confirmed.

In conclusion, PRG with a single gastropexy using BATD appears to be a safe and effective technique and results in lower radiation exposure and incidence of complications than using a PAS for tract dilatation.
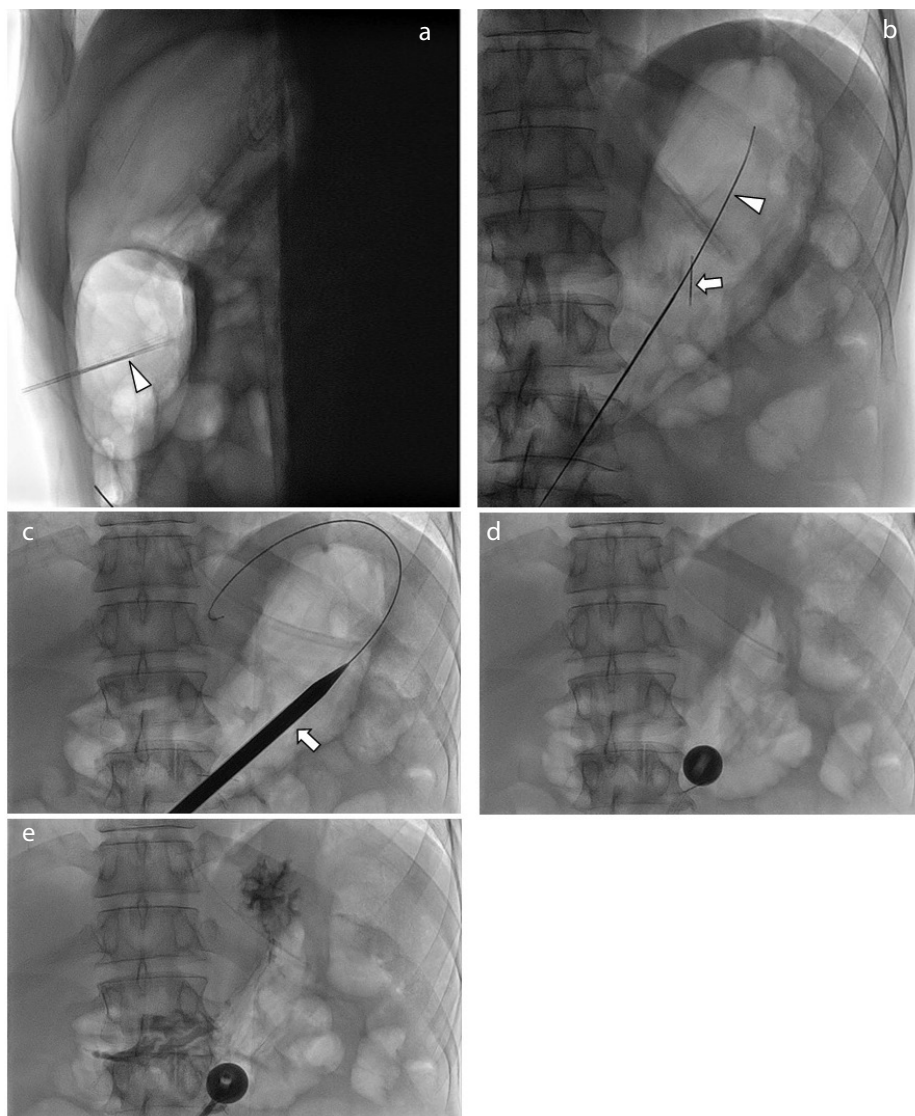


**Figure 2.** Successful percutaneous radiologic gastrostomy in patient with a single gastropexy using a 24-Fr peel-away sheath. **(a)** Introducer needle preloaded with anchor (arrowhead) was accessed to inflated stomach. **(b)** Suture anchor (arrow) was deployed into stomach. A guidewire (arrowhead) was inserted into the stomach through the needle. **(c)** Tract dilatation using a serial dilator and 24-Fr peel-away introducer sheath (arrow) was performed. **(d)** The gastrostomy tube was secured in place by inflation with a contrast–saline mixture. **(e)** Finally, a contrast medium was injected through the gastrostomy tube to fluoroscopically confirm the intragastric location.

### Conflict of interest disclosure

The authors declared no conflicts of interest.

## References

1. de Baere T, Chapot R, Kuoch V, et al. Percutaneous gastrostomy with fluoroscopic guidance: single-center experience in 500 consecutive cancer patients. *Radiology*. 1999;210(3):651-654. [CrossRef]

2. Perona F, Castellazzi G, De Iuliis A, Rizzo L. Percutaneous radiologic gastrostomy: a 12-year series. *Gut Liver*. 2010;4(Suppl 1):44-49. [CrossRef]

3. Preshaw RM. A percutaneous method for inserting a feeding gastrostomy tube. *Surg Gynecol Obstet*. 1981;152(5):658-660. [CrossRef]

4. Kim R, Park HS, Do YS, et al. Percutaneous radiologic gastrostomy with single gastropexy: outcomes in 636 patients. *Eur Radiol*. 2021;31(9):6531-6538. [CrossRef]

5. Kuo YC, Shlansky-Goldberg RD, Mondschein JI, et al. Large or small bore, push or pull: a comparison of three classes of percutaneous fluoroscopic gastrostomy catheters. *J Vasc Interv Radiol*. 2008;19(4):557-563. [CrossRef]

6. Funaki B, Zaleski GX, Lorenz J, et al. Radiologic gastrostomy placement: mushroom versus pigtail catheters. *Am J Roentgenol*. 2000;175(2):375-379. [CrossRef]

7. Maroun G, Pugash R, Meirovich H, David E. Efficiency and safety of balloon-assisted gastrostomy. *Cardiovasc Intervent Radiol*. 2021;44(9):1423-1429. [CrossRef]

8. Caplin DM, Nikolic B, Kalva SP, et al. Society of Interventional Radiology Standards of Practice Committee. Quality improvement guidelines for the performance of inferior vena cava filter placement for the prevention of pulmonary embolism. *J Vasc Interv Radiol*. 2011;22(11):1499-1506. [CrossRef]

9. Gehman KE, Elliott JA, Inculet RI. Percutaneous gastrojejunostomy with a modified Cope loop catheter. *Am J Roentgenol*. 1990:155(1);79-80. [CrossRef]

10. Ho CS, Yeung EY. Percutaneous gastrostomy and transgastric jejunostomy. *AJR Am J Roentgenol*. 1992;158(2):251-257. [CrossRef]

11. Han K, Kim MD, Kwon JH, et al. Randomized controlled trial comparing radiologic pigtail-retained gastrostomy and radiologic mushroom-retained gastrostomy. *J Vasc Interv Radiol*. 2017;28(12):1702-1707. [CrossRef]

12. Kim JW, Song HY, Kim KR, Shin JH, Choi EK. The one-anchor technique of gastropexy for percutaneous radiologic gastrostomy: results of 248 consecutive procedures. *J Vasc Interv Radiol*. 2008;19(7):1048-1053. [CrossRef]

13. Saini S, Mueller PR, Gaa J, et al. Percutaneous gastrostomy with gastropexy: experience in 125 patients. *Am J Roentgenol*. 1990;154(5):1003-1006. [CrossRef]

14. Brown AS, Mueller PR, Ferrucci JT Jr. Controlled percutaneous gastrostomy: nylon T-fastener for fixation of the anterior gastric wall. *Radiology*. 1986;158(2):543-545. [CrossRef]

15. Thornton FJ, Fotheringham T, Haslam PJ, McGrath FP, Keeling F, Lee MJ. Percutaneous radiologic gastrostomy with and without T-fastener gastropexy: a randomized comparison study. *Cardiovasc Intervent Radiol*. 2002;25(6):467-471. [CrossRef]

16. Ryan JM, Hahn PF, Boland GW, McDowell RK, Saini S, Mueller PR. Percutaneous gastrostomy with T-fastener gastropexy: results of 316 consecutive procedures. *Radiology*. 1997;203(2):496-500. [CrossRef]

17. Covarrubias DA, O'Connor OJ, McDermott S, Arellano RS. Radiologic percutaneous gastrostomy: review of potential complications and approach to managing the unexpected outcome. *AJR Am J Roentgenol*. 2013;200(4):921-931. [CrossRef]

18. Sydnor RH, Schriber SM, Kim CY. T-fastener migration after percutaneous gastropexy for transgastric enteral tube insertion. *Gut Liver*. 2014;8(5):495-499. [CrossRef]

19. Akinci D, Ciftci TT, Kaya D, Ozmen MN, Akhan O. Long-term results of percutaneous radiologic gastrostomy and gastrojejunostomy in children with emphasis on technique: single or double gastropexy? *Am J Roentgenol*. 2010;195(5):1231-1237. [CrossRef]

20. Lowe AS, Laasch HU, Stephenson S, et al. Multicentre survey of radiologically inserted gastrostomy feeding tube (RIG) in the UK. *Clin Radiol*. 2012;67(9):843-854. [CrossRef]

21. Shin JH, Song HY, Kim TH, Kim KR, Choi KE, Kim JH. Percutaneous radiologic gastrostomy: a modified Chiba needle puncture technique with single gastropexy. *Abdom Imaging*. 2010;35(2):189-194. [CrossRef]

22. Milovanovic L, Kennedy SA, Chrea B, Midia M. Safety and short-term complication rates using single-puncture T-fastener gastropexy. *J Vasc Interv Radiol*. 2016;27(6):898-904. [CrossRef]

23. Bendel EC, McKusick MA, Fleming CJ, et al. Percutaneous radiologic gastrostomy catheter placement without gastropexy: a co-axial balloon technique and evaluation of safety and efficacy. *Abdom Radiol*. 2016;41(11):2227-2232. [CrossRef]

24. Uffmann M, Schaefer-Prokop C. Digital radiography: the balance between image quality and required radiation dose. *Eur J Radiol*. 2009;72(2):202-228. [CrossRef]

# Efficacy and safety of transcatheter arterial embolization for hemodynamically unstable bleeding after percutaneous transthoracic needle biopsy

*Su Kyeong Yeon
*Yura Ahn
Ji Hoon Shin
Sang Young Oh
Gun Ha Kim

*Contributed equally to this work and share first authorship.

## PURPOSE

To evaluate the safety and efficacy of transcatheter arterial embolization (TAE) in controlling hemodynamically unstable bleeding following a percutaneous transthoracic needle biopsy (PTNB).

## METHODS

A total of seven patients (four men and three women; mean age, 62 ± 12 years) who received TAE for post-PTNB bleeding between May 2007 and March 2022 were included. The observed types of bleeding were hemothorax (n = 3), hemoptysis (n = 2), and a combination of both (n = 2). In patients with active bleeding, the technical success of TAE was defined as superselective embolization of the target artery with no active bleeding visible on post-TAE angiography. Clinical success was defined as sustained cessation of bleeding without hemodynamic instability, requirement of repeat TAE, or the need for post-TAE hemostatic surgery during the initial admission. The metrics analyzed included technical and clinical success rates, complications, and 30-day mortality.

## RESULTS

All seven patients achieved technical success, with a clinical success rate of 86% (6/7). Six patients were discharged alive, while one patient died of respiratory failure accompanied by hemothorax 19 days post-biopsy. The angiographic findings associated with bleeding were contrast media extravasation or pseudoaneurysm (n = 3) and vascular hypertrophy with tortuosity (n = 2). The implicated bleeding arteries included the intercostal artery (n = 2), bronchial artery (n = 2), and internal thoracic artery (n = 1). In two cases, no clear bleeding foci were identified; nonetheless, prophylactic embolization was performed on the right intercostal artery (n = 1) and right intercostobronchial trunk (n = 1). The embolic agents utilized included microcoils (n = 1), gelatin sponge particles (n = 2), polyvinyl alcohol (PVA) with gelatin sponge particles (n = 1), PVA with microcoils (n = 1), microcoils with gelatin sponge particles (n = 1), and microcoils with n-butyl-2-cyanoacrylate and gelatin sponge particles (n = 1). The 30-day mortality rate was 14% (1/7). No ischemic complications related to TAE were observed.

## CONCLUSION

The study suggests that TAE is safe and effective for controlling hemodynamically unstable bleeding following a PTNB.

## KEYWORDS

Transcatheter arterial embolization, percutaneous transthoracic needle biopsy, hemoptysis, hemothorax, angiography

From the Department of Radiology and Research Institute of Radiology (S.K.Y., Y.A., J.H.S. ✉jhshin@amc.seoul.kr, S.Y.O., G.H.K.), University of Ulsan College of Medicine, Asan Medical Center, Seoul, South Korea.

mage-guided percutaneous transthoracic needle biopsies (PTNBs) play a pivotal role in the histopathological evaluation of pulmonary parenchymal lesions.[1] Recognized as a safe and minimally invasive diagnostic procedure, a PTNB is nonetheless associated with a risk of procedure-related complications such as pneumothorax, hemorrhage, and air embolism.[2]

Risk estimates for bleeding complications following a PTNB fluctuate widely. Utilizing data from twelve single-institution retrospective case series, Wiener et al.[3] reported a median hemorrhage risk of 12%, ranging from 2% to 66%. This variation could be attributed to the differences in how the complications were defined across studies.[3] Such bleeding complications may encompass pulmonary parenchymal hemorrhage, hemoptysis, hemothorax, chest wall hematoma, and pulmonary artery pseudoaneurysm.

Hemoptysis is typically self-limiting, but there can be instances of massive, potentially fatal, hemoptysis following a PTNB.[4] In cases where massive hemoptysis is unmanageable through conservative methods, rigid bronchoscopy, transcatheter arterial embolization (TAE), or surgery might be employed in some centers.[5] The occurrence of significant chest wall hematoma and hemothorax, although rare, can transpire if any of the intercostal arteries or internal thoracic arteries are injured during the biopsy procedure.[6] Several studies have reported TAE of the injured arteries to be an effective treatment option for iatrogenic intercostal or internal thoracic arterial bleeding.[7-9] There are limited case reports and associated evidence concerning TAE for hemorrhage following a PTNB. This study aimed to evaluate the clinical efficacy and safety of TAE in patients with hemodynamically unstable PTNB-related hemorrhage.

## Methods

### Patients

This retrospective study received approval from the Asan Medical Center Institutional Review Board (no: S2023-0101-0001). Given its retrospective nature, the requirement for written informed consent for the procedures was waived. The study was conducted in a single tertiary referral hospital.

Between May 2007 and March 2022, a total of 18,118 consecutive PTNBs were performed on 16,576 adult patients. Among these, 356 patients (2.1%) experienced hemoptysis, and 13 (0.08%) developed hemothorax, as confirmed by imaging studies. The present study included seven patients (four men, three women; mean age, 62 ± 12 years) from this group who underwent TAE to control bleeding following a PTNB. These patients were specifically referred due to downtrending hemoglobin levels or hemodynamic instability. The median transfusion volume before and after angiography was five units of packed red blood cells (range: 0–16 units).

The medical records of each patient were reviewed to gather clinical data, including underlying diseases, clinical symptoms or signs, and laboratory findings. Initial presentation data such as vital signs, systolic and diastolic blood pressures, and coagulation study results [including hemoglobin concentration, platelet count, prothrombin time, activated partial thromboplastin time, and the international normalized ratio (INR)] were collected.

The variables analyzed in this study included the following: the time between biopsy sample collection and symptom onset; the interval from symptom onset to angiography; computed tomography (CT) findings; TAE details (e.g., angiographic findings and embolic materials used); procedure-related complications; and clinical outcomes after TAE, which comprised technical and clinical success, 30-day mortality, admission to the intensive care unit, and procedure-related complications related to post-PTNB bleeding.

### Biopsy procedures

Our established protocol mandates an INR of <1.6 and a platelet count of >50,000/μL. The PTNBs were either conducted by thoracic radiology faculty members or by chest imaging fellows under their direct supervision.

All patients underwent a prearranged chest CT scan prior to the PTNB. For each procedure, the operator delineated the most efficient and secure pathway for the needle based on the CT scans. Subsequently, the patients were positioned according to the selected pathways.

The pre-, intra-, and post-procedural CT scans of patients who underwent TAE were reviewed. First, variables such as target lesion characteristics (size, lobar location, and lesion type), patient position, puncture site location, needle penetration length from the pleura, number of specimen acquisitions, and complications were recorded. Moreover, the distance from the midline (spinous process) to the biopsy site for each patient who had biopsy specimen collection in the prone position was measured.

All patients were administered local anesthesia. The procedures were conducted under CT guidance, fluoroscopic guidance, or without imaging guidance, selecting the optimal route to circumvent ribs, vessels, fissures, and intercostal nerves. A standard core biopsy incorporating a coaxial technique was used, which employed a 19-G coaxial introducer and 20-G cutting needle (Stericut; TSK Laboratory). All specimens were immediately evaluated for diagnostic sufficiency. If the initial specimen was deemed insufficient, further aspirations were performed, with a maximum of three aspirations in one setting. Following the procedure, the patients were instructed to rest in the supine position. A chest X-ray follow-up was conducted 2–4 h post-biopsy to detect any procedure-related complications.

The CT-guided PTNB was performed with either a single-slice spectral detector CT scanner (HiSpeed CT/i; GE Healthcare) or 64-multidetector CT scanners (SOMATOM Definition AS; Siemens Healthineers) with parameters set to 100 or 120 kVp and 1.5 or 3.0 mm in axial slice thickness. The needle was inserted at an optimal angle until its tip reached the lesion's edge, as confirmed by several small-scale CT scans throughout the procedure. Once sufficient tissue samples were procured and the needle removed, a post-procedural CT was conducted to identify any complications.

During the fluoroscopic biopsy, the exposure parameters were set to 60 kVp. To mitigate radiation exposure, the operator manipulated the needle introducer using surgical forceps during fluoroscopy procedures. Real-time imaging was intermittently employed to visualize the position of the advancing needle tip.

### Main points

- The clinical success rate of transcatheter arterial embolization for hemodynamically unstable bleeding after percutaneous thoracic needle biopsy was 86%, with no complications.

- Delayed-onset (>24 h) bleeding complications were frequent, occurring in up to 43% of cases, highlighting the necessity of patient education and close monitoring.

- The angiography identified bleeding arteries as intercostal arteries, bronchial arteries, and an internal thoracic artery, and prophylactic embolization of non-bleeding sites also achieved clinical success, emphasizing the significance of diagnostic angiography and selective embolization in managing post- percutaneous transthoracic needle biopsy bleeding.

### Angiography and embolization techniques

Prior to embolization, the hemorrhage was located using pre-procedural CT scans or biopsy results. Thoracic aortography, bronchial arteriography, internal thoracic arteriography, and intercostal arteriography were performed with a specific reference to the CT-identified hemorrhage. Contrast extravasation, the existence of pseudoaneurysms or hypertrophy, and vascular tortuosity were indicators of active bleeding.[10] Experienced interventional radiologists, with a clinical tenure of 10–20 years in endovascular treatments, conducted the angiography and embolization procedures. The standard protocol included local anesthesia administration, specifically lidocaine, followed by routine access to the right common femoral artery. A 5F catheter (RH or C2 catheter, Cook Medical) and a 0.035-inch hydrophilic guidewire (Radifocus, Terumo Inc.) were employed. Descending thoracic aortography was performed with a 5F pigtail catheter, and the abnormal culprit arteries were evaluated. A selective bronchial arteriogram was then performed using either reverse-curved catheters (Mikaelson, SOS Omni) or forward catheters (Cobra). If the anomalous bronchial arteries remained unidentified, a thorough exploration of non-bronchial systemic arteries, including intercostal arteries, was pursued. The patients who had biopsies performed in a supine position underwent additional internal thoracic arteriography. Superselection of the bleeding arteries was accomplished with a 2.0F–2.4F microcatheter (Progreat, Terumo Inc.; Renegade, Boston Scientific). If the bleeding site could not be localized, prophylactic embolization was performed on the most-suspected arteries, with consideration of the previous biopsy site.

Embolic materials, chosen as per the operator's preference and based on angiographic findings, included microcoils (MicroNester or Tornado; Cook Medical), n-butyl-2-cyanoacrylate (NBCA) (Histoacryl, B. Braun), polyvinyl alcohol (PVA) (PVA 355–500 μm; Boston Scientific), or gelatin sponge particles (Spongostan; Johnson & Johnson). To ensure target vessel occlusion or cessation of contrast extravasation, completion angiography was performed post-embolization.

### Definitions

Coagulopathy was defined as an INR >1.5 or a platelet count of <50,000/μL.[11] Hemodynamic instability was characterized by either hypotension (systolic blood pressure <100 mmHg) or tachycardia (heart rate >100 beats/min). Any bleeding complications that occurred >24 h following biopsy specimen collection were deemed delayed events.[12]

In patients with active bleeding, technically successful TAE was defined as an embolization that successfully superselected the target artery, with no evidence of active bleeding noted in the post-TAE angiography. Clinical success was defined as the sustained cessation of bleeding without signs of hemodynamic instability, negating the need for either repeat TAE or post-TAE hemostatic surgery during the initial admission. Any com-plications were categorized as either major or minor based on the guidelines provided by the Society of Interventional Radiology Standards of Practice Committee.[13]

### Statistical analysis

The numerical results of the clinical data and measurements were expressed as means ± standard deviations or medians (ranges).

### Patient follow-up

Following TAE, all patients were closely monitored for clinical indications of ischemic complications or recurrent bleeding until either discharge or death. These clinical observations were augmented by laboratory studies, vital signs, and chest radiographs. The patients' long-term outcomes and mortality rates were established through a review of the medical charts. It is worth noting that conducting a CT scan following embolization is not standard practice within this hospital unit.

## Results

### Clinical characteristics

The characteristics and outcomes of the seven patients are summarized in Tables 1, 2. No coagulopathy was detected in any of the patients. The median INR was 1.09 (range: 0.93–1.22), and the median platelet count was 183,000/μL (range: 90,000–353,000/μL).

The median interval between biopsy sample collection and symptom onset was 2.0 h (mean: 50.0 h; range: 0.3–156.7 h). Hemoptysis occurred within 1 h post-biopsy in 43%

**Table 1.** Clinical characteristics

| No/ sex/age (years) | Image guidance | Bleeding type | Symptom or sign | Time interval (h) | | Hemoglobin (g/dL) | | Transfusion (units of pRBCs) | TXA administration duration (days) | Pathology | Underlying disease |
|---|---|---|---|---|---|---|---|---|---|---|---|
| | | | | Biopsy and symptom onset | Symptom onset and angiography | Before | After | | | | |
| 1/M/69 | None | Hemothorax | Chest pain | 2 | 5.3 | 6 | 8.8 | 5 | | Non-specific benign | DM, HTN, CKD |
| 2/M/74 | CT | Hemoptysis | Hemoptysis | 0.6 | 1.5 | 8.4 | 10.6 | 3 | 4 | Lung cancer | No |
| 3/F/50 | Fluoro | Hemothorax, hemoptysis | Dyspnea, hemoptysis | 35.6 | 85.9 | 9.8 | 10.5 | 16 | 5 | Lung cancer | No |
| 4/F/64 | CT | Hemothorax | Dyspnea, chest pain | 153.88 | 65.8 | 7.1 | 10.3 | 8 | | Lung cancer | HTN, hyperthyroidism |
| 5/M/63 | CT | Hemothorax, hemoptysis | Hemoptysis | 0.4 | 5.1 | 6.9 | 8.1 | 5 | 1 | Non-specific benign | HTN, CKD, kidney amyloidosis |
| 6/F/52 | CT | Hemothorax | Chest pain, dizziness | 156.7 | 9.5 | 8.8 | 11.6 | 2 | | Non-specific benign | HTN, Takayasu arteritis |
| 7/M/62 | CT | Hemoptysis | Hemoptysis | 0.3 | 3.3 | 7.5 | 9.4 | 4 | 2 | Lung cancer | DM, HTN, CKD, 3VD, HCC |

CKD, chronic kidney disease; CT, computed tomography; DM, diabetes mellitus; F, female; pRBCs, packed red blood cells; Fluoro, fluoroscopy; M, male; HTN, hypertension; HCC, hepatocellular carcinoma; TXA, tranexamic acid; 3VD, three-vessel disease.

**Table 2.** Endovascular interventions and outcomes

| No/sex/age (years) | Indication | Angiographic findings | Embolized vessels | Embolic materials | Technical success | Clinical success | Complications |
|---|---|---|---|---|---|---|---|
| 1/M/69 | Hb↓, BP↓ | PSA | Left ICA (10th) | Coils | Yes | Yes | None |
| 2/M/74 | Hb↓, BP↓ | Hypertrophic and tortuous | Left BA | PVA, GSP | Yes | Yes | None |
| 3/F/50 | Hb↓, BP↓ | Hypertrophic and tortuous | Right ICBT, right ITA | Coils, GSP | Yes | No | None |
| 4/F/64 | Hb↓, BP↓ | CE, PSA | Right ITA | NBCA, coils, GSP | Yes | Yes | None |
| 5/M/63 | Hb↓ | Normal | Right ICA (8th, 9th, 10th) | GSP | Yes | Yes | None |
| 6/F/52 | Hb↓, BP↓ | CE | Right ICA (8th) | PVA, coils | Yes | Yes | None |
| 7/M/62 | Hb↓, BP↓ | Normal | Right ICBT | GSP | Yes | Yes | None |

BA, bronchial artery; BP, blood pressure; CE, contrast extravasation; F, female; GSP, gelatin sponge particle; Hb, hemoglobin; ICBT, intercostobronchial trunk; ICA, intercostal artery; ITA, internal thoracic artery; M, male; NBCA, n-butyl-2-cyanoacrylate; PSA, pseudoaneurysm; PVA, polyvinyl alcohol.

**Table 3.** Pre-, intra-, and post-procedural parameters and computed tomography findings

| No/ sex/ age (years) | Nodule type | Nodule size (mm) | Biopsy number | Location | Total depth (mm) | Depth from pleura (mm) | Position | Distance from spinous process (mm) | Puncture site (intercostal space) | Pneumothorax | Parenchymal hemorrhage |
|---|---|---|---|---|---|---|---|---|---|---|---|
| 1/M/69 | NA | NA | 4 | Left hemithorax | 28 | 5 | Prone | 89 | Left 10th | No | No |
| 2/M/74 | Subsolid | 32 | 3 | LUL | 48 | 26 | Supine | | Right 3rd | Yes | Yes |
| 3/F/50 | Solid | 80 | 3 | RLL | 52 | 40 | Prone | 82 | Right 7th | No | No |
| 4/F/64 | Solid | 26 | 3 | RUL | 68 | 27 | Supine | | Right 1st | No | No |
| 5/M/63 | Solid | 39 | 2 | RLL | 57 | 32 | Prone | 79 | Right 7th | No | Yes |
| 6/F/52 | Solid | 20 | 2 | RLL | 73 | 32 | Prone | 110 | Right 8th | No | Yes |
| 7/M/62 | Subsolid | 14 | 2 | RUL | 94 | 56 | Supine | | Right 2nd | No | Yes |

NA, not available; M, male; F, female.

of the patients (3/7), while in another 43% (3/7), symptom onset was delayed until >24 h after the collection of the biopsy specimen. Four patients who had active hemoptysis were administered a 500 mg (5 mL) dose of tranexamic acid, combined with 5 mL of distilled water, four times daily. The median duration of this treatment was 2.5 days (range, 1–5 days).

### Computed tomography findings

The procedural parameters and CT findings of the study patients are summarized in Table 3. Four patients underwent the PTNB in the prone position, with the remaining three in the supine position. Among these patients, four exhibited solid lesions and two presented subsolid lesions. Patient 1 had a significant pleural effusion without a demonstrable mass or enhancing lesion and thus underwent a pleural biopsy. The mean size of the target lesion was 35.1 mm (median: 29.0 mm; range: 14.0–80.0 mm).

The mean distance from the skin to the target lesion was 61.3 mm (median: 62.5 mm;

range: 28.0–94.0 mm). In patients who were in the prone position, distances from the biopsy sites to the spinous processes were measured, yielding a mean value of 90.0 mm (median: 85.5 mm; range: 79.0–110.0 mm). For these four patients, the needle insertion sites were located at the right seventh intercostal space (n = 2), the right eighth intercostal space (n = 1), and the left tenth intercostal space (n = 1).

### Embolization details and outcomes

The angiographic details are shown in Table 2. The median interval between symptom onset and angiography was 5.3 h (mean: 25.2 h; range: 1.5–85.9 h).

In terms of angiographic findings, active bleeding indicators, such as contrast media extravasation or pseudoaneurysms, were evident in three patients. Two other patients exhibited vascular hypertrophy and tortuosity, whereas the final two patients presented no signs of active bleeding. Angiography identified the bleeding arteries as

intercostal arteries (n = 2) (Figure 1), bronchial arteries (n = 2) (Figure 2), and an internal thoracic artery (n = 1) (Figure 3). The two patients without demonstrable bleeding sites underwent prophylactic embolization of an intercostal artery (n = 1) and the intercostobronchial trunk (n = 1). The embolization procedures were technically successful for all seven patients. Three patients were treated using single embolic agents: one with microcoils and two with gelatin sponge particles. In contrast, four patients were treated using a combination of embolic agents: PVA with gelatin sponge particles (n = 1), PVA with microcoils (n = 1), microcoils with gelatin sponge particles (n = 1), and microcoils with NBCA and gelatin sponge particles (n = 1).

Clinical success was achieved in six patients (86%, 6/7). One patient (patient 3) experienced rebleeding with respiratory failure and died 19 days after the biopsy procedure. This resulted in a 30-day mortality rate of 14%. No embolization-related complications were observed.

## Discussion

Reports pertaining to embolization for active bleeding post-PTNB are currently limited. This study highlights the high technical feasibility and effectiveness of TAE for managing hemodynamically unstable bleeding complications following a PTNB, with a technical success rate of 100% and a clinical success rate of 86%. In the study cohort, the incidence of hemoptysis following a PTNB was 2.1%, which aligns with previously reported ranges of 2.8%–6.1% post-PTNB.[14-19] Although post-PTNB hemoptysis is generally self-limited,[20] it can sometimes be massive and life-threatening.[21] The medical literature typically defines massive hemoptysis as an episode involving >600 mL of hemoptysis within a 24-h span. The medical management of hemoptysis involves addressing the underlying etiology and administering tranexamic acid, an antifibrinolytic drug.[22] In instances where hemoptysis cannot be managed conservatively, TAE represents a viable therapeutic alternative.[5]

The incidence of hemothorax following a CT-guided PTNB is <0.1%; however, its occurrence is associated with substantial morbidity and mortality.[23,24] In the study patient group, hemothorax following a PTNB was observed in 0.08% of cases. One of these patients experienced a progressively worsening hemothorax and died despite intervention. Vascular structures vulnerable to injury during a PTNB primarily include large central vessels and certain systemic arteries, such as the subclavian, axillary, internal thoracic, and intercostal arteries.[25] Conventionally, the supracostal approach is the most frequently used and safest puncture route to circumvent intercostal artery injury during transthoracic puncture. However, the dynamics of target lesion positions during respiration and a limited intercostal window may necessitate deviation from this approach. Additionally, tortuosity is often observed among the third to eighth posterior intercostal arteries, increasing their exposure within the intercostal spaces in the first 6 cm from the spine, particularly in individuals over 60 years of age.[26,27] Of the four patients in the study who were in a prone position during their PTNB procedures, the mean distance from the biopsy site to the spinous process was 90.0 mm. The puncture sites were located at the right seventh to eighth intercostal spaces in 75% of these patients (3/4). Findings from a cadaveric study led to the recommendation that surgical instruments entering any of the third to eighth intercostal spaces should ideally be placed at least 120.0 mm lateral to the midline of the spinous processes.[27] Therefore, during such procedures, it is critical to consider these anatomical principles, particularly those concerning the intercostal arteries and collateral vessels. It is important to note that, given the high likelihood of tortuosity, supracostal puncture does not necessarily circumvent lacerations.

Diagnostic angiography is recommended when patients exhibit hemodynamic instability, progressively decreasing hemoglobin levels, or when follow-up CT scans demonstrate evidence of bleeding.[28] Even in instances with seemingly normal aortograms, an attempt at selective catheterization of the bronchial arteries should be made, as bleeding may originate from vessels of standard diameter.[29] A prior study confirmed complete clinical responses in patients who
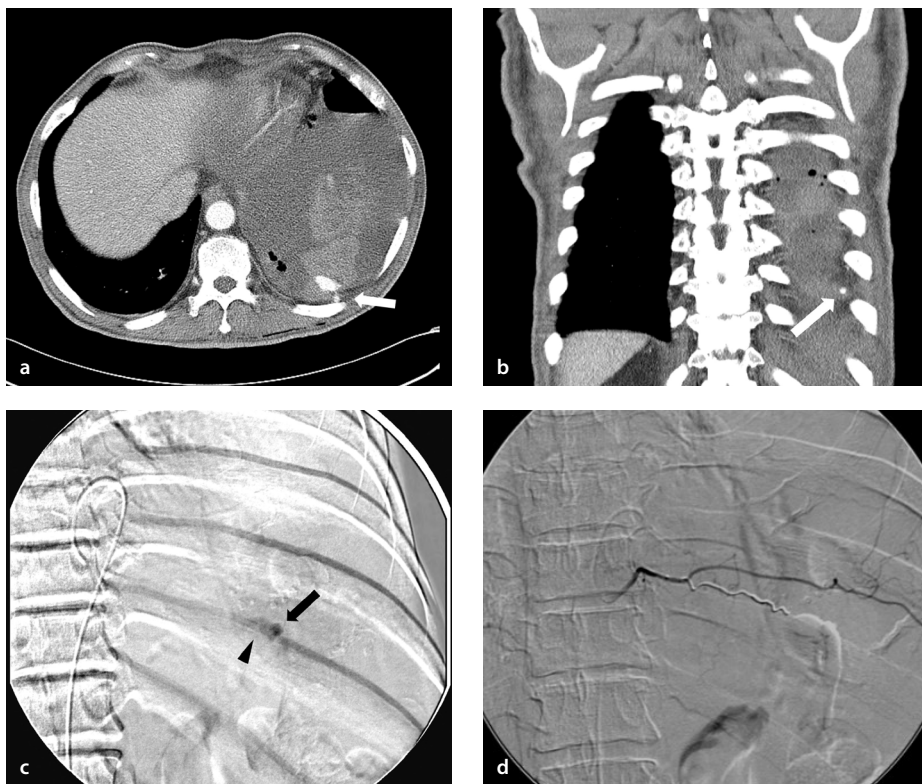


**Figure 1.** A 69-year-old man (no: 1) developed a hemothorax following a percutaneous thoracic needle biopsy (PTNB) of left pleural tissue. **(a, b)** Computed tomography images obtained immediately after a PTNB showed a hemorrhagic pleural effusion with extravasation of contrast medium at the left 10th intercostal artery. **(c)** The left intercostal angiogram showed a definite pseudoaneurysm (arrow) and contrast extravasation (arrowhead) at the left 10th intercostal artery. **(d)** The bleeding focus was embolized using two microcoils, and the completion angiogram showed no further bleeding.
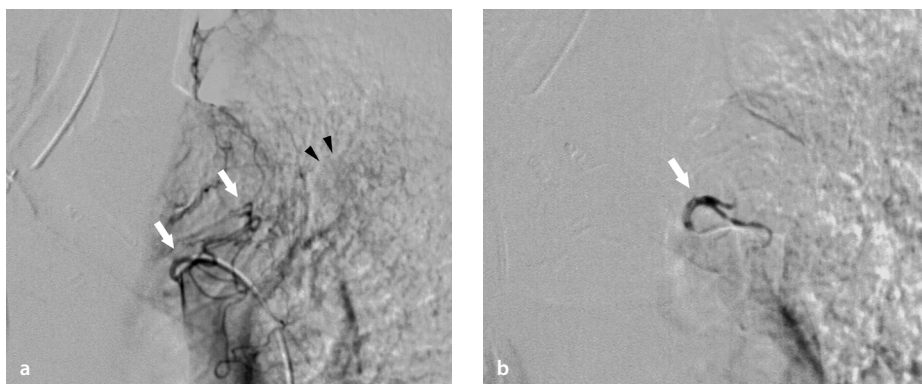


**Figure 2.** A 74-year-old man (no: 2) with massive hemoptysis following a percutaneous thoracic needle biopsy (PTNB) for an adenocarcinoma in the left upper lobe. **(a)** Selective left bronchial angiogram showing tortuous branches (arrows) that supply a hypervascular area, and mass staining (arrowheads). Hypertrophied left bronchial artery was embolized with polyvinyl alcohol (355–500 um) and gelatin sponge particles. **(b)** Postembolization angiogram revealing occlusion of the left bronchial artery with no opacification of the hypervascular lesion (arrow).
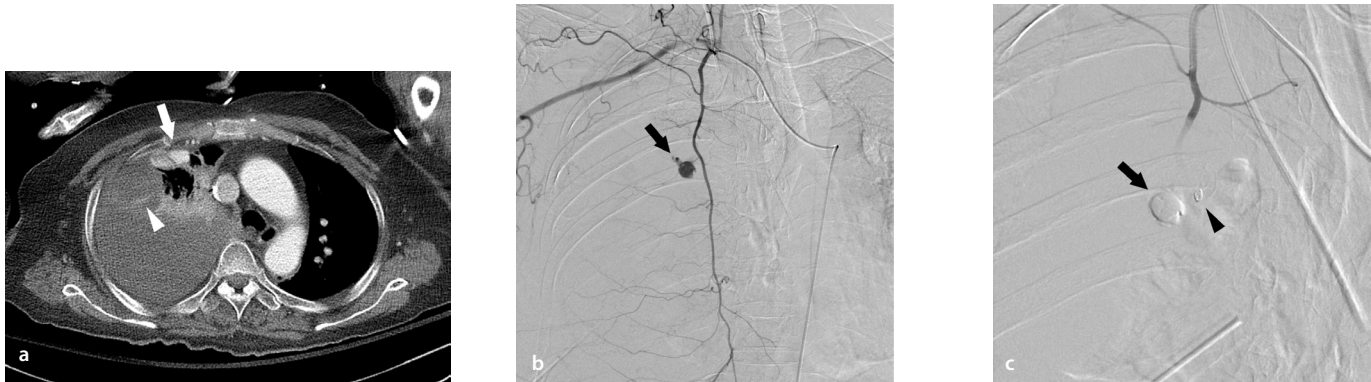
**Figure 3.** A 64-year-old woman (no: 4) developed a massive hemorrhagic pleural effusion following a percutaneous thoracic needle biopsy (PTNB) for an adenocarcinoma in the right upper lobe. **(a)** A computed tomography image obtained nine days after a PTNB showing a pseudoaneurysm (arrow) with linear contrast extravasation (arrowhead) from the right internal thoracic artery. **(b)** The right internal thoracic arteriogram shows a pseudoaneurysm and contrast extravasation (arrow). **(c)** The right internal thoracic artery distal to the pseudoaneurysm was embolized with one microcoil (arrowhead), and the pseudoaneurysm was embolized with n-butyl-2-cyanoacrylate and gelatin sponge particles (arrow), with no further bleeding.

underwent bronchial artery embolization with non-hypertrophied bronchial arteries.[30] In the present study, the angiograms of five patients exhibited evidence of bleeding; however, such evidence was absent for two patients. These two patients, without observable active bleeding, underwent prophylactic embolization of the intercostal arteries and the intercostobronchial trunk, respectively, both achieving clinical success.

Although instances of post-PTNB bleeding are infrequent, when they do occur, they can prove fatal. Upon the onset of bleeding, the likelihood of hemostasis is contingent upon platelet function and coagulation activity.[11] Patients suffering from chronic liver or kidney disease may exhibit hemorrhagic tendencies due to thrombocytopenia or platelet dysfunction.[31] In the study cohort, three patients had chronic kidney disease, with one of them also having concurrent chronic liver disease and hepatocellular carcinoma. However, no patient had a confirmed coagulopathy, which may have positively impacted the high technical and clinical success rates. A frequently occurring delayed onset (>24 h) of bleeding complications was observed in this study. All patients requiring immediate intervention post-PTNB presented with hemoptysis, whereas the three delayed-onset hemothorax cases displayed non-specific symptoms, such as dyspnea or chest pain. One of the three patients with delayed-onset hemothorax eventually succumbed to continuous bleeding despite the TAE. Therefore, educating patients about the signs and symptoms of bleeding is critical. Furthermore, close monitoring of clinical and radiologic characteristics is essential for the early identification of signs potentially indicative of early or delayed bleeding.

When interpreting the results of the study, certain limitations should be taken into consideration. First, the data collection was retrospective; as such, some patients with delayed symptom onset may have been overlooked in the analysis. Second, a relatively small number of patients underwent embolization for post-PTNB bleeding. Given the low incidence of clinically significant bleeding after a PTNB, this limitation was unavoidable despite the large pool of patients who underwent a PTNB. Third, a potential limitation was the absence of standardized protocols regarding the types of embolic materials and TAE techniques.

In conclusion, TAE demonstrated a high technical success rate and clinical effectiveness in managing patients who experienced bleeding post-PTNB.

### Conflict of interest disclosure

The authors declared no conflicts of interest.

## References

1. Manhire A, Charig M, Clelland C, et al. Guidelines for radiologically guided lung biopsy. *Thorax*. 2003;58(11):920-936. [CrossRef]

2. Wu CC, Maher MM, Shepard JA. Complications of CT-guided percutaneous needle biopsy of the chest: prevention and management. *AJR Am J Roentgenol*. 2011;196(6):W678-W682. [CrossRef]

3. Wiener RS, Wiener DC, Gould MK. Risks of transthoracic needle biopsy: how high? *Clin Pulm Med*. 2013;20(1):29-35. [CrossRef]

4. Yoon SH, Lee SM, Park CH, et al. 2020 Clinical Practice Guideline for Percutaneous Transthoracic Needle Biopsy of Pulmonary Lesions: A Consensus Statement and Recommendations of the Korean Society of Thoracic Radiology. *Korean J Radiol*. 2021;22(2):263-280. [CrossRef]

5. Davidson K, Shojaee S. Managing massive hemoptysis. *Chest*. 2020;157(1):77-88. [CrossRef]

6. Lal H, Neyaz Z, Nath A, Borah S. CT-guided percutaneous biopsy of intrathoracic lesions. *Korean J Radiol*. 2012;13(2):210-226. [CrossRef]

7. Whigham CJ Jr, Fisher RG, Goodman CJ, Dodds CA, Trinh CC. Traumatic injury of the internal mammary artery: embolization versus surgical and nonoperative management. *Emerg Radiol*. 2002;9(4):201-207. [CrossRef]

8. Psallidas I, Helm EJ, Maskell NA, et al. Iatrogenic injury to the intercostal artery: aetiology, diagnosis and therapeutic intervention. *Thorax*. 2015;70(8):802-804. [CrossRef]

9. Chemelli AP, Thauerer M, Wiedermann F, Strasak A, Klocker J, Chemelli-Steingruber IE. Transcatheter arterial embolization for the management of iatrogenic and blunt traumatic intercostal artery injuries. *J Vasc Surg*. 2009;49(6):1505-1513. [CrossRef]

10. Andersen PE. Imaging and interventional radiological treatment of hemoptysis. *Acta Radiol*. 2006;47(8):780-792. [CrossRef]

11. O'Connor SD, Taylor AJ, Williams EC, Winter TC. Coagulation concepts update. *AJR Am J Roentgenol*. 2009;193(6):1656-1664. [CrossRef]

12. Atwell TD, Spanbauer JC, McMenomy BP, et al. The timing and presentation of major hemorrhage after 18,947 image-guided percutaneous biopsies. *AJR Am J Roentgenol*. 2015;205(1):190-195. [CrossRef]

13. Filippiadis DK, Binkert C, Pellerin O, Hoffmann RT, Krajina A, Pereira PL. Cirse quality assurance document and standards for classification of complications: the cirse classification system. *Cardiovasc Intervent Radiol*. 2017;40(8):1141-1146. [CrossRef]

14. Heerink WJ, de Bock GH, de Jonge GJ, Groen HJ, Vliegenthart R, Oudkerk M. Complication rates of CT-guided transthoracic lung biopsy: meta-analysis. *Eur Radiol*. 2017;27(1):138-148. [CrossRef]

15. Choi JW, Park CM, Goo JM, et al. C-arm cone-beam CT-guided percutaneous transthoracic needle biopsy of small (≤ 20 mm) lung nodules: diagnostic accuracy and complications in 161 patients. *AJR Am J Roentgenol*. 2012;199(3):W322-W330. [CrossRef]

16. Yeow KM, Su IH, Pan KT, et al. Risk factors of pneumothorax and bleeding: multivariate analysis of 660 CT-guided coaxial cutting needle lung biopsies. *Chest*. 2004;126(3):748-754. [CrossRef]

17. Tai R, Dunne RM, Trotman-Dickenson B, et al. Frequency and severity of pulmonary hemorrhage in patients undergoing percutaneous CT-guided transthoracic lung biopsy: single-institution experience of 1175 cases. *Radiology*. 2016;279(1):287-296. [CrossRef]

18. Song YS, Park CM, Park KW, et al. Does antiplatelet therapy increase the risk of hemoptysis during percutaneous transthoracic needle biopsy of a pulmonary lesion? *AJR Am J Roentgenol*. 2013;200(5):1014-1019. [CrossRef]

19. Hwang EJ, Park CM, Yoon SH, Lim HJ, Goo JM. Risk factors for haemoptysis after percutaneous transthoracic needle biopsies in 4,172 cases: Focusing on the effects of enlarged main pulmonary artery diameter. *Eur Radiol*. 2018;28(4):1410-1419. [CrossRef]

20. Dennie CJ, Matzinger FR, Marriner JR, Maziak DE. Transthoracic needle biopsy of the lung: results of early discharge in 506 outpatients. *Radiology*. 2001;219(1):247-251. [CrossRef]

21. Lordan JL, Gascoigne A, Corris PA. The pulmonary physician in critical care * Illustrative case 7: assessment and management of massive haemoptysis. *Thorax*. 2003;58(9):814-819. [CrossRef]

22. Chen LF, Wang TC, Lin TY, et al. Does tranexamic acid reduce risk of mortality on patients with hemoptysis?: A protocol for systematic review and meta-analysis. *Medicine (Baltimore)*. 2021;100(20):e25898. [CrossRef]

23. Tomiyama N, Yasuhara Y, Nakajima Y, et al. CT-guided needle biopsy of lung lesions: a survey of severe complication based on 9783 biopsies in Japan. *Eur J Radiol*. 2006;59(1):60-64. [CrossRef]

24. Dewhurst C, O'Neill S, O'Regan K, Maher M. Demonstration of the course of the posterior intercostal artery on CT angiography: relevance to interventional radiology procedures in the chest. *Diagn Interv Radiol*. 2012;18(2):221-224. [CrossRef]

25. Wu CC, Maher MM, Shepard JA. Complications of CT-guided percutaneous needle biopsy of the chest: prevention and management. *AJR Am J Roentgenol*. 2011;196(6):W678-W682. [CrossRef]

26. Yoneyama H, Arahata M, Temaru R, Ishizaka S, Minami S. Evaluation of the risk of intercostal artery laceration during thoracentesis in elderly patients by using 3D-CT angiography. *Intern Med*. 2010;49(4):289-292. [CrossRef]

27. Shurtleff E, Olinger A. Posterior intercostal artery tortuosity and collateral branch points: a cadaveric study. *Folia Morphol (Warsz)*. 2012;71(4):245-251. [CrossRef]

28. Kim JW, Shin JH, Kim PN, et al. Embolization for bleeding after hepatic radiofrequency ablation. *J Vasc Interv Radiol*. 2017;28(3):356-365. [CrossRef]

29. Marshall TJ, Jackson JE. Vascular intervention in the thorax: bronchial artery embolization for haemoptysis. *Eur Radiol*. 1997;7(8):1221-1227. [CrossRef]

30. Chun HJ, Oh JS, Lee HG, Choi BG. Bronchial artery embolization in the management of hemoptysis in patients with hematologic diseases: feasibility and short-term efficacy. *Iran J Radiol*. 2018;15(1):e61838. [CrossRef]

31. Kaw D, Malhotra D. Platelet dysfunction and end-stage renal disease. *Semin Dial*. 2006;19(4):317-322. [CrossRef]

# Usefulness of antegrade foam sclerotherapy for portal hypertensive variceal bleeding

Go Woon Park ⓘD
Sun Young Choi ⓘD
Yong Jae Kim ⓘD
Jewon Jeong ⓘD

**PURPOSE**

This study investigates the usefulness of antegrade variceal embolization using sclerosant foam to evaluate technical success and clinical outcomes in cases of hypertensive variceal bleeding.

**METHODS**

A total of 16 patients underwent percutaneous antegrade variceal embolization using foam sclerotherapy from August 2019 to January 2022. Among the patients, 12 cases were of gastroesophageal varices, two were rectal varices, and one case each was duodenal and jejunal varices, respectively. Sodium tetradecyl sulfate (STS) foam was used as a detergent for variceal bleeding sclerotherapy at various anatomical locations. The detergent was used in a foam form to promote clinical outcomes and enable the effective embolization of the entire blood vessel wall, including the ventral side, against gravity. Furthermore, STS foam could be used to help sufficiently deliver the drug to distal segments. A balloon catheter was also used to block the antegrade flow and prevent the dilution of the sclerosant. Technical success was defined as the completion of sclerotherapy for variceal bleeding as planned before the procedure to achieve the disappearance of variceal bleeding. Clinical success was defined as the complete obliteration of varices without recurrent bleeding during the follow-up period after the procedure.

**RESULTS**

Technical success was 81.3%, and clinical success was 84.6%. Additionally, 15/16 of the procedures were emergencies, and there were no complications related to the procedure.

**CONCLUSION**

Antegrade foam sclerotherapy using 3% STS for variceal bleeding is clinically safe and effective. Moreover, antegrade foam sclerotherapy can be a useful treatment option for patients with active variceal bleeding in emergency cases.

**KEYWORDS**

Portal hypertension, variceal bleeding, percutaneous endovascular variceal embolization, foam sclerotherapy

From the Department of Radiology (G.W.P.), Ewha Womans University Mokdong Hospital, Seoul, Republic of Korea; Department of Radiology (S.Y.C. ✉ medmath@ hanmail.net, Y.J.K., J.J.), Soonchunhyang University Seoul Hospital, 04401 59, Daesagwan-ro, Seoul, 07441, Republic of Korea.

Endoscopic management is the recommended first-line treatment for variceal bleeding. However, in a significant number of patients with variceal bleeding, the endoscopic approach may fail due to the patient's unstable vital signs and difficulties in securing the visual field.[1-4] In these cases, an alternative interventional treatment option, such as transjugular intrahepatic portosystemic shunt (TIPS) and balloon-occluded retrograde transvenous obliteration (BRTO), should be considered. However, although the therapeutic results of TIPS are good, it cannot be performed in patients with hepatocellular carcinoma, and it carries the risk of complications such as encephalopathy.[5-9] Conversely, BRTO is known to show a very safe and high success rate while compensating for the shortcomings of TIPS.[10] Nevertheless, there

are some limitations to BRTO, e.g., it can only be performed when there is an accessible shunt through the systemic venous system, and without such a shunt, the procedure is not possible.

The drawbacks of BRTO can be partially overcome using an alternative method such as direct variceal embolization with an antegrade approach. Percutaneous antegrade varix obliteration (PAVO) can, theoretically, permanently obliterate the varices and all feeding veins. It is performed by approaching from the afferent vessels so as not to increase the risk of variceal development.[10,11] In addition, PAVO has the advantage of being able to quickly and easily access the bleeding focus in patients with active bleeding.[11]

Most variceal embolization procedures using the antegrade approach have been performed using liquids such as an n-butyl cyanoacrylate (NBCA) mixture or several detergents.[4,12-14] For effective bleeding control, the embolic material must be well-delivered to the varix where bleeding is suspected. In the case of the NBCA mixture, there is a high possibility of embolization of only the proximal segment of the selected blood vessel. Therefore, it is often difficult to deliver the NBCA mixture to the varix. This results in insufficient varix embolization, leading to the failure of bleeding control or re-bleeding. Sclerotherapy using a sclerosant is effective for drug delivery along the bloodstream to the distal segment; however, the concentration of the drug is lowered as the blood flow and the drug are mixed, thus decreasing the effect of sclerotherapy. Additionally, due to gravity, there is less contact with the wall of the blood vessel on the ventral side among the blood vessel walls through which the drug passes. Therefore, the effect of liquid sclerotherapy may decrease. Furthermore, drug distribution to the branching vessels other than the main flow can decrease in the case of multiple branching vessels to the varices. These factors may eventually decrease the therapeutic effect of varix embolization through the antegrade approach, which can potentially cause rebleeding.

Detergent agents have been used as sclerosing agents in a liquid or foam form. The effectiveness of foam sclerotherapy for varix bleeding control was first reported in BRTO.[15] According to this report, compared with liquid sclerosants, a foam has several advantages, including reducing the amount of sclerosant needed, maximizing the sclerotic effect by increasing the contact surface area with the wall of the varices, and providing even distribution of the sclerosing agent, thus decreasing the balloon inflation and procedure times.[12] Accordingly, to compensate for the shortcomings of liquid sclerosants, sodium tetradecyl sulfate (STS) was used as a detergent in a foam form to perform varix sclerotherapy for various variceal bleeding sites. Finally, this study aims to evaluate the clinical safety and effectiveness of the antegrade approach using foam sclerotherapy for variceal bleeding.

## Methods

### Patients

Sixteen patients who were treated with PAVO for gastroesophageal varices or non-gastroesophageal varices between August 2019 and January 2022 at Ewha Womans University Mokdong Hospital were retrospectively evaluated. This patient group comprised 16 men with a median age of 58 years (range, 38–66 years). Of these patients, 12 had gastroesophageal varices, 2 had rectal varices, 1 had duodenal varices, and 1 had jejunal varices. Additionally, 9 patients had a history of endoscopic treatment, such as endoscopic variceal ligation (EVL) or endoscopic injection sclerotherapy (EIS), 1 patient had received both endoscopic treatment and BRTO, and 1 patient had undergone liver transplantation a year before the procedure. Prior to the procedure, all patients underwent enhanced computed tomography (CT) or endoscopy to evaluate the severity of the varices and the effectiveness of the procedure (Figure 1a). All 16 patients underwent enhanced CT, and 13 patients underwent both endoscopy and enhanced CT. The clinical characteristics of the patients are listed in Table 1.



**Figure 1.** A 52-year-old man with gastroesophageal varices. **(a)** Endoscopy shows marked engorged gastroesophageal varices, grade GII (red color sign). **(b)** Antegrade venography through a transportal approach shows multiple gastric and esophageal varices (black arrow). Two branching vessels (white arrow) are denoted as feeding vessels to the varices. **(c)** Multiple varices (black arrow) are filled with foam sclerosant (3% sodium tetradecyl sulfate) under inflation by the balloon catheter (4Fr Fogarty catheter) (white arrow) at the coronary vein ostium. **(d)** Follow-up splenoportography after completing sclerotherapy shows the complete obliteration of previously noted gastric and esophageal varices. **(e)** Follow-up endoscopy nine days after percutaneous antegrade varix obliteration showing the complete thrombotic occlusion of a previously engorged varix with no red color.

### Main points

- The usefulness of antegrade variceal embolization using sclerosant foam to evaluate technical success and clinical outcomes in cases of hypertensive variceal bleeding was studied.

- Technical success was 81.3%, clinical success was 84.6%, 15/16 procedures were emergencies, and there were no complications related to the procedure.

- Antegrade foam sclerotherapy using 3% sodium tetradecyl sulfate for variceal bleeding is clinically safe and effective.

- Antegrade foam sclerotherapy can be a useful treatment option for patients with active variceal bleeding in emergency cases.

**Table 1.** Clinical characteristics of the 16 patients

| Pt. no. | Age (years) | Sex | Etiology of LC | Concomitant malignancy | Location of the varix | Past history of varix treatment | Endoscopic varix grade[a] | Pre-procedural imaging |
|---|---|---|---|---|---|---|---|---|
| 1 | 65 | M | Alcohol | No | Gastroesophageal varix | EVL | GII, LmF2Cb, RC (+) | CT, endoscopy |
| 2 | 47 | M | Alcohol | No | Gastroesophageal varix | EVL | GII, LmF2Cb, RC (+) | CT, endoscopy |
| 3 | 54 | M | Alcohol | No | Gastroesophageal varix | EVL | GII, LsF2Cb, RC (+) | CT, endoscopy |
| 4 | 58 | M | HBV | HCC | Gastroesophageal varix | EVL | GIII, LsF3Cb, RC (+) | CT, endoscopy |
| 5 | 54 | M | Alcohol | No | Gastroesophageal varix | No | GII, LmF2Cb, RC (-) | CT, endoscopy |
| 6 | 65 | M | Alcohol | No | Gastroesophageal varix | EVL | GII, LmF2Cb, RC (-) | CT, endoscopy |
| 7 | 41 | M | Alcohol | No | Rectal varix | No | GII, RC (-) | CT, endoscopy |
| 8 | 62 | M | Alcohol | No | Duodenal varix | No | GI, LiF1Cb, RC (-) | CT, endoscopy |
| 9 | 38 | M | Alcohol | No | Gastroesophageal varix | EVL, EIS, BRTO | GI, LiF1Cb, RC (-) | CT, endoscopy |
| 10 | 66 | M | Non-B and non-C | HCC | Gastroesophageal varix | No | N/A | CT |
| 11 | 57 | M | Alcohol | No | Gastroesophageal varix | EIS | GIII, LsF3Cb, RC (+) | CT, endoscopy |
| 12 | 59 | M | Non-B and non-C | No | Jejunal varix | No | N/A | CT |
| 13 | 60 | M | Alcohol | No | Gastroesophageal varix | EVL | GIII, LsF3Cb, RC (+) | CT, endoscopy |
| 14 | 58 | M | Alcohol | No | Rectal varix | LT | N/A | CT |
| 15 | 58 | M | Alcohol | No | Gastroesophageal varix | EVL | GIII, LsF3Cb, RC (+) | CT, endoscopy |
| 16 | 52 | M | HBV | No | Gastroesophageal varix | No | GII, RC (+) | CT, endoscopy |

[a]Esophageal and gastric varices were graded by the system presented in Tajiri et al.[16] M, male; Pt. no., patient number; HBV, hepatitis B virus; LC, liver cirrhosis; HCC, hepatocellular carcinoma; EVL, endoscopic variceal ligation; EIS, endoscopic injection sclerotherapy; BRTO, balloon-occluded retrograde transvenous obliteration; LT, liver transplantation; CT, computed tomography; N/A, not applicable.

This retrospective study was approved by the Institutional Review Board of the Ewha Womans University Mokdong Hospital (EUMC 2022-05-044 2022-06-02) with a waiver for informed patient consent.

## Procedures

The approach to variceal bleeding was initiated employing either the percutaneous transhepatic or trans-splenic approach under ultrasonographic and fluoroscopic guidance using local anesthesia. The decision to access the liver or the spleen was based on the operators' judgment at the time of the procedure. If liver function was maintained with no or a small amount of ascites, the transhepatic approach was considered first. Otherwise, the trans-splenic approach was used. Using a 22-gauge Chiba needle (Neff Percutaneous Access Set, Cook Medical, Bloomington, IN, USA), a percutaneous puncture of the intrahepatic portal or splenic veins was performed. Then, a pre-flushed vascular sheath (6-Fr Balkin sheath; Cook Medical, Bloomington, IN, USA) was inserted through the portal or splenic veins. Portography or splenoportography via the inserted sheath was performed to evaluate the feeding vein, draining vein, and varix collaterals. Subsequently, a 5-Fr catheter (KMP; Cook Medical, Bloomington, IN, USA) was inserted to select the main antegrade feeding vessel and perform antegrade venography to evaluate the varix (Figure 1b). If the selection was successful, an occlusion balloon catheter (4 or 5.5-F Fogarty catheter, Edwards, USA) was exchanged to occlude the main antegrade flow. Thereafter, a foam sclerosant was directly injected into the feeding veins to the entire varices through the occlusion balloon catheter under fluoroscopic guidance (Figure 1c). If the main feeding vessel was too thin or too tortuous to insert the balloon catheter, the sclerosant was injected through the 5-F catheter directly or by a coaxially inserted microcatheter (1.9-F microcatheter, Progreat Lambda 19, Terumo, Tokyo, Japan). Thereafter, 3% fibrovein (STD Pharmaceutical Products Ltd, Hereford, UK) was used as a sclerosant. The foam sclerosant was prepared using the following double syringe system method:[17] two 10 mL Luer-Lok syringes containing 3% STS, room air, and contrast media (Pamiray 300; Dongkook Pharm., Seoul, Korea) in a 1:2:1 ratio, respectively. The syringes were then connected through a three-way stopcock and their contents were mixed until a homogeneous foam was obtained. The approximate amount of 3% STS used depended on the variceal volume determined by antegrade venography. The sclerosant injection was administered until drug filling was observed in both the feeding vein and the target varix on fluoroscopy. Since the volume of the varix was too large, if an excessive amount was needed to fill the entire varix with STS, gelatin sponge particles (Caligel, 560–710 μm, Hangzhou Alicon Pharm SCI. & TEC. Co. Ltd., Hangzhou City, Zhejiang, China) were mixed and used together. When the operator judged that the sclerosant had been sufficiently injected, the contrast medium was manually injected through the catheter to evaluate whether there were any residual varices. If a residual varix was observed, the process of manually injecting the contrast medium after injecting an additional sclerosant was repeated. After finishing the infusion of the sclerosants, all the catheters used were slowly withdrawn after 30–60 minutes from the onset of infusion. Portography or splenoportography was then again performed to assess the obliteration of the varices, and if any feeding veins remained, the procedure was repeated to completely obliterate the varices (Figure 1d). In cases where the feeding vein was more than 2–3 mm in diameter, proximal segment feeding-vein embolization was performed using metallic materials such as coils. Finally, the puncture tract within the liver or spleen was embolized with an NBCA mixture and microcoils (Cook Medical, Bloomington, IN, USA).

During the procedure, each patient's blood pressure, heart rate, electrocardiogram, and arterial oxygen saturation were monitored. Furthermore, prophylactic antibiotics were administered before the procedure to prevent infection.

The medical records of the 16 patients were retrospectively reviewed for follow-up. The evaluation included the recurrence and bleeding of varices and the rate of survival. Moreover, the duration was measured in days from the procedure until the date of death, the most recent clinical visit, or a scheduled surgery, such as liver transplantation. Unless the follow-up examination was not possible due to the patient's death, or if clinical departments considered the exam unnecessary, an endoscopic examination or contrast-enhanced CT was performed after the procedure to evaluate the obliteration of the varices (Figure 1e).

Technical success was defined as the completion of the sclerotherapy for variceal bleeding as planned before the procedure to achieve the disappearance of variceal bleeding. If there was immediate variceal bleeding after the procedure, it was regarded as a technical failure. Clinical success was defined as the complete obliteration of varices without recurrent bleeding during the follow-up period from the procedure date. The recurrence and bleeding of varices were evaluated by endoscopic examination or contrast-enhanced CT after the procedure. Rebleeding from the varices was defined as the presence of hematemesis or melena with endoscopic visualization or confirmed bleeding from the varices in contrast-enhanced CT. Rebleeding was considered significant only if the hemoglobin level dropped compared with previous values and a blood transfusion was required. Complications were defined as any untoward events that required active treatment or prolonged hospitalization. Due to the small number of patients, no statistical analysis was performed.

## Results

PAVO was performed in 16 patients using 3% fibrovein. In all cases, the pre-procedural CT images showed no shunt available for retrograde obliteration of the varices. Of the 16 patients, 15 underwent emergency embolization due to acute bleeding from the varices and 1 (patient 13) had the procedure done for prophylaxis.

Technical success was achieved in 13 of 16 patients (81.3%); 3 of the 16 patients experienced recurrent bleeding during hospital admission (patients 2, 4, and 14 in Table 2) and all 3 had massive variceal rebleeding immediately after the procedure and received blood transfusions due to decreased hemoglobin levels. Patient 2 underwent liver

transplantation 14 days after the procedure and died 38 days after the initial procedure due to multiorgan failure. Patient 4 showed melena 1 day after the procedure and died due to septic shock caused by spontaneous bacterial peritonitis. Patient 14 showed hematochezia immediately after the procedure and died due to hypovolemic shock and hepatorenal syndrome.

The transhepatic approach was used in 11, and the trans-splenic approach in 5 patients. The amount of 3% fibrovein used ranged from 4–50 mL (median, 15 mL). Additional embolization using gelatin sponge particles (Caligel) was performed in 11 patients, and an occlusion balloon catheter was used in 12 patients. The median follow-up duration was 40 days (range, 1–702 days). The overall results are summarized in Table 2.

Among the 16 patients, 11 underwent follow-up examination (1 underwent endoscopy, 3 underwent CT scans, and 7 underwent both endoscopy and CT). However, 2 patients refused the follow-up examination (patients 4 and 8), and 3 patients died before the follow-up examination (patients 1, 5, and 10).

Clinical success was achieved in 11 of 13 patients (84.6%). Among these 11 patients, 7 with follow-up imaging showed a complete obliteration of varices with no recurrent bleeding during the follow-up period. In addition, 4/11 patients who did not undergo follow-up examinations did not have recurrent bleeding during the follow-up period (Table 2). Recurrent variceal bleeding was noted in 2 patients (patients 6 and 15). Moreover, patient 6 experienced two episodes of recurrent bleeding, the first occurring one year after the initial procedure and the second occurring two years after the procedure. Both episodes were successfully controlled through a sequential treatment approach involving additional PAVO and EVL. Patient 15 also experienced two episodes of recurrent bleeding, the first at 5 months and the second occurring 1 year after the initial procedure; the bleeding was also well controlled using PAVO and EVL, sequentially.

Recurrent bleeding also occurred in patients 3 and 16; however, it was unrelated to the variceal bleeding. Patient 3 developed hematemesis and melena 82 days after the embolization; however, only a gastric ulcer was noted in the endoscopy without evidence of variceal bleeding. Patient 16 developed hypotension and hematochezia 6 days after the procedure; arterial bleeding was confirmed on CT angiography, and hemosta-

sis was achieved by performing trans-arterial embolization of the left gastric artery. There were no complications related to the procedure in any of the patients.

## Discussion

Variceal bleeding is a serious complication in patients with portal hypertension and is associated with high mortality. Endoscopic treatments such as EIS or EVL are the first-line treatment options for variceal bleeding.[2] In case of difficulties performing endoscopic treatment, the alternative treatment is an endovascular procedure such as TIPS or BRTO.[5,18,19] In patients with portal hypertension, if clinical follow-up is good and endoscopic examinations are performed regularly, bleeding control can be achieved through scheduled procedures involving the above-mentioned treatment options in most cases. However, emergency bleeding situations may occur in patients who do not know their medical history or do not receive regular check-ups. These patients will experience sudden bleeding and are admitted to the hospital in an emergency situation. Most of these patients will exhibit unstable vital signs and active bleeding, making it difficult to achieve proper treatment in a short period, as the visual field cannot be secured endoscopically. There are many risks associated with the TIPS procedure as most of the patients were hemodynamically unstable. Therefore, in these emergencies, it is important to target and treat the bleeding varix quickly using an endovascular method. If the varix has an accessible shunt, BRTO can be prioritized in these cases. Many studies have been published on successful hemostasis with BRTO for ruptured varices.[20-22] However, if retrograde obliteration is difficult, as in the present study, PAVO may be an alternative and is considered one of the best hemostatic options for bleeding varices in emergencies. Therefore, in this study, 15 of 16 patients received PAVO in an emergency situation.

Different from BRTO, various types of variceal bleeding can be controlled using an antegrade approach. In this study, embolization was performed using an antegrade approach through the portal or splenic vein to access various types of varices, including esophageal, gastric, duodenal, jejunal, and rectal varices.

Detergents have previously been used either in a liquid or foam form in various vascular embolization procedures.[12,17,23-28] In this study, STS foam was used as a sclerosant.

**Table 2.** Overall results of percutaneous antegrade varix embolization

| Pt. no. | Approach vessel | Amount of STS (mL)[a] | Additional embolic material (varix) | Embolic material (feeder ostium) | Used catheter | No. of feeding veins | Follow-up duration (procedure to 1st following imaging) (day) | Follow-up imaging modality | Overall follow-up duration (day) | Technical success | Clinical success |
|---|---|---|---|---|---|---|---|---|---|---|---|
| 1 | Portal vein | 15 | Gelfoam | Microcoils | 5.5-F balloon, 5Fr catheter* | 2 | N/A | None | 4 | Success | Success |
| 2 | Portal vein | 15 | None | Vascular plug | Microcatheter | 1 | 17 | CT | 38 | Failure | N/A |
| 3 | Portal vein | 15 | None | Microcoils, NBCA mixture | Microcatheter | 1 | 6 | CT, endoscopy | 109 | Success | Success |
| 4 | Splenic vein | 20 | None | No | 4-F balloon | 1 | N/A | None | 17 | Failure | N/A |
| 5 | Splenic vein | 5 | Gelfoam | No | 4-F balloon | 1 | N/A | None | 1 | Success | Success |
| 6 | Portal vein | 10 | None | No | 4-F balloon | 1 | 395 | Endoscopy | 702 | Success | Failure |
| 7 | Portal vein | 5 | Gelfoam | No | 4-F balloon | 1 | 8 | CT, endoscopy | 353 | Success | Success |
| 8 | Portal vein | 25 | None | No | 5.5-F balloon | 2 | N/A | None | 12 | Success | Success |
| 9 | Splenic vein | 15 | Gelfoam | No | Microcatheter | 3 | 24 | CT, endoscopy | 42 | Success | Success |
| 10 | Portal vein | 15 | Gelfoam | No | 5.5-F balloon | 2 | N/A | None | 2 | Success | Success |
| 11 | Splenic vein | 15 | Gelfoam | No | 4-F balloon | 1 | 30 | CT | 49 | Success | Success |
| 12 | Portal vein | 4 | Gelfoam | Microcoils | Microcatheter | 1 | 637 | CT | 645 | Success | Success |
| 13 | Portal vein | 50 | Gelfoam | Microcoils | 5.5-F balloon | 2 | 28 | CT, endoscopy | 606 | Success | Success |
| 14 | Splenic vein | 10 | Gelfoam | No | 5.5-F balloon | 1 | 10 | CT, endoscopy | 34 | Failure | N/A |
| 15 | Portal vein | 6 | Gelfoam | No | 4-F balloon | 1 | 8 | CT, endoscopy | 633 | Success | Failure |
| 16 | Portal vein | 6 | Gelfoam | No | 4-F balloon | 1 | 6 | CT, endoscopy | 19 | Success | Success |

[a]Represents a 3% STS concentration, not the total volume of the mixture. *A 5.5Fr balloon catheter was used in one feeding vein, and a 5Fr catheter was used in another feeding vein. Pt. no., patient number; STS, sodium tetradecyl sulfate; NBCA, N-butyl cyanoacrylate; 4Fr/5.5Fr balloon, 4-French/5.5Fr balloon catheter; CT, computed tomography; N/A, not applicable.

The safety of using STS foam sclerotherapy has been well-documented in previous studies.[24-27,29] In addition, it is believed that the treatment effect was maximized, as the drug was sufficiently delivered to the varix, as embolization was performed using foam rather than a liquid. Foam sclerosant has low density, and its concentration is maintained along the bloodstream. It can be delivered not only in the main branch vessels but also in small branches and can be well-delivered to distal segments, providing even distribution of the sclerosing agent. Moreover, foam sclerosant is less affected by gravity; it can, therefore, contact the ventral side of the vessel wall, maximizing the sclerotic effect by increasing the contact surface area with the variceal walls. Therefore, a foam sclerosant can provide an increased sclerotic effect with a reduced drug amount compared with a liquid agent. For this reason, the results of the procedure were encouraging. In this study, 81.3% technical and 84.6% clinical success was achieved. There were also no complications related to the procedure. These results may have been due to embolization using a safe sclerosant, performing the antegrade approach appropriately in an emergency situation, and, finally, using the sclerosant in foam form. Therefore, PAVO is considered a safe and effective procedure for various forms of variceal bleeding in emergency situations.

Although there have been limited studies comparing the recurrent bleeding rate of BRTO and PAVO, one study compared recurrence of gastric varices and rebleeding rates among BRTO, percutaneous transhepatic obliteration (PTO), and combined BRTO and PTO. In that study, the gastric varix recurrence and rebleeding rate were higher in PTO than in BRTO.[30] However, the size of the PTO group was relatively smaller than the BRTO group (13 and 75 patients, respectively), and an ethanolamine oleate solution with iopamidol was used as a sclerosing agent, which may have limited the comparability of that study's results with those of the current study. Another study that used polidocanol foam in BRTO showed a technical success rate of 93.8% (15/16) and a clinical success rate of 91% (10/11).[15]

Although antegrade foam sclerotherapy showed effectiveness, this study has some limitations, including its retrospective design, small sample size, and the absence of long-term follow-up results. A prospective study with a larger sample size is necessary to further evaluate the effectiveness of the approach.

In conclusion, the study results demonstrate that antegrade foam sclerotherapy using 3% STS for variceal bleeding is clinically safe and effective. Additionally, antegrade foam sclerotherapy can be a useful treatment option for patients with active variceal bleeding in emergency cases.

### Conflict of interest disclosure

The authors declared no conflicts of interest.

# References

1. Westaby D, Hayes PC, Gimson AE, Polson RJ, Williams R. Controlled clinical trial of injection sclerotherapy for active variceal bleeding. *Hepatology*. 1989;9(2):274-277. [CrossRef]

2. Trudeau W, Prindiville T. Endoscopic injection sclerosis in bleeding gastric varices. *Gastrointest Endosc*. 1986;32(4):264-268. [CrossRef]

3. Zhang K, Sun X, Wang G, et al. Treatment outcomes of percutaneous transhepatic variceal embolization versus transjugular intrahepatic portosystemic shunt for gastric variceal bleeding. *Medicine (Baltimore)*. 2019;98(18):e15464. [CrossRef]

4. Chikamori F, Kuniyoshi N, Kagiyama S, Kawashima T, Shibuya S, Takase Y. Role of percutaneous transhepatic obliteration for special types of varices with portal hypertension. *Abdominal Imaging*. 2007;32(1):92-95. [CrossRef]

5. Henderson JM, Nagle A, Curtas S, Geisinger M, Barnes D. Surgical shunts and TIPS for variceal decompression in the 1990s. *Surgery*. 2000;128(4):540-547. [CrossRef]

6. Peter P, Andrej Z, Katarina SP, Manca G, Pavel S. Hepatic encephalopathy after transjugular intrahepatic portosystemic shunt in patients with recurrent variceal hemorrhage. *Gastroenterol Res Pract*. 2013;2013:398172. [CrossRef]

7. Routhu M, Safka V, Routhu SK, et al. Observational cohort study of hepatic encephalopathy after transjugular intrahepatic portosystemic shunt (TIPS). *Ann Hepatol*. 2017;16(1):140-148. [CrossRef]

8. Kim JJ, Dasika NL, Yu E, Fontana RJ. Transjugular intrahepatic portosystemic shunts in liver transplant recipients. *Liver Int*. 2008;28(2):240-248. [CrossRef]

9. Luo SH, Chu JG, Huang H, Yao KC. Safety and efficacy of transjugular intrahepatic portosystemic shunt combined with palliative treatment in patients with hepatocellular carcinoma. *World J Clin Cases*. 2019;7(13):1599-1610. [CrossRef]

10. Saad WE. Balloon-occluded retrograde transvenous obliteration of gastric varices: concept, basic techniques, and outcomes. *Semin Intervent Radiol*. 2012;29(2):118-128. [CrossRef]

11. Saad WE, Kitanosono T, Koizumi J. Balloon-occluded antegrade transvenous obliteration with or without balloon-occluded retrograde transvenous obliteration for the management of gastric varices: concept and technical applications. *Tech Vasc Interv Radiol*. 2012;15(3):203-225. [CrossRef]

12. Wang G, Meng D, Huang G, et al. Balloon-assisted percutaneous transhepatic antegrade embolization with 2-octyl cyanoacrylate for the treatment of isolated gastric varices with large gastrorenal shunts. *Biomed Res Int*. 2019;2019:2674758. [CrossRef]

13. Ishikawa T, Imai M, Ko M, et al. Percutaneous transhepatic obliteration and percutaneous transhepatic sclerotherapy for intractable hepatic encephalopathy and gastric varices improves the hepatic function reserve. *Biomed Rep*. 2017;6(1):99-102. [CrossRef]

14. Yoshimatsu R, Yamagami T, Miura H, Okuda K. Percutaneous transhepatic sclerotherapy with embolization of the drainage vein for a gastric varix. *Acta Radiol Short Rep*. 2014;3(7):2047981614530285. [CrossRef]

15. Choi SY, Won JY, Kim KA, Lee DY, Lee KH. Foam sclerotherapy using polidocanol for balloon-occluded retrograde transvenous obliteration (BRTO). *Eur Radiol*. 2011;21(1):122-129. [CrossRef]

16. Tajiri T, Yoshida H, Obara K, et al. General rules for recording endoscopic findings of esophagogastric varices (2nd edition). *Dig Endosc*. 2010;22(1):1-9. [CrossRef]

17. Kim YH, Kim YH, Kim CS, Kang UR, Kim SH, Kim JH. Comparison of balloon-occluded retrograde transvenous obliteration (BRTO) using ethanolamine oleate (EO), brto using sodium tetradecyl sulfate (STS) foam and vascular plug-assisted retrograde transvenous obliteration (PARTO). *Cardiovasc Intervent Radiol*. 2016;39(6):840-846. [CrossRef]

18. Koconis KG, Singh H, Soares G. Partial splenic embolization in the treatment of patients with portal hypertension: a review of the english language literature. *J Vasc Interv Radiol*. 2007;18(4):463-481. [CrossRef]

19. Saad WE, Sze DY. Variations of balloon-occluded retrograde transvenous obliteration (BRTO): balloon-occluded antegrade transvenous obliteration (BATO) and alternative/adjunctive routes for BRTO. *Semin Intervent Radiol*. 2011;28(3):314-324. [CrossRef]

20. Sonomura T, Ono W, Sato M, et al. Emergency balloon-occluded retrograde transvenous obliteration of ruptured gastric varices. *World J Gastroenterol*. 2013;19(31):5125-5130. [CrossRef]

21. Sonomura T, Horihata K, Yamahara K, et al. Ruptured duodenal varices successfully treated with balloon-occluded retrograde transvenous obliteration: usefulness of microcatheters. *AJR Am J Roentgenol*. 2003;181:725-727. [CrossRef]

22. Zamora CA, Sugimoto K, Tsurusaki M, et al. Endovascular obliteration of bleeding duodenal varices in patients with liver cirrhosis. *Eur Radiol*. 2006;16(1):73-79. [CrossRef]

23. Patel NR, Stella SF, Nasser M, et al. Safety of high-dose 3% sodium tetradecyl sulfate for sclerotherapy of renal cysts in patients with autosomal dominant polycystic kidney disease. *J Vasc Interv Radiol*. 2022;33(6):715-718. [CrossRef]

24. Mukund A, Deogaonkar G, Rajesh S, Shasthry SM, Sarin SK. Safety and efficacy of sodium tetradecyl sulfate and lipiodol foam in balloon-occluded retrograde transvenous obliteration (BRTO) for large porto-systemic shunts. *Cardiovasc Intervent Radiol*. 2017;40(7):1010-1016. [CrossRef]

25. Fischman AM, Ward TJ, Horn JC, et al. Portal vein embolization before right hepatectomy or extended right hepatectomy using sodium tetradecyl sulfate foam: technique and initial results. *J Vasc Interv Radiol*. 2014;25(7):1045-1053. [CrossRef]

26. Park HS, Do YS, Park KB, et al. Clinical outcome and predictors of treatment response in foam sodium tetradecyl sulfate sclerotherapy of venous malformations. *Eur Radiol*. 2016;26(5):1301-1310. [CrossRef]

27. Sabri SS, Swee W, Tyrba UC, et al. Bleeding gastric varices obliteration with balloon-occluded retrograde transvenous obliteration using sodium tetradecyl sulfate foam. *J Vasc Interv Radiol*. 2011;22(3):309-316. [CrossRef]

28. Jenkinson HA, Wilmas KM, Silapunt S. Sodium tetradecyl sulfate: a review of clinical uses. *Dermatol Surg*. 2017;43(11):1313-1320. [CrossRef]

29. Davies HO, Watkins M, Oliver R, Berhane S, Bradbury AW. Adverse neurological events after sodium tetradecyl sulfate foam sclerotherapy - a prospective, observational study of 8056 treatments. *Phlebology*. 2022;37(2):97-104. [CrossRef]

30. Arai H, Abe T, Takagi H, Mori M. Efficacy of balloon-occluded retrograde transvenous obliteration, percutaneous transhepatic obliteration and combined techniques for the management of gastric fundal varices. *World J Gastroenterol*. 2006;12(24):3866-3873. [CrossRef]

# Usefulness of tumor perfusion on cone-beam CT after hepatic arterial infusion port implantation for evaluating tumor response to hepatic arterial infusion chemotherapy in hepatocellular carcinoma treatment

Phan Nhan Hien
Ho Jong Chun
Jung Suk Oh
Su Ho Kim
Byung Gil Choi

**PURPOSE**

To compare tumor perfusion on cone-beam computed tomography (CBCT) after hepatic artery infusion port implantation with the tumor response to hepatic arterial infusion chemotherapy (HAIC) in patients with hepatocellular carcinoma (HCC).

**METHODS**

This retrospective study was conducted in patients with advanced HCC treated with HAIC from 2015 to 2020. We performed CBCT with contrast injection via a port on the day following implantation. We classified tumor perfusion on CBCT into three groups: hyperperfusion, isoperfusion, and hypoperfusion. We also evaluated tumor response to HAIC on follow-up images using RECIST 1.1 and compared it with tumor perfusion on CBCT.

**RESULTS**

This study included 206 tumors in 193 patients (mean: 60.5 years) with HCC. There were 100 hyperperfusion tumors (48.5%), 92 isoperfusion tumors (44.7%), and 14 hypoperfusion tumors (6.8%). The tumor response to HAIC included 10 tumors with a complete response (CR) (4.9%), 66 tumors with a partial response (32%), 60 tumors with stable disease (29.1%), and 70 tumors with progressive disease (34%). Hyperperfusion tumors had a 65% objective response rate (ORR) and a 92% disease control rate (DCR). Isoperfusion tumors had a 12% ORR and a 46.8% DCR, while hypoperfusion tumors had a 0% ORR and a 7.1% DCR. A CR was shown only in hyperperfusion tumors. The ORR and DCR of the three groups were different, with statistical significance ($P < 0.001$).

**CONCLUSION**

Hyperperfusion tumors on CBCT showed a better tumor response to HAIC, with a 65% ORR in patients with HCC. Tumor perfusion on CBCT after implantation of the hepatic arterial infusion port was associated with the tumor response to HAIC.

**KEYWORDS**

Cone-beam CT, hepatic arterial infusion chemotherapy, hepatocellular carcinoma, tumor perfusion, tumor response

From the Department of Radiology (P.N.H., H.J.C. ✉ hojongchun@gmail.com, J.S.O., S.H.K., B.G.C.), Seoul St. Mary's Hospital College of Medicine, The Catholic University of Korea, Seoul, Republic of Korea.

Hepatocellular carcinoma (HCC) is among the world's main causes of cancer-related deaths.[1] Many patients (42%–50%) are diagnosed at late stages, with short overall survival (OS) of only 4.2–7.9 months due to a lack of effective treatment. In recent years, the explosive development of systemic therapies has brought about increased treatment opportunities for patients with advanced HCC. However, the results have not been consistently effective, and significant side effects have been recorded.[2-5]

Hepatic arterial infusion chemotherapy (HAIC) has been widely approved as a monotherapy or combination therapy for treating patients with advanced HCC in East Asian countries.

The practical guidelines for HCC treatment in these countries recommend HAIC for treating patients with HCC and portal vein tumor thrombosis (PVTT) and for HCCs refractory to transarterial chemoembolization (TACE).[6-8] The primary purpose of HAIC treatment is to transport high concentrations of chemotherapeutic agents to tumors; accordingly, the distribution of such agents via infusion ports directly affects tumor responses.[9] Although there have been several studies on the distribution of chemotherapeutic agents in tumors after the placement of a HAIC port, none have investigated the relationship between this tumor perfusion and tumor response after treatment.[10-12] In our study, the contrast distribution pattern on cone-beam computed tomography (CBCT) after the insertion of a HAIC port was evaluated the day after port insertion to assess the relationship between tumor perfusion on CBCT and tumor response to HAIC treatment.

## Methods

### Patients

This retrospective study's protocol was approved by Seoul St. Mary's Hospital's Institutional Review Board (approval number: KC22RISI0706). Due to the study's design, we were permitted to remove the requirement for patient consent. Our study collected data on patients treated with HAIC from January 2015 to December 2020. HAIC was performed in patients with HCC plus PVTT or refractory TACE and in those unsuitable for local therapies because of tumor spread in both hemilivers. In this study, the inclusion criteria included the following: (a) patients who had undergone at least two cycles of HAIC after insertion, (b) age ≥18 years, (c) patients with full pre- and post-treatment images [CT or magnetic resonance imaging (MRI)], (d) contrast-enhanced CBCT performed on the day following implantation, and (e) patients presenting with at least one measurable hepatic lesion. The exclusion criteria included (a) patients with Barcelona Clinic Liver Cancer (BCLC) grade D, (b) those with a insufficient pre- and post-treatment images (CT or MRI), (c) those without CBCT after HAIC port implantation, (d) patients who underwent TACE or other local therapies combined with HAIC simultaneously, and (e) patients with fewer than two HAIC cycles after port implantation. All tumors were diagnosed as HCC based on biopsy or imaging criteria CT and/or MRI combined with tumor markers.

### Procedures

The procedure was performed by two interventional radiologists with over 10 years of experience. With the patient under local anesthesia, the procedure was performed via the right femoral artery or the left subclavian artery. The Seldinger technique was utilized to puncture the common femoral artery using a guide wire (Terumo, 0.035-inch diameter) and an Angiocath 18G catheter. Selective angiography was performed on the celiac artery, superior mesenteric artery, and the extrahepatic arteries feeding the tumor [right inferior phrenic artery (RIPA), internal mammary artery, etc.]. Before the infusion port was inserted, the collateral branches from the extrahepatic arteries were embolized to increase the effectiveness of the treatment. The left gastric artery was embolized by a pushable microcoil (Tornado, Cook, USA) or detachable microcoils (Concerto, Medtronic, USA) to prevent the reflux of chemotherapeutic agents into the stomach during treatment. Following the placement of a port catheter (Celsite® port and catheters, B. Braun Medical, USA) in the common hepatic artery, the distal end of the catheter was fixed to the gastroduodenal artery using microcoils (Concerto, Medtronic, USA). Sixteen patients had variant hepatic artery anatomy, with each main blood supplying artery in both hemilivers; therefore, two ports were required.[12] To prevent catheter occlusion after each cycle of HAIC therapy, 3,000–5,000 units of heparin were packed into the port chamber and catheter.

On the day following implantation, we routinely performed CBCT with contrast enhancement to evaluate both port performance and contrast distribution. Contrast media (Visipaque 270, GE Healthcare, USA) was infused via the port. A CT scan was started 40 sec after the injection of 40 mL of contrast media at a rate of 1 mL/sec.

### Tumor perfusion

We classified contrast perfusion of the tumor on CBCT into the following three perfusion types: (1) hyperperfusion type: the tumor was more contrast-enhanced than the rest of the hepatic parenchyma; (2) isoperfusion type: the tumor enhancement was homogeneous and indistinguishable from the rest of the hepatic parenchyma; (3) hypoperfusion type: the tumor had less contrast enhancement than the remaining hepatic parenchyma or no enhancement on CBCT (Figure 1). In each patient, each tumor perfusion type was selected based only on the largest tumor that could be measured.

### Chemotherapy

We adopted the following chemotherapy protocol for HAIC: an epirubicin–cisplatin-5-fluorouracil (ECF) chemotherapy regimen was repeated approximately every month. The ECF chemotherapy regimen consisted of 35 mg/m$^2$ of epirubicin on day 1, 60 mg/m$^2$ of cisplatin over 2 hours on day 2, and 500 mg/m$^2$ of 5-fluorouracil over 5 hours on days 1 to 3.

### Tumor response

Contrast-enhanced CT or MRI was performed after every two cycles of HAIC before

**Main points**

- Tumor perfusion on cone-beam computed tomography after the implantation of a hepatic arterial infusion port was associated with the tumor's response to hepatic arterial infusion chemotherapy (HAIC).

- The hyperperfusion tumor had the best tumor response. A complete response was shown only in hyperperfusion tumors.

- Most hypoperfusion tumors exhibited disease progression following treatment with HAIC. Hypoperfusion-type tumors were found predominantly in patients with hepatic artery anatomical variations or extrahepatic circulation that specifically involved the right inferior phrenic artery supplying the tumor.



**Figure 1.** Tumor perfusion type on cone-beam computed tomography. **(a)** Hyperperfusion type: the right hepatic tumor must be more enhanced with contrast media than the remaining hepatic parenchyma. **(b)** The isoperfusion-type tumor and hepatic parenchyma are heterogeneous, with no difference between the tumor and the normal hepatic parenchyma. **(c)** A hypoperfusion type observed at the posterior segment without contrast enhancement.

initiating the next cycle, with each cycle repeated every month. We used the Response Assessment Criteria in Solid Tumors (RECIST) version 1.1 instead of the modified RECIST guideline because the latter is unsuitable for use in cases of infiltrative tumors.[13-15] We selected the best overall tumor response to assess tumor response in comparison with tumor perfusion. The best overall tumor response was defined as the most favorable response observed from the start of HAIC treatment until the final follow-up time point collected for each patient. The overall response rate (ORR) was defined as a complete response (CR) or a partial response (PR). The disease control rate (DCR) was defined as CR, PR, and stable disease (SD).

### Statistical analysis

We expressed data for continuous variables as means ± standard deviations and data for categorical variables as frequencies. Fisher's exact test or the chi-squared test was used to compare tumor responses between groups. A value of $P \leq 0.05$ was regarded as significant. Statistical analyses were conducted using SPSS v.25.0 software (IBM Corp, Armonk, NY, USA).

## Results

We collected data between January 2014 and December 2021. A total of 193 patients with 206 tumors were selected, and the patients' characteristics are summarized in Table 1. The mean age was 60.5 ± 10.4 years (26–89 years), 171 patients were male (88.6%), and 22 patients were female (11.4%). A total of 145 patients were infected with hepatitis B (75.1%). The majority of patients were Child–Pugh stage A or B, with 153 patients at Child–Pugh stage A (79.3%). In our study, 180 patients were BCLC stage C (93.3%). One hundred seventy-two patients had PVTT (89.1%), of which 82 patients had PVTT in both hemilivers (42.5%). There were 121 patients (62.7%) with infiltrative tumors and 30 patients (15.5%) with solitary tumors.

The technical characteristics of HAIC and tumor perfusion on CBCT after port implantation are summarized in Table 2. Among the 193 patients with HAIC were 43 patients with hepatic arterial variations, of which 16 patients had dual ports inserted. The predominant anatomical variant observed was the right hepatic artery originating from the superior mesenteric artery in 29 patients (15%). All patients received contrast-enhanced CBCT on the day following port implantation.

**Table 1.** Basic characteristics of the patients

| Characteristic | Value n (%) |
| --- | --- |
| Age (years) ± standard deviation | 60.5 ± 10.4 |
| **Gender** | |
| Male | 171 (88.6) |
| Female | 22 (11.4) |
| **Cause of cirrhosis** | |
| HBV | 139 (72) |
| HCV | 9 (4.7) |
| HBV + HCV | 5 (2.6) |
| Alcohol | 6 (3.1) |
| **Child–Pugh class** | |
| A | 153 (79.3) |
| B | 39 (20.2) |
| C | 1 (0.5) |
| **BCLC class** | |
| A | 0 (0) |
| B | 13 (6.7) |
| C | 180 (93.3) |
| **PVTT** | |
| No | 21 (10.9) |
| Segmental | 20 (10.4) |
| Lobar | 70 (36.3) |
| Bilobar | 82 (4.5) |
| **HCC type** | |
| Multifocal nodular | 42 (21.8) |
| Focal massive | 30 (15.5) |
| Infiltrative | 121 (62.7) |

HBV, hepatitis B virus; HCV, hepatitis C virus; BCLC, Barcelona Clinic Liver Cancer; PVTT, portal vein tumor thrombosis; HCC: hepatocellular carcinoma.

**Table 2.** Features of port implantation and tumor classification

| Characteristic | Value n (%) |
| --- | --- |
| **Hepatic artery variations** | |
| No | 150 (77.7) |
| Yes | 43 (22.3) |
| **Number of ports** | |
| Mono | 177 (91.7) |
| Dual | 16 (8.3) |
| **Tumor perfusion type** | |
| Hyperperfusion | 100 (48.5) |
| Isoperfusion | 92 (44.7) |
| Hypoperfusion | 14 (6.8) |
| **Best tumor response** | |
| CR | 10 (4.9) |
| PR | 66 (32) |
| SD | 60 (29.1) |
| PD | 70 (34) |

CR, complete response; PR, partial response; SD, stable disease; PD, progressive disease.

The perfusion of 206 tumors was analyzed after CBCT, of which 100 were hyperperfusion tumors (48.5%), 92 were isoperfusion tumors (44.7%), and 14 were hypoperfusion tumors (6.8%). There was no association between tumor perfusion types after CBCT and the number of ports ($P = 0.114$) or hepatic arterial variations ($P = 0.427$) (Table 3). The most common locations for hypoperfusion tumors were in the posterior segment and the left hemiliver. Among the patients with hypoperfusion tumors, we encountered nine cases of variant hepatic arterial anatomy. In six of these patients, RIPA embolization was not performed prior to port implantation for hepatic perfusion redistribution, and in one case, a significant arterial portal venous shunt was identified within the right hepatic artery.

Tumor response and the relationship with tumor perfusion on CBCT: there were 10 tumors with a CR (4.9%), 66 tumors with a PR (32%), 60 tumors with SD (29.1%), and 70 tumors with PD (34%). Seventy-six tumors had an ORR of 36.9%, and 136 tumors had a DCR of 66%. Tumor response differed according to tumor perfusion on CBCT: the CR, PR, SD, and PD values in the hyperperfusion tumor group were 10%, 55%, 27%, and 8%, respectively; the values in the isoperfusion tumor group were 0%, 12%, 34.8%, and 53.2%, respectively; and the values in the hypoperfusion tumor group were 0%, 0%, 7.1%, and 92.9%, respectively (Figure 2). The hyperperfusion tumor group had a 65% ORR and a 92% DCR, the isoperfusion group had a 12% ORR and a 46.8% DCR, and the hypoperfusion group had a 0% ORR and a 7.1% DCR. All (100%) tumors with CR were of the hyperperfusion type. The ORR and DCR values among the three groups were different, with statistical significance ($P < 0.001$) (Table 3). There was no difference in ORR between the isoperfusion and hypoperfusion groups ($P = 0.171$); however, the DCR of these two groups differed ($P = 0.007$).

## Discussion

The factors affecting the OS of patients treated with HAIC include patients' status according to the Child–Pugh score, BCLC stage, the classification of PVTT, and tumor size and number. HCC with infiltrative characteristics or rim-like enhancement indicates a poor prognosis.[13,14] Several studies have shown that the response of a tumor to HAIC is related directly to OS. According to Kim et al.[13], when tumor did not initially respond to HAIC, which indicated a poor prognosis. The early prediction of tumor response based on

**Table 3.** Comparative analysis of tumor perfusion types

| Tumor perfusion type | Hyperperfusion | Isoperfusion | Hypoperfusion | P |
|---|---|---|---|---|
| **HCC type** | | | | |
| Multifocal nodular | 23 (23) | 20 (21.7) | 2 (14.3) | |
| Focal massive | 17 (17) | 12 (13) | 3 (21.4) | 0.833 |
| Infiltrative | 60 (60) | 60 (65.2) | 9 (64.3) | |
| **PVTT** | | | | |
| No | 14 (14) | 8 (8.7) | 0 (0) | |
| Segmental | 13 (13) | 7 (7.6) | 1 (7.1) | |
| Lobar | 41 (41) | 29 (31.5) | 4 (28.6) | 0.065 |
| Bilobar | 32 (32) | 48 (52.2) | 9 (64.3) | |
| **Hepatic artery variations** | | | | |
| No | 81 (81) | 68 (73.9) | 8 (57.1) | |
| Yes | 19 (19) | 24 (26.1) | 6 (42.9) | 0.114 |
| **Number of ports** | | | | |
| Mono | 93 (93) | 81 (88) | 12 (85.7) | |
| Dual | 7 (7) | 11 (12) | 2 (14.3) | 0.427 |
| **Best tumor response** | | | | |
| CR | 10 (10) | 0 (0) | 0 (0) | |
| PR | 55 (55) | 11 (12) | 0 (0) | |
| SD | 27 (27) | 32 (34.8) | 1 (7.1) | $P < 0.001$ |
| PD | 8 (8) | 49 (53.2) | 13 (92.9) | |
| ORR (%) | 65 | 12 | 0 | $P < 0.001$ |
| DCR (%) | 92 | 46.8 | 7.1 | $P < 0.001$ |

HCC, hepatocellular carcinoma; PVTT, portal vein tumor thrombosis; CR, complete response; PR, partial response; SD, stable disease; PD, progressive disease; ORR, objective response rate; DCR, disease control rate.
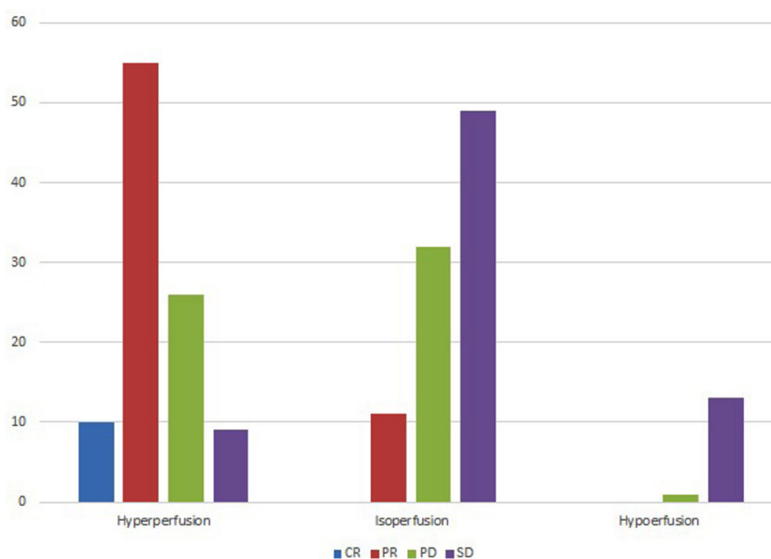


**Figure 2.** Comparison of tumor response in tumor perfusion types. CR, complete response; PR, partial response; SD, stable disease; PD, progressive disease.

tumor perfusion assessment immediately after HAIC port placement can facilitate the timely selection of optimal combined treatments or alternative therapies for tumors with poor response prognoses.

The initial tumor response to HAIC depends on a tumor's histological differentiation, its invasion and metastasis, and the distribution of chemotherapeutic agents within the tumor. The initial response assessment is usually performed after at least two cycles of HAIC.[13] The purpose of HAIC is to concentrate chemotherapeutic agents in the tumor rather than in the normal parenchyma, which increases the tumor's response to chemotherapy and reduces the side effects of chemotherapy on the normal liver parenchyma. To evaluate the distribution of chemotherapeutic agents in the liver parenchyma, several studies used the injection of tech-

netium-99m-labeled macroaggregated albumin via a port followed by single-photon emission CT. This method accurately determined chemotherapeutic agent distribution throughout the liver parenchyma.[10,11] Seki et al.[16] utilized slow-infusion MR arteriography to reflect the actual distribution of infused drugs. Meanwhile, CBCT can be performed following port implantation to check the port's function and detect the recanalization of embolized arteries and new anastomoses that could prevent chemotherapeutic agents from spreading to the surrounding organs, especially the stomach. Additionally, CBCT has been used following TACE to predict tumor response and prognosis and guide subsequent investigations.[17,18] As in some previous studies that have utilized CBCT to analyze perfusion patterns after port implantation, the technique may be useful for predicting tumor response to HAIC.[19,20]

In the present study, contrast-enhanced CBCT showed three tumor perfusion types, including 100 hyperperfusion tumors (48.5%), 92 isoperfusion tumors (44.7%), and 14 hypoperfusion tumors (6.3%). Ikeda et al.[11] classified intrahepatic perfusion into six groups according to lobes and segments, with three main types: homogeneous distribution, hyperperfusion, and perfusion defect. This classification method is similar to our method for classifying tumor perfusion types. The tumor responses in our study varied on CBCT according to the different types. Figure 2 shows a better tumor response in the hyperperfusion group (65% ORR, 92% DCR); the isoperfusion type had a 12% ORR and a 46.8% DCR, while the hypoperfusion type had a 0% ORR and a 7.1% DCR. A CR was demonstrated only in the hyperperfusion group (Figure 3). The ORR and DCR values of the three groups were significantly different ($P < 0.001$). There was no difference in ORR between the isoperfusion and hypoperfusion groups ($P = 0.171$); however, the DCR of these two groups differed significantly ($P = 0.007$). Unlike in our study, where all patients had HCC, Ikeda et al.[11] conducted their study on a heterogeneous group of patients, including those with primary and secondary liver tumors. They suggested that the homogeneous type had the best prognostic characteristics for HAIC for liver malignancies and was better than the hypoperfusion type and the perfusion defect type.[11]

We identified 14 tumors as the hypoperfusion type, and 13 out of those 14 tumors (92.9%) exhibited PD following HAIC treatment (Figure 4). Hypoperfusion-type tumors were found predominantly in patients with
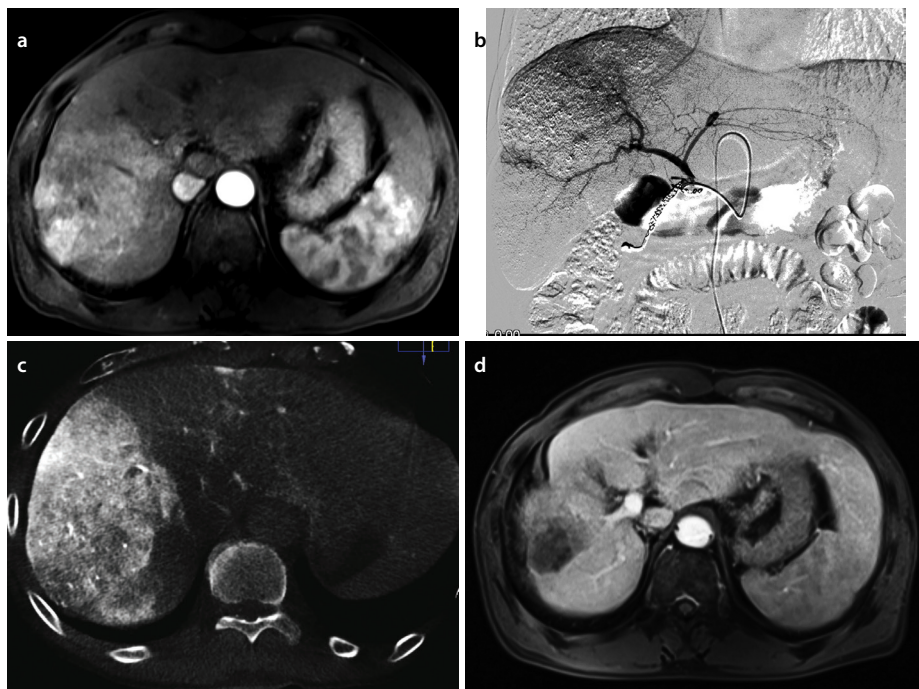


**Figure 3.** A 55-year-old male with hepatitis B virus, a Child–Pugh score of 5A, and refractory TACE. **(a)** An infiltrative right hepatic tumor with right portal vein tumor thrombosis. **(b)** Hepatic angiography via port when treated with hepatic arterial infusion chemotherapy (HAIC). **(c)** Contrast-enhanced cone-beam computed tomography (CT) on the day after port implantation: a right hyperperfusion tumor. **(d)** Follow-up contrast CT after five cycles of HAIC showing a complete response. TACE, transarterial chemoembolization.
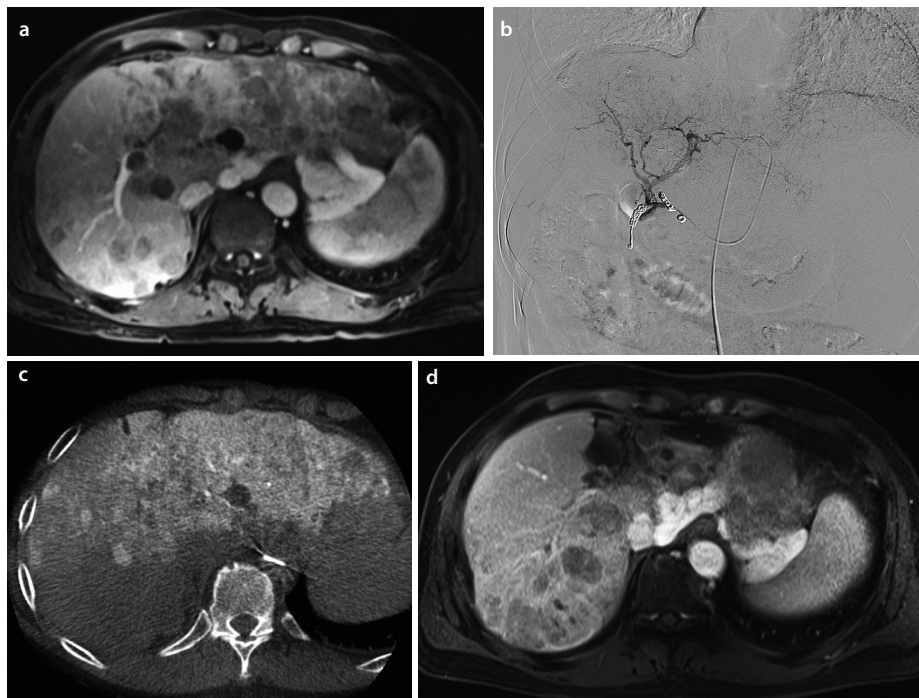


**Figure 4.** A 75-year-old male with hepatitis C virus and a Child–Pugh score of 7B. **(a)** Computed tomography (CT) image with multiple hepatocellular carcinoma nodes focusing mainly on the left hepatic lobe and the right posterior hepatic segment. **(b)** Hepatic angiography via port when treated with hepatic arterial infusion chemotherapy (HAIC). **(c)** Cone-beam CT on the day following port implantation: Hypoperfusion of the tumor was observed in the posterior segment and a segment of the left lobe located adjacent to the spleen, with isoperfusion tumors in the remaining liver parenchyma. **(d)** Follow-up contrast CT after four cycles of HAIC: the hypoperfusion tumor increased in size (progressive disease). A left hepatic tumor of the isoperfusion type, with decreased size and no enhanced-contrast media (partial response).

hepatic artery anatomical variations or extra-hepatic circulation that specifically involved the RIPA supplying the tumor. Yamagami et al.[9] reported that for patients with multiple hepatic arteries, redistribution was achieved by a single HAIC port implantation in the main artery and occluding the remaining arteries, thus maintaining the distribution of chemotherapeutic agents throughout the liver parenchyma. The authors also suggested that embolization of the RIPA is necessary to achieve the best distribution pattern.[9] Kobe et al.[20] reported that in patients with hepatic artery variants with a single port, redistribution after port placement did not alter the differences in reperfusion or change the tumor response to HAIC treatment when comparing both hemilivers. Kim et al.[19] also reported that patients with hepatic artery anatomical variations and two main blood supply sources could be implanted with dual ports, although there was no statistically significant difference in tumor response between monoport and dual-port groups.

Two limitations affected the present study. First, we used contrast injection on CBCT (1 mL/sec of contrast agent for 40 sec) to simulate the actual distribution of chemotherapeutic agents during HAIC as closely as possible; however, this injection condition still differed from the actual distribution of chemotherapeutic agents delivered via a port. Furthermore, the difference in viscosity between the contrast media and chemotherapeutic agents used may have led to discrepancies in the results. Second, the image quality on CBCT was not as good as that of conventional CT scanners, which may have reduced the accuracy of the evaluation. However, the utilization of CBCT following intervention has become increasingly prevalent and convenient in medical practice.

In conclusion, the hyperperfusion tumor type on CBCT had the best tumor response to HAIC, with a 65% ORR and a 92% DCR; of these, 10 tumors (10%) had a CR after HAIC treatment in patients with HCC. Tumor perfusion on CBCT after the implantation of a HAIC port in patients with HCC was associated with tumor response in HAIC-treated patients.

## Conflict of interest disclosure

The authors declared no conflicts of interest.

## References

1. McGlynn KA, Petrick JL, El-Serag HB. Epidemiology of hepatocellular carcinoma. Hepatology. 2021;73(Suppl 1):4-13. [CrossRef]

2. Reig M, Forner A, Rimola J, et al. BCLC strategy for prognosis prediction and treatment recommendation: The 2022 update. J Hepatol. 2022;76(3):681-693. [CrossRef]

3. Kudo M, Finn RS, Qin S, et al. Lenvatinib versus sorafenib in first-line treatment of patients with unresectable hepatocellular carcinoma: a randomised phase 3 non-inferiority trial. Lancet. 2018;391(10126):1163-1173. [CrossRef]

4. Lyu N, Kong Y, Mu L, et al. Hepatic arterial infusion of oxaliplatin plus fluorouracil/leucovorin vs. sorafenib for advanced hepatocellular carcinoma. J Hepatol. 2018;69(1):60-69. [CrossRef]

5. Kudo M, Ueshima K, Yokosuka O, et al. Sorafenib plus low-dose cisplatin and fluorouracil hepatic arterial infusion chemotherapy versus sorafenib alone in patients with advanced hepatocellular carcinoma (SILIUS): a randomised, open label, phase 3 trial. Lancet Gastroenterol Hepatol. 2018;3(6):424-432. [CrossRef]

6. Korean Liver Cancer Association (KLCA); National Cancer Center (NCC), Goyang, Korea. 2018 Korean Liver Cancer Association-National Cancer Center Korea Practice Guidelines for the Management of Hepatocellular Carcinoma. Korean J Radiol. 2019;20(7):1042-1113. [CrossRef]

7. Kudo M, Kawamura Y, Hasegawa K, et al. Management of hepatocellular carcinoma in Japan: JSH consensus statements and recommendations 2021 Update. Liver Cancer. 2021;10(3):181-223. [CrossRef]

8. Shao YY, Wang SY, Lin SM; Diagnosis Group; Systemic Therapy Group. Management consensus guideline for hepatocellular carcinoma: 2020 update on surveillance, diagnosis, and systemic treatment by the Taiwan Liver Cancer Association and the Gastroenterological Society of Taiwan. J Formos Med Assoc. 2021;120(4):1051-1060. [CrossRef]

9. Yamagami T, Kato T, Tanaka O, Hirota T, Nishimura T. Influence of extrahepatic arterial inflow into the posterior segment or caudate lobe of the liver on repeated hepatic arterial infusion chemotherapy. J Vasc Interv Radiol. 2005;16(4):457-463. [CrossRef]

10. Tamura Y, Ikeda O, Nakasone Y, et al. Effect of gravity on drug distribution after port-catheter implantation for hepatic arterial infusion chemotherapy: evaluation of the relationship between the injection posture and intrahepatic perfusion on fused images acquired with a combined SPECT/CT system. Acad Radiol. 2009;16(6):662-668. [CrossRef]

11. Ikeda O, Kusunoki S, Nakaura T, et al. Comparison of fusion imaging using a combined SPECT/CT system and intra-arterial CT: assessment of drug distribution by an implantable port system in patients undergoing hepatic arterial infusion chemotherapy. Cardiovasc Intervent Radiol. 2006;29(3):371-379. [CrossRef]

12. Ikeda O, Tamura Y, Nakasone Y, et al. Evaluation of intrahepatic perfusion on fusion imaging using a combined CT/SPECT system: influence of anatomic variations on hemodynamic modification before installation of implantable port systems for hepatic arterial infusion chemotherapy. Cardiovasc Intervent Radiol. 2007;30(3):383-391. [CrossRef]

13. Kim B, Won JH, Kim J, et al. Hepatic Arterial Infusion Chemotherapy for Advanced Hepatocellular Carcinoma: Radiologic and Clinical Factors Predictive of Survival. AJR Am J Roentgenol. 2021;216(6):1566-1573. [CrossRef]

14. Lee J, Han JW, Sung PS, et al. Comparative analysis of lenvatinib and hepatic arterial infusion chemotherapy in unresectable hepatocellular carcinoma: a multi-center, propensity score study. J Clin Med. 2021;10(18):4045. [CrossRef]

15. Eisenhauer EA, Therasse P, Bogaerts J, et al. New response evaluation criteria in solid tumours: revised RECIST guideline (version 1.1). Eur J Cancer. 2009;45(2):228-247. [CrossRef]

16. Seki H, Ozaki T, Takaki S, Ooi H, Oda J, Shiina M. Using slow-infusion MR arteriography and an implantable port system to assess drug distribution at hepatic arterial infusion chemotherapy. AJR Am J Roentgenol. 2003;180(3):681-686. [CrossRef]

17. Pung L, Ahmad M, Mueller K, et al. The role of cone-beam CT in transcatheter arterial chemoembolization for hepatocellular carcinoma: a systematic review and meta-analysis. J Vasc Interv Radiol. 2017;28(3):334-341. [CrossRef]

18. Oh JS, Chun HJ, Choi BG, Lee HG. Transarterial chemoembolization with drug-eluting beads in hepatocellular carcinoma: usefulness of contrast saturation features on cone-beam computed tomography imaging for predicting short-term tumor response. J Vas Interv Radiol. 2013;24(4):483-489. [CrossRef]

19. Kim SH, Oh JS, Chun HJ, Choi BG, Lee HG. Dual-Port versus mono-port implantation for intra-arterial chemoinfusion therapy for treatment of hepatocellular carcinoma in patients with anatomic hepatic artery variation. J Vasc Interv Radiol. 2019;30(1):23-30. [CrossRef]

20. Kobe A, Deschamps F, Meyblum L, et al. Coil embolization of variant hepatic arteries during percutaneous arterial port catheter placement for intraarterial chemotherapy: analysis of intrahepatic perfusion redistribution and treatment efficacy. Cardiovasc Intervent Radiol. 2023;46(1):69-79. [CrossRef]

# 2023 Author Index

# 2023 Author Index

# 2023 Author Index

# 2023 Author Index

## 2023 Author Index

# 2023 Subject Index